

This is to certify that the
thesis entitled

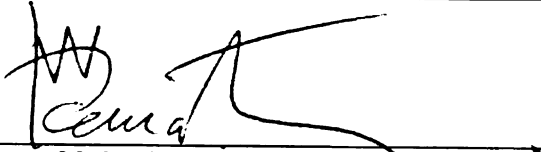
SUBSTITUTION STUDIES IN $CsPb_mBi_3Te_{5+m}$ AND $NaPb_mSbTe_{m+2}$
FOR THERMOELECTRIC APPLICATIONS

presented by

AURELIE GUEGUEN

has been accepted towards fulfillment
of the requirements for the

doctoral degree in Chemistry



Major Professor's Signature

12/30/08

Date

PLACE IN RETURN BOX to remove this checkout from your record.
TO AVOID FINES return on or before date due.
MAY BE RECALLED with earlier due date if requested.

DATE DUE	DATE DUE	DATE DUE

SUBSTITUTION STUDIES IN $\text{CsPb}_m\text{Bi}_3\text{Te}_{5+m}$ AND $\text{NaPb}_m\text{SbTe}_{m+2}$ FOR
THERMOELECTRIC APPLICATIONS

By

Aurélie Guéguen

A DISSERTATION

Submitted to
Michigan State University
in partial fulfillment of the requirements
for the degree of

DOCTOR OF PHILOSOPHY

Chemistry

2009

ABSTRACT

SUBSTITUTION STUDIES IN $\text{CsPb}_m\text{Bi}_3\text{Te}_{5+m}$ AND $\text{NaPb}_m\text{SbTe}_{m+2}$ FOR THERMOELECTRIC APPLICATIONS

By

Aur lie Gu g en

Thermoelectric devices convert thermal energy into electrical power or vice versa. If materials with thermoelectric figure of merit ≥ 3 can be synthesized, thermoelectric devices will not be restricted to niche applications such as spacecraft power generation and will have a significant impact on the economy. Power generation from waste heat recovery would be an alternative energy resource whereas electronic cooling would significantly increase computing processor speed. Good thermoelectric materials require high electrical conductivity, large thermopower and low thermal conductivity. Complex chalcogenides materials, such as CsBi_4Te_6 , exhibit promising thermoelectric properties. It consists of Cs^+ cations weakly bound to $[\text{Bi}_4\text{Te}_6]^-$ layers. The Cs^+ cations act as rattlers, hence contributing to a reduction of the lattice thermal conductivity. Partial substitution of Bi by Pb resulted in the discovery of the homologous family $\text{CsPb}_m\text{Bi}_3\text{Te}_{5+m}$. Further substitution studies both on the Cs and Bi sites lead to the synthesis of the new compounds $\text{Cs}_{0.76}\text{K}_{0.74}\text{Bi}_{3.5}\text{Te}_6$ (1), $\text{CsNa}_{0.98}\text{Bi}_{4.01}\text{Te}_7$ (2), $\text{Cs}_{0.69}\text{Ca}_{0.65}\text{Bi}_{3.34}\text{Te}_6$ (3),

$\text{Rb}_{0.82}\text{Pb}_{0.82}\text{Bi}_{3.18}\text{Te}_6$ (4), $\text{Rb}_{0.19}\text{K}_{1.31}\text{Bi}_{3.50}\text{Te}_6$ (5), $\text{RbSnBi}_3\text{Te}_6$ (6), $\text{Rb}_{0.94}\text{Ca}_{0.94}\text{Bi}_{3.06}\text{Te}_6$ (7), $\text{RbYbBi}_3\text{Te}_6$ (8) and $\text{KSnSb}_3\text{Te}_6$ (9). However synthesis conditions could not yet be optimized to prepared pure phase with good quality crystal.

Doped PbTe is used in commercial applications. Recent studies on preparation of bulk nanostructured PbTe have shown significant improvement in the thermoelectric figure of merit, achieved mainly through reduction of lattice thermal conductivity. The observation by TEM of nanoprecipitates embedded in the PbTe matrix is believed to be the origin of their low thermal conductivity. A figure of merit $ZT \sim 1.6$ at 650 K was reported for example for the p-type $\text{Na}_{1-x}\text{Pb}_m\text{Sb}_y\text{Te}_{m+2}$ (SALT) system. Partial substitution of Pb by Sn was studied through the synthesis of the $\text{NaPb}_{18-x}\text{Sn}_x\text{SbTe}_{20}$ series and increases the carrier concentration. As a result, an increase in electrical conductivity and a decrease in thermopower were observed with increasing amount of Sn. Such substitution did not affect the formation of nanoprecipitates, which were observed with TEM along with lamellar features. The substitutions did not result in higher figure of merit. Replacing Sb by Bi produced weaker samples. The K analog series, $\text{KPb}_{18-x}\text{Sn}_x\text{SbTe}_{20}$, was prepared as well and resulted in weaker and more water-sensitive specimens. These different studies show that the best p-type materials so far are $\text{Ag}(\text{Pb}_{1-y}\text{Sn}_y)_m\text{SbTe}_{2+m}$ (LASTT) and $\text{Na}_{1-x}\text{Pb}_m\text{Sb}_y\text{Te}_{m+2}$ (SALT) systems. Substituting Ag by Cu in the n-type $\text{AgPb}_m\text{SbTe}_{m+2}$ (LAST) system resulted in phase segregation of Cu_2Te and Sb_2Te_3 in the PbTe matrix. The figure of merit of the specimens was lower than that of LAST.

ACKNOWLEDGMENTS

First, I would like to thank my advisor, Prof. Mercouri G. Kanatzidis, for giving me the opportunity to join his lab and learn about solid state chemistry and thermoelectric materials.

Then, I would like to thank the Kanatzidis group, previous and current members, for their help, support and helpful discussions. I would like to thank particularly Joseph Sootsman and Melanie Francesco for their help and friendship.

I would like also to thank our collaborators. The Hall effect measurements were done at University of Michigan in collaboration with Prof. Ctirad Uher, Huijun Kong, Steven Moses and Chang-Pen Li. SEM studies were carried out using the facilities at the Center of Advanced Microscopy at Michigan State University and at the NUANCE center at Northwestern University. Part of the TEM studies was done by Robert Pcionek at the Center of Advanced Microscopy at Michigan State University. The rest of the TEM work was done by Dr. Jiaqing He and Prof. Vinayak Dravid at the NUANCE center at Northwestern University.

Finally, I would like to thank my family and friends for their support. I met great friends during my stay at the United-States.

TABLE OF CONTENTS

LIST OF TABLES	xi
----------------------	----

LIST OF FIGURES	xiii
-----------------------	------

CHAPTER 1. <i>Introduction to Thermoelectrics</i>	1
1.1 Thermoelectric concepts.....	1
1.2 Optimization of the figure of merit	5
1.3. Bulk thermoelectric materials.....	8
1.4. Complex chalcogenide systems as potential thermoelectric materials.....	11
1.5. Low-dimensional and nanostructured materials.....	16

CHAPTER 2. <i>Substitutions in the CsPb_mBi₃Te_{5+m} System</i>	27
2.1 Introduction	27
2.2 Experimental section	29
2.2.1 Synthesis	29
2.2.2 Characterization techniques	33
2.3. Results and discussion.....	35
2.3.1 Structure description	35
2.3.2 Characterizations.....	44
2.3.3 Preliminary thermoelectric results	53
2.4. Conclusions	54

CHAPTER 3. <i>Preparation and Characterization of Members of the Series NaPb_mSbTe_{m+2} with m=6, 8, 12</i>	57
3.1 Introduction	57
3.2 Experimental section	59
3.2.1 Synthesis	59
• Method 1	59
• Method 2	60
• Method 3	60
• Method 4	60
• Method 5	60
• Method 6	61
• Method 7	61

• Method 8	61
• Method 9	61
3.2.2 Characterization techniques	62
3.3. Results and discussion	65
3.3.1 Method 1	65
3.3.2 Method 2	81
3.3.3 Method 3	83
3.3.3 Method 4	84
3.3.3 Method 5	85
3.3.3 Method 6	86
3.3.3 Method 7	89
3.3.3 Method 8	96
3.3.3 Method 9	97
3.4. Concluding remarks	99

CHAPTER 4. Thermoelectric Properties of the Nanostructured Materials $\text{NaPb}_{18-x}\text{Sn}_x\text{MTe}_{20}$ ($M=\text{Sb, Bi}$)

$\text{NaPb}_{18-x}\text{Sn}_x\text{MTe}_{20}$ ($M=\text{Sb, Bi}$)	103
4.1 Introduction	103
4.2 Experimental section	105
4.2.1 Synthesis	105
4.2.2 Characterization techniques	106
4.3. Results and discussion	109
• Structure and characterization	109
• Scanning electron microscopy	115
• Electronic transport properties	119
• Optical spectroscopy	128
• Thermal transport properties	131
• High resolution transmission electron microscopy	137
4.4. Conclusions	144

CHAPTER 5. Synthesis and Characterization of the $\text{KPb}_{18-x}\text{Sn}_x\text{SbTe}_{20}$ ($x=0, 2, 5, 9, 13, 16$ and 18) series

$\text{KPb}_{18-x}\text{Sn}_x\text{SbTe}_{20}$ ($x=0, 2, 5, 9, 13, 16$ and 18) series	149
5.1 Introduction	149
5.2 Experimental section	152
5.2.1 Synthesis	152
5.2.2 Characterization techniques	154
5.3. Results and discussion	156
• Structure and characterization	156
• Scanning electron microscopy	158
• Optical band gap measurements	163
• Electronic transport properties	163
• Thermal transport properties	171
5.4. Conclusions	174

CHAPTER 6. The systems $CuPb_mSbTe_{m+2}$ ($m=8, 12, 18, 20, 22, 30, 40, 50$), $CuPb_{18-x}Sn_xSbTe_{20}$ ($x=0, 5, 9, 13, 18$), Cu_2Te/Sb_2Te_3 and $Cu_2Te/PbTe$.....	177
6.1. Introduction	177
6.2. $CuPb_mSbTe_{m+2}$ ($m = 8, 12, 18, 20, 22, 30, 40$ and 50)	179
6.2.1. Experimental section.....	179
6.2.1.1. Synthesis	179
6.2.1.2. Characterization techniques	180
6.2.2. Results and discussion	182
• Structure and characterization.....	182
• Scanning electron microscopy	183
• Thermal analysis	185
• Electronic transport properties	188
• Thermal transport properties	189
6.3. $CuPb_{18-x}Sn_xSbTe_{20}$ ($x=0, 5, 9, 13, 18$).....	192
6.3.1. Experimental section.....	192
6.3.2. Results and discussion	193
• Structure and characterization.....	193
• Scanning Electron Microscopy	193
• Electronic transport properties	198
• Thermal transport properties	199
6.4. Investigation of the system $Cu/Sb/Te$	201
6.4.1. Motivation.....	201
6.4.2. Experimental section.....	202
6.4.3. Results and discussion	202
• Structure and characterization.....	202
• Scanning electron microscopy	203
• DTA analysis.....	208
6.5. Doping studies of $PbTe$ with Cu_2Te	208
6.5.1. Motivation.....	208
6.5.2. Experimental section.....	209
6.5.3. Results and discussion	209
• Structure and characterization.....	209
• Scanning electron microscopy	209
• DTA analysis.....	213
• Electronic transport properties	214
6.6. Conclusions	215
CHAPTER 6. Conclusions and Future Directions	219

LIST OF TABLES

Table 2-1	Ratio and quantity of elements mixed for (1), (2), (3), (4), (5), (6), (7), (8) and (9).....	30
Table 2-2	Summary of the crystallographic data for (1), (2) (3), (4) and (5).....	38
Table 2-3	Summary of the crystallographic data for RbSnBi ₃ Te ₆ (6), Rb _{0.94} Ca _{0.94} Bi _{3.06} Te ₆ (7), RbYbBi ₃ Te ₆ (8) and KSnSb ₃ Te ₆ (9)	39
Table 2-4	Metal-tellurium and alkali site-tellurium bond distances (Å) in compounds (1), (3), (4), (5), (6), (7) and (8).....	40
Table 2-5	Metal-Te and alkali metal-Te1 bond distances (Å) in compound (2).....	41
Table 2-6	Metal-Te and alkali metal-Te bond distances (Å) in compound (9).....	41
Table 2-7	Atomic coordinates and equivalent isotropic displacement parameters (Å ² x 10 ³) of the metal and alkali metal positions for (1), (3), (4), (5), (6), (7) and (8). U(eq) is defined as one third of the traces of the orthogonalized U _{ij} tensors.	42
Table 2-8	Atomic coordinates and equivalent isotropic displacement parameters (Å ² x 10 ³) for (2). U(eq) is defined as one third of the traces of the orthogonalized U _{ij} tensors.	43
Table 2-9	Atomic coordinates and equivalent isotropic displacement parameters (Å ² x 10 ³) for (9). U(eq) is defined as one third of the traces of the orthogonalized U _{ij} tensors.	43
Table 2-10	Preliminary thermoelectric measurements on the compounds (1) and (4).....	53
Table 3-1	Concentrations of the standards used for the ICP-AES calibration.....	63
Table 3-2	Melting and crystallization points for NaPb ₈ SbTe _{m+2} (m=6, 8, 12).....	65
Table 3-3	Summary of the elemental concentrations of Na and Sb obtained with ICP-AES	70
Table 3-4	Comparison between experimental and theoretical mass percentages of Na and Sb in the powders analyzed with ICP-AES.....	71

Table 4-1	Amounts of elements used to prepare $\text{NaPb}_{18-x}\text{Sn}_x\text{SbTe}_{20}$	106
Table 4-2	Amounts of elements used to prepare $\text{NaPb}_{18-x}\text{Sn}_x\text{BiTe}_{20}$	106
Table 4-3	Summary of the physical and electronic properties of the materials $\text{NaPb}_{18-x}\text{Sn}_x\text{SbTe}_{20}$	130
Table 4-4	Summary of the physical and electronic properties of the materials $\text{NaPb}_{18-x}\text{Sn}_x\text{BiTe}_{20}$	130
Table 4-5	Total and lattice thermal conductivities of $\text{NaPb}_{18-x}\text{Sn}_x\text{SbTe}_{20}$ ($x=0, 3, 5, 9, 13$ and 16) at 300 and 550 K	136
Table 4-6	Total and lattice thermal conductivities of $\text{NaPb}_{18-x}\text{Sn}_x\text{BiTe}_{20}$ ($x=0, 3, 5, 9$ and 16) at 300 and 550 K	136
Table 5-1	Amounts of elements used to prepare $\text{KPb}_{18-x}\text{Sn}_x\text{SbTe}_{20}$	153
Table 5-2	Amounts of elements used to prepare $\text{KPb}_{18-x}\text{Sn}_x\text{BiTe}_{20}$	154
Table 5-3	Summary of the physical and electronic properties of the materials $\text{KPb}_{18-x}\text{Sn}_x\text{SbTe}_{20}$	170
Table 5-4	Summary of the physical and electronic properties of the materials $\text{KPb}_{18-x}\text{Sn}_x\text{BiTe}_{20}$	170
Table 6-1	Amounts of elements used to prepare the series $\text{CuPb}_m\text{SbTe}_{m+2}$	180
Table 6-2	Amount of elements used for to prepare the series $\text{CuPb}_{18-x}\text{Sn}_x\text{SbTe}_{20}$	192

LIST OF FIGURES

Figure 1-1	Scheme of (a) a cooling device and (b) a generator.....	2
Figure 1-2	Figure of merit ZT shown as a function of temperature for several bulk materials.....	5
Figure 1-3	Evolution of the Seebeck coefficient and the electrical conductivity as a function of the carrier concentration.....	6
Figure 1-4	Density of states for electrons in bulk semiconductors (3D), quantum wells (2D), quantum wires (1D) and quantum dots (0D)	7
Figure 1-5	Structure of a skutterutide antimonide.....	9
Figure 1-6	Various building blocks (shaded) based on different “cuts” of the NaCl-type structure. The diagram is view down with [011] plane. Black and white circles are bismuth and chalcogen atoms, respectively	13
Figure 1-7	Perspective view of the CsBi ₄ Te ₆ along the b-axis	14
Figure 1-8	The structures of (a) CsPbBi ₃ Te ₆ , (b) CsPb ₂ Bi ₃ Te ₇ , (c) CsPb ₃ Bi ₃ Te ₈ and (d) CsPb ₄ Bi ₃ Te ₈ in projection down the c axis for (a) and (c) and the a axis for (b) and (d).....	16
Figure 2-1	Structure type of (a) A _{1-x} M ₄ Te ₆ along the c axis and (b) of CsNa _{0.98} Bi _{4.01} Te ₇ along the a-axis	36
Figure 2-2	Crystal structure of KSnSb ₃ Te ₆ viewed along the b-axis	37
Figure 2-3	(a) Comparison between the calculated and experimental powder X-ray diffraction patterns of compound (1) and (b) DTA results for compound (1).....	44
Figure 2-4	Comparison between the powder X-ray diffraction patterns of ground samples taken from top and bottom of the ingot with nominal composition Cs _{0.76} K _{0.74} Bi _{3.5} Te ₆ prepared in the vertical furnace, the calculated powder pattern and that of CsBi ₄ Te ₆	46
Figure 2-5	DTA results on powders taken from (a) the top and (b) the bottom of the material Cs _{0.6} K _{0.9} Bi _{3.5} Te ₆ prepared in a vertical furnace.....	47

Figure 2-6	DTA results of the batch from which the compound $\text{Cs}_{0.69}\text{Ca}_{0.65}\text{Bi}_{3.34}\text{Te}_6$ was synthesized.....	48
Figure 2-7	Picture of the ingot with composition $\text{Rb}_{0.82}\text{Pb}_{0.82}\text{Bi}_{3.18}\text{Te}_6$ prepared with the Bridgman technique	49
Figure 2-8	(a) X-ray diffraction patterns of powders from top, middle and bottom of the ingot with composition (4) prepared by Bridgman technique and (b) DTA analysis of the powder from the middle of the ingot	50
Figure 2-9	(a) Comparison between the experimental and calculated powder X-ray diffraction patterns for compound (6) and that of BiTe and (b) DTA analysis of the powder from the middle of the ingot	51
Figure 2-10	SEM image of the needle with composition $\text{KSnSb}_3\text{Te}_6$.	52
Figure 3-1	Powder X-ray diffraction from samples from top and bottom part of the ingots with composition (a) $\text{NaPb}_6\text{SbTe}_8$, (b) the area between $2\theta = 80$ and 110 deg is enlarged to show peak splitting; (c) $\text{NaPb}_8\text{SbTe}_{10}$, the area between $2\theta = 60$ and 80 deg is enlarged to show peak splitting; and (e) $\text{NaPb}_{12}\text{SbTe}_{14}$, the area between $2\theta = 80$ and 110 deg is enlarged to show peak splitting. All three specimens were prepared with method 1	66
Figure 3-2	Thermal analysis for (a) $\text{NaPb}_6\text{SbTe}_8$, (b) $\text{NaPb}_8\text{SbTe}_{10}$ and (c) $\text{NaPb}_{12}\text{SbTe}_{14}$ prepared with method 1	67
Figure 3-3	BSE images of one of the surface of the sample $\text{NaPb}_{12}\text{SbTe}_{14}$ used for thermoelectric characterization. EDS analysis on the inclusions indicated the regions to contain $\sim 67\%$ Sb, $\sim 22\%$ Te and $\sim 1\%$ Pb. The matrix is pure PbTe.....	69
Figure 3-4	Diffuse reflectance absorption spectra of (a) $\text{NaPb}_6\text{SbTe}_8$, (b) $\text{NaPb}_8\text{SbTe}_{10}$, (c) $\text{NaPb}_{12}\text{SbTe}_{14}$ and (d) $\text{NaPb}_{18}\text{SbTe}_{20}$ prepared with method 1	72
Figure 3-5	Temperature dependence of (a) the electrical conductivity, (b) the thermopower and (c) the power factor the compounds $\text{NaPb}_m\text{SbTe}_{m+2}$ ($m=6, 8, 12$ and 18) and $\text{Na}_{0.95}\text{Pb}_{20}\text{SbTe}_{22}$ prepared with method 1	74

Figure 3-6	Comparison of (a) electrical conductivity and (b) thermopower collected during the first and second measurement for $\text{NaPb}_8\text{SbTe}_{10}$ prepared with method 1	75
Figure 3-7	Temperature dependence of (a) electrical conductivity and (b) thermopower measured for 2 different samples with composition $\text{NaPb}_8\text{SbTe}_{10}$ prepared with method 1.....	76
Figure 3-8	Temperature dependence of (a) the total and (b) lattice thermal conductivity for the materials $\text{NaPb}_m\text{SbTe}_{m+2}$ ($m=6, 8, 12, 18$) and $\text{Na}_{0.95}\text{Pb}_{20}\text{SbTe}_{22}$ prepared with method 1	78
Figure 3-9	Figure of merit ZT for $\text{NaPb}_m\text{SbTe}_{m+2}$ ($m=6, 8, 12, 18$) and $\text{Na}_{0.95}\text{Pb}_{20}\text{SbTe}_{22}$ prepared with method 1	79
Figure 3-10	Typical HRTEM images obtained for $\text{NaPb}_8\text{SbTe}_{10}$ prepared with method 1.....	80
Figure 3-11	Powder X-ray diffraction of $\text{NaPb}_8\text{SbTe}_{10}$ prepared by method 2	81
Figure 3-12	Comparison of (a) the electrical conductivity, (b) the thermopower and (c) the power factor of the compounds $\text{NaPb}_8\text{SbTe}_{10}$ prepared by methods 1 and 2	82
Figure 3-13	Comparison of the (a) total and (b) lattice thermal conductivities for samples prepared by methods 1 and 2	83
Figure 3-14	Powder X-ray diffraction of $\text{NaPb}_8\text{SbTe}_{10}$ prepared with method 3. The area between $2\theta = 35$ and 60 deg is enlarged to show the presence of extra peaks can be assigned to NaSbTe_2	84
Figure 3-15	Powder X-ray diffraction of $\text{NaPb}_8\text{SbTe}_{10}$ prepared with method 4.....	85
Figure 3-16	Powder X-ray diffraction of $\text{NaPb}_8\text{SbTe}_{10}$ prepared with method 5.....	86
Figure 3-17	Powder X-ray diffraction patterns of (a) $\text{NaPb}_{7.6}\text{Sn}_{0.4}\text{SbTe}_{10}$, (b) $\text{NaPb}_6\text{Sn}_2\text{SbTe}_{10}$, (c) $\text{NaPb}_4\text{Sn}_4\text{SbTe}_{10}$ and (d) $\text{NaPb}_2\text{Sn}_6\text{SbTe}_{10}$	87
Figure 3-18	BSE images from areas close to (a) the top and (b) the bottom of the ingot $\text{NaPb}_4\text{Sn}_4\text{SbTe}_{10}$. (c) BSE image from s sample from the middle of the sample $\text{NaPb}_2\text{Sn}_6\text{SbTe}_{10}$	88

Figure 3-19	Powder X-ray diffraction of powders from (a) $\text{Na}_{0.5}\text{Pb}_8\text{SbTe}_{10}$, (b) $\text{Na}_{0.5}\text{Pb}_8\text{Sb}_{0.75}\text{Te}_{10}$, (c) $\text{Na}_{0.5}\text{Pb}_8\text{Sb}_{0.5}\text{Te}_{10}$ and (d) $\text{Na}_{0.5}\text{Pb}_8\text{Sb}_{0.25}\text{Te}_{10}$	89
Figure 3-20	BSE images of areas from a part close to the top of the ingot $\text{Na}_{0.5}\text{Pb}_8\text{Sb}_{0.75}\text{Te}_{10}$	91
Figure 3-21	BSE images of sample from (a) bottom and (b) middle of the ingot $\text{Na}_{0.5}\text{Pb}_8\text{Sb}_{0.5}\text{Te}_{10}$	92
Figure 3-22	Temperature dependence of the (a) electrical conductivity, (b) thermopower and (c) power factor of $\text{Na}_{0.5}\text{Pb}_8\text{Sb}_{0.25}\text{Te}_{10}$ and $\text{NaPb}_8\text{SbTe}_{10}$	94
Figure 3-23	First and second sets of measurements for the (a) electrical conductivity and (b) thermopower of the compound $\text{Na}_{0.5}\text{Pb}_8\text{Sb}_{0.25}\text{Te}_{10}$	95
Figure 3-24	Temperature dependence of the (a) electrical conductivity and (b) thermopower of two different ingots with composition $\text{Na}_{0.5}\text{Pb}_8\text{Sb}_{0.25}\text{Te}_{10}$	96
Figure 3-25	Powder X-ray diffraction patterns from powders from the composition $\text{NaPb}_8\text{SbTe}_{10}$ using Na_2Te as a source of Na	96
Figure 3-26	Comparison between the X-ray diffraction patterns from powders from the original ingot and the two pellets prepared from that ingot	97
Figure 3-27	SEM images of the surface of (a) HP1 and (2) HP2.....	98
Figure 4-1	Powder X-ray diffraction patterns of $\text{NaPb}_{18-x}\text{Sn}_x\text{MTe}_{20}$ with $x=5, 9, 13, 16$ for (a) $M=\text{Sb}$ and (b) $M=\text{Bi}$; variation of the unit cell parameter as a function of x for (c) $M=\text{Sb}$ and (d) $M=\text{Bi}$	111
Figure 4-2	X-ray powder diffraction patterns of (a) $\text{Na}_{0.8}\text{Pb}_{13}\text{Sn}_5\text{SbTe}_{20}$, (b) $\text{Na}_{0.8}\text{Pb}_{13}\text{Sn}_5\text{Sb}_{0.4}\text{Te}_{20}$. For each composition, powder from both top and bottom of the ingot was analyzed to check homogeneity along the ingot. The small arrows indicate diffraction peaks that do not belong to the PbTe structure-type and indicate the presence of Sb_2Te_3 as a minor phase	112
Figure 4-3	(a) Typical DTA results of the composition $\text{NaPb}_5\text{Sn}_{13}\text{SbTe}_{20}$, (b) variation of the melting and crystallization points of $\text{NaPb}_{18-x}\text{Sn}_x\text{SbTe}_{20}$ as a function of x	114

Figure 4-4	Infrared absorption spectra near the band edge of samples $\text{NaPb}_{18-x}\text{Sn}_x\text{SbTe}_{20}$ with $x=9, 13, 16$ and 18	115
Figure 4-5	BSE imaging of inclusions observed from (a) part close to the top and (b) part close to the bottom of the ingot $\text{NaPb}_9\text{Sn}_9\text{SbTe}_{20}$, (c) middle part of $\text{NaPb}_{13}\text{Sn}_5\text{SbTe}_{20}$	117
Figure 4-6	BSE imaging of samples from middle part of the ingots (a) $\text{NaPb}_{13}\text{Sn}_5\text{BiTe}_{20}$ and (b)-(c) $\text{NaPb}_2\text{Sn}_{16}\text{BiTe}_{20}$	118
Figure 4-7	Electronic transport properties of the $\text{NaPb}_{18-x}\text{Sn}_x\text{SbTe}_{20}$ samples: (a) electrical conductivity, (b) variation of the power law dependence of the electrical conductivity ($T^{-\lambda}$) as a function of x (the λ parameters were extracted from the data of panel (a)), (c) thermopower, (d) power factor. The point marks in the inset of panel (a) identify all samples and apply to panels (c) and (d).....	121
Figure 4-8	Temperature dependence of (a) the carrier concentration and (b) carrier mobility for $\text{NaPb}_{13}\text{Sn}_5\text{MTe}_{20}$ ($M=\text{Sb, Bi}$).....	122
Figure 4-9	(a) Temperature dependence of the thermoelectric properties of the $\text{NaPb}_{13}\text{Sn}_5\text{SbTe}_{20}$ and $\text{Na}_{0.8}\text{Pb}_{13}\text{Sn}_5\text{Sb}_y\text{Te}_{20}$ ($y=0.4, 0.6, 0.8, 1$) compositions: (a) electrical conductivity, (b) thermopower, (c) power factor. The point marks in the inset of panel (b) apply to plots (a) and (c).....	124
Figure 4-10	T Electronic transport properties of the $\text{NaPb}_{18-x}\text{Sn}_x\text{BiTe}_{20}$ samples: (a) electrical conductivity, (b) variation of the power law dependence of the electrical conductivity ($T^{-\lambda}$) as a function of x (the λ parameters were extracted from the data of panel (a)), (c) thermopower, (d) power factor. The point marks in the inset of panel (a) identify all samples and apply to all panels (c) and (d).....	127
Figure 4-11	Specular reflectance spectra of (a) $\text{NaPb}_{18-x}\text{Sn}_x\text{SbTe}_{20}$ ($x=3, 5, 9$) and (b) $\text{NaPb}_{18-x}\text{Sn}_x\text{BiTe}_{20}$ ($x=3, 5, 9$).....	129
Figure 4-12	Temperature dependence of (a) the total thermal conductivity of the $\text{NaPb}_{18-x}\text{Sn}_x\text{SbTe}_{20}$ compositions and (b) their lattice thermal conductivity component (the electronic thermal conductivity was estimated using the Wiedemann-Franz law with $L_0=2.45 \cdot 10^{-8} \text{ W}\Omega\text{K}^{-1}$); (c) the total thermal conductivity of the $\text{NaPb}_{18-x}\text{Sn}_x\text{BiTe}_{20}$ compositions and (d) their lattice thermal conductivity component.	

Figure 4-13	Temperature dependence of the thermal conductivity for the compositions (a) $\text{NaPb}_{18}\text{SbTe}_{20}$, (b) $\text{NaPb}_9\text{Sn}_9\text{SbTe}_{20}$ and (c) $\text{NaPb}_5\text{Sn}_{13}\text{SbTe}_{20}$	133
Figure 4-14	Temperature dependence of the figure of merit ZT for (a) $\text{NaPb}_{18-x}\text{Sn}_x\text{SbTe}_{20}$ ($x=0, 3, 5, 9, 13, 16$) and (b) $\text{NaPb}_{18-x}\text{Sn}_x\text{BiTe}_{20}$ ($x=0, 3, 5, 9$ and 16)	135
Figure 4-15	Typical HRTEM images of (a) and (b) $\text{NaPb}_{13}\text{Sn}_5\text{BiTe}_{20}$ and (c) and (d) $\text{NaPb}_{13}\text{Sn}_5\text{SbTe}_{20}$	138
Figure 4-16	(a) A multitude of precipitates were observed in low magnification Z-contrast image for $\text{NaPb}_{13}\text{Sn}_5\text{BiTe}_{20}$; (b) high magnification STEM image showing the weak contrast of some small precipitates; (c) Line scanning profile of the selected atomic array in (b), the positions that the dark arrows point out are Te, and those marked by gray arrows mainly come from Pb.....	139
Figure 4-17	(a) High magnification high resolution TEM image for $\text{NaPb}_{13}\text{Sn}_5\text{BiTe}_{20}$ and (b) enlarged part show the lattice parameters of the precipitate and that of the matrix are different; (c) and (d) FFT images of the two regions C and D in (a)	140
Figure 4-18	(a) Different precipitate from $\text{NaPb}_{13}\text{Sn}_5\text{BiTe}_{20}$ with different contrast lamella structure labeled as ABAB... (b-f) are strain mapping for this precipitate; (b) power spectrum image in (a) with $\mathbf{g}_1=002$ and $\mathbf{g}_2=220$. (c) and (d) 4.2.1. show the strain map profile along the 001 direction (ϵ_{yy}) and the shear direction(ϵ_{xy}), respectively	142
Figure 4-19	(a)-(d) Different magnification images for $\text{NaPb}_{13}\text{Sn}_5\text{BiTe}_{20}$ with another type of lamellar structure. (a) only shows the saw shape at the edge of sample; (b) further ion milling for sample, the lamella profile appear in the region close to edge, (c) strong contrast was observed in the area far from the edge; (d) From the high resolution image, the lamella was indexed as 112 direction, which is different from the first type lamella in Figure 4-16.....	143
Figure 5-1	X-ray powder diffraction patterns of $\text{KPb}_{18-x}\text{Sn}_x\text{MTe}_{20}$ with $x=0, 2, 5, 9, 13, 16$ and 18 for (a) $M=\text{Sb}$ and (c) $M = \text{Bi}$; variation of the unit cell parameter as a function of x for (b) $M = \text{Sb}$ and (d) $M = \text{Bi}$	157

Figure 5-2	Typical DTA results of the composition $\text{KPb}_{18}\text{SbTe}_{20}$, (b) variation of the melting and crystallization points of $\text{KPb}_{18-x}\text{Sn}_x\text{SbTe}_{20}$ as a function of x	158
Figure 5-3	BSE images of the surface of (a) $\text{KPb}_{13}\text{Sn}_5\text{SbTe}_{20}$ showing a precipitate with the atomic percentages Pb:2.73, K: 4.59, Sb:27.59 and Te:65.09 and (b) $\text{KPb}_9\text{Sn}_9\text{SbTe}_{20}$ showing an inclusion with atomic percentages Pb:2.32, K: 14.87, Sb:23.38 and Te:59.43. EDS analysis on the matrices indicated Pb, Sn and Te with ratios consistent with the nominal composition.....	160
Figure 5-4	BSE image of (a) a Sb-rich inclusion and (b) a mixed-phase inclusion in $\text{KPb}_5\text{Sn}_{13}\text{SbTe}_{20}$. EDS on area 1 showed the presence of Sb_2Te_3 and EDS on area 2 gave the atomic percentages Pb: 6.32, K: 3.80, Sb:13.51 and Te:76.37.....	161
Figure 5-5	BSE images of inclusions (a) and (b) observed for $\text{KPb}_9\text{Sb}_9\text{BiTe}_{20}$. Different phases are visible in the inclusion (a): area 1 is pure Bi whereas area 2 contains Pb, Sn, Bi and Te with the following atomic percentages: 8.14, 15.02, 32.17 and 44.67. EDS analysis on inclusion (b) gave the atomic percentages Pb: 1.36, K: 4.77, Sn: 22.90 and Te: 70.95.....	162
Figure 5-6	Electronic transport properties of the $\text{KPb}_{18-x}\text{Sn}_x\text{SbTe}_{20}$ samples: (a) electrical conductivity, (b) thermopower, (c) power factor. The point marks in the inset of panel (b) identify all samples and apply to panels (a) and (c).....	165
Figure 5-7	Electronic transport properties of the $\text{KPb}_{18-x}\text{Sn}_x\text{BiTe}_{20}$ samples: (a) electrical conductivity, (b) thermopower, (c) power factor. The point marks in the inset of panel (a) identify all samples and apply to all panels (b) and (c).....	167
Figure 5-8	Band-structure of PbTe doped with (a) (Ag, Sb), (b) (Ag, Bi). Ag and Sb/Bi atoms in the pair are the second-nearest neighbors of one another in a 64-atom supercell.....	169
Figure 5-9	Temperature of the (a) total thermal conductivity, (b) lattice thermal conductivity and (c) electronic thermal conductivity for $\text{KPb}_{18-x}\text{Sn}_x\text{SbTe}_{20}$ ($x=5, 9, 13$ and 16).....	172
Figure 5-10	Temperature dependence of the figure of merit ZT for $\text{KPb}_{18-x}\text{Sn}_x\text{SbTe}_{20}$ ($x=0, 3, 5, 9, 13, 16$).....	173

Figure 6-1	Powder X-ray diffraction of the series $\text{CuPb}_m\text{SbTe}_{m+2}$ ($m=5, 12, 18, 20, 22, 30, 40$ and 50), the area between $2\theta = 25$ and 50 deg is enlarged to show the presence of extra peaks that do not belong to the NaCl structure-type. Two small peaks at 28 and 38 deg are characteristic of Sb_2Te_3 . Small peaks ~ 42 - 43 deg belong to Cu_2Te184
Figure 6-2	BSE images of a sample with composition $\text{CuPb}_{18}\text{SbTe}_{20}$ showing regions rich in Cu_2Te and Sb_2Te_3 embedded in the PbTe matrix. The two phases form dendritic ribbons as long as 3 mm in all directions.....185
Figure 6-3	BSE images of the compound $\text{CuPb}_{40}\text{SbTe}_{42}$. More dispersed regions composed of Cu_2Te and Sb_2Te_3 are visible in the PbTe matrix186
Figure 6-4	DTA results: (a) first cycle and (b) second cycle for $\text{CuPb}_8\text{SbTe}_{10}$; (c) first and (d) second cycle of $\text{CuPb}_{30}\text{SbTe}_{32}$; (e) first cycle and (f) second cycle of $\text{CuPb}_{50}\text{SbTe}_{52}$187
Figure 6-5	Temperature dependence of (a) the electrical conductivity, (b) the thermopower and (c) the power factor for the series $\text{CuPb}_m\text{SbTe}_{m+2}$ ($m=8, 12, 18, 20, 22, 30, 40, 50$); (d) carrier concentration as a function of temperature for $\text{CuPb}_{18}\text{SbTe}_{20}$ and $\text{CuPb}_{22}\text{SbTe}_{24}$189
Figure 6-6	Temperature dependence of the (a) total and (b) lattice thermal conductivity for the compounds $\text{CuPb}_m\text{SbTe}_{m+2}$ ($m=8, 18, 20, 30, 40$)190
Figure 6-7	Figure of merit ZT for the compounds $\text{CuPb}_m\text{SbTe}_{m+2}$ ($m= 8, 18, 20, 30, 40$)191
Figure 6-8	Powder X-ray diffraction for (a) $\text{CuPb}_{18}\text{SbTe}_{20}$, (b) $\text{CuPb}_9\text{Sn}_9\text{SbTe}_{20}$ and (c) $\text{CuSn}_{18}\text{SbTe}_{20}$194
Figure 6-9	BSE images of $\text{CuPb}_{13}\text{Sn}_5\text{SbTe}_{20}$. Complex regions rich in Cu_2Te and Sb_2Te_3 are clearly visible in the $\text{Pb}_{1-x}\text{Sn}_x\text{Te}$ matrix195
Figure 6-10	BSE images of (a) $\text{CuPb}_9\text{Sn}_9\text{SbTe}_{20}$ and (b) $\text{CuPb}_5\text{Sn}_{13}\text{SnTe}_{20}$196
Figure 6-11	BSE images obtained for $\text{CuSn}_{18}\text{SbTe}_{20}$. Only Cu_2Te regions segregated in the SnTe matrix.....197

Figure 6-12	Temperature dependence of the (a) electrical conductivity, (b) thermopower and (c) power factor of the series $\text{CuPb}_{18-x}\text{Sn}_x\text{SbTe}_{20}$ ($x=0, 5, 9, 13, 18$).....	200
Figure 6-13	Total, electronic and lattice thermal conductivities of $\text{CuSn}_{18}\text{SbTe}_{20}$	201
Figure 6-14	Powder X-ray diffraction patterns for samples with nominal composition CuSbTe_2 ratios prepared by water-quenching, air-quenching and slow cooling.	203
Figure 6-15	BSE images of the sample with nominal composition CuSbTe_2 quenched in water	204
Figure 6-16	BSE images of the sample with nominal composition CuSbTe_2 quenched in air	205
Figure 6-17	BSE images of the sample with nominal composition CuSbTe_2 prepared by slow cooling	206
Figure 6-18	BSE imaging of a sample prepared with nominal composition CuSbTe_2 with the furnace being rocked during the reaction	207
Figure 6-19	DTA analysis of the sample prepared by mixing Cu, Sb and Te with the ratio 1:1:1:2 by rocking the furnace: (a) first cycle, (b) 2 nd cycle	208
Figure 6-20	Powder X-ray diffraction of PbTe doped with 1, 2 and 5 % Cu_2Te . The small stars indicate diffraction peaks that do not belong to the PbTe structure-type and indicate the presence of Cu_2Te as a minor phase	210
Figure 6-21	BSE images of PbTe doped with 5 % Cu_2Te	211
Figure 6-22	BSE images of PbTe samples doped with (a) 2 % and (b) 1 % Cu_2Te	212
Figure 6-23	Differential thermal analysis results for (a) the first run and (b) second for the PbTe doped with 1% Cu_2Te ; (c) the first run and (d) second run of PbTe doped with 2 % Cu_2Te	213
Figure 6-24	Temperature dependence of (a) the electrical conductivity and (b) the thermopower of PbTe doped with 1 % Cu_2Te , temperature dependence of (c) the electrical conductivity and (d) the thermopower of PbTe doped with 2 % Cu_2Te	214

CHAPTER 1

Introduction to Thermoelectrics

1.1. Thermoelectric concepts

Thermoelectric devices are solid state systems able to convert heat into electricity (power generation) or vice versa electrical energy to cooling (refrigeration). Typical applications of thermoelectric devices include supplying power to NASA spacecraft, power generation in remote areas, electronic equipment along fuel pipelines, and cooling for electronic devices.

Thermoelectric devices are based on thermoelectric phenomena, the Seebeck¹ and Peltier² effects. The former was discovered by Thomas Seebeck in 1823. An electrical potential is generated within any isolated conducting material that is subjected to a temperature gradient. In thermoelectric devices, a junction is formed between two different conducting materials, one containing positive charge carriers and the other negative charge carriers. A heat source at the junction will make the carriers flow away from the junction, making an electrical generator (Figure 1-1b). The Seebeck coefficient (or thermopower) S is defined as follows:

$$S = \frac{dV}{dT} \quad (1)$$

With dV the potential difference generated and dT the temperature difference.

The Peltier effect is the reverse process. Heat is absorbed or liberated when a current crosses an interface between two different conductors. This is the basis for cooling

devices: when an electric current is passed in the appropriate direction through the junction, both types of carriers move away from the junction and convey heat away (Figure 1-1a).

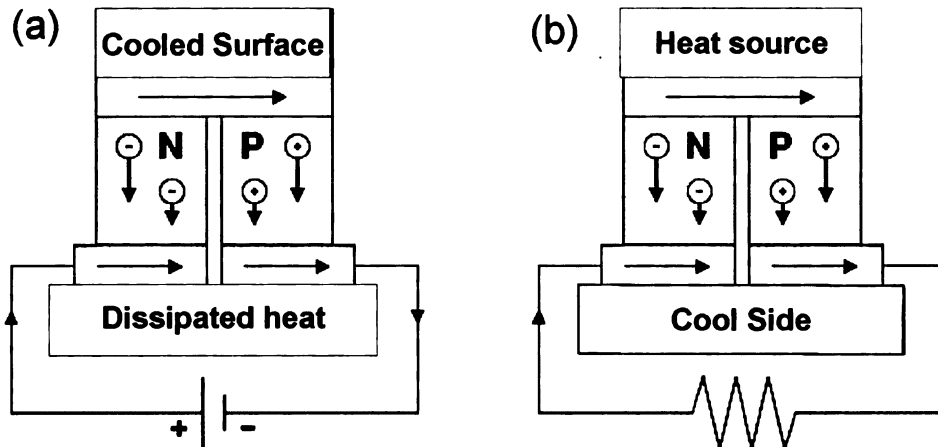


Figure 1-1. Scheme of (a) a cooling device and (b) a power generator.

Thermoelectric devices (power generators and coolers) present several advantages compared to other systems. They are light, small, reliable and vibrationless. For example, radioisotopes thermoelectric generators (called RTGs) produce electrical power by converting the nuclear decay of radioactive isotopes (typically plutonium-238) into electricity and have been successfully used to power a number of long-time space missions (tens of years).³ There are many economic and environmental benefits of thermoelectric devices as well. Waste heat can be recovered and used as a source for power generation. Thermoelectric coolers can replace environmentally harmful chlorofluorocarbons in refrigeration compressors. The automotive industry is also interested in the development of thermoelectrics. Only 25 % of the fuel energy is used for vehicle mobility, the remainder is lost in the form of waste heat in the exhaust and

coolant as well as friction and parasitic losses. Applications such as electrical power generation and refrigeration (seat coolers, electronic component cooling) are currently being investigated. Refrigeration of electronics is an important technology that thermoelectric could greatly impact. More efficient coolers are predicted to produce speed gains of 30 % to 200 % in some computer processors based on complementary metal oxide semiconductor (CMOS) technology. However, so far the market of thermoelectric systems has been restricted to small niches because of their low efficiencies.^{4, 5} Typically, for cooling applications, the coefficient of performance of thermoelectric devices is about 10% of the Carnot efficiency whereas kitchen refrigerators for example operate at about 30% of the Carnot efficiency.⁵

The efficiency of a thermoelectric material is based on the so-called figure of merit ZT defined by the expression:

$$ZT = \frac{\sigma S^2}{\kappa} T \quad (2)$$

where S is the thermopower (or Seebeck coefficient) of the compound, σ its electrical conductivity, κ its thermal conductivity and T the absolute temperature. The numerator σS^2 is often referred as the power factor. The thermal conductivity has two contributions: one from the lattice vibrations (called lattice thermal conductivity) and the other from the charge carriers (called electronic thermal conductivity). The electronic component is related to the electrical conductivity through the Wiedemann-Franz law:

$$\kappa_e = L \cdot \sigma \cdot T \quad (3)$$

where L is the Lorenz factor, σ the electrical conductivity and T the temperature. L is typically taken as $2.45 \cdot 10^{-8} \text{ W}\Omega/\text{K}$ for degenerate semiconductors.⁶

For a thermoelectric device to be competitive with compressor-based refrigerators, materials with $ZT \sim 3 - 4$ have to be discovered.⁵ So far, the materials used for thermoelectric applications exhibit ZT not higher than 1. Today's commercial materials are alloys discovered decades ago. For example, PbTe with $ZT \sim 0.8$ at 700K is used for temperature range 600 – 700 K and $\text{Bi}_2\text{Te}_3/\text{Sb}_2\text{Te}_3/\text{Bi}_2\text{Se}_3$ alloys are used for electronic refrigerators ($ZT=0.9$ at 400 K). The RTG systems are based on $(\text{AgSbTe}_2)_{1-x}(\text{GeTe})_x$ (TAGS) materials and SiGe alloys. Figure 1-2 shows the figure of merit as a function of temperature for several bulk materials. Several systems clearly exhibit ZT higher than unity at temperatures above 600 K and hold promise for technological applications. Since 1990, the field of thermoelectrics is experiencing a rebirth because of the interest of the US Department of Energy in the potential of thermoelectrics. Progress in solid state science such as the discovery of new complex materials, more reliable band-structure calculations, and the progress in structure determination by X-ray diffraction have contributed to the renewal of the field. A new research direction for high ZT materials is to prepare known compounds in low dimensional scale such as quantum wells,^{7, 8} quantum wires,⁹ superlattices and quantum dots.^{10, 11} These materials exhibit higher ZT than their bulk counterpart.

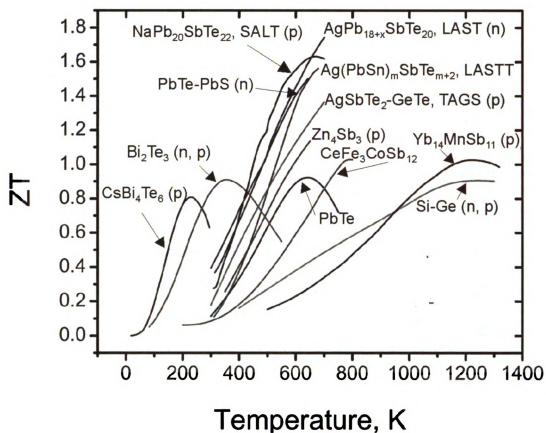


Figure 1-2. Figure of merit ZT shown as a function of temperature for several bulk materials.

1.2. Optimization of the figure of merit

According to equation (2), good thermoelectric materials should have large thermopower, high electrical conductivity and low thermal conductivity. A good description of such a material was given by Slack and is known as the “PGEC” concept: “Phonon Glass Electron Crystal”.¹² Good thermoelectric materials would conduct electricity like a crystalline solid but conduct heat like a glass. The problem is that the electrical conductivity, the thermopower and the electronic thermal conductivity are

determined by the details of the electronic and crystal structures and the scattering of charge carriers. Therefore they are not independent from each other. This makes the design of materials with high ZT a challenge. Two approaches can be considered to improve the figure of merit: the first consists of increasing the power factor while the second focuses on reducing the lattice thermal conductivity.

As metals have high electrical conductivity and low thermopower and insulators low electrical conductivity and high thermopower, optimum power factors are achieved in degenerate semiconductors with carrier concentrations $\sim 10^{20} / \text{cm}^3$ (Figure 1-3).

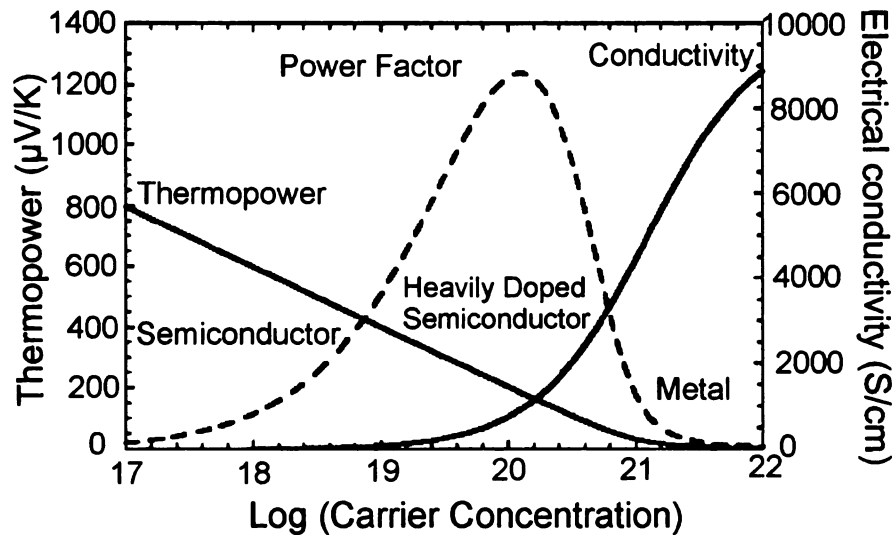


Figure 1-3. Evolution of the Seebeck coefficient and the electrical conductivity as a function of the carrier concentration.¹²

The Boltzmann transport theory provides a general understanding of the thermopower using the Mott formula¹³:

$$S = \frac{\pi^2}{3} \frac{k^2 T}{e} \left. \frac{d \ln \sigma(E)}{dE} \right|_{E=E_f} \quad (4)$$

The conductivity $\sigma(E)$ is determined as a function of band filling. If the carrier scattering is independent of energy, then $\sigma(E)$ is just proportional to the density of states at E . The thermopower is a measure of the difference in $\sigma(E)$ above and below the Fermi surface. Therefore thermoelectric materials with high thermopower require high compositional and structural complexity contributing to complex electronic structure since the thermopower is a measure of the asymmetry in electronic structure near the Fermi level. Theoretical studies pursued by Hicks et al.^{7, 14} predicted dramatic changes in the density of states as the system size decreases and approaches nanometer length scales (Figure 1-4). As a result, an increase in thermopower is expected in reduced dimensionality systems.

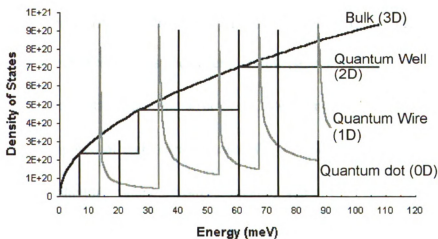


Figure 1-4. Density of states for electrons in bulk semiconductors (3D), quantum wells (2D), quantum wires (1D) and quantum dots (0D).

One way to optimize ZT is to minimize the lattice thermal conductivity by increasing phonon scattering. In bulk materials, phonon scattering can be enhanced by introducing heavy atoms and mass fluctuation in the lattice. Large unit cells will also tend

to exhibit low lattice thermal conductivity.¹⁵ The presence of a weakly bound atom that rattles inside a cavity will also reduce the thermal conductivity of the material without severely affecting the electronic conduction. Different systems based on this concept are under investigation: skutterudites, clathrates, complex chalcogenides. They are described in the following section. Another strategy is to scatter phonons at interfaces, leading to the use of multiphase composites mixed on the nanoscale.¹⁶

1.3. Bulk Thermoelectric Materials

Different bulk systems are under investigation for thermoelectric applications: skutterudites, clathrates, Half-Heusler, zintl phases, oxides, complex chalcogenides. A brief overview of these different systems is presented in this section. Further details are available in the references and several review papers.¹⁷⁻¹⁹

The skutterudite-type structure (CoAs₃-type) is a cubic structure with the space group composed of eight corner-shared TX₆ (T=Co, Rh, Ir, X=P, As, Sb) octahedra. The linked octahedra produce a void or vacancy site at the center of the (TX₆)₈ cluster. The metal atoms occupy the corners of the eight “cubes” with six Sb rings inside the cube and two voids in the remaining cubes. Figure 1-5 shows the structure of a skutterudite antimonide compound. Many different elements have been introduced into the voids of skutterudites, including lanthanides, actinides, alkaline-earth, alkali, thallium and group IV elements, resulting in significant reduction of the lattice thermal conductivity.^{20, 21} Skutterudite antimonides possess the largest voids. ZT ~ 1.4 above 1173 K was reported for LaFe₃CoSb₁₂ and CeFe₃CoSb₁₂.²²

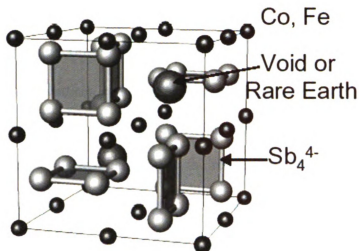


Figure 1-5. Structure of a skutterudite antimonide.

Clathrates, like skutterudites, exhibit cage-like structures with rattling mechanisms. They can be thought of as periodic solids in which tetrahedrally bonded atoms form a framework of cages. Their crystal structures are closely related to those of type-I and type-II clathrate hydrides such as $(\text{Cl}_2)_8(\text{H}_2\text{O})_{48}$ and $(\text{CO}_2)_{24}(\text{H}_2\text{O})_{136}$. A wide variety of different elements have been encapsulated inside these polyhedra, including alkali-metal, alkaline earth and rare earth atoms. As a result, low thermal conductivity was measured for type I clathrates.²³ For example, the thermal conductivity of $\text{Sr}_8\text{Ga}_{16}\text{Ge}_{30}$ shows a similar magnitude and temperature dependence to that of amorphous materials.²⁴⁻²⁶

Half-Heusler alloys, with general formula MNiSn (with M a group IV transition metal), have the MgAgAs crystal structure (space group $F4-3m$) consisting of three interpenetrating fcc sublattices with one Ni sublattice vacant. They are small band gap semiconductors with $E_g \sim 0.1-0.5 \text{ eV}$.²⁷⁻²⁹ The Half-Heusler alloys exhibit a high

negative thermopower (-40 to -250 $\mu\text{V/K}$) and low electrical resistivity (0.1 to 8 $\text{m}\Omega/\text{cm}$).¹⁸ However the thermal conductivity is relatively, high, $\sim 10 \text{ W/m}\cdot\text{K}$. The chemistry of the three sublattices can be tuned independently. For example, in TiNiSn, doping the Sn site provides the charge carriers while partial substitution of the Ti and Ni sites causes mass fluctuations that can lead to the reduction of thermal conductivity. A power factor as high as $4.5 \text{ W/m}\cdot\text{K}^2$ was reported at 650 K for $\text{TiNiSn}_{0.95}\text{Sb}_{0.5}$.¹⁸ Partial substitution of Ni by Pd in the system ZrNiSn resulted in $\kappa_L \sim 2 \text{ W/m}\cdot\text{K}$ at 800 K for $\text{Zr}_{0.5}\text{Hf}_{0.5}\text{Ni}_{0.5}\text{Pb}_{0.5}\text{Sn}_{0.99}\text{Sb}_{0.01}$.³⁰

The discovery of high ZT at high temperature ($ZT \sim 1$ at 1223 K) in the p-type $\text{Yb}_{14}\text{MnSb}_{11}$ material demonstrates the successful combination of electron-crystal phonon glass-properties displayed by Zintl phases.^{31, 32} The structure is isostructural to $\text{Ca}_{14}\text{AlSb}_{11}$ ³³ and consists of $[\text{MnSb}_4]^{9-}$ tetrahedra, polyatomic $[\text{Sb}_3]^{7-}$ anions and isolated Sb^{3-} anions. X-ray magnetic circular dichroism (XMCD) and XPS (X-ray Photoelectron Spectroscopy) measurements show that the Yb is in the 2+ oxidation state replacing Ca^{2+} but the Mn was found to be Mn^{2+} , supplying one less electron than Al^{3+} . The material is p-type and Hall effect measurement showed carrier concentration $\sim 1.3 \cdot 10^{21} \text{ holes/cm}^3$. The total thermal conductivity is remarkably low ranging between $\sim 0.7 - 0.9 \text{ W/m}\cdot\text{K}$ for the temperature range 300-1275 K. Subtracting the electronic contribution results in low lattice thermal conductivity, comparable to that of a glass. The reason of such low values can be attributed to the complexity of the structure and the heavy atomic mass of the crystal.

Complex oxide materials are a good example of hybrid materials. Layered cobalt oxide materials such as $\text{Na}_x\text{Co}_2\text{O}_4$ ³⁴ and $\text{Ca}_3\text{Co}_4\text{O}_9$ ³⁵ are composed of CoO_2 nanosheets and sodium ion layers or calcium cobalt oxide misfit layers. The CoO_2 nanosheets possess a strong correlated electron system that serves as electronic transport layers while the sodium ion nanoblock layers or calcium cobalt oxide misfit layers serve as phonon-scattering boundaries that reduce the thermal conductivity.^{36, 37}

1.4. Complex chalcogenide systems as potential thermoelectric materials

Exploratory synthesis of ternary and quaternary chalcogenides has led to the discovery of a wide range of compounds. Some of them, notably thallium chalcogenides, show promising thermoelectric properties. Ternary and quaternary bismuth chalcogenides exhibit a wide compositional and structural diversity. Some of them are good examples of the PGEC concept with alkali metal rattlers.

Thallium chalcogenides, particularly Tl_9BiTe_6 ³⁸ and Tl_2SnTe_5 ,³⁹ tend to possess very low thermal conductivity. Tl_9BiTe_6 is derived from the isostructural Tl_5Te_3 ⁴⁰ and optimized compositions exhibit $ZT \sim 1.2$ at 500 K mainly because of its extremely low lattice thermal conductivity (0.39 W/m·K at 300 K). In Tl_2SnTe_5 , chains of $(\text{SnTe}_5)^{2-}$ run parallel to each other and charge-balancing Tl^+ . The long Te-Tl bonds (~ 3.49 - 3.66 Å) produce low-frequency phonons which results in a very low lattice thermal conductivity (0.5 W/m·K over 50-300 K). However these compounds are unlikely to be used for practical use because of toxicity issues.

The ternary and quaternary bismuth sulfide and selenide systems have been extensively studied in our laboratory.⁴¹⁻⁴⁷ The systems exhibit a wide compositional and structural diversity because of the presence of bismuth. The element possesses a lone pair of $6s^2$ electrons. The lone pair can be stereochemically expressed as a distortion the Bi coordination or can be suppressed by hybridization with adjacent p- or d-orbitals resulting in symmetrical octahedral coordination geometry. Bismuth atoms adopt different coordination environment from 3 to 9 near neighbors. Among the various Bi-Q (Q=S, Se, Te) coordination geometries, BiQ_6 octahedral coordination is the most abundant. Furthermore, octahedral and square pyramidal geometry when combined can produce several common building fragments such as $\text{NaCl-(NaCl}^{100})$, $\text{Sb}_2\text{Se}_3\text{-(NaCl}^{100})$, $\text{Bi}_2\text{Te}_3\text{-(NaCl}^{111})$, $\text{CdI}_2\text{-(NaCl}^{111})$, and galena types (NaCl^{311}) (Figure 1-6).

Some of these materials, particularly $\beta\text{-K}_2\text{Bi}_8\text{Se}_{13}$ ⁴³ and CsBi_4Te_6 ,^{48, 49} show promising thermoelectric properties. These ternary chalcogenides materials are made of layers separated by channels filled with the alkali metal. The presence of the alkali metals rattling inside the channels leads to low thermal conductivity.

$\beta\text{-K}_2\text{Bi}_8\text{Se}_{13}$ is made up of Bi_2Te_3 , NaCl and CdI_2 -type infinite rod-shaped blocks. The CdI_2 and Bi_2Te_3 -type blocks are arranged side by side to form layers. NaCl-type blocks serve as connectors between these layers to build a 3D framework with channels filled with potassium cations. As a result, thermal conductivity of ~ 1.28 W/m·K was measured at room temperature for a polycrystalline sample.

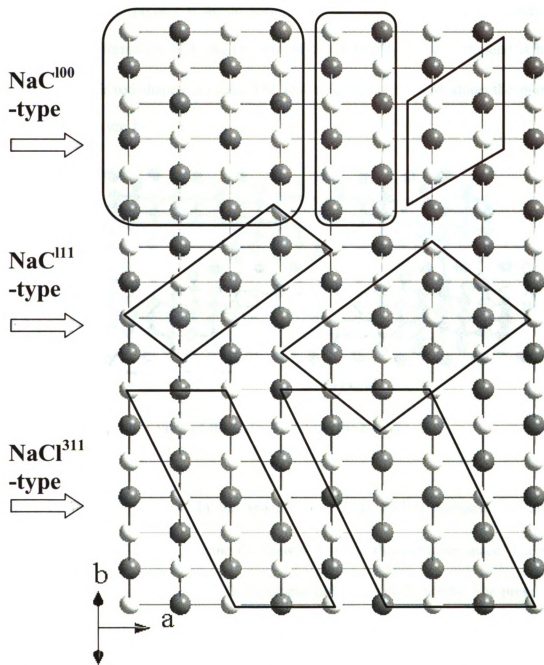


Figure 1-6. Various building blocks (shaded) based on different “cuts” of the NaCl-type structure. The diagram is view down with [011] plane. Black and white circles are bismuth and chalcogen atoms, respectively.

Attempts to prepare telluride analogs of these sulfide and selenide compounds resulted in the formation of CsBi_4Te_6 instead of $\text{Cs}_2\text{Bi}_8\text{Te}_{13}$. The compound is highly anisotropic with rod-shaped crystals. The crystal structure viewed along the b-axis is displayed on Figure 1-7.

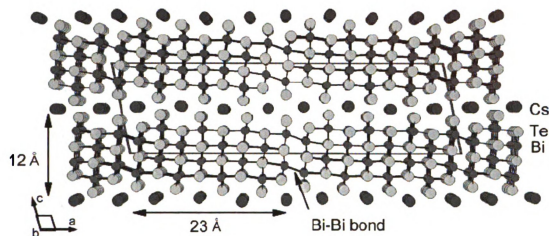


Figure 1-7. Perspective view of the CsBi_4Te_6 along the b-axis.

CsBi_4Te_6 crystallizes in the space group $C2/m$ and is composed of anionic infinitely long $[\text{Bi}_4\text{Te}_6]^-$ blocks and Cs^+ ions residing in the interlayer space. The Bi/Te layers consist only of Na-Cl-type Bi/Te blocks linked by Bi-Bi bonds. The presence of Bi-Bi bonds (3.2383 (10) Å) in the Bi/Te blocks is remarkable. The addition of one electron per 2 equivalent of Bi_2Te_3 does not give a formal intercalation compound but causes a dramatic reorganization of the Bi_2Te_3 framework and reveal an inability to delocalize such electrons. Isolated Bi-Bi bonds in solids are rare with the only other example reported for $\text{Bi}_2\text{Ga}_2\text{Q}_8$ (Q=S, Se).⁵⁰

CsBi₄Te₆ is a promising candidate for cooling applications, with a thermoelectric figure of merit of about 0.8 at 225 K. This is the highest ZT reported for a material at such low temperature. Undoped samples have room temperature electrical conductivity between 900-2500 S/cm and thermopower values between 90 and 120 μV/K. Doping studies on CsBi₄Te₆ showed that the system is significantly affected by low doping levels. The highest ZT of 0.8 at 225 K was achieved by doping CsBi₄Te₆ with 0.05% SbI₃. In that case, a power factor as high as 51.5 μW/cm·K² was attained at 184 K. The total thermal conductivity measured along the direction parallel to the needles are in the range 1.25-1.85 W/m·K at room temperature.

Attempts to introduce Pb in CsBi₄Te₆ led to the discovery of the homologous family of materials CsPb_mBi₃Te_{5+m} (m=1, 2, 3, 4) (Figure 1-8).^{51, 52} The expression “homologous family” was introduced by Magneli⁵³ to characterize chemical series that are expressed by a general formula and built on common structural principles. The only difference between members of the family is the dimensions of these building units. The concept of phase homologies has become a useful tool in solid state chemistry to design and target new compounds.^{54, 55} The exploration of the quaternary system A/M'/M''/Se (A=K, Rb, Cs, Sr, Ba; M'=Sn, Pb, Eu; M''=Sb, Bi) led to numerous compounds.^{42, 43} This includes members of the homologous megaseries A_m[M_{1+n}Se₂₊₁]_{2m}[M_{2l+n}Se_{2+3l+n}].⁵⁶⁻⁵⁸

The four members of the family were prepared by introducing various equivalents of PbTe in the layered framework of CsBi₄Te₆. As CsBi₄Te₆, these compounds are made of layered Bi/Te frameworks separated by Cs⁺ cations. However the partial substitution

of Bi by Pb causes the loss of the Bi-Bi bond. As can be observed in Figure 1-8, the difference between the four members is the thickness of the anionic layers. This thickness increases with increasing Pb content. All four members of the family show reduced thermal conductivity compared to that of Bi_2Te_3 and CsBi_4Te_6 (1.8 and 1.5 $\text{W/m}\cdot\text{K}$ for $\text{CsPbBi}_3\text{Te}_6$ and $\text{CsPb}_4\text{Bi}_3\text{Te}_9$ at room temperature).⁵²

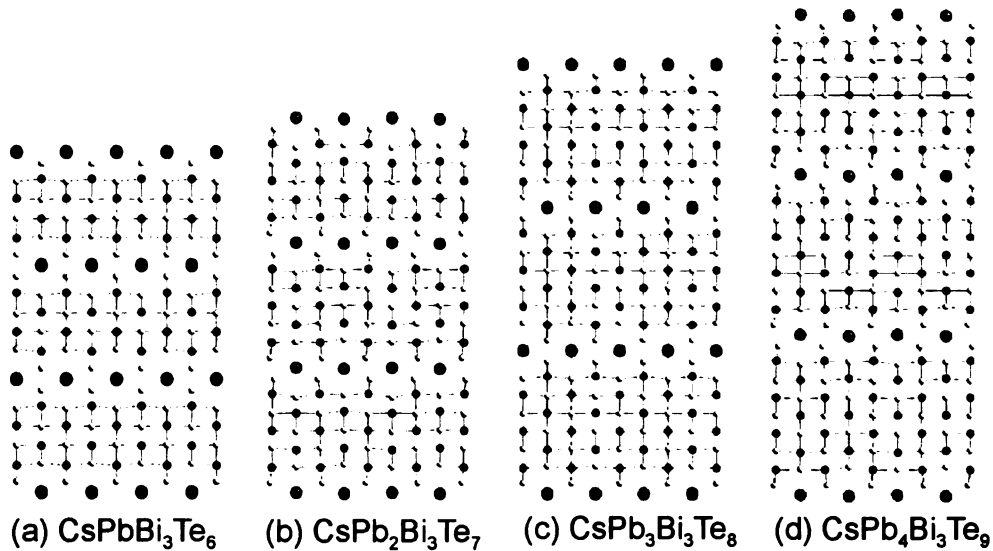


Figure 1-8. The structures of (a) $\text{CsPbBi}_3\text{Te}_6$, (b) $\text{CsPb}_2\text{Bi}_3\text{Te}_7$, (c) $\text{CsPb}_3\text{Bi}_3\text{Te}_8$ and (d) $\text{CsPb}_4\text{Bi}_3\text{Te}_9$ in projection down the c axis for (a) and (c) and the a axis for (b) and (d).

1.5. Low-dimensional and nanostructured materials

Till now, this chapter focused mainly on bulk materials. However a different approach is under investigation by several groups. Many experimental and theoretical studies on low dimensional nanostructured materials⁵⁹⁻⁶¹ and mixed-phase nanocomposites^{7, 14, 62, 63} provide encouraging results in getting high ZT by reducing lattice thermal conductivity while maintaining high power factors. The idea of using

reduced dimensionality to improve ZT was first discussed by M. S. Dresselhaus et al.^{7, 14} The quantum confinement effect could be used to enhance the thermopower whereas the lattice thermal conductivity could be reduced through the presence of numerous interfaces that scatter phonons more effectively than electrons. The superlattice thin-film structures of $\text{Bi}_2\text{Te}_3/\text{Sb}_2\text{Te}_3$ grown from chemical vapor deposition⁶⁴ and of $\text{PbSe}_{0.98}\text{Te}_{0.02}/\text{PbTe}$ formed by molecular beam epitaxy^{59, 60} claimed ZT values greater than 2 (at ~ 300 and 550 K respectively). Studies have shown that significant thermal conductivity reduction occurs regardless of the orientation of the superlattices or nanostructures to the measurement direction.⁶⁴

Large scale production and utilization of such materials is significantly jeopardized by their low thermal stability and the complex and costly synthesis process. Bulk analogues of such systems with similar figures of merit emerge as alternative candidate materials for thermoelectric energy conversion. Different synthetic routes can be considered to prepare such materials. For example, nanostructured PbTe bulk materials could be achieved through matrix encapsulation,^{65, 66} spinodal decomposition,^{67, 68} nucleation and growth.⁶⁹⁻⁷¹ Recently our group reported on the n-type systems $\text{AgPb}_m\text{SbTe}_{m+2}$ (LAST)⁶⁹, and $\text{Pb}_{1-x}\text{Sn}_x\text{Te}-\text{PbS}$ ⁶⁷ and the p-type systems $\text{Na}_{1-x}\text{Pb}_m\text{Sb}_y\text{Te}_{m+2}$ (SALT)⁷¹ and $\text{Ag}(\text{Pb}_{1-y}\text{Sn}_y)_m\text{SbTe}_{2+m}$ (LASTT)⁷⁰, that exhibit high thermoelectric figure of merit. The compositions $\text{AgPb}_{18}\text{SbTe}_{20}$ and $\text{Na}_{0.95}\text{Pb}_{20}\text{SbTe}_{22}$ reach ZT of ~ 1.8 and 1.6 at 700 and 650 K respectively. These outstanding values are due essentially to their very low thermal conductivity. The total thermal conductivity drops very rapidly with rising temperatures and reaches a minimum value of 0.85 W/m·K

at 700 K for $\text{Na}_{0.95}\text{Pb}_{20}\text{SbTe}_{22}$. Careful analysis of high resolution transmission electron microscopy images of these materials revealed the presence of nanostructuring coherently embedded in what is essentially a PbTe matrix. The precise composition of these nanostructures could not be determined due to instrumental limitation. These clusters are believed to be rich in monovalent cations (Ag^+ , Na^+) and trivalent cations Sb^{3+} because of the Coulombic forces that do not allow charge imbalances around the atoms. Ab initio calculations within density functional theory were pursued for PbTe with and without monovalent impurities (Na, K, Rb, Cs, Cu and Ag).⁷² The result showed an increase of the density of states near the top of the valence band for K, Rb, Cs, Cu and Ag dopants. Further studies on these systems have been investigated: the partial substitution of Pb by Sn in $\text{NaPb}_{18}\text{SbTe}_{20}$ and $\text{KPb}_{18}\text{SbTe}_{20}$, the preparation of members with low m values for $\text{NaPb}_m\text{SbTe}_{m+2}$, the substitution of Ag by Cu in $\text{AgPb}_m\text{SbTe}_{m+2}$. The systems $\text{NaSn}_m\text{MTe}_{m+2}$ (M=Sb, Bi) were prepared as well and their properties are compared to that of the Pb analogs. These studies are detailed in chapters 3, 4, 5, 6 and 7.

Tl-doped PbTe materials also hold promise to improve the thermoelectric figure of merit of PbTe. Heremans et al.⁷³ reported $ZT \sim 1.5$ at 773 K for $\text{Pb}_{0.98}\text{Tl}_{0.2}\text{Te}$. Contrary to the nanostructured systems described above where an increase in ZT is achieved mainly through a reduction in lattice thermal conductivity, the enhancement of ZT in Tl-doped PbTe is attributed to an increase in the thermopower. Calculations indicated that Tl creates resonant energy levels located in the valence band of Tl-PbTe.^{72,}

A recent study has revealed that co-nanostructuring PbTe with two different phases (Pb and Sb in that case) could significantly impact the temperature dependence of the electrical conductivity compared to that of PbTe or PbTe nanostructured either with Pb or Sb nanodots.⁷⁵ For PbTe –Pb(2 %)-Sb (3 %), the electrical conductivity increases with temperature. Thermopower measurements and Hall effect data support the theory of a slower rate of decrease in mobility of the charge carriers. As a result, for that composition, an increase in power factor with temperature was observed. This is a significant improvement towards increasing the power factor of thermoelectric materials because so far improved thermoelectric figures of merit were achieved through reduction of the lattice thermal conductivity.

In this dissertation, substitution studies on CsPbBi₃Te₆ and Na_{1-x}Pb_mSb_yTe_{m+2} were pursued in order to characterize the resulting materials and particularly to evaluate their thermoelectric materials. Chapter 2 describes the studies of partial substitution of Pb and Cs by other elements such as Sn, Na, K, Ca, Yb in the compound CsPbBi₃Te₆, the first member of the homologous family CsPb_mBi₃Te_{5+m} described in section 4. Single-crystal X-ray diffraction data, collected on several needle-shape crystals, indicate the compositions Cs_{0.76}K_{0.74}Bi_{3.5}Te₆ (1), CsNa_{0.98}Bi_{4.01}Te₇ (2), Cs_{0.69}Ca_{0.65}Bi_{3.34}Te₆ (3), Rb_{0.82}Pb_{0.82}Bi_{3.18}Te₆ (4), Rb_{0.19}K_{1.31}Bi_{3.50}Te₆ (5), RbSnBi₃Te₆ (6), Rb_{0.94}Ca_{0.94}Bi_{3.06}Te₆ (7), RbYbBi₃Te₆ (8) and KSnSb₃Te₆ (9). However optimum synthesis conditions have not yet been found to prepare a pure phase of the compounds.

Chapters 3, 4 and 5 concern the preparation and characterization of bulk nanostructured PbTe materials. In section 5, the promising thermoelectric properties of

the p-type system $\text{Na}_{1-x}\text{Pb}_m\text{Sb}_y\text{Te}_{m+2}$ (SALT)⁷¹ were discussed. However only high m values (m higher than 19) were studied. In Chapter 3, the synthesis and characterization of members with lower m values are discussed. Addition of Sn to the LAST system resulted in the promising p-type system $\text{Ag}(\text{Pb}_{1-y}\text{Sn}_y)_m\text{SbTe}_{2+m}$ (LASTT).⁷⁰ Similar studies with the SALT system were performed, resulting in the preparation of the series of samples with composition $\text{NaPb}_{18-x}\text{Sn}_x\text{SbTe}_{20}$. The detailed synthesis procedures and characterizations are described in Chapter 4. To assess the role of the alkali metal on the properties of the bulk nanostructured PbTe, potassium analogs of the $\text{NaPb}_{18-x}\text{Sn}_x\text{SbTe}_{20}$ were prepared. This study is reported in Chapter 5.

Substitution of Ag by Na or K did not affect the presence of nanostructures inside the PbTe matrix. However, replacing Ag by Cu in the LAST system resulted in the precipitation of Cu_2Te and Sb_2Te_3 phases in PbTe. Details about the characterization and the thermoelectric properties of the cast ingots are reported in Chapter 6.

References

1. Seebeck, T. J., *Abh. K. Akad. Wiss.* **1823**, 265.
2. Peltier, J. C., *Ann. Chem.* **1834**, LV 1, 371.
3. Yang, J.; Caillat, T., *Mater. Res. Bull.* **2006**, 31, 224.
4. Mahan, G.; Sales, B.; Sharp, J., *Physics Today* **1997**, 42.
5. Di Salvo, F. J., *Science* **1999**, 285, 703.
6. Kittel, C., *Introduction to Solid State Physics*. Wiley: 2005.
7. Hicks, L. D.; Dresselhaus, M. S., *Phys. Rev. B* **1993**, 47, (19), 12727.
8. Hicks, L. D.; Harman, T. C.; Dresselhaus, M. S., *Appl. Phys. Lett.* **1993**, 63, 3230.
9. Sofo, J. O.; D., M. G., *Appl. Phys. Lett.* **1994**, 65, 2690.
10. Harman, T. C.; Spears, P. J.; Manfra, M. J., *J. Electron. Mater.* **1996**, 25, 1121.
11. Harman, T. C.; Taylor, P. J.; Spears, P. J.; Walsh, M. P., *J. Electron. Mater.* **2000**, 29, L1.
12. Slack, G. A., *CRC Handbook of Thermoelectrics*. 1995.
13. Mott, N. F.; Jones, H., *The Theory of the Principles of Metals and Alloys*. Dover Publications, NY: 1958.
14. Hicks, L. D.; Dresselhaus, M. S., *Phys. Rev. B* **1993**, 47, 16631.
15. Kanatzidis, M. G., *Semicond. Semimet.* **2000**, 69, 51.

16. Dresselhaus, M. S.; Chen, G.; Tang, M. Y.; Yang, R.; Lee, H.; Wang, D.; Ren, Z.; Fleurial, J.-P.; Gogna, P., *Adv. Mater.* **2007**, 19, 1043.
17. Snyder, G. J.; Toberer, E. S., *Nat. Mater.* **2008**, 7, 105.
18. Tritt, T. M., *Mater. Res. Soc. Symp. Proc.* **2002**, 691, G1.1.1.
19. Chen, G.; Dresselhaus, M. S.; Dresselhaus, G.; Fleurial, J.-P.; Caillat, T., *Int. Mater. Rev.* **2003**, 48, 1.
20. Nolas, G. S.; Morelli, D. T.; Tritt, T. M., *Annu. Rev. Mater. Sci.* **1999**, 29, 89.
21. Uher, C., *Semicond. Semimet.* **2000**, 69, 139.
22. Sales, B.; Mandrus, D.; Williams, R. K., *Science* **1996**, 272, 1325.
23. Nolas, G. S.; Slack, G. A.; Schujman, S. B., *Semicond. Semimet.* **2001**, 69, 255.
24. Cohn, J. L.; Nolas, G. S.; Fessatidis, V.; Metcalf, T. H.; Slack, G. A., *Phys Rev. Lett.* **1999**, 82, 779.
25. Nolas, G. S.; Weakley, T. J. R.; Cohn, J. L., *Chem. Mater.* **1999**, 11, 2470.
26. Sales, B.; Chakamoukos, B. C.; Jin, R.; Thompson, J. R.; Mandrus, D., *Phys Rev. B* **2001**, 63, 245113.
27. Aliev, F. G., *Z. Phys. B* **1989**, 75, 167.
28. Aliev, F. G., *Z. Phys. B* **1990**, 80, 353.
29. Ogut, S.; Rabe, K. M., *Phys. Rev. B* **1995**, 51, 10443.
30. Shen, Q.; Chen, L.; Goto, T.; Hirai, T.; Yang, J.; Meissner, G. P.; Uher, C., *Appl. Phys. Lett.* **2002**, 79, 4165.

31. Brown, S. R.; Kauzlarich, S. M.; Gascoin, F.; Snyder, G. J., *Chem. Mater.* **2006**, 18, 1873.
32. Kauzlarich, S. M.; Brown, S. R.; Snyder, G. J., *Dalton Trans.* **2007**, 2099.
33. Cordier, G.; Schaefer, H.; Stelter, M., *Z. Anorg. Allg. Chem.* **1984**, 519, 183.
34. Terasaki, I.; Sasago, Y.; Uchinokura, K., *Phys. Rev. B* **1997**, 56, R12685.
35. Funahashi, R.; Matsubara, I.; Ikuta, H.; Takeuchi, U.; Mizutani, U.; Sodeoka, S., *Jpn J. Appl. Phys.* **2000**, 39, L1127.
36. Satake, A.; Tanaka, H.; T., O.; Fujii, T.; Terasaki, I., *J. Appl. Phys.* **2004**, 96, 931.
37. Shikano, M.; Funahashi, R., *Appl. Phys. Lett.* **2003**, 82, 1851.
38. Wolfing, B.; Kloc, C.; Teubner, J.; Buchner, E., *Phys. Rev. Lett.* **2001**, 86, 4350.
39. Sharp, J. W.; Sales, B. C.; Mandrus, D. G., *Appl. Phys. Lett.* **1999**, 74, 3794.
40. Babanly, M. B.; Gotuk, A. A.; Kuliev, A. A., *Inorg. Mater.* **1979**, 15, (7), 1292.
41. Chung, D. Y.; Iordanidis, L.; Choi, K. S.; Kanatzidis, M. G., *Bull. Korean Chem. Soc.* **1998**, 19, 1283.
42. Kanatzidis, M. G.; McCarthy, T. J.; Tanzer, T. A.; Chen, L.-H.; Iordanidis, L.; Hogan, T.; Kannewurf, C. R.; Uher, C.; Chen, B., *Chem. Mater.* **1996**, 8, 1465.
43. Chung, D. Y.; Choi, K. S.; Iordanidis, L.; Schindler, J. L.; Brazis, P. W.; Kannewurf, C. R.; Chen, B.; Hu, S.; Uher, C.; Kanatzidis, M. G., *Chem. Mater.* **1997**, 9, 3060.
44. Chung, D. Y.; Iordanidis, L.; Rangan, K. K.; Brazis, P. W.; Kannewurf, C. R.; Kanatzidis, M. G., *Chem. Mater.* **1999**, 11, 1352.

45. Iordanidis, L.; Brazis, P. W.; Kyratsi, T.; Ireland, J. R.; Lane, M.; Kannewurf, C. R.; Chen, W.; Dyck, J. S.; Uher, C.; Ghelani, N. A.; Hogan, T.; Kanatzidis, M. G., *Chem. Mater.* **2001**, 13, 622.
46. Kim, J. H.; Chung, D. Y.; Bilec, D.; Loo, S.; Short, J.; Mahanti, S. D.; Hogan, T.; Kanatzidis, M. G., *Chem. Mater.* **2005**, 17, 3606.
47. Choi, K. S.; Chung, D. Y.; Mroczek, A.; Brazis, P. W.; Kannewurf, C. R.; Uher, C.; Chen, W.; Hogan, T.; Kanatzidis, M. G., *Chem. Mater.* **2001**, 13, 756.
48. Chung, D.-Y.; Hogan, T.; Brazis, P.; Rocci-Lane, M.; Kannewurf, C.; Bastea, M.; Uher, C.; Kanatzidis, M. G., *Science* **2000**, 287, 1024.
49. Chung, D.-Y.; Hogan, T. P.; Rocci-Lane, M.; Brazis, P.; Ireland, J. R.; Kannewurf, C. R.; Bastea, M.; Uher, C.; Kanatzidis, M. G., *J. Am. Chem. Soc.* **2004**, 126, 6414.
50. Kalpen, H.; Hoerle, W.; Somer, M.; Schwartz, U.; Peters, K.; Von Schnering, H. G.; Blachnik, R. Z., *Anorg. Allg. Chem.* **1998**, 624, 1137.
51. Hsu, K. F.; Chung, D. Y.; Lal, S.; Mroczek, A.; Kyratsi, T.; Hogan, T.; Kanatzidis, M. G., *J. Am. Chem. Soc.* **2002**, 124, 2410.
52. Hsu, K. F.; Lal, S.; Hogan, T.; Kanatzidis, M. G., *Chem. Commun.* **2002**, 13, 1380.
53. Magneli, A., *Acta Crystallogr.* **1953**, 6, 495.
54. Mroczek, A.; Kanatzidis, M. G., *Acc. Chem. Res.* **2003**, 36, 111.
55. Kanatzidis, M. G., *Acc. Chem. Res.* **2005**, 38, 359.
56. Mroczek, A.; Chung, D. Y.; Hogan, T.; Kanatzidis, M. G., *J. Mater. Chem.* **2000**, 10, 1667.
57. Mroczek, A.; Kanatzidis, M. G., *J. Solid. State Chem.* **2002**, 167, 299.

58. Mrotzek, A.; Kanatzidis, M. G., *Chem. Commun.* **2001**, 17, 1648.
59. Harman, T. C.; Taylor, P. J.; Walsh, M. P.; LaForge, B. E., *Science* **2002**, 297, 2229.
60. Harman, T. C.; Taylor, P. J.; Walsh, M. P.; LaForge, B. E., *J. Electron. Mater.* **2005**, 34, L19.
61. Venkatasubramanian, R.; Siivola, E.; Colpitts, T.; O'Quinn, B., *Nature* **2001**, 413, 597.
62. Kim, W.; Singer, K. L.; Majumdar, A.; Vashaee, D.; Bian, Z.; Shakouri, A.; G., Z.; Bowers, E. J.; Zide, J. M. O.; Gossard, C., *Appl. Phys. Lett.* **2006**, 88, 242107.
63. Caylor, J. C.; Coonley, K.; Stuart, J.; Colpitts, T.; Venkatasubramanian, R., *Appl. Phys. Lett.* **2005**, 87, (2), 023105.
64. Venkatasubramanian, R.; Siivola, E.; Colpitts, T.; O'Quinn, B., *Nature* **2001**, 413, 597.
65. Sootsman, J. R.; Pcionek, R. J.; Kong, H.; Uher, C.; Kanatzidis, M. G., *Chem. Mater.* **2006**, 18, 4993.
66. Heremans, J. P.; Thrush, C. M.; Morelli, D. T., *J. Appl. Phys.* **2005**, 98, 063703.
67. Androulakis, J.; Lin, C. H.; Kong, H. J.; Uher, C.; Wu, C. I.; T., H.; Cook, B. A.; T., C.; Paraskevopoulos, M.; Kanatzidis, M. G., *J. Am. Chem. Soc.* **2007**, 129, 9780.
68. Ikeda, T.; Collins, L. A.; Ravi, V. A.; Gascoin, F. S.; Haile, S. M.; Snyder, G. M., *Chem. Mater.* **2007**, 19, 763.
69. Hsu, K. F.; Loo, S.; Guo, F.; Chen, W.; Dyck, J. S.; Uher, C.; Hogan, T.; Polychroniadis, E. K.; Kanatzidis, M. G., *Science* **2004**, 303, 818.
70. Androulakis, J.; Hsu, K. F.; Pcionek, R.; Kong, H. J.; Uher, C.; D'Angelo, J.; Downey, A. D.; Hogan, T.; Kanatzidis, M. G., *Adv. Mater.* **2006**, 18, 1170.

71. Poudeu, P. F. P.; D'Angelo, J.; Downey, A. D.; Short, J. L.; Hogan, T.; Kanatzidis, M. G., *Angew. Chem., Int. Ed.* **2006**, *45*, 3835.
72. Ahmad, S.; Mahanti, S. D., *Phys. Rev. B* **2006**, *74*, 155205.
73. Heremans, J. P.; Jovovic, V.; Toberer, E. S.; Saramat, A.; Kurosaki, K.; Charoenphakdee, A.; Yamanaka, S.; Snyder, G. J., *Science* **2008**, *321*, 554.
74. Nemov, S. A.; Ravich, Y. I., *Uspekhi Fizicheskikh Nauk* **1998**, *168*, 735.
75. Sootsman, J. R.; Kong, H.; Uher, C.; D'Angelo, J.; Wu, C. I.; Hogan, T.; Caillat, T.; Kanatzidis, M. G., *Angew. Chem., Int. Ed.* **2008**, *47*, 8618.

Chapter 2

Substitutions in the $\text{CsPb}_m\text{Bi}_3\text{Te}_{5+m}$ system

2.1. Introduction

Good thermoelectric materials should combine a particular set of properties. High electrical conductivity, large thermopower and low thermal conductivity are required to reach a high thermoelectric figure of merit ZT ($ZT = \sigma S^2 T / \kappa$). Thermal conductivity κ is comprised of two contributions, one from the lattice, the other one from the charge carriers. Consequently both constituents are usually considered separately. Because the electrical conductivity, the thermopower and the electronic thermal conductivity both depend on the electronic structure and the carrier transport properties of the compound, optimizing ZT remains a big challenge. Two approaches can be followed to improve the figure of merit, one is to maximize the so-called power factor (defined as σS^2), the other to minimize the lattice thermal conductivity.

The best known and used materials for room temperature application are Bi_2Te_3 alloys with $ZT \sim 1$.¹⁻³ The incorporation of alkali metals in the Bi_2Te_3 and Bi_2Se_3 structures resulted in the discovery of $\beta\text{-K}_2\text{Bi}_8\text{Se}_{13}$ ⁴⁻⁹ and of CsBi_4Te_6 .^{10, 11} Both compounds, anisotropic, show promising thermoelectric properties. Particularly, CsBi_4Te_6 exhibits the highest reported figure of merit at low temperature (~ 0.8 at 225 K). The structure consists of $[\text{Bi}_4\text{Te}_6]^-$ layers separated by Cs^+ cations. The presence of Bi-Bi bonds inside the layers contributes to the complexity of the electronic band

structure and gives the largest contribution to the states near the conduction band minimum.¹² The thermal conductivity is also low (~ 1.48 W/m·K in the direction parallel to the crystal growth, i.e. along the b direction), in part due to the large unit cell and the mass fluctuation between Bi and Te that favors phonon scattering.¹³ The alkali cations are loosely bound to the Te atoms via ionic interactions and tend to rattle under the influence of the temperature, thus reducing further the lattice thermal conductivity. In an effort to produce materials that resemble CsBi_4Te_6 , Pb metal was introduced to the layered material. A new homologous family, $\text{CsPb}_m\text{Bi}_3\text{Te}_{5+m}$ ($m=1, 2, 3, 4$),^{14, 15} was discovered.

The expression “homologous family” was introduced by Magneli¹⁶ to characterize chemical series that are expressed by a general formula and built on common structural principles. This concept has been very useful in predicting the existence and design of new compounds such as the megaseries $A_m[M_{1+l}\text{Se}_{2+l}]_{2m}[M_{2l+n}\text{Se}_{2+3l+n}]$ ($A=\text{K, Rb, Cs, Sr}$; $M=\text{Sn, Pb, Eu, Bi, Sb}$)^{17, 18} and $A_2[M_{5+n}\text{Se}_{9+n}]$.¹⁹ The four members have a structure similar to that of CsBi_4Te_6 . The main difference is the loss of Bi-Bi bonds as some Bi sites are now occupied by Pb atoms. Their moderate thermopower and metallic-like temperature dependence of the electrical conductivity indicate heavily-doped materials. The Sn analogs $\text{CsSnBi}_3\text{Te}_6$ and $\text{CsSn}_2\text{Bi}_3\text{Te}_7$ could be synthesized as well.¹⁴ Substitutions of Pb by other elements and Cs by other alkali metals could be a tool to fine-tune the electronic properties of the system without affecting its low dimensional structure. Here we report the results of such substitution experiments on $\text{CsPbBi}_3\text{Te}_6$. Nine new compounds were identified: $\text{Cs}_{0.76}\text{K}_{0.74}\text{Bi}_{3.5}\text{Te}_6$ (1), $\text{CsNa}_{0.98}\text{Bi}_{4.01}\text{Te}_7$ (2),

$\text{Cs}_{0.69}\text{Ca}_{0.65}\text{Bi}_{3.34}\text{Te}_6$ (3), $\text{Rb}_{0.82}\text{Pb}_{0.82}\text{Bi}_{3.18}\text{Te}_6$ (4), $\text{Rb}_{0.19}\text{K}_{1.31}\text{Bi}_{3.50}\text{Te}_6$ (5), $\text{RbSnBi}_3\text{Te}_6$ (6), $\text{Rb}_{0.94}\text{Ca}_{0.94}\text{Bi}_{3.06}\text{Te}_6$ (7), $\text{RbYbBi}_3\text{Te}_6$ (8) and $\text{KSnSb}_3\text{Te}_6$ (9). Single crystal diffraction studies indicated that all these compounds except $\text{CsNa}_{0.98}\text{Bi}_{4.01}\text{Te}_7$ and $\text{KSnSb}_3\text{Te}_6$ are isostructural to $\text{CsPbBi}_3\text{Te}_6$. $\text{CsNa}_{0.98}\text{Bi}_{4.01}\text{Te}_7$ is isostructural to $\text{CsPb}_2\text{Bi}_3\text{Te}_7$, the second member of the family. $\text{KSnSb}_3\text{Te}_6$ exhibits a different crystal structure found for the selenides $\text{CsAg}_{0.5}\text{Bi}_{3.5}\text{Se}_6$ and $\text{CsCdBi}_3\text{Se}_6$.¹⁹

2.2. Experimental section

2.2.1. Synthesis

For each compound, all the elements were loaded in a silica tube under a dry nitrogen atmosphere in a Vacuum Atmosphere Dry-Lab glove-box. The alkali metal was first weighed in the tube using a Pasteur pipette. Few small chunks of tellurium were then added to the molten alkali metal in order to prereact the two elements. The other metals were then added inside the tube. The tubes were sealed under residual pressure of $\sim 10^{-4}$ torr. For (1), (2), (3), (4), (5), (6), (7) and (9), the tubes were then heated in a flame at a temperature above 600 °C in order to prereact the elements before introducing the tube in a furnace. The products were washed with degased dimethylformamide in order to remove residual cesium/rubidium telluride formed during the reaction. For $\text{CsNa}_{0.98}\text{Bi}_{4.01}\text{Te}_7$, tellurium and bismuth were introduced in one side of a H-shape silica tube. Then sodium and cesium metal was introduced in the other part of the H-tube. The stoichiometries used to prepare the materials are summarized in Table 2-1.

Table 2-1. Ratio and quantity of elements mixed for (1), (2), (3), (4), (5), (6), (7), (8) and (9).

Compounds	Elements			
Cs_{0.74}K_{0.76}Bi_{3.5}Te₆ (1)	Cs	K	Bi	Te
Ratio	1.44	0.72	7.28	12
Amount, g (mmol)	0.086, (0.65)	0.013, (0.32)	0.684, (3.27)	0.688, (5.39)
CsNa_{0.98}Bi_{4.01}Te₆ (2)	Cs	Na	Bi	Te
Ratio	0.74	1	3.5	6
Amount, g (mmol)	0.150, (1.13)	0.035, (1.53)	1.116, (5.34)	1.168, (9.15)
Cs_{0.69}Ca_{0.65}Bi_{3.34}Te₆ (3)	Cs	CaTe	Bi	Te
Ratio	1	2	3	4
Amount, g (mmol)	0.093, (0.70)	0.235, (1.40)	0.439, (2.10)	0.357, (2.80)
Rb_{0.82}Pb_{0.82}Bi_{3.18}Te₆ (4)	Rb	Pb	Bi	Te
Ratio	1	1	3	6
Amount, g (mmol)	0.090, (1.05)	0.218, (1.05)	0.660, (3.16)	0.806, (6.32)
Rb_{0.19}K_{1.31}Bi_{3.50}Te₆ (5)	Rb	K	Bi	Te
Ratio	1g	1	3	6
Amount, g (mmol)	0.183, (2.14)	0.084, (2.14)	1.342, (6.42)	1.639, (12.84)
RbSnBi₃Te₆ (6)	Rb	Sn	Bi	Te
Ratio	2	1	3	6
Amount, g (mmol)	0.201, (2.35)	0.140, (1.18)	0.737, (3.53)	0.900, (7.06)
Rb_{0.94}Ca_{0.94}Bi_{3.06}Te₆ (7)	Rb	CaTe	Bi	Te
Ratio	1	2	3	4
Amount, g (mmol)	0.165, (1.93)	0.647, (3.86)	1.210, (5.79)	0.985, (7.72)
RbYbBi₃Te₆ (8)	Rb	Yb	Bi	Te
Ratio	1.5	1.5	3	6
Amount, g (mmol)	0.105, (1.23)	0.213, (1.23)	0.513, (2.36)	0.627, (4.91)
KSnSb₃Te₆	K	Sn	Sb	Te
Ratio	1	1	3	6
Amount, g (mmol)	0.030, (0.77)	0.091, (0.77)	0.280, (2.30)	0.587, (4.60)

Temperature profiles

Cs_{0.74}K_{0.76}Bi_{3.5}Te₆. The tube was placed in a furnace set at 700 °C for an hour, then cooled down to 450 °C at a rate of 125 °C/h, kept at 450 °C for 12 hours and cooled down to 50 °C at a rate of 200 °C/hour. After removal of the excess of cesium telluride with DMF, the material consisted of silvery, thin needles. These needles were a mixture of CsBi₄Te₆ and Cs_{0.74}K_{0.74}Bi_{3.5}Te₆.

A large scale ingot was prepared for preliminary evaluation of the thermoelectric properties of the compound. The tube was placed vertically in a regular furnace in order to grow oriented needles. Another good technique to grow oriented needles is the Bridgman method. In this technique, the elements are loaded in a silica tube terminated by a tip and are placed in a temperature gradient. This technique has been successfully applied for needle-shape selenide compounds. However it was not successful for Cs_{0.74}K_{0.76}Bi_{3.5}Te₆ because cesium reacts with the silica tube. Examination under microscope of the ingot obtained with the tube in the vertical position reveals bunches of oriented needles. However they are not well oriented with each other.

CsNa_{0.98}Bi_{4.01}Te₇. The tube was placed overnight in a furnace set at 300 °C to allow a progressive vaporization and transfer of cesium and sodium to the other side of the H-tube where they will react with tellurium and bismuth. Once all cesium and sodium vaporized, the tube was heated to 700 °C at a rate of 100 °C/hour, held at 700 °C for one hour and cooled down to 50 °C at a rate of 32 °C/hour. When the tube was removed, both sides of the tube contained materials, plate material (Bi₂Te₃) in the tellurium/bismuth side and silvery, thin needle-shape material in the cesium/sodium side.

Cs_{0.69}Ca_{0.65}Bi_{3.34}Te₆. The tube was placed in a furnace set at 900 °C for 10 hours, then cooled down to 450 °C at a rate of 10 °C/hour, then kept at 450 °C for twelve hours and cooled down to 50 °C at a 200 °C/hour. After isolation with DMF, silvery thin needles were obtained. EDS analysis on several needles gave the average composition Cs_{0.60}Ca_{0.22}Bi_{3.85}Te₆.

Rb_{0.82}Pb_{0.82}Bi_{3.18}Te₆. The tube was placed in a furnace set at 650 °C for six hours, then cooled down to 50 °C at a rate of 20 °C/hour. After isolation with DMF, silvery, thin needles were obtained. EDS analysis gave the average composition Rb_{1.81}Pb_{0.51}Bi_{2.96}Te₆.

Rb_{0.19}K_{1.31}Bi_{3.50}Te₆. The tube was placed into a furnace set at 700 °C for three hours, cooled down to 50 °C at a rate of 125 °C/hour. After isolation with DMF, silvery, thin needles were obtained. EDS analysis on several needles gave an average composition RbK_{0.77}Bi_{4.00}Te_{5.74}.

RbSnBi₃Te₆. The tube was then heated in a flame and placed into a furnace set at 700 °C for six hours, cooled down to 450 °C at a rate of 83 °C/hour, kept at 450 °C twelve hours and cooled down to 50 °C at a rate of 200 °C/hour. After isolation with DMF, silvery, thin needles were obtained. The needles consisted of a mixture of RbBi_{3.66}Te₆ and RbSnBi₃Te₆.

Rb_{0.94}Ca_{0.94}Bi_{3.06}Te₆. The tube was placed into a furnace set at 900 °C for ten hours, cooled down to 450 °C at a rate of 125 °C, kept at 450 °C for twelve hours and cooled down to 50 °C at a rate of 100 °C/hour. After isolation with DMF, silvery, a mixture of

silvery, thin needle (EDS analysis gave the average composition $\text{Rb}_{0.83}\text{Ca}_{0.41}\text{Bi}_{3.9}\text{Te}_6$) and chunks of Bi_2Te_3 .

RbYbBi₃Te₆. The tube was placed into a furnace set at 900 °C for ten hours, cooled down to 450 °C at a rate of 45 °C/hour, kept at 450 °C for twelve hours and cooled down to 50 °C at a rate of 100 °C/hour. The resulting product after washing in degassed DMF consisted of silvery, thin needle-shape crystals. EDS analysis on needles gave the average composition $\text{RbYb}_{0.16}\text{Bi}_{3.14}\text{Te}_{5.27}$.

KSnSb₃Te₆. The tube was placed in a furnace set at 700 °C for 6 hours and cooled down to 50 °C at a rate of 22 °C/hour. The majority of the material consisted of plate-like crystals (Sb_2Te_3) but a few needle-shape crystals were also found.

2.2.2. Physical measurements

Powder X-ray diffraction. Powder X-ray patterns of the grinded materials were recorded using Ni-filtered Cu K_α radiation on a CPS-120 Inel X-ray powder diffractometer operating at 40 kV and 20 mA equipped with a position sensitive detector.

Energy Dispersive Spectroscopy analysis (EDS). Semiquantitative microprobe analysis of the crystals were performed with a JEOL JSM-35C scanning electron microscope equipped with a Tracer Northern energy dispersive spectrometer. Data were acquired using an acceleration voltage of 25 kV and a 30s accumulation time.

Single crystal X-ray diffraction. For the single crystal of $\text{Cs}_{0.74}\text{K}_{0.76}\text{Bi}_{3.5}\text{Te}_6$, $\text{Cs}_{0.69}\text{Ca}_{0.65}\text{Bi}_{3.34}\text{Te}_6$, $\text{Rb}_{0.82}\text{Pb}_{0.82}\text{Bi}_{3.18}\text{Te}_6$, $\text{Rb}_{0.19}\text{K}_{1.31}\text{Bi}_{3.50}\text{Te}_6$ and $\text{KSnSb}_3\text{Te}_6$, intensity data were collected at room temperature on a Bruker SMART Platform CCD.

The single crystal of $\text{CsNa}_{0.98}\text{Bi}_{4.01}\text{Te}_7$ was collected on a similar machine at 173 K. The SMART software was used for the data acquisition and SAINT for data extraction and reduction.

The intensity data for the crystals of $\text{RbSnBi}_3\text{Te}_6$, $\text{Rb}_{0.94}\text{Ca}_{0.94}\text{Bi}_{3.06}\text{Te}_6$ and $\text{KSnSb}_3\text{Te}_6$ were collected at 100 K on a STOE IPDS-II diffractometer using graphite-monochromatized Mo K_α radiation. A numerical absorption correction was applied with the program X-RED²⁰ based on a crystal shape description. For the structure refinement, the SHELXTL package of programs²¹ was used. To refine the occupancy of the mixed metal sites, linear functions constraining the Bi and metal atoms on the various sites were used. The first type of function was to constrain the sum of site occupancy factors (SOF) in the metal sites to be equal to 1 (i.e., metals sites fully occupied). The second type of constraint was to consider the sum of the formal charge of metal atoms multiplied by their own SOF equal to 2 (i.e., average charge = +2).

Thermal analysis. In order to check the purity and the melting point of the compounds, differential thermal analysis (DTA) was performed using a computer-controlled Shimadzu DTA-50 thermal analysis. A small quantity (~30 mg) of the crushed material was loaded in a silica ampoule and flame-sealed under vacuum. Another silica tube containing a similar amount of α -alumina was placed on the reference side of the detector. The samples were heated to 750 °C at a rate of 10 °C/min, held at 750 °C for one minute and cooled to 50 °C at a rate of -10 °C/min.

Electrical property measurements. The electrical conductivity of the samples was measured using a 4-probe apparatus. The sample size was about 3 x 3 x 8 mm. Copper wires and silver paste were used for the contacts. A MMR Technologies system was used

to measure the thermopower of the compounds. Samples were measured with reference to a constantan wire (~ 1 x 1 x 4 mm).

2.3. Results and discussion

2.3.1. Structure description

$\text{Cs}_{0.74}\text{K}_{0.76}\text{Bi}_{3.5}\text{Te}_6$, $\text{Cs}_{0.69}\text{Ca}_{0.65}\text{Bi}_{3.34}\text{Te}_6$, $\text{Rb}_{0.82}\text{Pb}_{0.82}\text{Bi}_{3.18}\text{Te}_6$, $\text{Rb}_{0.19}\text{K}_{1.31}\text{Bi}_{3.50}\text{Te}_6$, $\text{RbSnBi}_3\text{Te}_6$ and $\text{Rb}_{0.94}\text{Ca}_{0.94}\text{Bi}_{3.06}\text{Te}_6$ crystallize in the orthorhombic space group *Cmcm* and are isostructural to $\text{CsPbBi}_3\text{Te}_6$. These compounds can be expressed with the general formula $\text{A}_{1-x}\text{M}_4\text{Te}_6$: $(\text{Cs}_{0.74}\text{K}_{0.26})(\text{K}_{0.5}\text{Bi}_{3.5})\text{Te}_6$, $\text{Cs}_{0.69}(\text{Ca}_{0.65}\text{Bi}_{3.34})\text{Te}_6$, $\text{Rb}_{0.82}(\text{Pb}_{0.82}\text{Bi}_{3.18})\text{Te}_6$, $\text{Rb}_{0.19}\text{K}_{0.81}(\text{K}_{0.50}\text{Bi}_{3.50})\text{Te}_6$, $\text{Rb}(\text{SnBi}_3)\text{Te}_6$, $\text{Rb}_{0.94}(\text{Ca}_{0.94}\text{Bi}_{3.06})\text{Te}_6$, $\text{Rb}(\text{YbBi}_3)\text{Te}_6$. The compounds exhibit a layered structure with infinite anionic $[\text{M}_4\text{Te}_6]^-$ slabs separated by alkali metal cations (Figure 2-1a). Each slab contains two crystallographically distinct metal sites M1 and M2, mixed sites of bismuth and the other metal, and three crystallographically independent tellurium sites. Both metal sites are octahedrally coordinated with Te atoms. The Te sites have several coordination environment with Te1, Te2 and Te3 being respectively 2, 4 and 6-coordinated with the metal atoms. The slabs can be viewed as a fragment excised from the NaCl-structure type along the [011] directions with a thickness of four monolayers.

$\text{CsNa}_{0.98}\text{Bi}_{4.01}\text{Te}_7$ also crystallizes in the space group *Cmcm* but is isostructural to $\text{CsPb}_2\text{Bi}_3\text{Te}_7$, the second member of the family (Figure 2-1b). In this case, the slabs are one monolayer {NaCl} thicker. Each slab contains four crystallographically distinct

metal sites M1, M2, M3, and M4, all octahedrally coordinated by the tellurium atoms. In both structures, the alkali metal sites are surrounded by nine Te atoms.

$\text{KSnSb}_3\text{Te}_6$ crystallizes in the orthorhombic space group $Pnma$ (Figure 2-2). In the structure, K^+ cations separate $[\text{SnSb}_3\text{Te}_6]^-$ layers. Their arrangement differs from that of the previously mentioned compounds in the orientation of the layers. For the crystals crystallizing in the $Cmcm$ space-group, the building blocks are NaCl^{100} type whereas for $\text{KSnSb}_3\text{Te}_6$ the layers are made of NaCl^{111} . This reorganization is probably due to the smaller size of the K^+ cation.

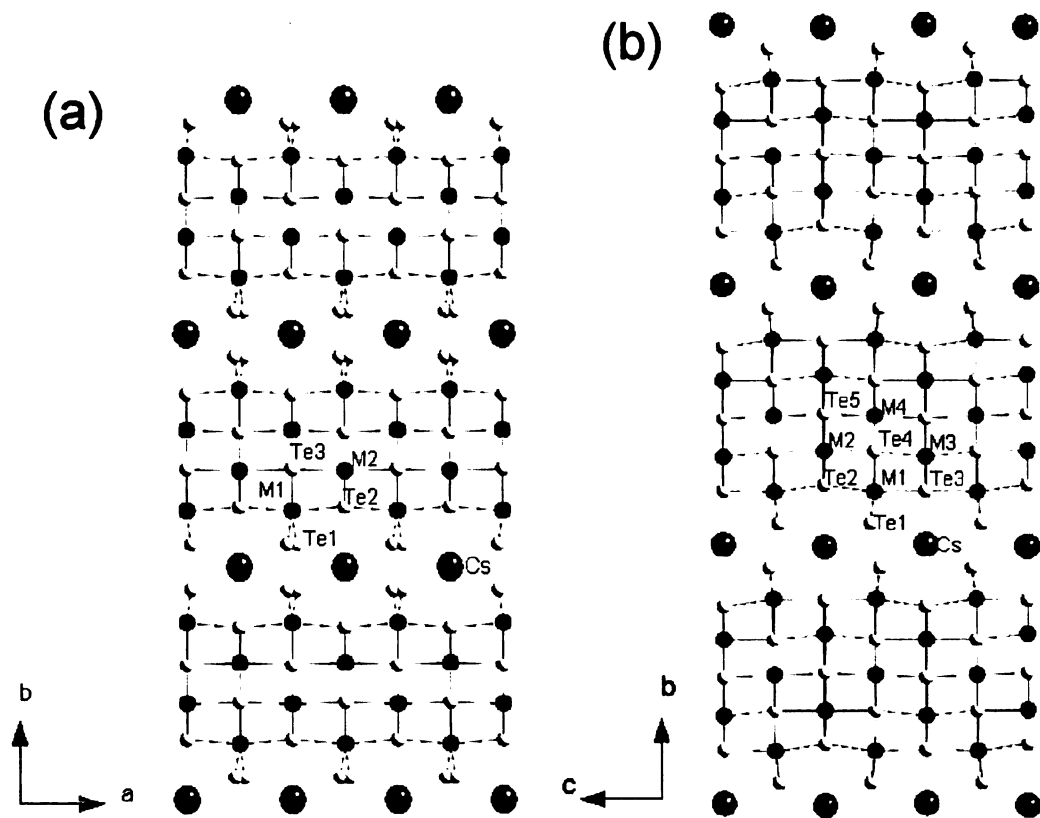


Figure 2-1. Structure type of (a) $\text{A}_{1-x}\text{M}_4\text{Te}_6$ along the c axis and (b) of $\text{CsNa}_{0.98}\text{Bi}_{4.01}\text{Te}_7$ along the a -axis.

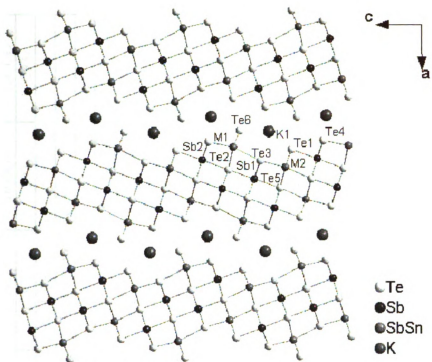


Figure 2-2. Crystal structure of $\text{KSnSb}_3\text{Te}_6$ viewed along the b -axis.

The refinement data for all crystals are summarized in Tables 2-2 and 2-3. It must be noticed that the position of Te1 is close to a special position but the atom does not sit exactly at this position. It is a split site that alternates between 2 positions close to the special position

Table 2-2. Summary of the crystallographic data for (1), (2) (3), (4) and (5).

	(1)	(2)	(3)	(4)	(5)
Formula weight	1625.10	1886.65	1565.53	1670.14	1564.49
Temperature (K)	293	173	293	293	293
Wavelength (Å)	0.71073				
Diffractometer	Siemens SMART Platform CCD				
Space group	<i>Cmcm</i>				
Unit cell (Å)	6.3810 (9)	4.4314 (2)	6.339 (9)	6.3124 (2)	6.313 (6)
	28.326 (4)	32.784 (2)	28.11 (4)	28.340 (6)	27.97 (3)
	4.4134 (2)	12.742 (4)	4.383 (6)	4.3939 (2)	4.395 (4)
Volume (Å ³)	797.72 (2)	1851.1 (2)	781.0 (2)	786.0 (3)	776.1 (2)
Z	2	4	2	2	2
Density (mg/m ³)	6.768	6.770	6.727	7.056	6.695
Absorption coefficient (mm ⁻¹)	57.079	50.748	50.265	57.636	51.524
Θ range for data collection (°)	1.44 to 28.04	2.02 to 28.78	1.45 to 28.37	1.44 to 28.32	1.46 to 28.29
Independent reflections	579	1345	580	570	546
R _{int}	0.0524	0.0561	0.0360	0.0454	0.01696
Refinement method	Full matrix least-square on F ²				
Goodness of fitness	1.216	1.055	1.125	1.164	1.116
Final R indices	R ₁ ^a = 0.0455 wR ₂ ^b = 0.1222	R ₁ ^a = 0.0491 wR ₂ ^b = 0.0971	R ₁ ^a = 0.0367 wR ₂ ^b = 0.1158	R ₁ ^a = 0.0287 wR ₂ ^b = 0.0733	R ₁ ^a = 0.0458 wR ₂ ^b = 0.1330
Extinction coefficient	0.0012 (2)	0.000095 (2)	0.00117 (2)	0.00038 (5)	0.00042 (2)
Largest diff. peak and hole (e.Å ⁻³)	4.580 and -2.344	3.014 and -3.333	3.348 and -2.966	2.625 and -3.449	5.227 and -3.449

Table 2-3. Summary of the crystallographic data for RbSnBi₃Te₆ (6), Rb_{0.94}Ca_{0.94}Bi_{3.06}Te₆ (7), RbYbBi₃Te₆ (8) and KSnSb₃Te₆ (9).

	(6)	(7)	(8)	(9)
Formula weight	1523.10	1596.70	1651.05	1288.64
Temperature (K)	100	100	293	100
Wavelength (Å)	0.71073	0.71073	0.71073	0.71073
Diffractometer	STOE IPDS-II		Siemens SMART Platform CCD	STOE IPDS-II
Space group	<i>Cmcm</i>			<i>Pnma</i>
Unit cell (Å)	6.2722 (2)	6.2382 (2)	6.3470 (3)	26.610 (5)
	28.151 (6)	28.284 (6)	28.280 (6)	4.2480 (8)
	4.3562 (9)	4.3429 (9)	4.3990 (9)	12.845 (3)
Volume (Å ³)	769.2 (3)	766.3 (3)	789.96 (3)	1452.0 (5)
Z	2	2	2	4
Density (mg/m ³)	6.576	6.920	6.944	5.895
Absorption coefficient (mm ⁻¹)	49.294	50.263	53.081	19.278
Θ range for data collection (°)	2.89 to 33.22	2.88 to 31.85	1.44 to 27.96	1.76 to 29.42
Independent reflections	882	794	562	2224
R _{int}	0.1441	0.1317	0.0473	0.1596
Refinement method	Full matrix least-square on F ²			
Goodness of fitness	1.218	1.122	1.339	0.732
Final R indices	R ₁ ^a = 0.0498 wR ₂ ^b = 0.1212	R ₁ ^a = 0.0560 wR ₂ ^b = 0.1431	R ₁ ^a = 0.0356 wR ₂ ^b = 0.1350	R ₁ ^a = 0.0419 wR ₂ ^b = 0.0942
Extinction coefficient	0.000642 (2)	0.000395 (2)	0.00086 (2)	none
Largest diff. peak and hole (e.Å ⁻³)	4.905 and -6.490	4.457 and -7.118	3.325 and -2.039	2.512 and -2.499

$${}^a R_1 = \sum \|F_o\| - \|F_c\| / \sum \|F_o\|$$

$${}^b wR_2 = \left\{ \sum [w(F_o^2 - F_c^2)]^2 / \sum [w(F_o^2)]^2 \right\}^{1/2}$$

The metal-Te and alkali metal-Te bond distances are summarized in Tables 2-4, 2-5 and 2-6.

Table 2-4. Metal-tellurium and alkali site-tellurium bond distances (Å) in compounds (1), (3), (4), (5), (6), (7) and (8).

Compound	(1)	(3)	(4)	(5)
Metal-Te bonds	(M= Bi/K)	(M=Bi/Ca)	(M=Bi/Pb)	(M=Bi/K)
M1-Te1	2.9993 (17)	2.977 (3)	2.9881 (15)	2.980 (3)
M1-Te2	3.2014 (5)	3.180 (4)	3.1701 (7)	3.166 (3)
M1-Te3	3.3818 (13)	3.355 (3)	3.3978 (12)	3.371 (3)
M2-Te2	3.1067 (15)	3.085 (3)	3.1076 (13)	3.095 (3)
M2-Te3	3.1925 (5)- 3.2231 (13)	3.172 94)- 3.196 (3)	3.1616 (6)- 3.2428 (11)	3.159 (3)- 3.208 (3)
Alkali metal-Te bonds	A=Cs	A=Cs	A=Rb	A=Rb
A-Te1	3.196 (3) x 2 3.703 (2) x 2 3.941 (2) x 3	3.168 (5) x 2 3.683 (5) x 2 3.914 (4) x 4	3.212 (5) x 2 3.620 (4) x 2 3.938 (4) x 4	3.167 (6) x 2 3.628 (6) x 2 3.912 (6) x 3

Compound	(6)	(7)	(8)
Metal-Te bonds	(M= Bi/Sn)	(M=Bi/Ca)	(M=Bi/Yb)
M1-Te1	2.9542 (16)	2.9713 (7)	2.9869 (18)
M1-Te2	3.1414 (7)	3.1473 (6)	3.1846 (7)
M1-Te3	3.3817 (13)	3.3754 (7)	3.3951 (14)
M2-Te2	3.0691 (14)	3.0809 (7)	3.1040 (14)
M2-Te3	3.1288 (7)- 3.1994 (13)	3.1390 (6)- 3.2037 (7)	3.1762 (7)- 3.2216 (13)
Alkali metal-Te bonds	A=Rb	A=Rb	A=Rb
A-Te1	3.208 (6) x 2 3.571 (6) x 2 3.909 (6) x 4	3.228 (3) x 2 3.556 (2) x 2 3.927 (2) x 4	3.234 (8) x 2 3.620 (8) x 2 3.960 (7) x 4

In all the compounds isostructural to CsPbBi₃Te₆, the distance between the metal and the tellurium sites are comparable to those in CsPbBi₃Te₆ (average M-Te distance 3.173 (1))

Å).¹⁴ The bond distances in CsNa_{0.98}Bi_{4.01}Te₇ are in the same range as those in CsPb₂Bi₃Te₇.

Table 2-5. Metal-Te and alkali metal-Te1 bond distances (Å) in compound (2)

Metal-Te bond	Distance (Å)
Bi1-Te1	2.9890 (10)
Bi1-Te3	3.1754 (11)
Bi1-Te2	3.2280 (12)
Bi1-Te4	3.3831 (11)
Bi2-Te2	3.0829 (14)
Bi2-Te4	3.2174 (13)
Bi2-Te5	3.2905 (15)
Bi3-Te3	3.0607 (12)
Bi3-Te4	3.1708 (13)
Bi3-Te5	3.2593 (13)
Bi4-Te4	3.1549 (10)
Bi4-Te5	3.1888 (11)
Cs-Te1	3.7270 (15) x 2 3.9295 (12) x 4

Table 2-6. Metal-Te and alkali metal-Te bond distances (Å) in compound (9).

Metal-Te bond	Distance (Å)
Sb1-Te3	3.0149 (16)
Sb1-Te5	3.037 (2)
Sb1-Te2	3.0946 (16)
Sb2-Te4	3.0132 (17)
Sb2-Te2	3.148 (2)
Sb2-Te5	3.1573 (17)
M1-Te6	2.8981 (15)
M1-Te2	3.3280 (16)
M1-Te3	3.353 (2)
M2-Te1	2.9776 (16)
M2-Te5	3.1824 (17)
K-Te1	3.842 (6)
K-Te3	3.396 (6)
K-Te6	3.899 (6)

Atomic coordinates, equivalent isotropic displacement parameters and occupancy refinements for the metal sites for all compounds are reported on Tables 2-7, 2-8 and 2-9.

Table 2-7. Atomic coordinates and equivalent isotropic displacement parameters ($\text{\AA}^2 \times 10^3$) of the metal and alkali metal positions for (1), (3), (4), (5), (6), (7) and (8). $U(\text{eq})$ is defined as one third of the traces of the orthogonalized U_{ij} tensors.

Position	x	y	z	$U(\text{eq})$	Occupancy
M1					
(1), Bi/K	0.5	0.3800 (1)	0.75	23 (1)	0.904/0.096
(3), Bi/Ca	0.5	0.3798 (1)	0.75	21 (1)	0.855/0.145
(4) Bi/Pb	0.5	0.3811 (10)	0.75	24 (1)	0.826/0.174
(5), Bi/K	0.5	0.3808 (1)	0.75	21 (10)	0.905/0.095
(6), Bi/Sn	0.5	0.3814 (1)	0.75	15 (1)	0.751/0.249
(7), Bi/Ca	0.5	0.3810 (1)	0.75	5 (1)	0.766/0.234
(8), Bi/Yb	0.5	0.3808 (1)	0.75	24 (1)	0.833/0.167
M2					
(1), Bi/K	0	0.2934 (1)	0.25	24 (1)	0.847/0.153
(2), Bi/Ca	0	0.2933 (1)	0.25	23 (1)	0.813/0.187
(4) Bi/Pb	0	0.2943 (91)	0.25	27 (1)	0.763/0.237
(5), Bi/K	0	0.2942 (1)	0.25	24 (1)	0.846/0.154
(6), Bi/Sn	0	0.2937 (1)	0.25	17 (1)	0.755/0.245
(7), Bi/Ca	0	0.2941 (1)	0.25	8 (1)	0.765/0.235
(8), Bi/Yb	0	0.2939 (1)	0.25	25 (1)	0.667/0.333
A					
(1), Cs/K	0	0.4971 (1)	0.25	40 (1)	0.740/0.260
(3), Cs	0	0.4969 (2)	0.25	27 (1)	0.693
(4), Rb	0	0.4977 (3)	0.25	112 (4)	0.821
(5), Rb/K	0	0.4070 (4)	0.25	40 (3)	0.191/0.809
(6), Rb	0	0.4983 (4)	0.25	101 (7)	0.791
(7), Rb	0	0.4983 (2)	0.25	120 (4)	0.791
(8), Rb	0	0.4975 (4)	0.25	114 (4)	1

Table 2-8. Atomic coordinates and equivalent isotropic displacement parameters ($\text{\AA}^2 \times 10^3$) for (2). U(eq) is defined as one third of the traces of the orthogonalized U_{ij} tensors.

Position	x	y	z	U(eq)	Occupancy
M1, Bi/Na	0.5	0.1465 (1)	0.4967 (1)	15 (1)	0.945/0.055
M2, Bi/Na	0	0.787 (1)	0.75	18 (1)	0.588/0.412
M3, Bi/Na	0	0.684 (1)	0.25	17 (1)	0.827/0.173
M4, Bi/Na	0.5	0	0.5	15 (1)	0.702/0.298
Cs	0.5	0.2523 (1)	0.25	22 (1)	1

Table 2-9. Atomic coordinates and equivalent isotropic displacement parameters ($\text{\AA}^2 \times 10^3$) for (9). U(eq) is defined as one third of the traces of the orthogonalized U_{ij} tensors.

Position	x	y	z	U(eq)	Occupancy
Sb1	0.4801 (1)	-0.75	0.8601 (1)	14 (1)	1
Sb2	0.3978 (1)	0.25	0.3114 (1)	24 (1)	1
M1, Sn/Sb	0.3461 (1)	-0.25	0.389 (1)	12 (1)	0.513/0.487
M2, Sn/Sb	0.4322 (10)	-0.25	0.5874 (1)	16 (1)	0.557/0.443
K	0.2822 (1)	-0.25	0.7271 (5)	41 (2)	1

For compounds (1), (3), (4), (5), (6), (7) and (8), refinement data indicated all sites to be mixed occupied. In the case of (1) and (5), the alkali sites are also mixed-occupied with K. K has a larger ionic radius than the other elements inserted in the structure; its radius is close to that of Cs and Rb. However, in the system Rb/K/Bi/Te, there is less Rb and more K in the formula. The inverse situation was found in the system Cs/K/Bi/Te. This can be due to the fact that the size of K is closer to that of Rb than that of Cs. K can more easily replace Rb than Cs. The alkali metal sites are not fully occupied in (3), (4) and (6). The substitutions show the flexibility of $\text{CsPbBi}_3\text{Te}_6$ and $\text{CsPb}_2\text{Bi}_3\text{Te}_7$ structure types towards chemical modifications and that the divalent Pb atom can be replaced by atoms with slightly smaller (Na, Ca, Yb) and larger (K) atomic radii. The alkali metals located

between the layers show very large thermal displacement parameters indicating that they may be rattling in their local environment.

2.3.2. Characterization

$\text{Cs}_{0.74}\text{K}_{0.76}\text{Bi}_{3.5}\text{Te}_6$. The comparison between the experimental and calculated X-ray powder diffraction patterns showed a good agreement (Figure 2-3a). EDS measurements on five needles gave the average formula $\text{Cs}_{0.52}\text{K}_{0.22}\text{Bi}_{3.20}\text{Te}_6$. However the DTA analysis (Figure 2-3b) showed two melting peaks at 821 and 831 K. Upon cooling, only one recrystallization peak appears at 807 K. The second run showed two melting points (543 and 841 K) and two crystallization points (807 and 834 K). This is probably due to a melting/decomposition process happening during the heating process. The melting point at 821 K indicates the presence of CsBi_4Te_6 as a second phase. This can be expected as the ternary and quaternary phases have similar crystal structure. The X-ray patterns taken after DTA are similar to those taken before.

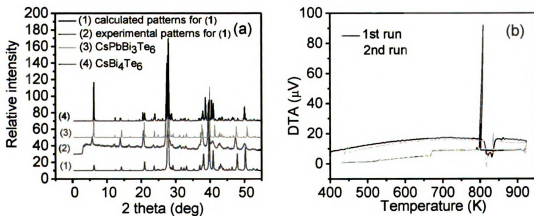


Figure 2-3. (a) Comparison between the calculated and experimental powder X-ray diffraction patterns of compound (1) and (b) DTA results for compound (1).

A large scale ingot was prepared for preliminary evaluation of the thermoelectric properties of the compound. The tube was placed vertically in a tube furnace in order to grow oriented needles. Another good technique to grow oriented needles is the Bridgman method. In this technique, the elements are loaded in a silica tube terminated by a tip and are placed in a temperature gradient. This technique has been successfully applied for needle-shaped selenide compounds. However it was not successful for $\text{Cs}_{0.74}\text{K}_{0.76}\text{Bi}_{3.5}\text{Te}_6$ because cesium reacted with the silica tube. Examination under microscope of the ingot obtained with the tube in the vertical position revealed bunches of oriented needles. However they were not well oriented with each other. Powder patterns were taken from the top and bottom of the ingot. The theoretical diffraction pattern calculated from the single crystal refinement, the experimental pattern from the first ingot, and that of the larger ingot are similar. An extra peak at 17° was observed from the powder from the bottom of the tube and indicates the presence of Bi_2Te_3 as a side product.

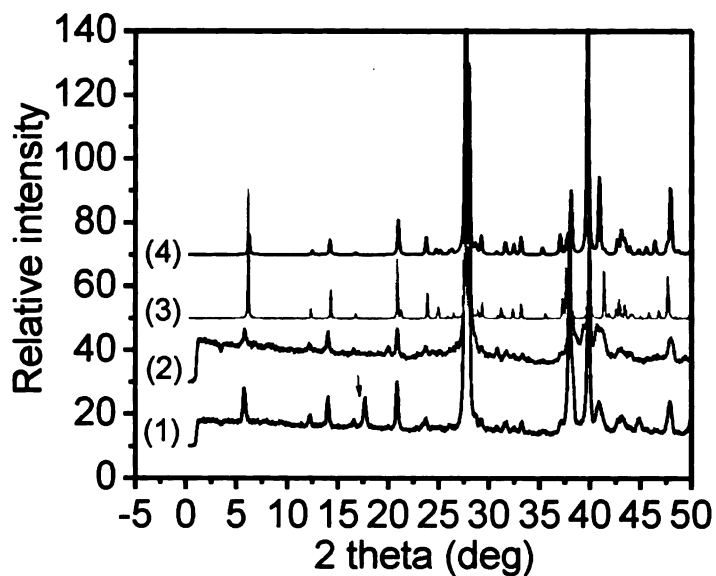


Figure 2-4. Comparison between the powder X-ray diffraction patterns of ground samples taken from bottom (1) and top (2) of the ingot with nominal composition $\text{Cs}_{0.76}\text{K}_{0.74}\text{Bi}_{3.5}\text{Te}_6$ prepared in the vertical furnace, the calculated powder pattern (4) and that of CsBi_4Te_6 (3).

Single crystal diffraction refinement on a needle from the large ingot indicated the composition $\text{Cs}_{0.6}\text{K}_{0.9}\text{Bi}_{3.5}\text{Te}_6$. A single melting and single crystallization peaks (at 850 and 828 K respectively) were observed on DTA data from the top of the ingot (Figure 2-5a). However, DTA analysis from the bottom showed two melting points (815 and 839 K), the first corresponding to CsBi_4Te_6 (Figure 2-5a).

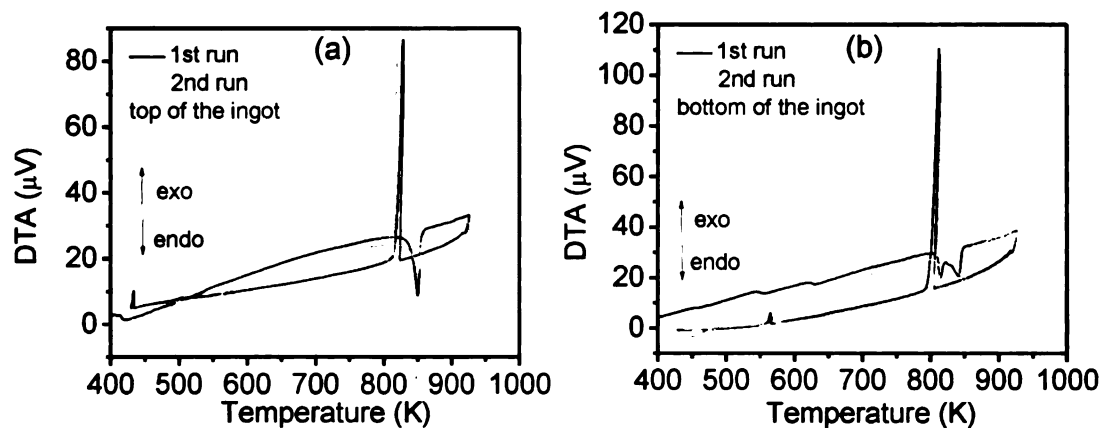


Figure 2-5. DTA results on powders taken from (a) the top and (b) the bottom of the material $\text{Cs}_{0.6}\text{K}_{0.9}\text{Bi}_{3.5}\text{Te}_6$ prepared in a vertical furnace.

$\text{CsNa}_{0.98}\text{Bi}_{4.01}\text{Te}_7$. Attempts to prepare the compound in a silica tube were not successful; the reactions resulted in a mixture of needles (CsBi_4Te_6), plates (Bi_2Te_3), and chunks containing all four elements. From EDS analysis, some needles showed quaternary composition, but no suitable needle was found for single crystal diffraction. A suitable needle was found from the Cs/Na side of the H-tube for single crystal diffraction. Comparison between the X-ray powder patterns from the Cs/Na side and calculated patterns from data refinement show good agreement. Materials prepared with cesium in one side and the other elements in the other side also contained needles randomly oriented on the top of the material. The X-ray powder patterns from the two preparations (Cs/Na or Cs only in one side) are similar.

$\text{Cs}_{0.69}\text{Ca}_{0.65}\text{Bi}_{3.34}\text{Te}_6$. Attack of the silica tube by reagents was observed after the reaction. The material was not well-formed and had needles grown on the walls of the tube. The experimental and calculated X-ray powder diffraction agreed well. EDS

analysis on several needles ($\text{Cs}_{0.60}\text{Ca}_{0.22}\text{Bi}_{3.85}\text{Te}_6$) confirmed the presence of all four elements.

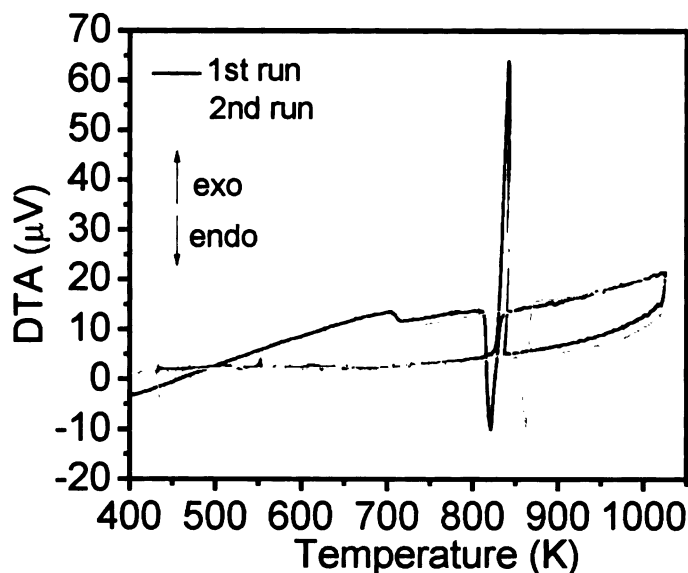


Figure 2-6. DTA results of the batch from which the compound $\text{Cs}_{0.69}\text{Ca}_{0.65}\text{Bi}_{3.34}\text{Te}_6$ was synthesized.

The first run of DTA (Figure 2-6) showed a melting point at 820 K (CsBi_4Te_6) and a crystallization point at 842 K. The bump ~ 700 K indicates the presence of impurities. The fact that the melting point is lower than the crystallization point indicates that the impurities reacted with the main product. The second run shows a melting point at 863 K and a crystallization point at 846 K. The powder patterns after DTA corresponded to Bi_2Te_3 .

$\text{Rb}_{0.82}\text{Pb}_{0.82}\text{Bi}_{3.18}\text{Te}_6$. Comparison between experimental and calculated X-ray powder diffraction showed the presence of an extra peak on the experimental data at $2\theta = 10^\circ$ that may be attributed to the presence of the Bi_2Te_3 phase. EDS analysis confirmed the

presence of all four elements in the needles but the average composition $\text{Rb}_{1.81}\text{Pb}_{0.51}\text{Bi}_{2.96}\text{Te}_6$ shows a higher Rb/Pb ratio.

In order to have a first evaluation of the thermoelectric properties, an experiment using the Bridgman technique resulted in an ingot with well-oriented needles. A very thin layer of impurity about 1 mm thick could be seen on the top of the ingot. The X-ray powder diffraction patterns indicated that the layer is a mixture of $\text{Rb}_{0.82}\text{Pb}_{0.82}\text{Bi}_{3.18}\text{Te}_6$ and $\text{Pb}_{1.71}\text{Bi}_{6.86}\text{Te}_{12}$ ²² (Figure 2-7a). Comparison between the experimental X-ray powder patterns of other parts of the ingot and the calculated ones showed good agreement but the presence of three melting points at 828, 839 and at 846 K on the DTA results reveals the presence of side-products (Figure 2-7b).

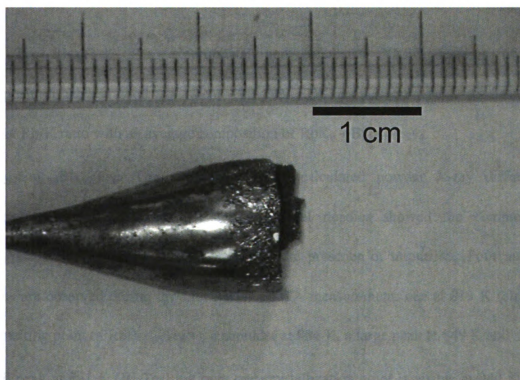


Figure 2-7. Picture of the ingot with composition $\text{Rb}_{0.82}\text{Pb}_{0.82}\text{Bi}_{3.18}\text{Te}_6$ prepared with the Bridgman technique.

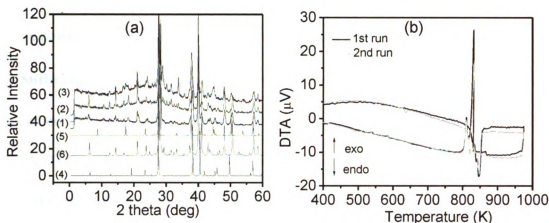


Figure 2-8. (a) Comparison between X-ray diffraction patterns of powders from bottom (1), middle (2) and top (3) of the ingot with composition (4) prepared by Bridgman technique and the calculated X-ray diffraction patterns of $\text{Pb}_{1.77}\text{Bi}_{6.86}\text{Te}_{12}$ (4), Bi_2Te_3 (5) and compound (4) (6); (b) DTA analysis of the powder from the middle of the ingot.

$\text{Rb}_{0.19}\text{K}_{1.31}\text{Bi}_{3.50}\text{Te}_6$. The experimental and calculated XRPD patterns of this composition showed good agreement. However EDS analysis on several needles show higher Rb/K ratio with an average composition of $\text{RbK}_{0.77}\text{Bi}_{4.00}\text{Te}_{5.74}$.

$\text{Rb}_{0.94}\text{Ca}_{0.94}\text{Bi}_{3.06}\text{Te}_6$. The experimental and calculated powder X-ray diffraction patterns agreed well. EDS analysis on several needles showed the composition $\text{Rb}_{0.83}\text{Ca}_{0.41}\text{Bi}_{3.9}\text{Te}_6$. DTA analysis indicates the presence of impurities. Four melting points are observed during the first run of a DTA measurement: one at 813 K (close to the melting point of $\text{RbBi}_{3.66}\text{Te}_6$ ¹³), a shoulder at 834 K, a large peak at 849 K and a very small peak at 861 K (Bi_2Te_3) but only one crystallization point is visible at 840 K. The

second run shows only one melting point at 867 K and one crystallization point at 849 K.

X-ray powder diffraction on the sample indicated only the presence of Bi_2Te_3 .

$\text{RbSnBi}_3\text{Te}_6$. Comparison between calculated and experimental XRPD showed a good agreement but two extra peaks were visible in the experimental spectra at 10.3° and 18.7° . DTA analysis confirmed the presence of two phases. EDS analysis on the needle gave the composition $\text{Rb}_{1.44}\text{Sn}_{0.55}\text{Bi}_{3.27}\text{Te}_6$. Two melting points at 822 K (close to the melting point of $\text{RbBi}_{3.66}\text{Te}_6$) and at 834 K and two crystallization points at 822 and 835 K are observed during the first ramp of the DTA measurements. A second run gave similar results. Powder patterns after DTA are similar to that before DTA.

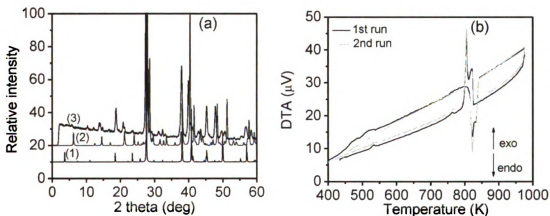


Figure 2-9. (a) Comparison between the experimental (3) and calculated (2) powder X-ray diffraction patterns for compound (6) and that of BiTe (3) and (b) DTA analysis of the powder from the middle of the ingot.

$\text{RbYbBi}_3\text{Te}_6$. The comparison between calculated and experimental powder X-ray diffraction presents a good agreement. EDS analysis on the needles gave the average

composition $\text{RbYb}_{0.16}\text{Bi}_{3.14}\text{Te}_{5.27}$. DTA analysis showed a single melting point at 861 K followed by a single crystallization point at 846 K.

$\text{KSnSb}_3\text{Te}_6$. Figure 2-10 shows a SEM picture of the needle used for single-crystal X-ray diffraction. EDS analysis on the needle gave the composition $\text{KSn}_{0.27}\text{Sb}_3\text{Te}_{5.19}$. The content of tin is low. There is an uncertainty on the relative ratios of Sn/Sb/Te because all three elements have close L X-ray emission lines.

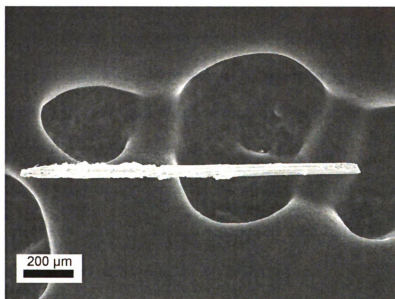


Figure 2-10. SEM image of the needle with composition $\text{KSnSb}_3\text{Te}_6$.

The attempts to substitute lead by silver, strontium and barium have not been successful. The ionic radius of octahedral Ag is 1.15\AA , which is close to that of lead (1.19\AA). It should be possible to replace some Bi by Ag atoms in the metal sites. When Pb was replaced by Ag, only a mixture of Bi_2Te_3 and RbAg_3Te_2 ²³ was obtained. Substituting Pb with Ba gave shiny BaBiTe_3 rods.²⁴⁻²⁶ EDS analysis from needles

obtained from a mixture of Rb, Sr, Bi and Te indicated only the ternary phase $\text{RbBi}_{3.66}\text{Te}_6$.

2.3.3. Preliminary Thermoelectric Results

This family of compounds combines numerous structural features that make them interesting for thermoelectric investigations. These are low dimensionality, preferential site occupancy of metal positions and isomorphous substitutions of Pb by a wide range of elements with different charges and atomic radii. In addition, the alkali metals located between the layers show very large thermal displacement parameters indicating that they may be rattling in their local environment, which may contribute in suppressing the thermal conductivity of the compounds.

Preliminary charge transport properties have been measured on $\text{Cs}_{0.74}\text{K}_{0.76}\text{Bi}_{3.5}\text{Te}_6$ (1) and $\text{Rb}_{0.82}\text{Pb}_{0.82}\text{Bi}_{3.18}\text{Te}_6$ (4) and are reported in Table 2-10. These two compositions were selected because of the better quality of the crystals.

Table 2-10. Preliminary thermoelectric measurements on the compounds (1) and (4).

	(1)		(4)**		$\text{CsPbBi}_3\text{Te}_6$
	top	bottom	top	bottom	
Electrical conductivity σ (S/cm)	601	986	1437	1811	830
Thermopower S ($\mu\text{V/K}$)	-26	-37	-20	-22	-40
Power factor ($= S^2\sigma$) ($\mu\text{W/K.cm}^2$)	0.406	1.350	0.575	0.877	1.328

*ingot prepared with a regular furnace in vertical position

**ingot prepared with the Bridgman method

2.4. Conclusions

This study showed it is possible to substitute Pb by other elements such as Na, K, Ca, Sn, Yb in $\text{CsPbBi}_3\text{Te}_6$, the first member of the homologous family $\text{CsPb}_m\text{Bi}_3\text{Te}_{5+m}$. $\text{Cs}_{0.74}\text{K}_{0.76}\text{Bi}_{3.5}\text{Te}_6$, $\text{Cs}_{0.69}\text{Ca}_{0.65}\text{Bi}_{3.34}\text{Te}_6$, $\text{Rb}_{0.82}\text{Pb}_{0.82}\text{Bi}_{3.18}\text{Te}_6$, $\text{Rb}_{0.19}\text{K}_{1.31}\text{Bi}_{3.50}\text{Te}_6$, $\text{RbSnBi}_3\text{Te}_6$ and $\text{Rb}_{0.94}\text{Ca}_{0.94}\text{Bi}_{3.06}\text{Te}_6$ are isostructural to $\text{CsPbBi}_3\text{Te}_6$ whereas $\text{CsNa}_{0.98}\text{Bi}_{4.01}\text{Te}_7$ is isostructural to $\text{CsPb}_2\text{Bi}_3\text{Te}_7$, the second member of the family. Substitution of Cs by K resulted in a reorganization of the layers around the alkali metal. The crystal structure of $\text{KSnSb}_3\text{Te}_6$ is similar to that of the selenides $\text{CsAg}_{0.5}\text{Bi}_{3.5}\text{Se}_6$ and $\text{CsCdBi}_3\text{Se}_6$.¹⁹ However these compounds can not be prepared as pure phases so far. Alkali tellurides and the ternary phases CsBi_4Te_6 and $\text{RbBi}_{3.66}\text{Te}_6$ were identified as side products. The quality of the needles also was quite poor. Using A_2Te as starting materials did not help improving the yield of the reactions.

References

1. Jeon, H.-W.; Ha, H.-P.; Hyun, D.-B.; Shim, J.-D., *J. Phys. Chem. Solids* **1991**, *52*, 579.
2. Champness, C. H.; Chiang, P. T.; Parekh, P., *Can. J. Phys.* **1965**, *43*, 653.
3. Champness, C. H.; Chiang, P. T.; Parekh, P., *Can. J. Phys.* **1967**, *45*, 3611.
4. Chung, D. Y.; Choi, K. S.; Iordanidis, L.; Schindler, J. L.; Brazis, P. W.; Kannewurf, C. R.; Chen, B.; Hu, S.; Uher, C.; Kanatzidis, M. G., *Chem. Mater.* **1997**, *9*, 3060.
5. Kyratsi, T.; Chung, D.-Y.; Kanatzidis, M. G., *J. Alloys Compd.* **2002**, *338*, (1-2), 36-42.
6. Kyratsi, T.; Dyck, J. S.; Chen, W.; Chung, D.-Y.; Uher, C.; Paraskevopoulos, K. M.; Kanatzidis, M. G., *Journal of Applied Physics* **2002**, *92*, (2), 965-975.
7. Kyratsi, T.; Chung, D.-Y.; Ireland, J. R.; Kannewurf, C. R.; Kanatzidis, M. G., *Chemistry of Materials* **2003**, *15*, (15), 3035-3040.
8. Kyratsi, T.; Kanatzidis, M. G., *Z. Anorg. Allg. Chem.* **2003**, *629*, (12-13), 2222-2228.
9. Kyratsi, T.; Hatzikraniotis, E.; Paraskevopoulos, K. M.; Malliakas, C. D.; Dyck, J. S.; Uher, C.; Kanatzidis, M. G., *Journal of Applied Physics* **2006**, *100*, (12), 123704/1-123704/11.
10. Chung, D.-Y.; Hogan, T.; Brazis, P.; Rocci-Lane, M.; Kannewurf, C.; Bastea, M.; Uher, C.; Kanatzidis, M. G., *Science* **2000**, *287*, 1024.
11. Chung, D.-Y.; Hogan, T. P.; Rocci-Lane, M.; Brazis, P.; Ireland, J. R.; Kannewurf, C. R.; Bastea, M.; Uher, C.; Kanatzidis, M. G., *J. Am. Chem. Soc.* **2004**, *126*, 6414.
12. Larson, P.; Mahanti, S. D.; Chung, D.-Y.; Kanatzidis, M. G., *Physical Review B* **2002**, *65*, 045205.

13. Kanatzidis, M. G., *Semicond. Semimet.* **2000**, 69, 51.
14. Hsu, K. F.; Chung, D. Y.; Lal, S.; Mrotzek, A.; Kyratsi, T.; Hogan, T.; Kanatzidis, M. G., *J. Am. Chem. Soc.* **2002**, 124, 2410.
15. Hsu, K. F.; Lal, S.; Hogan, T.; Kanatzidis, M. G., *Chem. Commun.* **2002**, 13, 1380.
16. Magneli, A., *Acta Crystallogr.* **1953**, 6, 495.
17. Mrotzek, A.; Kanatzidis, M. G., *Acc. Chem. Res.* **2003**, 36, 111.
18. Kanatzidis, M. G., *Acc. Chem. Res.* **2005**, 38, 359.
19. Kim, J. H.; Chung, D. Y.; Kanatzidis, M. G., *Chem. Commun.* **2006**, 15, 1628.
20. Darmstadt, Germany, 2001.
21. Sheldrick, G. M. *SHELXTL NT*, 5.1; Bruker: 1998.
22. Zhukova, T. B.; Zaslavskii, A. I., *Kristallografiya* **1971**, 16, 918.
23. Eanes, M. E.; Schimek, G. L.; Kolis, J. W., *J. Chem. Crystallogr.* **2000**, 30, (4), 223-226.
24. Cook, R.; Schaefer, H., *Stud. Inorg. Chem.* **1983**, 3, (Solid State Chem.), 757-60.
25. Chung, D.-Y.; Jovic, S.; Hogan, T.; Kannewurf, C. R.; Brec, R.; Rouxel, J.; Kanatzidis, M. G., *Journal of the American Chemical Society* **1997**, 119, (10), 2505-2515.
26. Chung, D.-Y.; Jovic, S.; Hogan, T.; Kannewurf, C. R.; Brec, R.; Rouxel, J.; Kanatzidis, M. G., *Mater. Res. Soc. Symp. Proc.* **1997**, 453, (Solid-State Chemistry of Inorganic Materials), 15-22.

Chapter3

Preparation and Characterization of Members of the

Series $\text{NaPb}_m\text{SbTe}_{m+2}$ with $m=6, 8, 12$

3.1. Introduction

Doped PbTe is used as a thermoelectric material in power generation devices running in temperature conditions ~ 700 K. Both p-type and n-type thermoelements can be produced by doping with acceptors (e.g., Na_2Te , K_2Te or Ag_2Te)¹⁻⁴ or donors (e.g., PbI_2 , PbBr_2).⁵ The ZT value of PbTe solid solutions is low near room temperature but rises to ~ 0.8 at 700 K. Several studies on low dimensional nanostructured systems have shown significant improvement in the thermoelectric figure of merit, mainly through a reduction of the lattice thermal conductivity while maintaining a high power factor. For example, high ZT values, ranging from $ZT \sim 1.6$ at 300 K to $ZT \sim 3$ at 550 K, were reported by Harman and coworkers for Bi-doped n-type PbSe-PbTe quantum-dot superlattices grown by molecular beam epitaxy.⁶ However, the cost of such fabrication processes is quite high for mass production. Nanostructured bulk analogs of such systems would be more sustainable. Excess Pb in PbTe results in Pb precipitates with sizes on the order 30-40 nm in the PbTe matrix and an increase in the thermopower compared to that of pure PbTe for the same carrier concentration was observed.⁷

Our group is investigating bulk analogs of such devices, meaning bulk materials containing nanostructures. We reported first on the n-type system $\text{AgPb}_m\text{SbTe}_{m+2}$ (so-called LAST).⁸ Several members of that system exhibit a figure of merit above 1 at high temperature. $ZT \sim 1.7$ at 700 K was obtained for $\text{AgPb}_{18}\text{SbTe}_{20}$. This value is achieved mainly through low total thermal conductivity (~ 1.1 W/m·K at 700 K). Careful TEM studies on the samples indicated the presence of nanostructures embedded in the PbTe matrix. These nanostructures scatter phonons more efficiently than charge carriers, thus reducing the lattice thermal conductivity without any significant impact on the electronic properties. We used the LAST system as a platform for optimization. Substituting Ag by the alkali metal Na resulted in p-type materials.⁹ To understand the reason for the change of charge carriers, *ab initio* calculations within the density functional theory were carried out.¹⁰ The study showed an increase in the density of states near the top of the valence band for PbTe doped with Ag whereas no change in the DOS within 0.5 eV of the band maxima was observed for Na-doped PbTe. This new system, $\text{Na}_{1-x}\text{Pb}_m\text{Sb}_y\text{Te}_{m+2}$, also holds promise as thermoelectric materials. $ZT \sim 1.6$ was reported for $\text{Na}_{0.95}\text{Pb}_{20}\text{SbTe}_{22}$ at 650 K, which is nearly twice that of p-type PbTe. Low total thermal conductivity ~ 0.85 W/m·K at 700 K was obtained for that composition. TEM analysis on specimens also indicated the presence of nanocrystals embedded in the PbTe matrix. In this chapter, we describe the synthesis of members with low m values ($m=6, 8, 12$), members which were not studied in the reference 9. Structural and thermoelectric characterization results are also reported.

3.2. Experimental section

3.2.1. Synthesis

All samples were prepared as polycrystalline ingots by mixing high purity elements in the appropriate stoichiometric ratio in 10 mm outer diameter fused silica tubes. Prior to use, the tubes were carbon-coated in order to avoid reaction between the sodium metal and the glass. All components (except Na) were loaded into the tubes under ambient atmosphere and the corresponding amount of Na was later added under nitrogen atmosphere in a dry nitrogen glove box. The silica tubes were then flame-sealed under a residual pressure of $\sim 10^{-4}$ Torr and placed into a tube furnace (mounted on a rocking table). Cast ingots were first prepared following the same temperature profile as the parents system $\text{Na}_{1-x}\text{Pb}_m\text{Sb}_y\text{Te}_{m+2}$ (method 1).⁹ The ingots were found quite brittle. As the $m=8$ composition exhibited the more promising thermoelectric properties, other synthesis conditions (methods 2-9) were investigated to try to improve its mechanical properties.

Method 1. Ingots with nominal compositions $\text{NaPb}_6\text{SbTe}_8$, $\text{NaPb}_8\text{SbTe}_{10}$, $\text{NaPb}_{12}\text{SbTe}_{14}$ were prepared using the same cooling profile as the parent system $\text{Na}_{1-x}\text{Pb}_m\text{Sb}_y\text{Te}_{m+2}$. Namely, the furnace was heated to 1250 K for 4 h to allow complete melting of all components. While molten, the furnace was rocked for 2 h to facilitate complete mixing and homogeneity of the liquid phase. The furnace was finally immobilized at a vertical position and was cooled from 1250 to 820 K over 43 h followed by a fast cool to room temperature. The resulting ingots were silvery-metallic in color with a smooth surface.

The samples were quite brittle. Different strategies, described below, were attempted to improve the mechanical strength of the samples.

Method 2. Slow cooling profile. Stoichiometric amounts of the elements were -loaded in a carbon-coated tube. After being sealed, the tube was introduced in a furnace mounted on a rocking table. The furnace was heated overnight to 1253 K and kept at that temperature 24 hours. During that period, the furnace was rocked for 4 hours. Then the tube was slowly cooled down to 773 K over 99 hours and kept at that temperature 12 hours. Finally the furnace was cooled down to 323 K fast.

Method 3. Slow cooling profile. Stoichiometric amounts of the elements were -loaded in a carbon-coated tube. After sealing, the tube was introduced in a furnace mounted on a rocking table. The furnace was heated overnight to 1253 K and kept at that temperature 4 hours. During that period, the furnace was rocked for 2 hours. Then the tube was slowly cooled down to 973 K over 140 hours. The furnace was then cooled to 323 K in 12 hours.

Method 4. Faster cooling profile. Stoichiometric amounts of the elements were -loaded in a carbon-coated tube. After sealing, the tube was introduced in a furnace mounted on a rocking table. The furnace was heated overnight to 1273 K and kept at that temperature 6 hours. During that period, the furnace was rocked for 2 hours. Then the tube was cooled down to 323 K over 48 hours.

Method 5. Faster cooling followed by slower cooling step. Stoichiometric amounts of the elements were loaded in a carbon coated tube. The furnace was heated in 12 hours to 1253 K and kept at that temperature 4 hours. During that period, the furnace was rocked for 2 hours. The furnace was then cooled down to 1023 K within an hour and down to 323 K within 48 hours.

Method 6. Addition of Sn to the system. Alloying Pb with Sn helped improving the mechanical properties of the LAST material. In a first experiment, 5% of Pb was substituted by Sn. The cooling profile was as described in method 1. In a different set of experiments, 25, 50 and 75 % of Pb was substituted by Sn. The ingots were prepared using the temperature profile described in method 5.

Method 7. Preparation of off-stoichiometric compositions. One reason of the low mechanical strength of the samples may be a high concentration of nanostructures inside the matrix. Several compositions with deficiency in Na and Sb were prepared: $\text{Na}_{0.5}\text{Pb}_8\text{SbTe}_{10}$, $\text{Na}_{0.5}\text{Pb}_8\text{Sb}_{0.75}\text{Te}_{10}$, $\text{Na}_{0.5}\text{Pb}_8\text{Sb}_{0.5}\text{Te}_{10}$ and $\text{Na}_{0.5}\text{Pb}_8\text{Sb}_{0.25}\text{Te}_{10}$. The temperature profile used was as described in method 1.

Method 8. Use of Na_2Te as starting material. After reactions, peelings in the carbon coating are often visible along the top/middle part of the tube. For this experiment, Na_2Te was used as starting material: as Na metal already reacted with Te, less glass attack issue is expected. The temperature profile was the one described in method 1.

Method 9. Hot-press experiments. First, ingots with nominal composition $\text{NaPb}_8\text{SbTe}_{10}$ were synthesized using the method described in part I. The ingots were then grinded in air using mortar and pestle. Particles with size $\leq 125 \mu\text{m}$ were collected using sieves. A first pellet was prepared using a pressure $\sim 10,000$ pounds. House vacuum was applied to the system for 15 min before supplying heat to the press. The chamber was heated to 373 K in 8 min and kept at that temperature 30 min. The furnace was then turned off. The resulting pellet (named HP1) was 1.98 mm thick with a diameter of 12.77 mm. A second pellet was prepared using the same method but the press was kept at 423 K. The diameter of the final pellet (HP2) was 12.78 mm and its thickness 1.71 mm. For the third pellet

(HE

atr

as

Y

r

r

r

P

re

X-

sen

DT

DT

wa

An

use

12

Se

ver

lik

(HP3), the ingot was grinded into a fine powder in a glove-box under nitrogen atmosphere. Particles with size $\leq 46 \mu\text{m}$ were collecting using sieves. House vacuum was applied to the system for 15 min before starting heating the press. The chamber was heated to 473 K in 15 min and kept at that temperature for 30 min. The furnace was then turned off. The final pellet had a diameter of 12.78 mm and was 1.86 mm thick. A rectangular sample was cut from the pellet using a wire saw and was annealed in a quartz tube at 400 °C for 2 hrs.

3.2.2. Characterization techniques

Powder X-ray Diffraction. Powder X-ray patterns of the grinded materials were recorded using Cu K_{α} radiation ($\lambda = 1.54056 \text{ \AA}$) in reflection geometry on a CPS-120 Inel X-ray powder diffractometer operating at 40 kV and 20 mA equipped with a position sensitive detector.

DTA Analysis. Differential thermal analysis (DTA) data were collected with a Shimadzu DTA-50 thermal analyzer. Approximately 35 mg of finely ground powder of material was sealed in a carbon-coated quartz ampoule under residual pressure of $\sim 10^{-4}$ torr. Another ampoule containing similar amount of alumina and prepared the same way was used as a reference. The samples were heated to 1273 K at a rate of 10 K/min, held at 1273 K for 2 min and cooled to 323 K at a rate of -10 K/min.

Scanning Electron Microscopy (SEM). The surface of several samples was polished very carefully using silica suspension solution (0.05 μm) in order to get a smooth, mirror-like surface. The samples were then studied with a scanning electron microscope (Hitachi

S3400N-II) with 25 kV acceleration voltage using both energy-dispersive spectroscopy (EDS) and back-scattered electron imaging (BSE).

Inductively Coupled Plasma Atomic Emission Spectroscopy (ICP-AES). The amounts of Na and Sb from five powdered samples from the top, middle and bottom part of an ingot with composition $\text{NaPb}_8\text{SbTe}_{10}$ were studied by ICP-AES using a Varian model ICP spectrometer. ~ 20 mg of the samples were dissolved in 8.4 mL of freshly prepared aqua regia. Then 1.6 mL of ultra pure water was added to the solution. The final solution was diluted 10 times with ultra pure water. Five standards were prepared for the calibration. The concentrations of the standards are reported in Table 3-1. The wavelength used for Na was 589.592 nm and for Sb 206.834 and 217.582 nm. The correlation factors were respectively 0.995690, 0.999292 and 0.999264. A blank containing the same amount of acid was measured as well.

Table 3-1. Concentrations of the standards used for the ICP-AES calibration.

Standard	Concentration of Na (ppm)	Concentration of Sb (ppm)
1	1.007	5
2	1.24868	6
3	1.49036	7
4	1.73204	8
5	2.014	9

Electrical Transport Properties. Thermopower and electrical conductivity properties were measured simultaneously under helium atmosphere using a ZEM-3 Seebeck coefficient/electrical resistivity measurement system (ULVAC-RIKO, Japan). Samples for transport measurement were cut to size 10 x 3 x 3 mm using a diamond saw (Buehler isomet 1000), a wire saw (South Bay Technology) and a polishing machine (Buehler

ecomet 3000). Rectangular shape samples with approximately 3×3 mm cross-section were sandwiched vertically by two nickel electrodes (current injection) with two Pt/PtRh thermocouples (for temperature difference and voltage measurements) attached on one side. The sample and measurement probes were covered by a nickel can to maintain a constant temperature during the measurement and the base temperature was measured by a thermocouple attached to the outside of the can. The sample, electrodes, and nickel can were placed in a vacuum chamber then evacuated and refilled with He gas (0.1 atm) to provide necessary heat transfer. Properties were measured from room temperature to 670 K under helium atmosphere.

Thermal Conductivity. The thermal conductivity was determined as a function of temperature using the flash diffusivity method on a LFA 457/2/G Microflash NETZSCH. The front face of a small disc-shaped sample (diameter ~ 8 mm; thickness ~ 2 mm) coated with a thin layer of graphite is irradiated with a short laser burst, and the resulting rear face temperature rise is recorded and analyzed. The experiments were carried out under nitrogen atmosphere. Thermal conductivity values were calculated using the equation $\kappa = \alpha C_p d$, where α is the thermal diffusivity, C_p the specific heat and d the bulk density of the material calculated from the sample's geometry and mass. A pyroceram reference was used to determine the heat capacity of the sample. The thermal diffusivities were measured typically over the temperature range 300-670 K. The electronic component of the thermal conductivity was quantified through the Wiedemann-Franz law according to which $\kappa_{el} = \sigma.T.L_o$ (L_o being the Lorenz number, $L_o=2.45.10^{-8} \text{ W}\Omega\text{K}^{-1}$).¹¹ The lattice contribution was then derived by subtracting the electronic component from the total thermal conductivity.

3.3. Results and discussion

3.3.1. Method 1

Structure and characterization. Figures 3-1a, 3-1c and 3-1e shows the X-ray diffraction patterns from powders prepared from the compositions $\text{NaPb}_m\text{SbTe}_{m+2}$ ($m=6, 8, 12$). All the peaks observed can be indexed to the PbTe -structure. However some of the peaks at high angle appear to be split (Figures 3-1b, 3-1d and 3-1f). There may be two reasons for that splitting. The splitting may result from the differentiation of the $K\alpha_1$ and $K\alpha_2$ rays. It may be also the result of phase segregation between two phases with similar lattice constants.

Thermal analysis. Figure 3-2 shows the DTA results for $\text{NaPb}_m\text{SbTe}_{m+2}$. The first and second sets of measurements for $\text{NaPb}_m\text{SbTe}_{m+2}$ are similar and a single melting upon heating and a single crystallization point upon cooling were observed. Table 3-2 summarizes the melting and crystallization temperature for $\text{NaPb}_m\text{SbTe}_{m+2}$ ($m=6, 8, 12$).

Table 3-2. Melting and crystallization points for $\text{NaPb}_8\text{SbTe}_{m+2}$ ($m=6, 8, 12$).

m	6	8	12
T_m (K)	1165	1180	1178
T_c (K)	1111	1144	1149

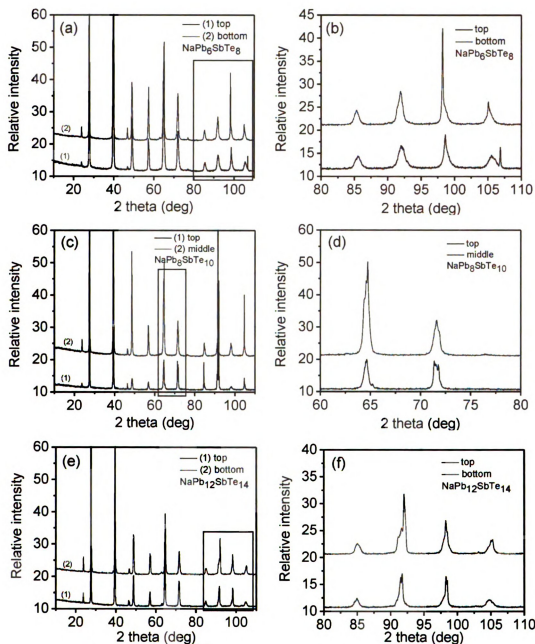


Figure 3-1. Powder X-ray diffraction from samples from top and bottom part of the ingots with composition (a) $\text{NaPb}_6\text{SbTe}_8$, (b) the area between $2\theta = 80$ and 110 deg is enlarged to show peak splitting; (c) $\text{NaPb}_8\text{SbTe}_{10}$, the area between $2\theta = 60$ and 80 deg is enlarged to show peak splitting; and (e) $\text{NaPb}_{12}\text{SbTe}_{14}$, the area between $2\theta = 80$ and 110 deg is enlarged to show peak splitting. All three specimens were prepared with method 1.

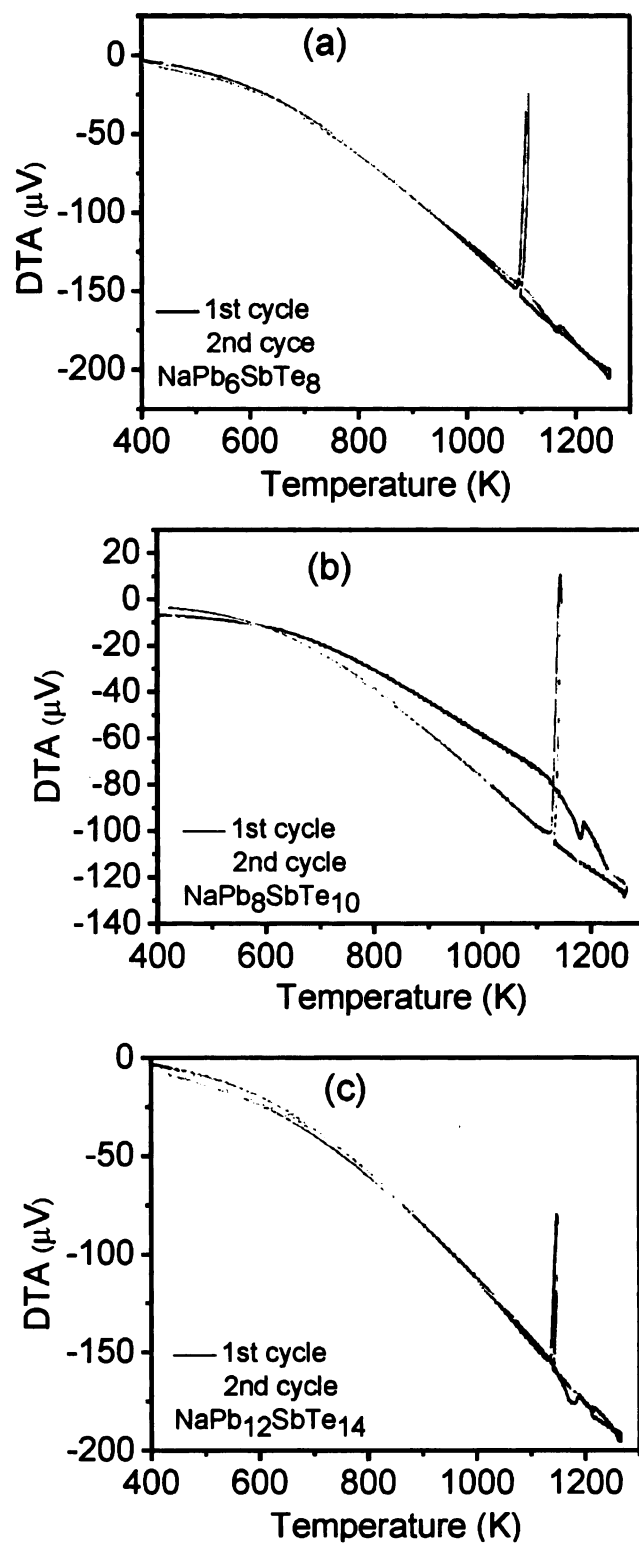


Figure 3-2. Thermal analysis for (a) $\text{NaPb}_6\text{SbTe}_8$, (b) $\text{NaPb}_8\text{SbTe}_{10}$ and (c) $\text{NaPb}_{12}\text{SbTe}_{14}$ prepared with method 1.

Scanning electron microscopy. Finely-polished surfaces were analyzed by SEM. Very disperse inclusions could be observed in the case of $\text{NaPb}_{12}\text{SbTe}_{14}$. Figure 3-3 shows pictures of two such inclusions observed on the sample used for thermoelectric characterization. For a surface $\sim 10 \times 3 \text{ mm}^2$, only three round-shape inclusions with diameter $\sim 30 \text{ }\mu\text{m}$ were observed far apart from each other. For the sample used for thermal diffusivity measurements, a single inclusion was observed. EDS analysis on the different inclusions gave similar results: Sb $\sim 67 \text{ at. } \%$, Te $\sim 22 \text{ at. } \%$ and Pb $\sim 1 \text{ at. } \%$. EDS analysis on the matrix indicated the presence of Pb and Te in ratio close to 1:1. BSE analysis on samples $\text{NaPb}_8\text{SbTe}_{10}$ and $\text{NaPb}_6\text{SbTe}_8$ did not show evidence of a second phase. EDS analysis on several areas indicated the presence of Na in the matrix ($\sim 5 \text{ at. } \%$) but no reliable information about Sb could be obtained because of overlapping between Sb and Te peaks.

ICP-AES. As accurate amount of Na and Sb elements in the sample is not possible by EDS, several powders from the ingot with composition $\text{NaPb}_8\text{SbTe}_{10}$ were analyzed by ICP-AES. Tables 3-3 summarizes the elemental concentrations of Na and Sb in the different samples and gives the Na/Sb ratio obtained. It can be observed that for the samples from the bottom of the ingot, the Na/Sb ratio is lower than 1, indicating that Sb is in excess compared to the nominal composition. For the samples from middle and top parts of the ingot, the Na/Sb is ~ 1 , close to the nominal composition.

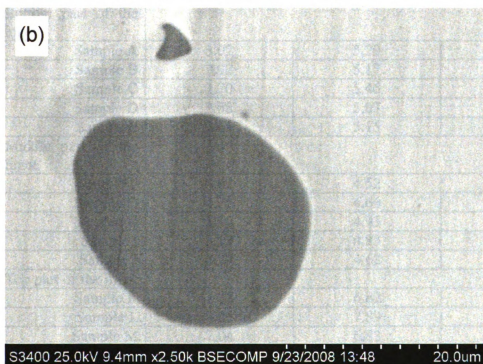
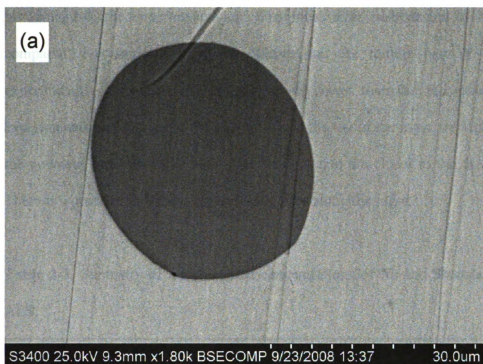


Figure 3-3. BSE images of one of the surface of the sample $\text{NaPb}_{12}\text{SbTe}_{14}$ used for thermoelectric characterization. EDS analysis on the inclusions indicated the regions to contain ~ 67 % Sb, ~ 22 Te and ~ 1% Pb. The matrix is pure PbTe.

In Table 3-4, the experimental and theoretical mass percentages of Na and Sb are compared. For samples from the bottom and the middle part of the ingot, the experimental percentages of Na and Sb are lower than the theoretical values. The experimental percentages of the powders from the top of the ingot are higher than that of the powders from the other parts of the ingots and are closer to the theoretical values. There is a gradient in Sb and Na concentrations along the ingot.

Table 3-3. Summary of the elemental concentrations of Na and Sb obtained with ICP-AES.

	Concentration of Na (mmol)	Concentration of Sb (mmol)	Na/Sb
Bottom part of the ingot			
Sample A	3.02	5.29	0.57
Sample B	2.92	5.17	0.56
Sample C	2.70	5.46	0.49
Sample D	2.58	5.07	0.51
Sample E	2.65	5.15	0.51
Middle part of the ingot			
Sample F	4.62	4.52	1.02
Sample G	4.75	4.66	1.02
Sample H	5.10	4.93	1.03
Sample I	5.17	4.83	1.07
Sample J	4.77	4.62	1.03
Top part of the ingot			
Sample K	7.36	6.82	1.08
Sample L	8.45	7.89	1.07
Sample M	7.04	6.83	1.03
Sample N	7.55	6.92	1.09
Sample O	6.04	5.95	1.02

Table 3-4. Comparison between experimental and theoretical mass percentages of Na and Sb in the powders analyzed with ICP-AES.

	Mass % Na (experimental)	Mass % Na (theoretical)	Mass % Sb (experimental)	Mass % Sb (theoretical)
Bottom part of the ingot				
Sample A	0.74	0.75	2.82	3.96
Sample B	0.60	0.75	3.13	3.96
Sample C	0.58	0.75	3.31	3.96
Sample D	0.53	0.75	2.93	3.96
Sample E	0.54	0.75	2.96	3.96
Middle part of the ingot				
Sample F	0.48	0.75	2.62	3.96
Sample G	0.50	0.75	2.61	3.96
Sample H	0.57	0.75	2.94	3.96
Sample I	0.54	0.75	2.66	3.96
Sample J	0.52	0.75	2.65	3.96
Top part of the ingot				
Sample K	0.75	0.75	3.67	3.96
Sample L	0.80	0.75	3.93	3.96
Sample M	0.66	0.75	3.69	3.96
Sample N	0.81	0.75	3.92	3.96
Sample O	0.66	0.75	3.46	3.96

Optical band gap measurements. Infrared spectroscopy of $\text{NaPb}_m\text{SbTe}_{m+2}$ ($m=6, 8, 12$) shows that the three members are narrow gap semiconductors (Figure 3-4). The band gap slightly decreases with increasing m value: $\text{NaPb}_6\text{SbTe}_8$, $\text{NaPb}_8\text{SbTe}_{10}$ and $\text{NaPb}_{12}\text{SbTe}_{14}$ have band gaps $\sim 0.43, 0.39$ and 0.26 eV respectively.

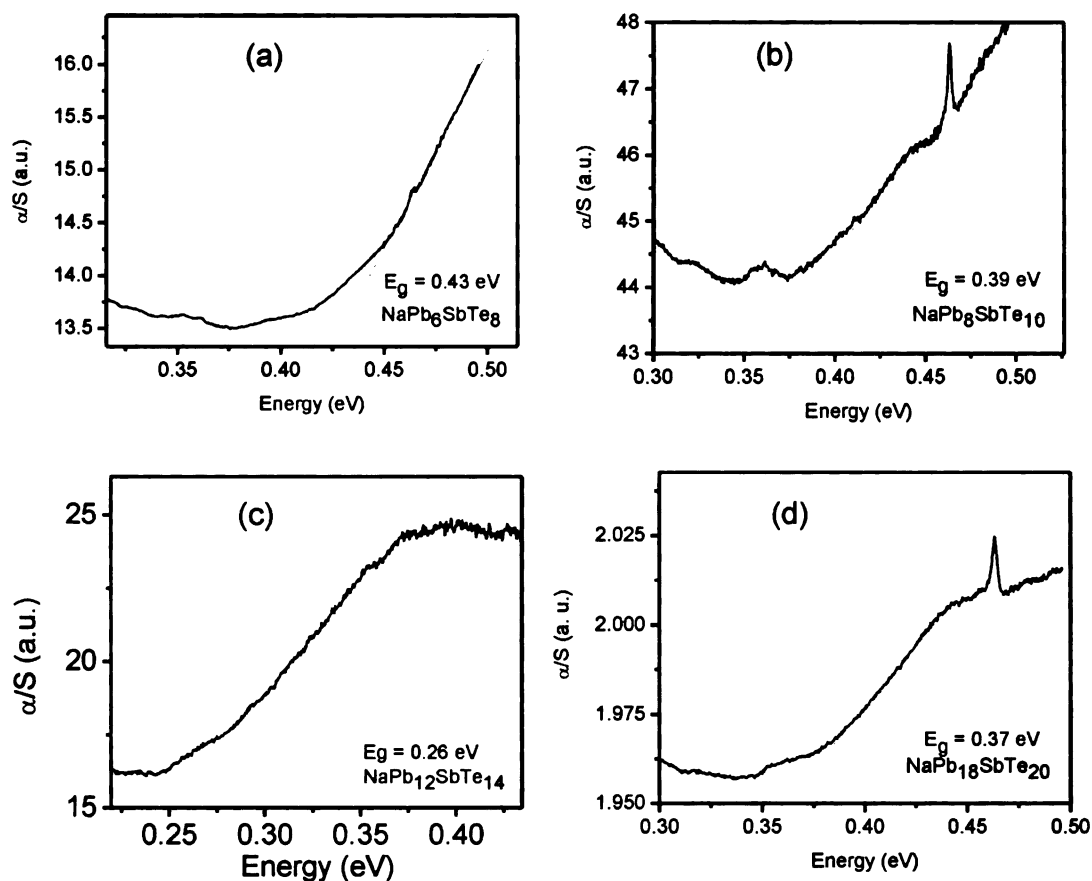


Figure 3-4. Diffuse reflectance absorption spectra of (a) $\text{NaPb}_6\text{SbTe}_8$, (b) $\text{NaPb}_8\text{SbTe}_{10}$, (c) $\text{NaPb}_{12}\text{SbTe}_{14}$ and (d) $\text{NaPb}_{18}\text{SbTe}_{20}$ prepared with method 1.

Electronic Transport Properties. The temperature dependence of the electrical conductivity for the compounds $\text{NaPb}_m\text{SbTe}_{m+2}$ ($m=6, 8, 12, 14$) is plotted on Figure 3-5a. For comparison, the data collected previously for $\text{NaPb}_{18}\text{SbTe}_{20}$ and $\text{Na}_{0.95}\text{Pb}_{20}\text{SbTe}_{22}$ were also added to the graph. At room temperature, there is a significant difference between the different members: the value ~ 1540 S/cm for $\text{Na}_{0.95}\text{Pb}_{20}\text{SbTe}_{22}$ is almost three times the value for $\text{NaPb}_6\text{SbTe}_8$ (~ 540 S/cm). At high

temperature, the electrical conductivity varies between 90 S/cm for $\text{NaPb}_6\text{SbTe}_8$ and $\text{NaPb}_{12}\text{SbTe}_{14}$ and 170 S/cm for $\text{Na}_{0.95}\text{Pb}_{20}\text{SbTe}_{22}$. Compositions with high m values tend to have higher electrical conductivity with the exception of the $m=8$. This might be the results of the quality of the samples. The $m=6$ and $m=12$ samples were more brittle than the $m=8$.

All compositions showed p-type behavior (Figure 3-5b). Room temperature thermopower varies between 96 $\mu\text{V/K}$ for $\text{Na}_{0.95}\text{Pb}_{20}\text{SbTe}_{22}$ and 170 $\mu\text{V/K}$ for $\text{NaPb}_6\text{SbTe}_8$. At temperatures above 650 K, all compositions have thermopower values above 300 $\mu\text{V/K}$, the highest value being $\sim 360 \mu\text{V/K}$ at 670 K for $\text{NaPb}_6\text{SbTe}_8$.

In order to check the values measured for the composition $\text{NaPb}_8\text{SbTe}_{10}$, the data were recollected on the same sample. A good agreement between the two data sets was observed (Figure 3-6).

Using the above data, the power factor values were calculated and are reported in Figure 3-5c. Clearly the composition $\text{Na}_{0.95}\text{Pb}_{20}\text{SbTe}_{22}$ exhibits the highest power factors over the temperature range 300-675K with a maximum $\sim 24 \mu\text{W/m}\cdot\text{K}^2$ at 450 K. $\text{NaPb}_8\text{SbTe}_{10}$ and $\text{NaPb}_{18}\text{SbTe}_{20}$ have similar power factors with maximum values $\sim 19 \mu\text{W/m}\cdot\text{K}^2$ at 460 K.

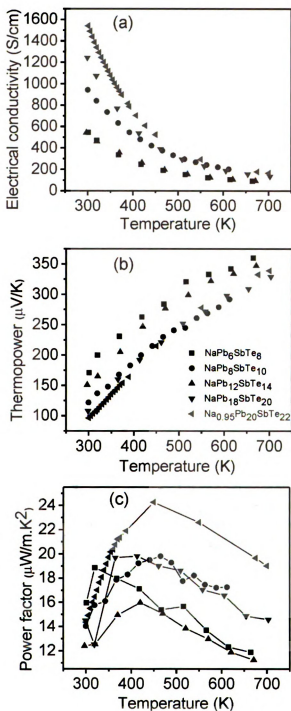


Figure 3-5. Temperature dependence of (a) the electrical conductivity, (b) the thermopower and (c) the power factor the compounds $\text{NaPb}_m\text{SbTe}_{m+2}$ ($m=6, 8, 12$ and 18) and $\text{Na}_{0.95}\text{Pb}_{20}\text{SbTe}_{22}$ prepared with method 1.

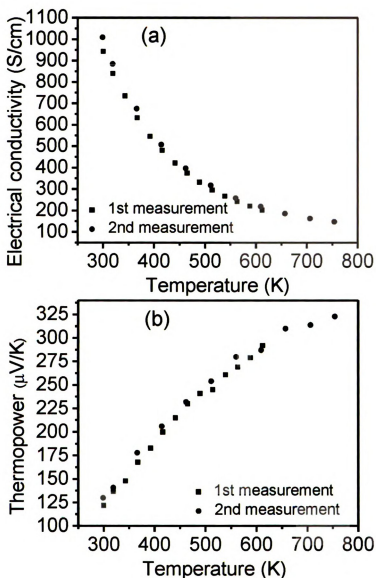


Figure 3-6. Comparison of (a) electrical conductivity and (b) thermopower collected during the first and second measurement for NaPb₈SbTe₁₀ prepared with method 1.

In order to check the reproducibility of the properties, other ingots with composition NaPb₈SbTe₁₀ were prepared using the method. Many of the samples were found brittle during the polishing step. A second sample could be measured and the data

set was compared with that measured for the first sample (Figure 3-7). The room temperature electrical conductivity was ~ 650 S/cm for the second sample, much lower than that of the first sample (1000 S/cm) (Figure 3-7a). At high temperature, the difference in electrical conductivity decreases: (the electrical conductivity of the first sample was only 70 S/cm higher than that of the second sample). Over the range 300-700 K, the second sample exhibits higher thermopower than the first sample, with an average difference $\sim 3-40$ $\mu\text{V/K}$ with the highest value ~ 360 $\mu\text{V/K}$ at 715 K. The reason for such difference in electrical properties is probably a difference in carrier concentration as both electrical conductivity and thermopower are affected.

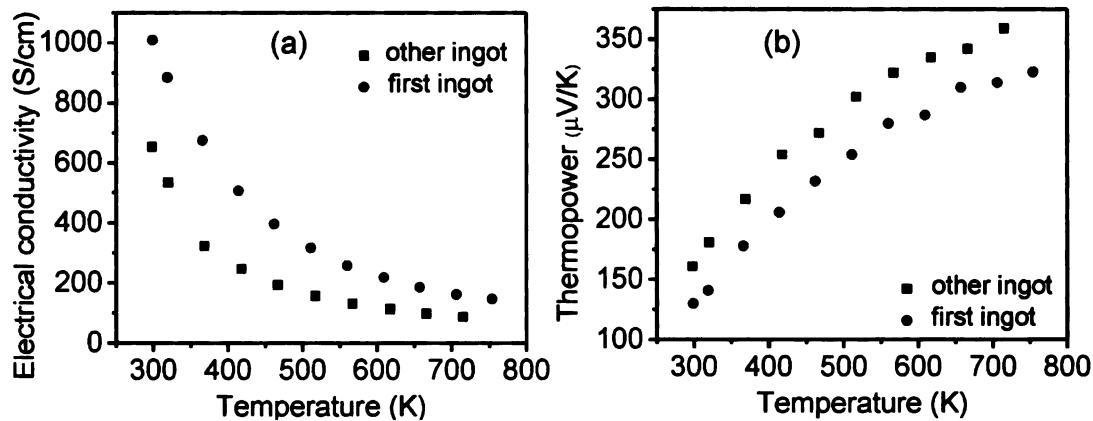


Figure 3-7. Temperature dependence of (a) electrical conductivity and (b) thermopower measured for 2 different samples with composition $\text{NaPb}_8\text{SbTe}_{10}$ prepared with method 1.

Thermal Transport Properties. Thermal diffusivity measurements were collected for the compositions $\text{NaPb}_m\text{SbTe}_{m+2}$ ($m=6, 8, 12$). The resulting thermal conductivity data are plotted in Figure 8a. For all compositions, the thermal conductivity decreases as a

function of temperature. $\text{NaPb}_{18}\text{SbTe}_{20}$ and $\text{Na}_{0.95}\text{Pb}_{20}\text{SbTe}_{22}$ have the highest thermal conductivity over the temperature range 300-670 K with values varying between 1.85 $\text{W/m}\cdot\text{K}$ at room temperature and 0.9 $\text{W/m}\cdot\text{K}$ at 675 K. $\text{NaPb}_8\text{SbTe}_{10}$ and $\text{NaPb}_{12}\text{SbTe}_{14}$ have lower thermal conductivity, with values $\sim 1.3 \text{ W/m}\cdot\text{K}$ at 300 K and $\sim 0.8 \text{ W/m}\cdot\text{K}$ at 670 K. The $m=6$ compound exhibits the lowest thermal conductivity, with values between 1.05 $\text{W/m}\cdot\text{K}$ at 300 K and 0.65 $\text{W/m}\cdot\text{K}$ at 670 K. Figure 3-8b shows the lattice thermal conductivity obtained by subtracting the electronic component from the total thermal conductivity. The lowest lattice components are found for the compositions $\text{NaPb}_8\text{SbTe}_{10}$ and $\text{NaPb}_6\text{SbTe}_8$ with the lowest lattice thermal conductivity $\sim 0.45 \text{ W/m}\cdot\text{K}$ at 650 K for $\text{NaPb}_8\text{SbTe}_{10}$. This value is slightly lower than that reported for $\text{Na}_{0.95}\text{Pb}_{20}\text{SbTe}_{22}$ (0.55 $\text{W/m}\cdot\text{K}$ at 600 K).

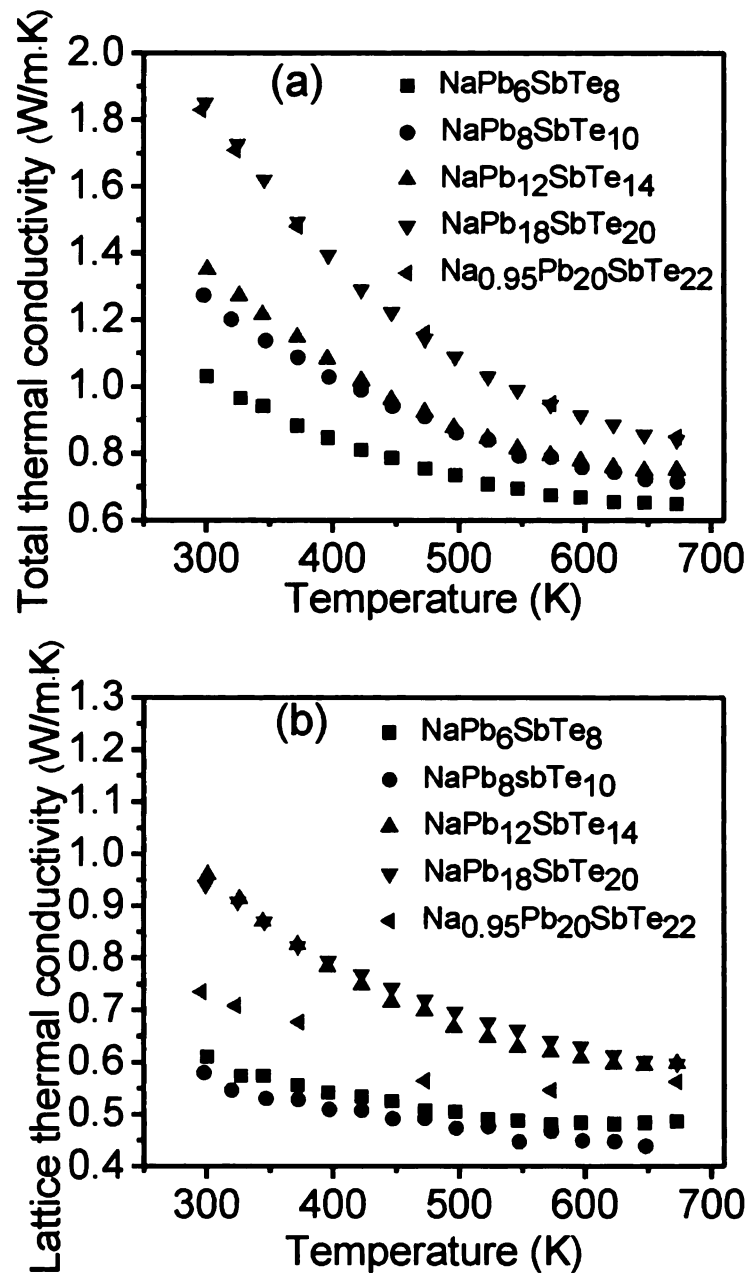


Figure 3-8. Temperature dependence of (a) the total and (b) lattice thermal conductivity for the materials NaPb_mSbTe_{m+2} (m=6, 8, 12, 18) and Na_{0.95}Pb₂₀SbTe₂₂ prepared with method 1.

The estimated ZT values are given in Figure 3-9. It must first be observed that for all compositions ZT ≥ 0.9 were observed at high temperature. The composition

$\text{Na}_{0.95}\text{Pb}_{20}\text{SbTe}_{22}$ exhibits the highest figure of merit with a maximum $ZT \sim 1.7$ at 650 K.

For $\text{NaPb}_8\text{SbTe}_{10}$, a maximum of ~ 1.5 was observed at 650 K.

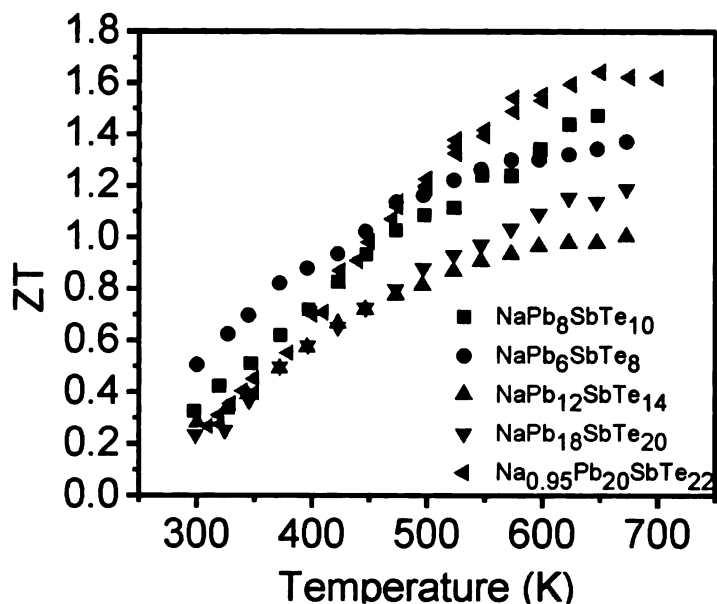


Figure 3-9. Figure of merit ZT for $\text{NaPb}_m\text{SbTe}_{m+2}$ ($m=6, 8, 12, 18$) and $\text{Na}_{0.95}\text{Pb}_{20}\text{SbTe}_{22}$ prepared with method 1.

High Resolution Transmission Electron Microscopy (HRTEM). Figure 3-10a and 3-10b-d show low and high magnification HRTEM images of the specimen $\text{NaPb}_8\text{SbTe}_{10}$. Low magnification images (Figure 10a) revealed the presence of nanometer size inhomogeneities embedded inside the matrix. Although no accurate elemental analysis could be performed, we anticipate these regions to be rich in Na and Sb, based on the chemistry of the system. Because low m members of the family $\text{NaPb}_m\text{SbTe}_{m+2}$ are rich in Na and Sb, we can think that such specimen have higher densities of nanoregions

embedded in the matrix, thus contributing to lower the lattice thermal conductivity compared to higher m members.

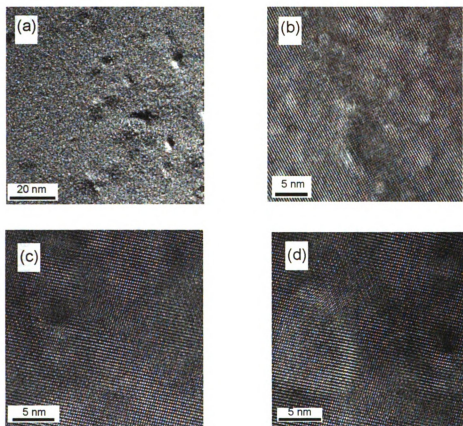


Figure 3-10. Typical HRTEM images obtained for $\text{NaPb}_8\text{SbTe}_{10}$ prepared with method

1.

As the samples were quite brittle, samples with composition $\text{NaPb}_8\text{SbTe}_{10}$ were prepared with different synthesis conditions.

3.3.2. Method 2

A sample for electronic transport measurements could be prepared but very careful polishing work was necessary as the edges of the samples were brittle. Figure 3-11 shows X-ray diffraction patterns taken for powder from both top and bottom of the sample. All peaks could be indexed as belonging to the PbTe-structure.

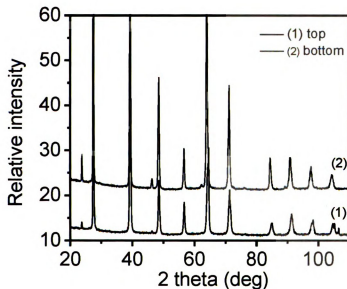


Figure 3-11. Powder X-ray diffraction of $\text{NaPb}_8\text{SbTe}_{10}$ prepared by method 2.

Temperature dependence of the electrical conductivity of the compound $\text{NaPb}_8\text{SbTe}_{10}$ prepared by method 2 is presented in Figure 3-12a. The electrical conductivity of the sample prepared with method 2 is much lower (almost half) than that prepared by method 1. The values for sample obtained by method 2 are ~ 490 and 72 S/cm at 300 and 675 K respectively whereas they were ~ 1008 and 173 S/cm for the sample prepared by method 1. This difference in electrical conductivity may be the result of cracks present inside the sample prepared with method 2 or of difference in carrier

concentrations. The sample prepared with method 2 has higher thermopower than that prepared with method 1 (Figure 3-12b). The difference increases with temperature. The sample prepared with method 1 has thermopower $\sim 313 \mu\text{V/K}$ at 685 K whereas the thermopower of the sample prepared with method 2 reaches $285 \mu\text{V/K}$ at the same temperature. This behavior indicates a difference in carrier concentrations between samples prepared with methods 1 and 2. When comparing the power factors, the sample prepared with method 1 has the highest power factor over the range 300-700 K (Figure 3-12c). The reason is the highest electrical conductivity measured for the sample prepared with method 1.

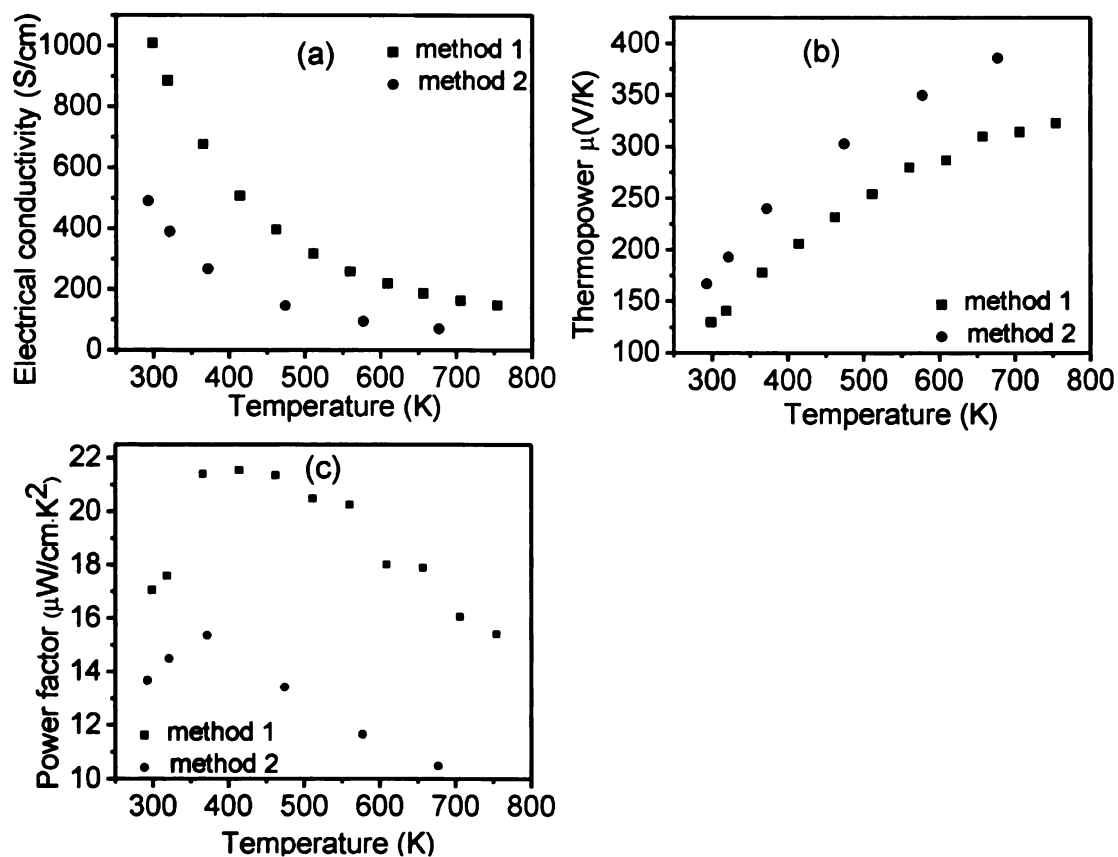


Figure 3-12. Comparison of (a) the electrical conductivity, (b) the thermopower and (c) the power factor of the compounds NaPb₈SbTe₁₀ prepared by methods 1 and 2.

Thermal diffusivity measurements were carried on the sample prepared with method 2. The resulting thermal conductivity data are compared to those measured for the sample prepared with method 1 (Figure 3-13a). The values are similar with ~ 1.25 and 0.75 W/m \cdot K at 300 and 625 K respectively. The sample prepared with method 1 has lower lattice conductivity with value ~ 0.6 - 0.45 W/m \cdot K at 300 and 650 K respectively.

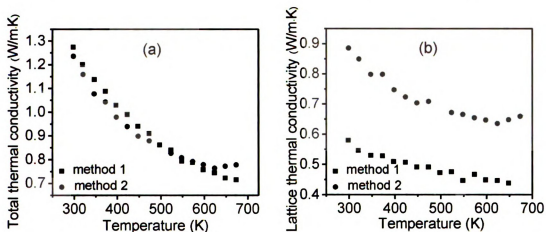


Figure 3-13. Comparison of the (a) total and (b) lattice thermal conductivities for samples prepared by methods 1 and 2.

3.3.3. Method 3

The X-ray diffraction patterns for prepared from top, middle and bottom of the ingot are showed in Figure 3-14a. The patterns from the different parts of the sample look similar. The ingot seems to be homogeneous. A zoom of the region 38 - 60° (Figure 3-14b) showed the presence of a second phase with the cubic PbTe structure. The indexing of these peaks indicated the position of these peaks to be close to those of NaSbTe₂.^{12,13} BSE imaging of a finely polished sample did not show any indication of the presence of a second phase in the PbTe matrix.

No thermoelectric properties could be measured because of the fragility of the sample.

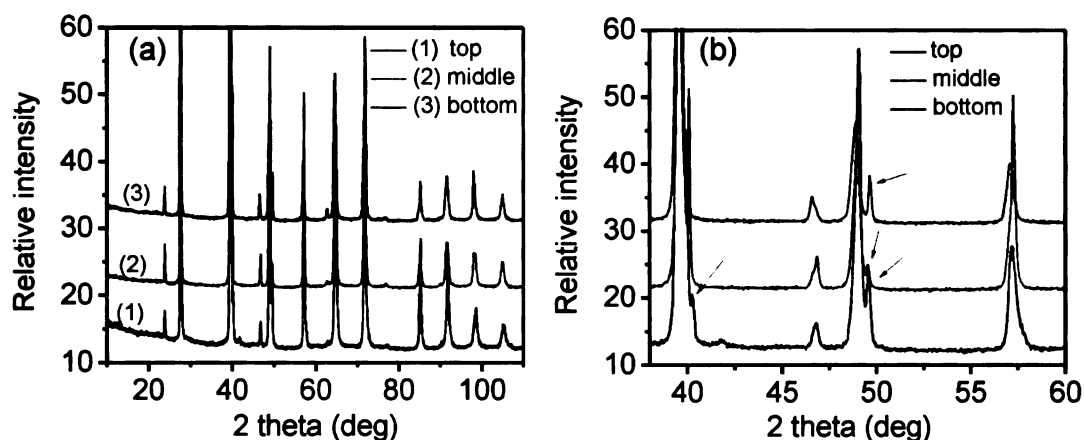


Figure 3-14. Powder X-ray diffraction of $\text{NaPb}_8\text{SbTe}_{10}$ prepared with method 3. The area between $2\theta = 35$ and 60 deg is enlarged to show the presence of extra peaks can be assigned to NaSbTe_2 .

3.3.4. Method 4

The X-ray diffraction patterns for prepared from powders both top and bottom of the ingot are showed in Figure 3-15. All peaks could be indexed as belonging to the PbTe-structure. However some peaks at high angles seem to split. No thermoelectric measurements could be performed because of the low mechanical properties of the sample.

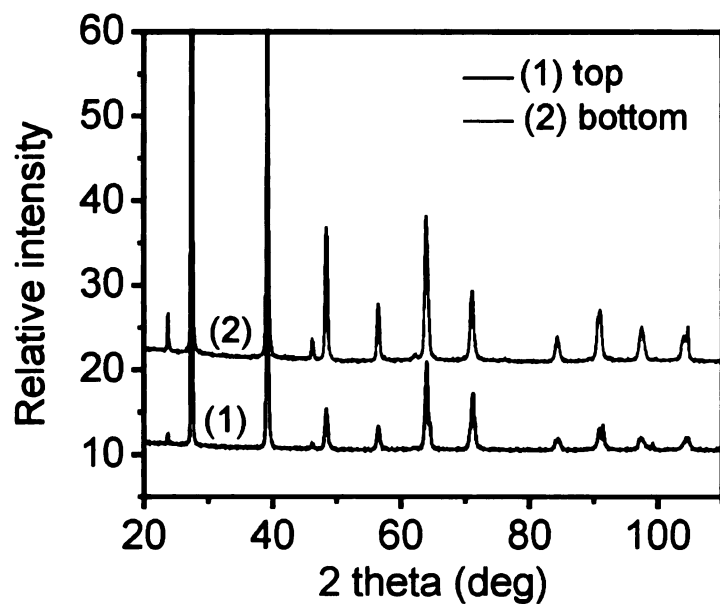


Figure 3-15. Powder X-ray diffraction of $\text{NaPb}_8\text{SbTe}_{10}$ prepared with method 4.

3.3.5. Method 5

The X-ray diffraction patterns for powders prepared from both top and bottom of the ingots are showed in Figure 3-16. The patterns look like clean PbTe patterns. No thermoelectric properties could be measured because of the fragility of the sample.

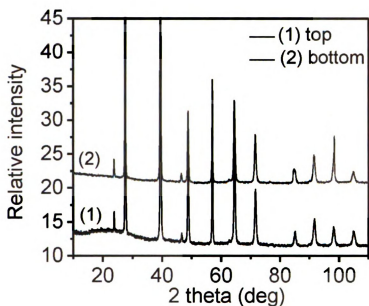


Figure 3-16. Powder X-ray diffraction of $\text{NaPb}_8\text{SbTe}_{10}$ prepared with method 5.

3.3.6. Method 6

Figure 3-17 shows the X-ray diffraction patterns from samples from both top and bottom of the ingots $\text{NaPb}_{7.6}\text{Sn}_{0.4}\text{SbTe}_{10}$, $\text{NaPb}_6\text{Sn}_2\text{SbTe}_{10}$, $\text{NaPb}_4\text{Sn}_4\text{SbTe}_{10}$ and $\text{NaPb}_2\text{Sn}_6\text{SbTe}_{10}$. The peaks could be indexed as PbTe phase, but splitting in the peaks located at high angles is visible.

Careful analysis on fine polished surface was done on the samples $\text{NaPb}_4\text{Sn}_4\text{SbTe}_{10}$ and $\text{NaPb}_2\text{Sn}_6\text{SbTe}_{10}$ with SEM. BSE images from areas from top (Figure 3-18a) and bottom (Figure 3-18b) of the material $\text{NaPb}_4\text{Sn}_4\text{SbTe}_{10}$ showed areas with different composition than that of the matrix. EDS analysis for the sample from the top of the ingot gave the atomic percentages: Pb: 1.14, Sn: 10.96, Sb: 62.24, Te 25.57. No accurate information on the presence of Na could be obtained as Na is a light element and

was introduced in low amount. EDS on the inclusion in the sample from the bottom part of the ingot gave similar result: Sn1.11, Sb: 63.83, Te: 25.05. EDS analysis on the matrix gave a ratio consistent with the nominal composition: Pb: 20.23, Sn: 19.94, Sb: 6.94, Te: 51.92. A sample from the middle of the ingot $\text{NaPb}_2\text{Sn}_6\text{SbTe}_{10}$ was also analyzed, inclusions were also observed (Figure 3-17c). EDS analysis indicated a composition similar to that observed for $\text{NaPb}_4\text{Sn}_4\text{SbTe}_{10}$: Sn: 13.51 at. %, Sb: 63.37 at. % and Te: 23.01 at. %.

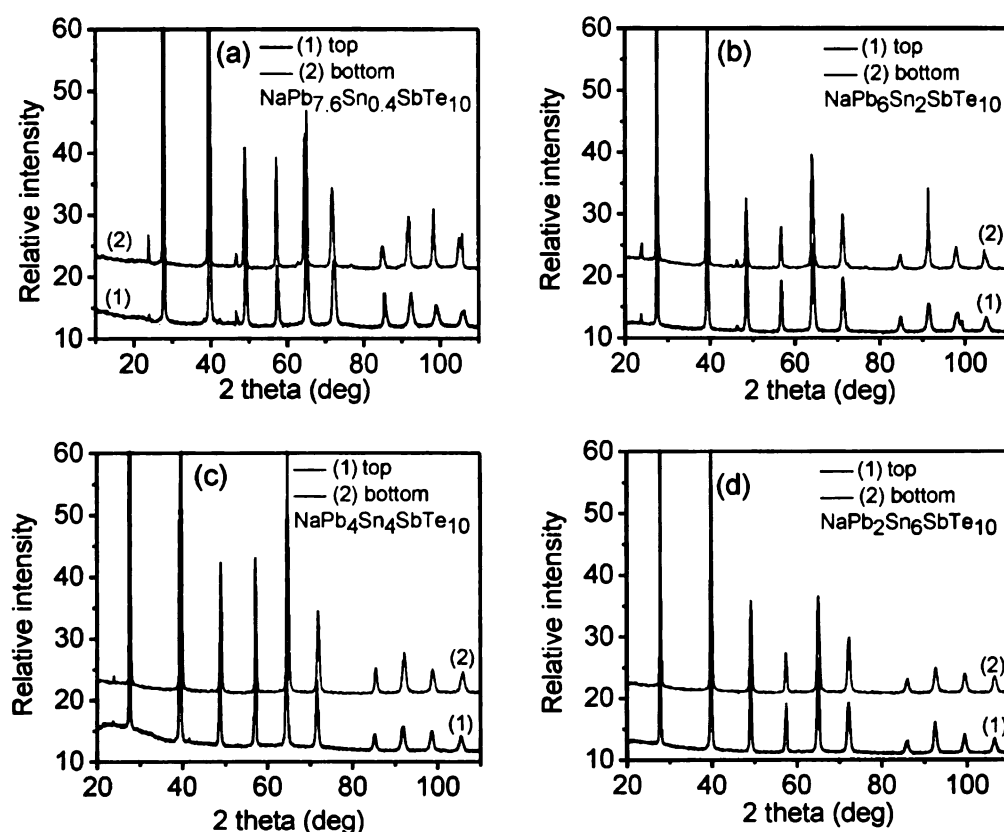


Figure 3-17. Powder X-ray diffraction patterns of (a) $\text{NaPb}_{7.6}\text{Sn}_{0.4}\text{SbTe}_{10}$, (b) $\text{NaPb}_6\text{Sn}_2\text{SbTe}_{10}$, (c) $\text{NaPb}_4\text{Sn}_4\text{SbTe}_{10}$ and (d) $\text{NaPb}_2\text{Sn}_6\text{SbTe}_{10}$.

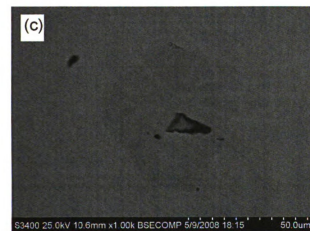
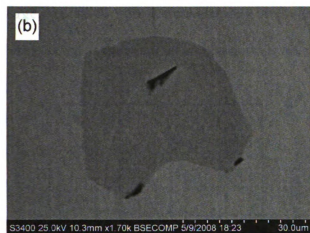
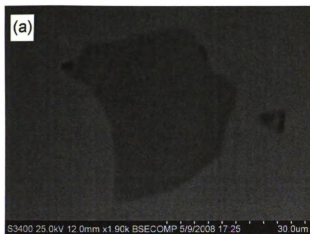


Figure 3-18. BSE images from areas close to (a) the top and (b) the bottom of the ingot $\text{NaPb}_4\text{Sn}_4\text{SbTe}_{10}$. (c) BSE image from a sample from the middle of the sample $\text{NaPb}_2\text{Sn}_6\text{SbTe}_{10}$.

3.3.7. Method 7

The X-ray diffraction patterns for powders prepared from both top and bottom of the ingots are shown in Figure 3-19. Analysis of the patterns for $\text{Na}_{0.5}\text{Pb}_8\text{SbTe}_{10}$, $\text{Na}_{0.5}\text{Pb}_8\text{Sb}_{0.75}\text{Te}_{10}$ showed the presence of Sb_2Te_3 as a second phase. In the case of $\text{Na}_{0.5}\text{Pb}_8\text{Sb}_{0.75}\text{Te}_{10}$, the presence of small peaks ~ 28 and 39° indicates the presence of a small amount of Sb_2Te_3 . In the case of $\text{Na}_{0.5}\text{Pb}_8\text{Sb}_{0.75}\text{Te}_{10}$, two small peaks close to the large peak at 40° are visible and may be the indication of the presence of Te, which can be expected as the nominal composition is not charge-balanced with an excess of Te.

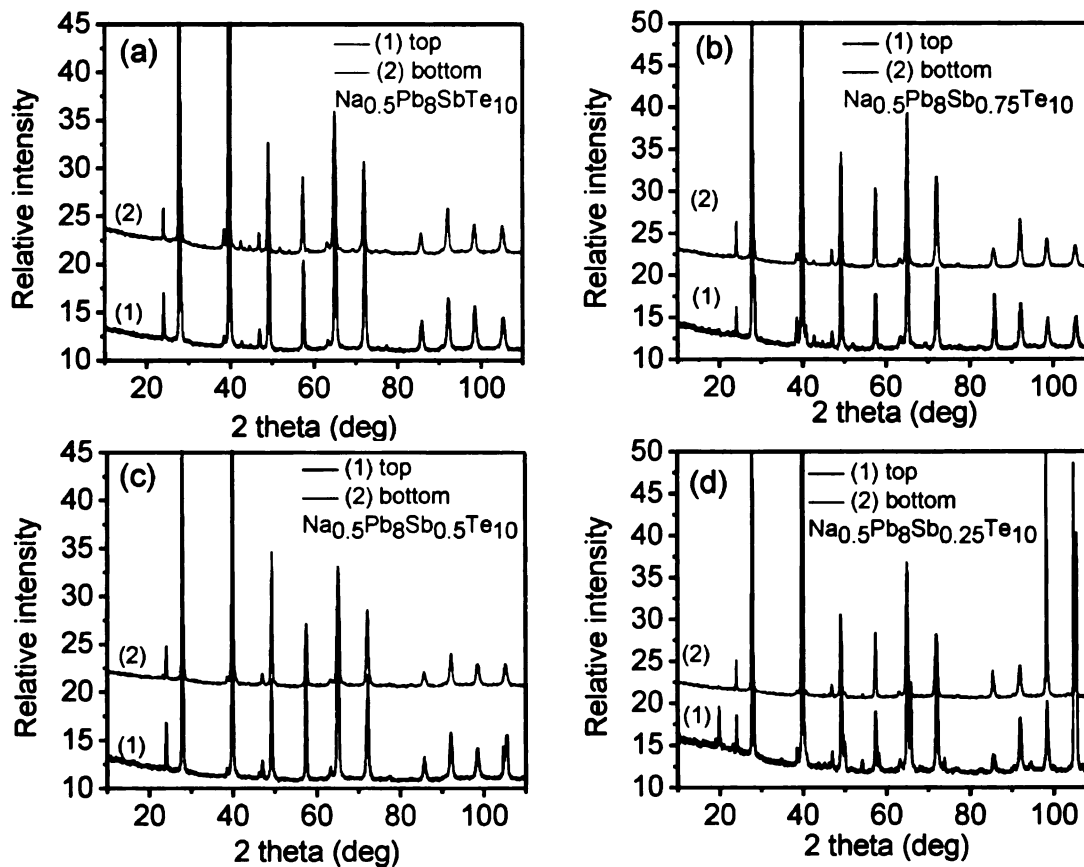


Figure 3-19. Powder X-ray diffraction of powders from (a) $\text{Na}_{0.5}\text{Pb}_8\text{SbTe}_{10}$, (b) $\text{Na}_{0.5}\text{Pb}_8\text{Sb}_{0.75}\text{Te}_{10}$, (c) $\text{Na}_{0.5}\text{Pb}_8\text{Sb}_{0.5}\text{Te}_{10}$ and (d) $\text{Na}_{0.5}\text{Pb}_8\text{Sb}_{0.25}\text{Te}_{10}$.

Figure 3-20 shows two BSE images from a sample close to the top of the ingot $\text{Na}_{0.5}\text{Pb}_8\text{Sb}_{0.75}\text{Te}_{10}$. Inclusions were observed embedded in the matrix. EDS on the dark ribbon indicated the region to be Sb_2Te_3 with a small percentage of Pb (3.24 at. %). Analysis on the dark areas contained in the lace part of the inclusion showed only the presence of Te. Finally analysis on the bright areas in the lace part showed the presence of Na (7.82 at. %), Pb (11.90 at. %), Sb (10.01 at. %) and Te (70.27 at. %). Samples from the ingot $\text{Na}_{0.5}\text{Pb}_8\text{Sb}_{0.5}\text{Te}_{10}$ were also analyzed (Figure 3-21). Composite inclusions were observed in the PbTe matrix. The picture 21a is from a sample close to the bottom of the sample. EDS analysis on area 1 reveals the presence of the elements Na (18.53 at. %), Sb (14.19 at. %), Pb (19.94 at. %) and Te (52.34 at. %). Darker areas such as 2 contain only elemental Te. The image 20b is from an area close to the middle of the ingot. Complex inclusions are also observed. Area 1 contains mostly Te (80.87 at. %), but also some Na (17.21 at. %) and Pb (2.12 at. %). Area 2 contains more Te (89.49) and small amount of Na (10.51 at. %). Finally, Na (16.08 at. %), Pb (18.21 at. %), Sb (14.59 at. %) and Te (51.11 at. %) were present in area 3.

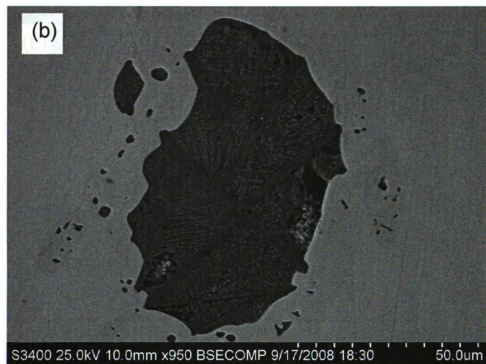
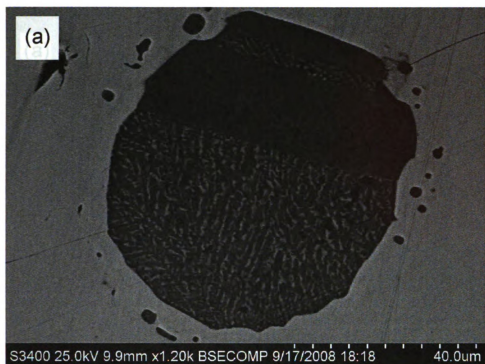


Figure 3-20. BSE images of areas from a part close to the top of the ingot $\text{Na}_{0.5}\text{Pb}_8\text{Sb}_{0.75}\text{Te}_{10}$.

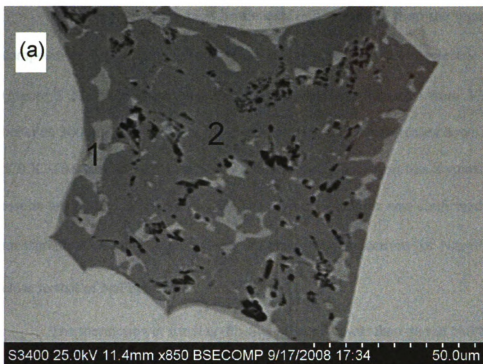


Figure 3-21. BSE images of sample from (a) bottom and (b) middle of the ingot $\text{Na}_{0.5}\text{Pb}_8\text{Sb}_{0.5}\text{Te}_{10}$.

Because of the very high brittleness, only a sample from the ingot with nominal composition $\text{Na}_{0.5}\text{Pb}_8\text{Sb}_{0.25}\text{Te}_{10}$ could be prepared for thermoelectric measurements (Figure 3-22). Surprisingly the electrical conductivity increases from 379 to 440 S/cm between 300 and 370 K. Then the electrical conductivity decreases down to 210 S/cm at 570 K. The sample was measured a second time to check on this atypical behavior. The results are plotted on Figure 3-23a. The atypical behavior was confirmed by the second measurement. At high temperature, the electrical conductivity of $\text{Na}_{0.5}\text{Pb}_8\text{Sb}_{0.25}\text{Te}_{10}$ is close to that of $\text{NaPb}_8\text{SbTe}_{10}$.

The thermopower for $\text{Na}_{0.5}\text{Pb}_8\text{Sb}_{0.25}\text{Te}_{10}$ is lower than that of $\text{NaPb}_8\text{SbTe}_{10}$ but at high temperature the values are almost similar for both compositions, $\sim 274 \mu\text{V/K}$ at 575 K (Figure 3-22b).

The values measured during the first run were confirmed by running the same sample a second time (Figure 3-23a). Over the range 300-570 K, $\text{NaPb}_8\text{SbTe}_{10}$ exhibit higher power factors than $\text{Na}_{0.5}\text{Pb}_8\text{Sb}_{0.25}\text{Te}_{10}$ (Figure 3-23b).

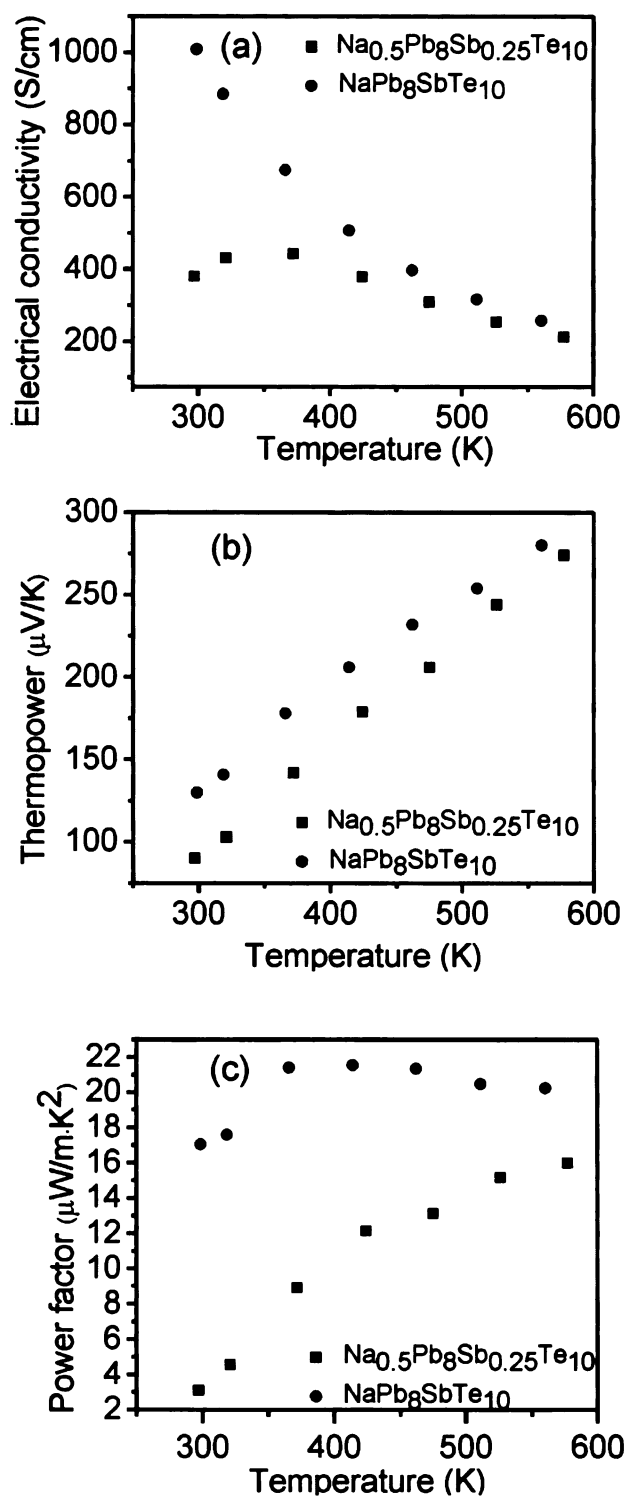


Figure 3-22. Temperature dependence of the (a) electrical conductivity, (b) thermopower and (c) power factor of $\text{Na}_{0.5}\text{Pb}_8\text{Sb}_{0.25}\text{Te}_{10}$ and $\text{NaPb}_8\text{SbTe}_{10}$.

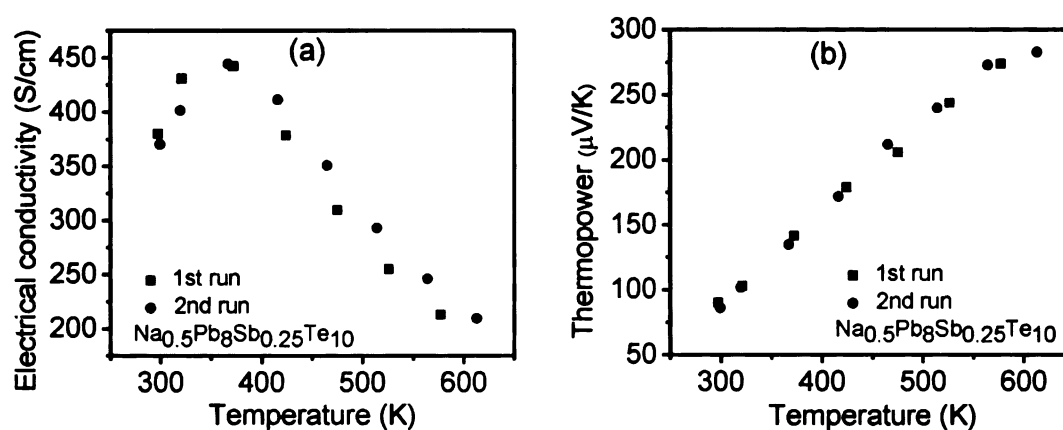


Figure 3-23. First and second sets of measurements for the (a) electrical conductivity and (b) thermopower of the compound $\text{Na}_{0.5}\text{Pb}_8\text{Sb}_{0.25}\text{Te}_{10}$.

In order to check if this behavior was reproducible, a second sample with the composition $\text{Na}_{0.5}\text{Pb}_8\text{Sb}_{0.25}\text{Te}_{10}$ was prepared in the same conditions. The electronic transport properties are reported in Figure 3-24. At room temperature the electrical conductivity is higher for the second ingot but the electrical conductivity at 300 and 320 K are close (590 and 600 S/cm respectively). At temperatures > 425 K, similar values for the electrical conductivity are found for both samples.

Both ingots have similar thermopowers at room temperature (Figure 3-24b) but as the temperature increases the second ingot exhibits higher values with the maximum ~ 326 $\mu\text{V/K}$ at 620 K.

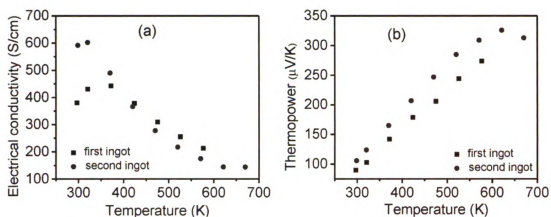


Figure 3-24. Temperature dependence of the (a) electrical conductivity and (b) thermopower of two different ingots with composition $\text{Na}_{0.5}\text{Pb}_8\text{Sb}_{0.25}\text{Te}_{10}$.

3.3.8. Method 8

The X-ray diffraction patterns for powders prepared from both top and bottom of the ingots are shown in Figure 3- 25. The sample was brittle and no thermoelectric properties could be measured.

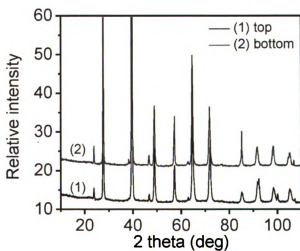


Figure 3-25. Powder X-ray diffraction patterns from powders from the composition $\text{NaPb}_8\text{SbTe}_{10}$ using Na_2Te as a source of Na.

3.3.9. Method 9

Resistance measurements on HP1 and HP2 gave values $\sim 0.6-1 \Omega$ for HP1 and 1.6Ω . Each coin was cut with the wire saw to prepare a parallelized sample. Both samples showed high resistance. Figure 3-26 shows the powder X-ray diffraction patterns of the original ingot before grinding and of the two pellets. All patterns are similar and can be indexed as PbTe phase.

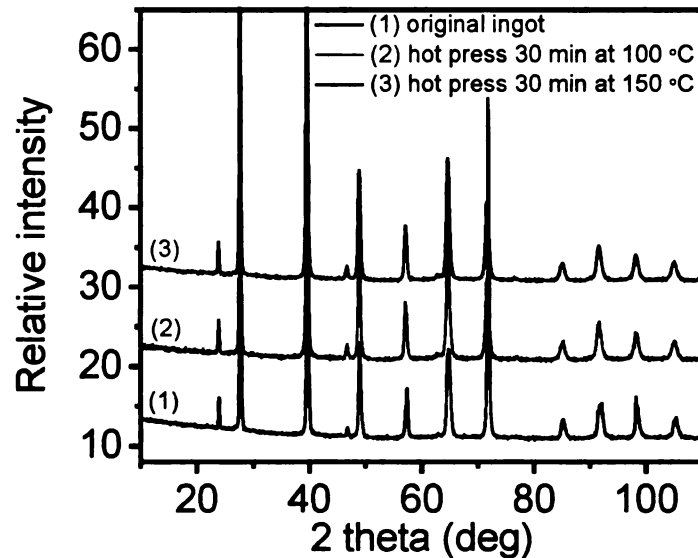


Figure 3-26. Comparison between the X-ray diffraction patterns from powders from the original ingot and the two pellets prepared from that ingot.

The surface of the pressed pellets HP1 and HP2 were examined through SEM (Figure 3-27).

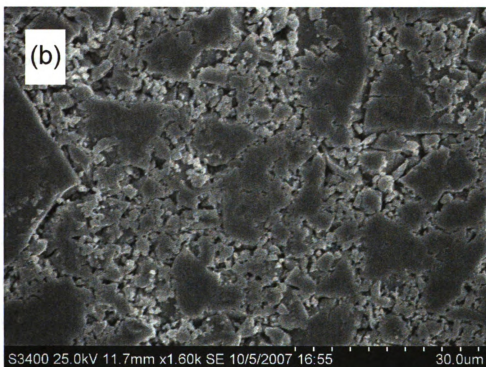
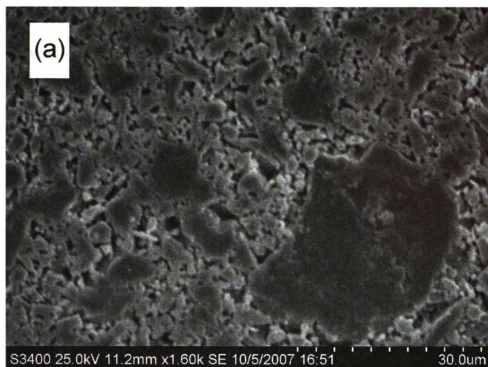


Figure 3-27. SEM images of the surface of (a) HP1 and (2) HP2.

A wide distribution of grains size and the presence of a significant amount of voids between grains could be observed. This explains the high resistivity of the pellets. The HP3 sample was found broken into two pieces when removed from the tube after annealing. Figure 3-27 shows SEM pictures of HP1 and HP2. Further pressing conditions need to be investigated.

3.4. Concluding remarks

Thermoelectric characterization of the low m members $\text{NaPb}_m\text{SbTe}_{m+2}$ shows promising TE properties. The composition $\text{NaPb}_8\text{SbTe}_{10}$ exhibited particularly low lattice thermal conductivity ($\sim 0.45 \text{ W/m}\cdot\text{K}$ at 650 K). Electron transport properties are also similar to what was reported to $\text{Na}_{0.95}\text{Pb}_{20}\text{SbTe}_{22}$. High resolution TEM revealed the presence of nanostructuring inside the matrix. However this does not give us information about the density of such regions. The brittleness of these samples is a serious drawback for industrial application. Using a slower or faster cooling profile did not improve the mechanical properties. Further hot-press experiments should be pursued. Due to limitation on our press system, experiments using higher temperature conditions could not be done. Several groups have reported on hot-press experiment on the LAST system. For example, Kosuga et al. prepared various $\text{Ag}_{1-x}\text{Pb}_{18}\text{SbTe}_{20}$ pellets ($x=0, 0.1$ and 0.2) by sintering powders under a pressure of 80 MPa at 723 K under nitrogen atmosphere.¹⁴ The bulk densities of the samples were $\sim 90 \%$ of the theoretical density. Mechanical alloying and spark plasma sintering techniques were used by Wang et al. to prepare $\text{Ag}_{0.8}\text{Pb}_{18+x}\text{SbTe}_{20}$.¹⁵ Densities were found above 95 % of the theoretical value and SEM

studies indicated the average grain size $\sim 1 \mu\text{m}$. Samples prepared by hot press or spark plasma sintering have low electrical conductivity at room temperature but the electrical conductivity increases with temperature. The thermal conductivity is also reduced because of the fine-grain microstructure. Yang et al. prepared TAGS materials with compositions $(\text{GeTe})_x(\text{AgSbTe}_2)_{100-x}$ ($x=75, 80, 85$ and 90) using hot-press technique (773 K , 70 MPa pressure).¹⁶ It is hoped that the application of these processing techniques will be helpful in producing strong specimens of SALT-m samples as well.

References

1. Rogers, L. M., *Brit. J. Appl. Phys.* **1967**, 18, 1227.
2. Noda, Y.; Orihashi, M.; Nishida, I. A., *Mater. Trans., JIM* **1998**, 39, (5), 602.
3. Crocker, A. J., *J. Phys. Chem. Solids* **1967**, 28, 1903.
4. Borisova, L. D., *Phy. Stat. Sol. A* **1979**, 53, K19.
5. Orihashi, M.; Noda, Y.; Kaibe, H. T.; Nishida, I. A., *Mater. Trans., JIM* **1998**, 39, (6), 672.
6. Harman, T. C.; Taylor, P. J.; Walsh, M. P.; Laforge, B. E., *Science* **2002**, 297, 2229.
7. Heremans, J. P.; Thrush, C. M.; Morelli, D. T., *J. Appl. Phys.* **2005**, 98, 063703.
8. Hsu, K. F.; Loo, S.; Guo, F.; Chen, W.; Dyck, J. S.; Uher, C.; Hogan, T.; Polychroniadis, E. K.; Kanatzidis, M. G., *Science* **2004**, 303, 818.
9. Poudeu, P. F. P.; D'Angelo, J.; Downey, A. D.; Short, J. L.; Hogan, T.; Kanatzidis, M. G., *Angew. Chem., Int. Ed.* **2006**, 45, 3835.
10. Ahmad, S.; Mahanti, S. D., *Phys. Rev. B* **2006**, 74, 155205.
11. Kittel, C., *Introduction to Solid State Physics*. Wiley: 2005.
12. Eisenmann, B.; Schaefer, H., *Z. Anorg. Allg. Chem.* **1979**, 456, 87.
13. Zhou, G.-T.; Pol, V. G.; Palchik, O.; Kerner, R.; Sominski, E.; Koltypin, Y.; Gedanken, A., *J. Solid State Chem.* **2004**, 177, (1), 361.
14. Kosuga, A.; Uno, M.; Kurosaki, K.; Yamanaka, S., *J. Alloys Compd.* **2005**, 391, 288.

15. Wang, H.; Li, J.-F.; Nan, C.-W.; Zhou, M.; Liu, W.; Zhang, B.-P.; Kita, T., *Appl. Phys. Lett.* **2006**, 88, 092104.

16. Yang, S. H.; Zhu, T. J.; Sun, T.; He, J.; Zhang, S. N.; Zhao, X. B., *Nanotechnology* **2008**, 19, (24), 245707.

Chapter 4

Thermoelectric Properties of the Nanostructured

Materials $\text{NaPb}_{18-x}\text{Sn}_x\text{MTe}_{20}$ (M=Sb, Bi)

4.1. Introduction

Thermoelectric-based cooling systems and power generators have limited applications because of their relatively low efficiency.¹ As a consequence, worldwide research for systems with higher performance is currently underway.^{2, 3} The performance of a thermoelectric material is defined by its figure of merit $ZT = (\sigma S^2)T/\kappa$, where σ = electrical conductivity, S = Seebeck coefficient (also called thermopower) and κ = thermal conductivity. The numerator (σS^2) is called the power factor. Many recent experimental and theoretical studies on low dimensional nanostructured materials⁴⁻⁶ and mixed-phase nanocomposites⁷⁻¹⁰ point to encouraging results in how to get low lattice thermal conductivity while maintaining high power factors. The superlattice thin-film structures of $\text{Bi}_2\text{Te}_3/\text{Sb}_2\text{Te}_3$ grown from chemical vapor deposition⁶ and of $\text{PbSe}_{0.98}\text{Te}_{0.02}/\text{PbTe}$ formed by molecular beam epitaxy^{4, 5} claimed ZT values greater than 2 (at ~ 300 and 550 K respectively). Bulk silicon has poor thermoelectric properties, however silicon nanowires show thermal conductivity which approaches the amorphous limit.^{11, 12} We are interested in investigating bulk analogues of such systems with similar figures of merit.

Recently, we have reported on the bulk n-type systems $\text{AgPb}_m\text{SbTe}_{m+2}$ (LAST),^{13, 14} $\text{Pb}_{1-x}\text{Sn}_x\text{Te-PbS}$ ¹⁵ and $\text{Pb}_{9.6}\text{Sb}_{0.2}\text{Te}_{10-x}\text{Se}_x$ ¹⁶ and the p-type systems $\text{Na}_{1-x}\text{Pb}_m\text{Sb}_y\text{Te}_{m+2}$ (SALT)¹⁷ and $\text{Ag}(\text{Pb}_{1-y}\text{Sn}_y)_m\text{SbTe}_{2+m}$ (LASTT),¹⁸ all bulk materials that exhibit high thermoelectric figure of merit. High resolution transmission electron microscopy images of these materials revealed the presence of nanoparticles coherently embedded in what is essentially a PbTe matrix. These features are believed to be the origin of very low lattice thermal conductivity, which is a common property of all these systems. For example, the p-type composition $\text{Na}_{0.95}\text{Pb}_{20}\text{SbTe}_{22}$ reached ZT of ~ 1.6 at 650 K, which is nearly twice that of p-type PbTe, and arising predominantly from a very low thermal conductivity. Namely, the total thermal conductivity in these materials drops very rapidly with rising temperature and reaches a minimum value of 0.85 W/m-K at 700 K for $\text{Na}_{0.95}\text{Pb}_{20}\text{SbTe}_{22}$. In a recent study, we showed also that the influence of the trivalent element in $\text{AgPb}_{18}\text{MTe}_{20}$ (M=Sb, Bi) on the power factor and the lattice thermal conductivity is significant with the presence Sb of producing more favorable properties than that of Bi.¹⁹

In this chapter, we examine the partial substitution of Pb by Sn in the high ZT material $\text{NaPb}_{18}\text{SbTe}_{20}$ to produce the solid solutions $\text{NaPb}_{18-x}\text{Sn}_x\text{SbTe}_{20}$ and study their physical and thermoelectric properties. To better understand the role of the pnictogen on the properties of the system, Bi analogs with general formula $\text{NaPb}_{18-x}\text{Sn}_x\text{BiTe}_{20}$ were prepared as well. Partial substitution of Pb by Sn results in a increase of the hole concentration and a decrease of their mobility. The electrical conductivity of $\text{NaPb}_{18-x}\text{Sn}_x\text{MTe}_{20}$ (M=Sb, Bi) increases and the thermopower decreases with increasing fraction

of Sn. All the compositions examined showed p-type behavior and exhibit low lattice thermal conductivity. That is attributed to a combination of point defect scattering associated with solid solution behavior and also the presence of nano-sized inclusions in the crystalline matrix.

4.2. Experimental section

4.2.1. Synthesis.

All samples were prepared as polycrystalline ingots in silica tubes by mixing high purity elements in the appropriate stoichiometric ratio. To prevent reaction between the sodium metal and silica, the tubes were carbon-coated prior to use. All components (except Na) were loaded into the silica tubes under ambient atmosphere and the corresponding amount of Na was later added under nitrogen atmosphere in a dry glove box. The silica tubes were then flame-sealed under a residual pressure of $\sim 10^{-4}$ Torr, placed into a tube furnace (mounted on a rocking table) and heated at 1250 K for 4 h to allow complete melting of all components. While molten, the furnace was allowed to rock for 2 h to facilitate complete mixing and homogeneity of the liquid phase. The furnace was finally immobilized at the vertical position and was cooled from 1250 to 820 K over 43 h followed by a fast cool to room temperature. The resulting ingots were silvery-metallic in color with a smooth surface.

Table 4-1 and 4-2 summarize the amount of elements used for each reaction.

Table 4-1. Amounts of elements used to prepare NaPb_{18-x}Sn_xSbTe₂₀.

Composition	Na, g (mmol)	Pb, g (mmol)	Sn, g (mmol)	Sb, g (mmol)	Te, g (mmol)
NaPb ₁₈ SbTe ₂₀	0.045 g (1.96)	7.3003 g (35.23)	0	0.2383 g (1.96)	4.9953 g (39.15)
NaPb ₁₅ Sn ₃ SbTe ₂₀	0.060 g (2.61)	8.1114 g (39.15)	0.9294 g (7.83)	0.3178 g (2.61)	6.6604 g (52.20)
NaPb ₁₃ Sn ₅ SbTe ₂₀	0.050 g (2.17)	5.8583 g (28.27)	1.2909 g (10.87)	0.2648 g (2.17)	5.5503 g (43.50)
NaPb ₉ Sn ₉ SbTe ₂₀	0.060 g (2.61)	4.8669 g (23.49)	2.7883 g (23.49)	0.3178 g (2.61)	6.6604 g (52.20)
NaPb ₅ Sn ₁₃ SbTe ₂₀	0.060 g (2.61)	2.7038 g (13.05)	4.0276 g (33.93)	0.3178 g (2.61)	6.6604 g (52.20)
NaPb ₂ Sn ₁₆ SbTe ₂₀	0.055 g (2.39)	0.9914 g (4.78)	4.5440 g (38.28)	0.2913 g (2.39)	6.1053 g (47.85)
NaSn ₁₈ SbTe ₂₀	0.070 g (3.04)	0	6.5061 g (54.81)	0.3707 g (3.04)	7.7704 g (60.90)

Table 4-2. Amounts of elements used to prepare NaPb_{18-x}Sn_xBiTe₂₀.

Composition	Na, g (mmol)	Pb, g (mmol)	Sn, g (mmol)	Sb, g (mmol)	Te, g (mmol)
NaPb ₁₈ BiTe ₂₀	0.045 g (1.96)	7.3003 g (35.23)	0	0.2383 g (1.96)	4.9953 g (39.15)
NaPb ₁₅ Sn ₃ BiTe ₂₀	0.060 g (2.61)	8.1114 g (39.15)	0.9294 g (7.83)	0.5454 g (2.61)	6.6604 g (52.20)
NaPb ₁₃ Sn ₅ BiTe ₂₀	0.039 g (1.71)	4.6047 g (22.22)	1.0147 g (8.55)	0.3572 g (1.71)	4.3626 g (34.19)
NaPb ₉ Sn ₉ BiTe ₂₀	0.046 g (2.00)	3.7219 g (17.96)	1.6265 g (17.96)	2.1324 g (2.00)	5.0935 g (30.45)
NaPb ₅ Sn ₁₃ BiTe ₂₀	0.035 g (1.52)	1.5772 g (7.61)	2.3494 g (19.79)	0.3182 g (1.52)	3.8852 g (30.45)
NaPb ₂ Sn ₁₆ BiTe ₂₀	0.050 g (2.16)	0.8952 g (4.32)	4.1033 g (34.57)	0.4515 g (2.16)	5.5132 g (43.21)
NaSn ₁₈ BiTe ₂₀	0.070 g (3.04)	0	6.5061 g (54.81)	0.6363 g (3.04)	7.7704 g (60.90)

4.2.2. Characterization techniques

Powder X-ray Diffraction. Powder X-ray patterns of the ground materials were recorded using Cu K_α radiation ($\lambda = 1.54056 \text{ \AA}$) in reflection geometry on a CPS-120 Inel

X-ray powder diffractometer operating at 40 kV and 20 mA equipped with a position sensitive detector. The lattice parameters were refined from the X-ray powder diffraction patterns using the software Jade 6.0 from Materials Data Inc.

Infrared Spectroscopy. Room temperature optical diffuse reflectance measurements were performed on finely ground powder to probe the optical band gap of the materials. The spectra were monitored in the mid-IR region ($4000\text{-}400\text{ cm}^{-1}$) using a Nicolet 6700 FTIR spectrometer. Absorption (α/S) data were calculated from reflectance data using the Kubelka-Munk function.²⁰⁻²² The optical band gaps were derived from α/S versus E (eV) plots. Specular IR reflectivity measurements were carried out on polished specimens in the spectral range $100\text{-}2500\text{ cm}^{-1}$, at room temperature, with non-polarized light, using a Bruker IFS 113V Fourier transform interferometer working under vacuum and equipped with the special reflectance unit. The angle of incidence was less than 10 deg.

DTA Analysis. Differential thermal analysis (DTA) data were collected with a Shimadzu DTA-50 thermal analyzer. Approximately 35 mg of finely ground powder of material was sealed in a carbon-coated quartz ampoule under residual pressure of $\sim 10^{-4}$ torr. Another ampoule containing similar amount of alumina and prepared the same way was used as a reference. The samples were heated to 1273 K at a rate of 10 K/min, held at 1273 K for two minutes and cooled to 323 K at a rate of -10 K/min.

Scanning Electron Microscopy. The surface of several samples was polished very carefully using silica suspension solution ($0.05\text{ }\mu\text{m}$) in order to get a smooth, mirror-like surface. The samples were then studied with a scanning electron microscopy (Hitachi S3400N-II) with 25 kV acceleration voltage using both energy-dispersive spectroscopy (EDS) and back-scattered electron imaging (BSE).

Electrical Transport Properties. Thermopower and electrical conductivity properties were measured simultaneously under helium atmosphere using a ZEM-3 Seebeck coefficient/electrical resistivity measurement system (ULVAC-RIKO, Japan). Samples for transport measurement were cut to size 10 x 3 x 3 mm using a diamond saw (Buehler isomet 1000), a wire saw (South Bay Technology) and a polishing machine (Buehler comet 3000). Rectangular shape samples with approximately $3 \times 3 \text{ mm}^2$ cross-section were sandwiched vertically by two nickel electrodes (current injection) with two Pt/PtRh thermocouples (for temperature difference and voltage measurements) attached on one side. The sample and measurement probes were covered by a nickel can to maintain a constant temperature during the measurement and the base temperature was measured by a thermocouple attached to the outside of the can. The sample, electrodes, and nickel can were placed in a vacuum chamber then evacuated and refilled with He gas (0.1 atm) to provide necessary heat transfer. Properties were measured from room temperature to 670 K under helium atmosphere.

Hall Measurements. Above 300 K, Hall measurements were carried out by an in-house high temperature/high magnetic field Hall apparatus. It consists of a nine Tesla air-bore superconducting magnet with a water-cooled oven inside the bore of the magnet, and a Linear Research AC bridge with 16 Hz excitation. Four-wire AC Hall measurements were performed on parallelepiped samples with the typical size of $1.5 \times 3 \times 10 \text{ mm}^3$ to temperatures of at least 800 K with the protection of Argon gas.

Thermal Conductivity. The thermal conductivity was determined as a function of temperature using the flash diffusivity method on a LFA 457/2/G Microflash Netzsch. The front face of a small disc-shaped sample (diameter $\sim 8 \text{ mm}$; thickness $\sim 2 \text{ mm}$) coated

with a thin layer of graphite is irradiated with a short laser burst, and the resulting rear face temperature rise is recorded and analyzed. The experiments were carried out under nitrogen atmosphere. Thermal conductivity values were calculated using the equation $\kappa = \alpha C_p d$, where α is the thermal diffusivity, C_p the specific heat and d the bulk density of the material calculated from the sample's geometry and mass. A pyroceram reference was used to determine the heat capacity of the sample. The thermal diffusivities were measured typically over the temperature range 300-670 K. The electronic component of the thermal conductivity was quantified through the Wiedemann-Franz law according to which $\kappa_{el} = \sigma.T.L_0$ (L_0 being the Lorenz number, $L_0=2.45.10^{-8} \text{ W}\Omega\text{K}^{-1}$).²³ The lattice contribution was then derived by subtracting the electronic component from the total thermal conductivity.

Transmission Electron Microscopy. The microstructures of several pieces cut from different locations of the ingots were examined by high resolution electron microscopy (HRTEM). Specimens for the investigation were prepared by conventional standard methods which was described elsewhere¹⁶. The HRTEM images were recorded at 200 kV using a JEOL 2200FS and JEOL 2100FS for $\text{NaPb}_{13}\text{Sn}_5\text{SbTe}_{20}$ and $\text{NaPb}_{13}\text{Sn}_5\text{BiTe}_{20}$ respectively. Composition analysis was done by Energy Dispersive X-ray Spectroscopy (EDS) using a spot size ~ 1 nm in scanning transmission electronic microscopy (STEM) mode.

4.3. Results and discussion

Structure and Characterization. During the course of this study, we observed that ingots containing antimony tended to be mechanically more robust than their bismuth

analogs. The Bi containing samples were extremely brittle and often cleaved into lamellar pieces. Nevertheless all ingots were found to be brittle and great care was taken to select specimens that were free of cracks.

Figure 4-1a shows the X-ray diffraction patterns for samples with general formula $\text{NaPb}_{18-x}\text{Sn}_x\text{SbTe}_{20}$ ($x = 5, 9, 13$ and 16). The patterns can be indexed to a NaCl-type structure. No extra peaks of a potential second phase were observed. The Bragg peaks shift towards higher diffraction angle with increasing Sn/Pb ratio, indicating contraction of the lattice constant. This result is consistent with the expected substitution of Pb^{2+} cations by the smaller Sn^{2+} cations in the lattice. Diffraction patterns of the bismuth analogs (general composition $\text{NaPb}_{18-x}\text{Sn}_x\text{BiTe}_{20}$) are depicted in Figure 4-1b. Again, the patterns indicated NaCl-type structure and with higher fraction of Sn displayed a similar shifting of the diffraction peaks towards higher angles. Lattice parameters for $\text{NaPb}_{18-x}\text{Sn}_x\text{SbTe}_{20}$ and $\text{NaPb}_{18-x}\text{Sn}_x\text{BiTe}_{20}$ samples refined from the diffraction patterns are plotted as a function of x in Figures 4-1c and 4-1d. For example, the lattice constant varies from $6.444(1) \text{ \AA}$ for $\text{NaPb}_{15}\text{Sn}_3\text{BiTe}_{20}$, which is closer to PbTe (6.459 \AA)²⁴ to $6.342(1) \text{ \AA}$ for $\text{NaPb}_2\text{Sn}_{16}\text{BiTe}_{20}$, which is closer to SnTe (6.328 \AA).²⁵

To achieve doping in these systems, stoichiometric deficiency was created on Na as it was done on the parent composition $\text{Na}_{1-y}\text{Pb}_m\text{Sb}_y\text{Te}_{m+2}$.¹⁷ X-ray powder diffraction was taken on powder from both top and bottom of the ingot to assess homogeneity along the samples. Analysis of the powder diffraction patterns of Na-deficient compositions revealed the presence of Sb_2Te_3 as a minor impurity. For example, in the diffraction patterns of compositions $\text{Na}_{0.8}\text{Pb}_{13}\text{Sn}_5\text{SbTe}_{20}$ (Figure 4-2a) and $\text{Na}_{0.8}\text{Pb}_{13}\text{Sn}_5\text{Sb}_{0.4}\text{Te}_{20}$

(Figure 4-2b), extra peaks attributed to Sb_2Te_3 were clearly observed. This suggests that vacancies of Na^+ cations are not created in the NaCl-type lattice. Instead Sb_2Te_3 is expelled according to equation (1):

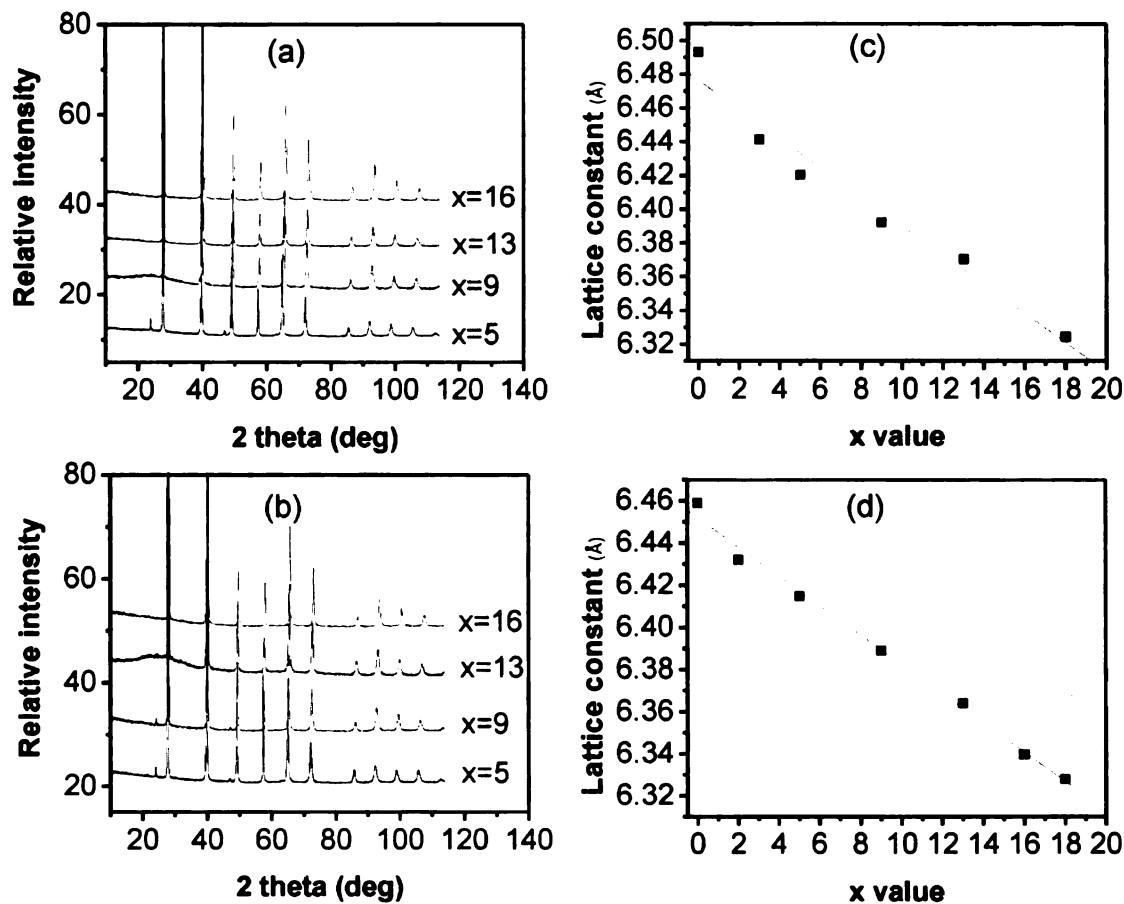


Figure 4-1. Powder X-ray diffraction patterns of $\text{NaPb}_{18-x}\text{Sn}_x\text{MTe}_{20}$ with $x=5, 9, 13, 16$ for (a) $\text{M}=\text{Sb}$ and (b) $\text{M}=\text{Bi}$; variation of the unit cell parameter as a function of x for (c) $\text{M}=\text{Sb}$ and (d) $\text{M}=\text{Bi}$.

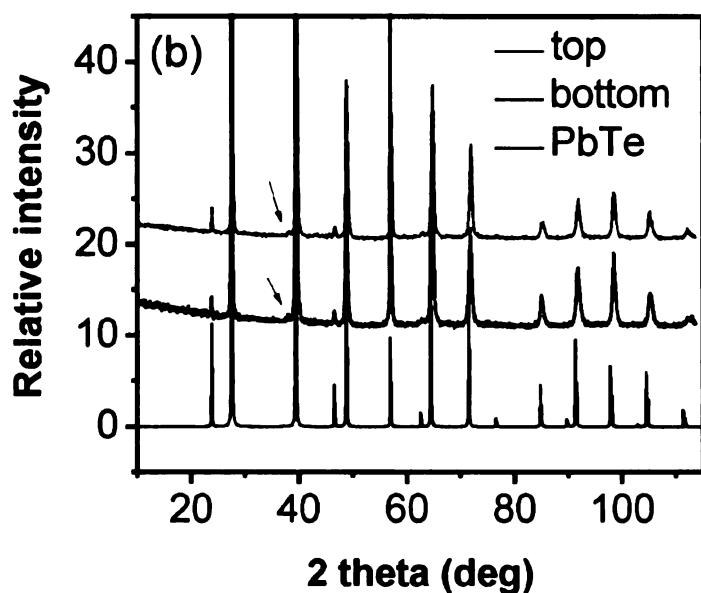
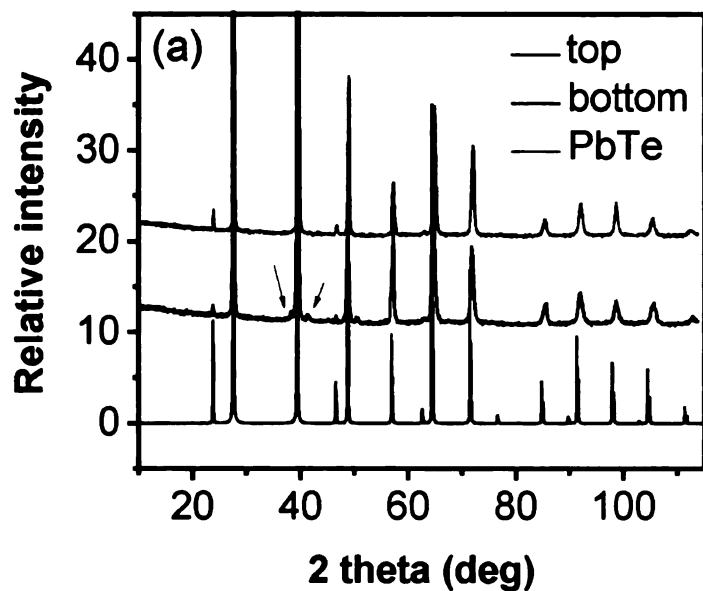


Figure 4-2. X-ray powder diffraction patterns of (a) $\text{Na}_{0.8}\text{Pb}_{13}\text{Sn}_5\text{SbTe}_{20}$, (b) $\text{Na}_{0.8}\text{Pb}_{13}\text{Sn}_5\text{Sb}_{0.4}\text{Te}_{20}$. For each composition, powder from both top and bottom of the ingot was analyzed to check homogeneity along the ingot. The small arrows indicate diffraction peaks that do not belong to the PbTe structure-type and indicate the presence of Sb_2Te_3 as a minor phase.

Figure 4-3a shows DTA data for $\text{NaPb}_5\text{Sn}_{13}\text{SbTe}_{20}$. The plot shows only one endothermic peak of melting during the heating cycle and one exothermic peak of crystallization on the cooling cycle. Similar curves were obtained for the other compositions $\text{NaPb}_{18-x}\text{Sn}_x\text{SbTe}_{20}$ and their Bi analogs. Melting and crystallization points for the $\text{NaPb}_{18-x}\text{Sn}_x\text{MTe}_{20}$ series are summarized in Tables 4-3 and 4-4. The melting point decreases with increasing Sn fraction and varies from 1160 K for $\text{NaPb}_{15}\text{Sn}_3\text{SbTe}_{20}$ to 1081 K for $\text{NaPb}_2\text{Sn}_{16}\text{SbTe}_{20}$ (Figure 4-3b). This trend is consistent with the expected solid solution alloying between the high melting PbTe (1196 K) and the lower melting SnTe (1063 K) compounds.

The band-gap energy values obtained from electronic absorption spectra for $\text{NaPb}_{18-x}\text{Sn}_x\text{MTe}_{20}$ are reported in Tables 4-3 and 4-4. For $\text{NaPb}_{18-x}\text{Sn}_x\text{SbTe}_{20}$, the lowest band gap was observed for $x=9$, the band gap decreases in going from $x=18$ to $x=9$, Figure 4-4. The same behavior is observed for the Bi analogs with band gaps below 0.1 eV for $x=3, 5, 9, 13$ and 16. The band gap increases again then for $x=18$. This is consistent with trends reported previously: for example, several investigations have shown that the band gap of the $\text{Pb}_{1-x}\text{Sn}_x\text{Te}$ system decreases as the tin content increases, goes through zero and then increases again with further increase in tin content.²⁶

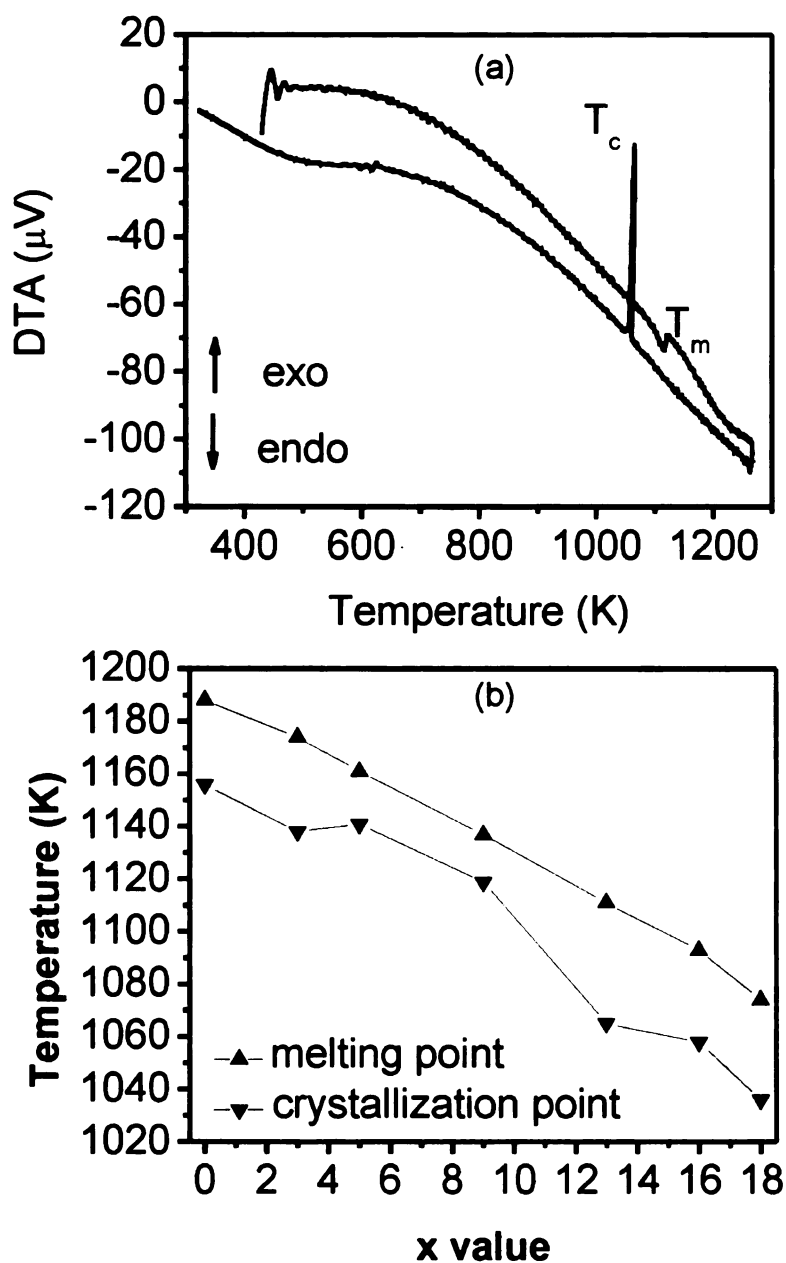


Figure 4-3. (a) Typical DTA results of the composition $\text{NaPb}_5\text{Sn}_{13}\text{SbTe}_{20}$, (b) variation of the melting and crystallization points of $\text{NaPb}_{18-x}\text{Sn}_x\text{SbTe}_{20}$ as a function of x.

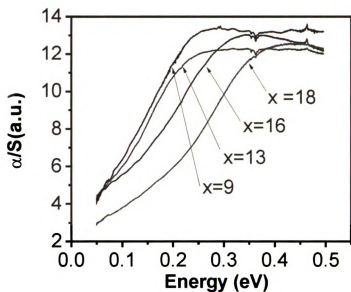


Figure 4-4. Infrared absorption spectra near the band edge of samples $\text{NaPb}_{18-x}\text{Sn}_x\text{SbTe}_{20}$ with $x=9, 13, 16$ and 18 .

$\text{NaPb}_{18-x}\text{Sn}_x\text{SbTe}_{20}$ with $x=9, 13, 16$ and 18 .

Scanning Electron Microscopy. The surface of several samples was polished very carefully and analyzed using both secondary and back-scattered electron microscopies. In the case of Sb analogs, micro-size inclusions were observed for the different compositions. Such inclusions are randomly dispersed in the $\text{Pb}_{1-y}\text{Sn}_y\text{Te}$ matrix and typical distance between inclusions is in the millimeter range. For example, Figure 4-5 shows BSE imaging of inclusions for different parts of the ingots $\text{NaPb}_9\text{Sn}_9\text{SbTe}_{20}$ and $\text{NaPb}_{13}\text{Sn}_5\text{SbTe}_{20}$. EDS analysis on the inclusions observed in Figure 4-5a gave the following atomic percentages: Te: 20.21, Sb: 67.63 and Sn 10.50. Similar ratios were obtained for the precipitate in Figure 4-5b. The inclusion observed in Figure 4-5c had less Sb, the atomic percentages of Pb, Te, Sb and Sn were 5.22, 40.05, 46.42 and 8.31

respectively. The formation of such precipitates rich in Sb could be expected because of the low solubility of Sb in PbTe.²⁷

Similar SEM studies were done for the Bi samples. Micro-size precipitates could be observed as well. Figure 4-6a shows a Bi precipitate ~ 23 μm diameter embedded in the $\text{Pb}_{1-y}\text{Sn}_y\text{Te}$ matrix for the composition $\text{NaPb}_{13}\text{Sn}_5\text{BiTe}_{20}$. Some of these precipitate are actually multi-phase. Examples of such inclusions are visible in Figure 4-6b and 4-6c. Both inclusions were observed for the same sample from the middle area for $\text{NaPb}_2\text{Sn}_{16}\text{BiTe}_{20}$. Only Bi was present in the bright area 1 of the precipitate shown in Figure 4-6b but EDS analysis on the darker zone 2 gave the following atomic percentages: Pb 2.35, Sn 22.74, Bi 25.79, Te 48.50. The composition of the matrix was analyzed with EDS and the respective atomic percentages for Pb, Sn, Bi and Te were 6.14, 37.07, 4.20 and 52.66 respectively. EDS analysis on the bright area 1 of the precipitate on Figure 4-6c indicated only the presence of Bi whereas the darker zone 2 contained Pb, Sn and Bi as well. The atomic percentages were Pb 1.58, Sn 20.88, Bi 32.59 and Te 43.84. The variety of the shapes and dimensions of the inclusions suggest that they form randomly in the $\text{Pb}_{1-y}\text{Sn}_y\text{Te}$ matrix. As these phases have lower melting point than $\text{Pb}_{1-y}\text{Sn}_y\text{Te}$, they are trapped in the matrix which starts to crystallize before them upon cooling.

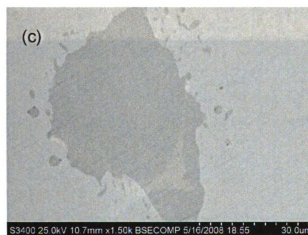
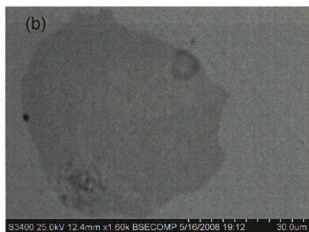
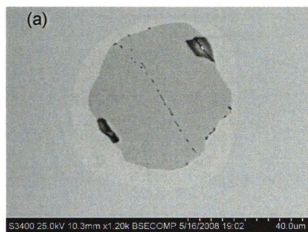


Figure 4-5. BSE imaging of inclusions observed from (a) part close to the top and (b) part close to the bottom of the ingot $\text{NaPb}_9\text{Sn}_9\text{SbTe}_{20}$, (c) middle part of $\text{NaPb}_{13}\text{Sn}_5\text{SbTe}_{20}$.

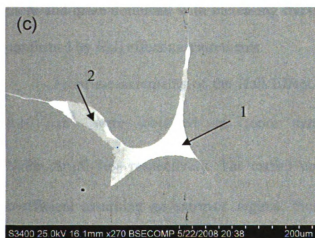
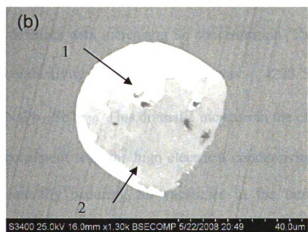


Figure 4-6. BSE imaging of samples from middle part of the ingots (a) $\text{NaPb}_{13}\text{Sn}_5\text{BiTe}_{20}$ and (b)-(c) $\text{NaPb}_2\text{Sn}_{16}\text{BiTe}_{20}$.

Electronic Transport Properties.

NaPb_{18-x}Sn_xSbTe₂₀. The electronic transport properties of the *NaPb_{18-x}Sn_xMTe₂₀* systems can be tuned by varying the Sn:Pb ratio. Figure 4-7a shows the evolution of the electrical conductivity as a function of temperature for the Sb analogs *NaPb_{18-x}Sn_xSbTe₂₀* ($x=0, 3, 5, 9, 13, 16$ and 18). Regardless of the composition, the electrical conductivity monotonically decreases with increasing temperature, indicating degenerate conduction for the whole temperature range examined. The electrical conductivity increases with increasing Sn concentration. The room temperature value of the electrical conductivity of *NaSn₁₈SbTe₂₀* was ~ 4220 S/cm, which is about three times that of *NaPb₁₈SbTe₂₀*. This dramatic increase in the electrical conductivity with addition of Sn is consistent with the high electrical conductivity of SnTe, which is the result of massive, naturally occurring Sn vacancies in the lattice that drastically increases the carrier concentration.²⁵ Presumably, in the *NaPb_{18-x}Sn_xSbTe₂₀* system, these vacancies become more and more dominant with increasing fraction of SnTe (i.e. x). This hypothesis was confirmed by Hall effect measurements.

From measurements of the Hall Effect, carrier concentrations of $\sim 1.2 \cdot 10^{20}$ and $8 \cdot 10^{19}/\text{cm}^3$ were obtained at room temperature for *NaPb₁₃Sn₅SbTe₂₀* and *NaPb₁₅Sn₃SbTe₂₀* respectively. The carrier concentration was extracted from the hall coefficient assuming an extrinsic regime, thus using the formula for a single carrier transport $n = 1/eR$ (with e being the electron charge and R the Hall coefficient). For comparison, the room temperature hole concentration of *Na_{0.95}Pb₂₀SbTe₂₂* was $\sim 6.3 \cdot 10^{19}/\text{cm}^3$. This indicates an increase in hole concentration with increasing Sn content.

NaPb₁₃Sn₅BiTe₂₀ has similar hole concentration than its Sb analog (Figure 4-8a). For both materials, the carrier concentration increases up to $\sim 2.4 \cdot 10^{20} / \text{cm}^3$ at 675 K. This increase in the carrier concentration is due probably to the very low band gap of the material. Higher temperature allows more valence electrons enough energy to be promoted to higher energy levels. The higher carrier concentrations of the Sn-rich compositions were independently confirmed by the spectroscopic infrared reflectivity studies of these systems (see below). The carrier mobility was calculated using the electrical conductivity data from Figure 4-7a. The values of the mobility vary from 54 cm²/V·s at room temperature to 7 cm²/V·s at 675 K for NaPb₁₃Sn₅SbTe₂₀ and from 38 to 5 cm²/V·s for its Bi analog (Figure 4-8b). Such relatively low mobility values are a result of the very high carrier concentration and the cation disorder in the NaCl-type lattice which scatters carriers more strongly.

The temperature dependence of the electrical conductivity of NaPb_{18-x}Sn_xSbTe₂₀ samples is in accordance with the power law $T^{-\lambda}$, where the power exponent λ ranges from 2.64 (for x=0) to 0.99 (for x=18) (Figure 4-7b). The power law dependence of the electrical conductivity (also found in PbTe) results from the phonon scattering of charge carriers.²⁸ The value of λ decreases with increasing content of Sn. The electrical conductivity of the composition NaSn₁₈SbTe₂₀ decreases as 1/T ($\lambda = 1$), which is similar to SnTe and more typical of a metal. The electrical conductivity of NaPb₁₈SbTe₂₀ decreases with increasing temperature according to the power law $T^{-2.64}$. This is consistent with the trends observed in the Na_{1-x}Pb_mSb_yTe_{m+2} system¹⁷ and similar to p-type PbTe.

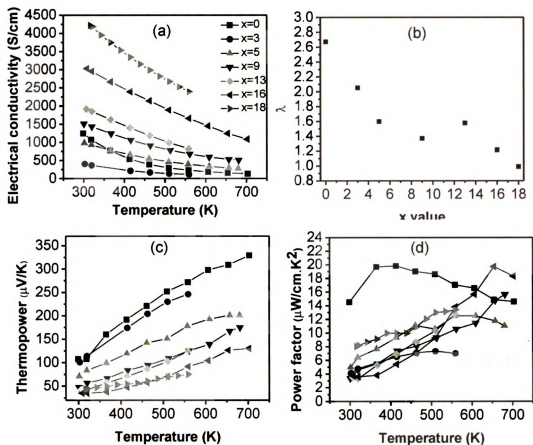


Figure 4-7. Electronic transport properties of the $\text{NaPb}_{18-x}\text{Sn}_x\text{SbTe}_{20}$ samples: (a) electrical conductivity, (b) variation of the power law dependence of the electrical conductivity ($T^{-\lambda}$) as a function of x (the λ parameters were extracted from the data of panel (a)), (c) thermopower, (d) power factor. The point marks in the inset of panel (a) identify all samples and apply to panels (c) and (d).

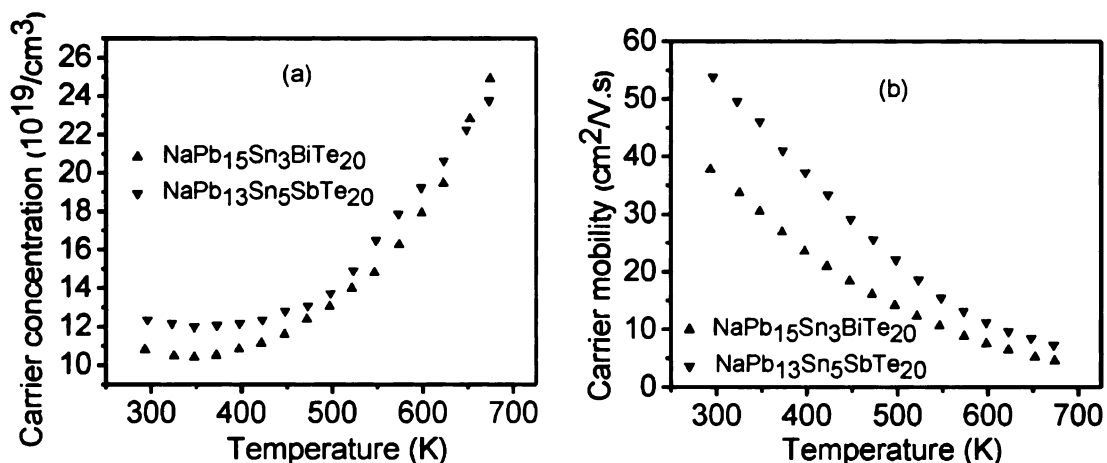


Figure 4-8. Temperature dependence of (a) the carrier concentration and (b) carrier mobility for NaPb₁₃Sn₅MTe₂₀ (M=Sb, Bi).

All compositions showed positive thermopower indicating p-type transport. The thermopower trend as a function of Pb/Sn ratio is opposite to that of the electrical conductivity, Figure 4-7c. The thermopower of NaPb₁₈SbTe₂₀ starts at ~105 μ V/K at 300 K increases rapidly with rising temperature reaching the high value of 329 μ V/K at 700 K. The corresponding Sn analog (NaSn₁₈SbTe₂₀) showed only ~ 44 μ V/K at room temperature and the thermopower did not exceed 75 μ V/K at 560 K. One interesting feature of the NaPb_{18-x}Sn_xSbTe₂₀ system is the high rising slope of the thermopower with increasing temperature. For example, in the case of NaPb₁₅Sn₃SbTe₂₀, the value at 560 K is 2.5 times larger than that at room temperature (101 μ V/K at 302 K and 246 μ V/K at 560 K).

The power factors for each composition are shown as a function of temperature in Figure 4-7d. Clearly, the Sn-free composition NaPb₁₈SbTe₂₀ has a much higher power factor reaching 20 μ W/cm²·K² at ~ 400 K. For Pb-Sn mixed compositions, the graph can

be divided into two temperature regions, the first ranging from 300 to 500 K and the second above 500 K. Within the first region, $\text{NaPb}_{13}\text{Sn}_5\text{SbTe}_{20}$ exhibits the highest power factor at 460 K whereas in the second region, $\text{NaPb}_2\text{Sn}_{16}\text{SbTe}_{20}$ surpasses the other compositions, reaching a power factor of $20 \mu\text{W}/\text{cm}\cdot\text{K}^2$ at 650 K, see Figure 4-7d.

Doping studies on the previously reported $\text{Na}_{1-x}\text{Pb}_m\text{Sb}_y\text{Te}_{m+2}$ system¹⁷ showed a slight increase of electrical conductivity with decreasing Sb content and an increase of thermopower with decreasing Na/Sb ratio. It was found that the power factor of the $\text{Na}_{0.8}\text{Pb}_{20}\text{Sb}_y\text{Te}_{22}$ materials increases with decreasing Na/Sb ratio.¹⁷ In order to investigate the role of these ratios on the thermoelectric properties of the title materials we chose the composition $\text{NaPb}_{13}\text{Sn}_5\text{SbTe}_{20}$. Figure 4-9a shows the temperature dependence of the electrical conductivity for the compositions $\text{Na}_{0.8}\text{Pb}_{13}\text{Sn}_5\text{SbTe}_{20}$, $\text{Na}_{0.8}\text{Pb}_{13}\text{Sn}_5\text{Sb}_{0.8}\text{Te}_{20}$, $\text{Na}_{0.8}\text{Pb}_{13}\text{Sn}_5\text{Sb}_{0.6}\text{Te}_{20}$ and $\text{Na}_{0.8}\text{Pb}_{13}\text{Sn}_5\text{Sb}_{0.4}\text{Te}_{20}$. Other compositions $\text{Na}_{0.9}\text{Pb}_{13}\text{Sn}_5\text{SbTe}_{20}$, $\text{Na}_{0.9}\text{Pb}_{13}\text{Sn}_5\text{Sb}_{0.8}\text{Te}_{20}$, $\text{Na}_{0.9}\text{Pb}_{13}\text{Sn}_5\text{Sb}_{0.6}\text{Te}_{20}$ and $\text{Na}_{0.9}\text{Pb}_{13}\text{Sn}_5\text{Sb}_{0.4}\text{Te}_{20}$ were also prepared but the ingots were too brittle to allow proper electrical characterization. The transport data show that for similar Na concentration, the electrical conductivity decreases and the thermopower increases with increasing amount of Sb (Figure 4-9b). The composition $\text{Na}_{0.8}\text{Pb}_{13}\text{Sn}_5\text{SbTe}_{20}$ reaches a maximum $\sim 257 \mu\text{V}/\text{K}$ at 650 K compared to $201 \mu\text{V}/\text{K}$ for $\text{NaPb}_{13}\text{Sn}_5\text{SbTe}_{20}$. In the range of 450 – 500 K, similar power factors were obtained for samples with various Sb fractions (Figure 4-9c). At higher temperature, the power factor plots diverge. The composition

$\text{Na}_{0.8}\text{Pb}_{13}\text{Sn}_5\text{SbTe}_{20}$ reaches a maximum of $11.5 \mu\text{W}/\text{cm}\cdot\text{K}^2$ at 550 K whereas $\text{Na}_{0.8}\text{Pb}_{13}\text{Sn}_5\text{Sb}_{0.4}\text{Te}_{20}$ reaches $\sim 16 \mu\text{W}/\text{cm}\cdot\text{K}^2$ at 675 K.

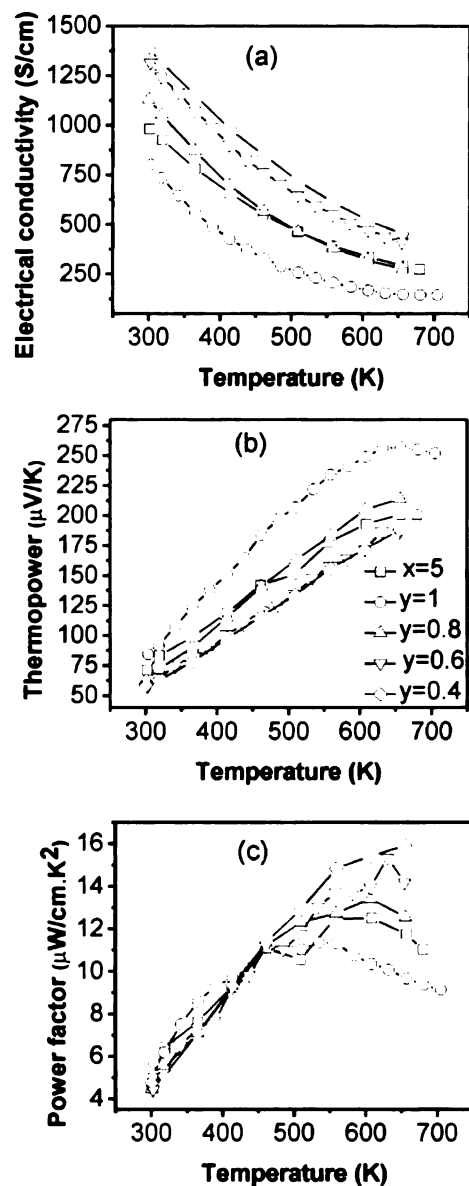


Figure 4-9. (a) Temperature dependence of the thermoelectric properties of the $\text{NaPb}_{13}\text{Sn}_5\text{SbTe}_{20}$ and $\text{Na}_{0.8}\text{Pb}_{13}\text{Sn}_5\text{Sb}_y\text{Te}_{20}$ ($y=0.4, 0.6, 0.8, 1$) compositions: (a) electrical conductivity, (b) thermopower, (c) power factor. The point marks in the inset of panel (b) apply to plots (a) and (c).

NaPb_{18-x}Sn_xBiTe₂₀. Similar general trends as above were observed for the Bi analog series (*NaPb_{18-x}Sn_xBiTe₂₀*). Increasing the Sn concentration also resulted in an increase in conductivity and decrease in thermopower. Electrical conductivity data for *NaPb_{18-x}Sn_xBiTe₂₀* (x=0, 3, 5, 9, 13, 16, 18) are shown in Figure 4-10a. First it must be noticed that *NaPb₅Sn₁₃BiTe₂₀* has similar electrical conductivity than *NaPb₉Sn₉BiTe₂₀*, this is probably due the presence of cracks in the sample *NaPb₅Sn₁₃BiTe₂₀*. At room temperature, the compositions x=3 and x=5 have lower electrical conductivities than *NaPb₁₈BiTe₂₀* but similar values are observed at higher temperature. *NaPb₉Sn₉BiTe₂₀* and *NaPb₁₈BiTe₂₀* have similar electrical conductivities at 300 K but at higher temperature the electrical conductivity decreases more rapidly for *NaPb₁₈BiTe₂₀*. As the Sn:Pb ratio increases, the conductivity is progressively dominated by the properties of SnTe. Thus, the electrical conductivity of the Sn-rich *NaPb₂Sn₁₆BiTe₂₀* and *NaSn₁₈BiTe₂₀* is much higher than that of *NaPb₁₈BiTe₂₀*. Regarding the power law dependence of the electrical conductivity ($T^{-\lambda}$), the parameter λ decreases with increasing tin content with value ~ 1 for x = 13, 16 and 18 (Figure 4-10b).

The thermopower values for the *NaPb_{18-x}Sn_xBiTe₂₀* series are shown in Figure 4-10c. The composition *NaPb₁₈BiTe₂₀* clearly exhibits the highest thermopower over the temperature range 350-650 K. The other compositions can be classified into two groups. The first group includes the compositions *NaPb₁₅Sn₃BiTe₂₀* and *NaPb₁₃Sn₅BiTe₂₀* with thermopower values ranging from 80 to 270 $\mu\text{V/K}$ between 300 and 675 K. The second

group comprises the compositions $\text{NaPb}_9\text{Sn}_9\text{BiTe}_{20}$, $\text{NaPb}_5\text{Sn}_{13}\text{BiTe}_{20}$ and $\text{NaPb}_2\text{Sn}_{16}\text{BiTe}_{20}$ with values $< 170 \mu\text{V/K}$ at 675 K, much lower than that of $\text{NaPb}_{18}\text{BiTe}_{20}$.

Similar to the Sb analogs described above, the Sn-free composition exhibits the highest power factor over the range 300-600 K, Figure 4-10d. For Pb-Sn mixed compositions, $\text{NaPb}_{15}\text{Sn}_3\text{BiTe}_{20}$ exhibits the highest power factor in the range 300-475 K with a maximum of $11 \mu\text{W/cm}\cdot\text{K}^2$ at 510 K. There is a markedly different behavior between $\text{NaPb}_{18}\text{BiTe}_{20}$ and the other compositions. For $\text{NaPb}_{18}\text{BiTe}_{20}$, the power factor reaches a maximum of $\sim 22 \mu\text{W/cm}\cdot\text{K}^2$ at 470K and then decreases at higher temperatures whereas the power factors for the other compositions rise almost linearly with temperature (Figure 4-9d). The trend suggests that the maximum values lie well above 570 K. The Pb-free composition $\text{NaSn}_{18}\text{BiTe}_{20}$ exhibits higher power factor than the mixed Pb-Sn compositions reaching a value $\sim 16.8 \mu\text{W/cm}\cdot\text{K}^2$ at 618 K. The higher power factor in this material arises from the very high electrical conductivity.

In order to evaluate the influence of the pnictogen metal M on the electronic transport properties of $\text{NaPb}_{18-x}\text{Sn}_x\text{MTe}_{20}$, the properties of corresponding compositions need to be compared. Such comparison can be done by looking at Tables 4-3 and 4-4 where the electronic properties data for $\text{NaPb}_{18-x}\text{Sn}_x\text{SbTe}_{20}$ and $\text{NaPb}_{18-x}\text{Sn}_x\text{BiTe}_{20}$ are summarized. No particular trend could be observed with the nature of the pnictogen. At room temperature $\text{NaPb}_{18}\text{BiTe}_{20}$, $\text{NaPb}_{15}\text{Sn}_3\text{BiTe}_{20}$ and $\text{NaSn}_{18}\text{BiTe}_{20}$ had higher electrical conductivity than their Sb counterparts but the values converged at high temperature. The thermopowers were similar at room temperature but at high temperature the Bi analog exhibited a slightly higher value. For the $x=5$ stoichiometry, the Sb analog

exhibited higher electrical conductivity than the Bi counterpart but a lower thermopower. The electrical conductivity for $\text{NaPb}_9\text{Sn}_9\text{SbTe}_{20}$ and $\text{NaPb}_2\text{Sn}_{16}\text{SbTe}_{20}$ were higher than their Bi analogs over the temperature range 300-670 K.

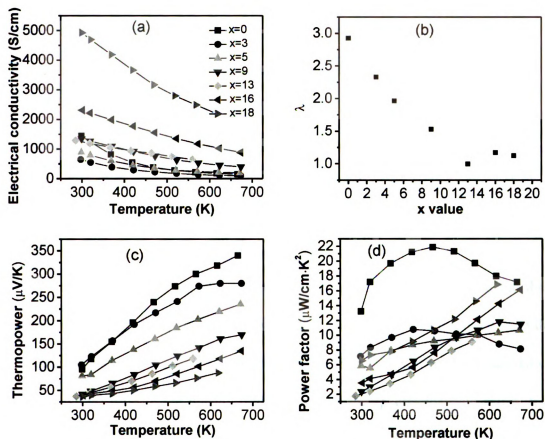


Figure 4-10. Electronic transport properties of the $\text{NaPb}_{18-x}\text{Sn}_x\text{BiTe}_{20}$ samples: (a) electrical conductivity, (b) variation of the power law dependence of the electrical conductivity ($T^{-\lambda}$) as a function of x (the λ parameters were extracted from the data of panel (a)), (c) thermopower, (d) power factor. The point marks in the inset of panel (a) identify all samples and apply to all panels (c) and (d).

Optical spectroscopy. Infrared specular reflectance spectroscopy was performed on polished single crystal surfaces for further characterization of the transport parameters of these heavily doped semiconductors. This technique allows a direct estimation of the carrier effective mass by analyzing the infrared reflectivity data within the context of single band Drude model. Figure 4-11 shows the room temperature specular reflectance spectra of the compounds $\text{NaPb}_{18-x}\text{Sn}_x\text{MTe}_{20}$ (M=Sb, Bi; x=3, 5, 9). The numerical analysis of the experimental data was done using a form of the dielectric function that takes into account the existence of a plasmon-LO phonon interaction. The average effective mass of carriers m^* was obtained from the relation:

$$\omega_p = \left(\frac{ne^2}{\epsilon_0 \epsilon_\infty m^*} \right)^{1/2} \quad \text{Eq (2)}$$

where ω_p , n and ϵ_∞ are the plasma frequency, carrier concentration and the dielectric permittivity at high frequency, respectively. The value of n was determined from the Hall effect experiments and ω_p , and ϵ_∞ were extracted from fitting the reflectance data. From the relative position of the plasma frequency ω_p in the spectra for each series, it can be concluded that the number of carriers increases with the amount of tin as expected. This is in agreement with the Hall effect experiments described above. The spectral analyses gave room temperature effective mass of ~ 0.295 and $0.224 m_0$ for $\text{NaPb}_{15}\text{Sn}_3\text{SbTe}_{20}$ and $\text{NaPb}_{13}\text{Sn}_5\text{SbTe}_{20}$. These results are in agreement with values reported for hole effective mass in $\text{Pb}_{1-x}\text{Sn}_x\text{Te}$ by Kushev and coworkers.²⁹

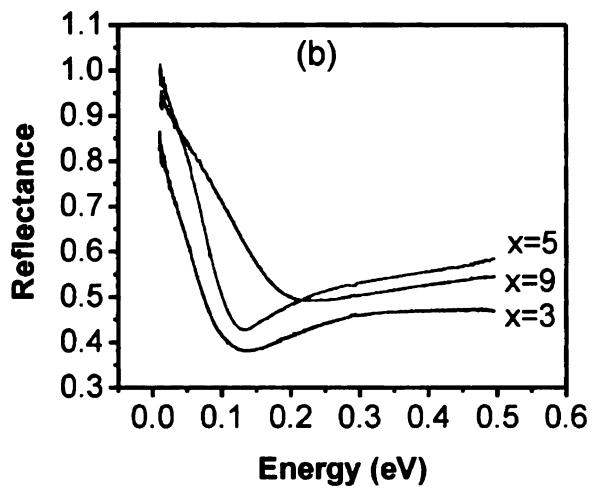
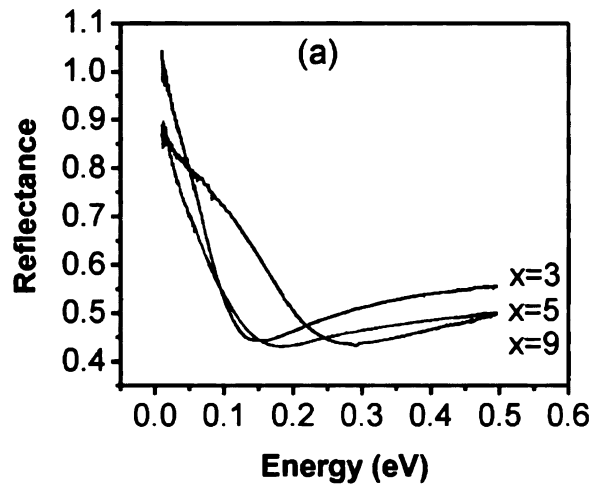


Figure 4-11. Specular reflectance spectra of (a) $\text{NaPb}_{18-x}\text{Sn}_x\text{SbTe}_{20}$ ($x=3, 5, 9$) and (b)

$\text{NaPb}_{18-x}\text{Sn}_x\text{BiTe}_{20}$ ($x=3, 5, 9$).

Table 4-3. Summary of the physical and electronic properties of the materials $\text{NaPb}_{18-x}\text{Sn}_x\text{SbTe}_{20}$

Composition	a (Å)	T_m (K)	E_g (eV)	σ (S/cm)			S ($\mu\text{V}/\text{K}$)	
				300 K	550K	300 K	550K	
$\text{NaPb}_{18}\text{SbTe}_{20}$	6.510 (1)	1188	0.37	1240	244	106	268	
$\text{NaPb}_{15}\text{Sn}_3\text{SbTe}_{20}$	6.441 (2)	1150	0.16	410	118	99	244	
$\text{NaPb}_{13}\text{Sn}_5\text{SbTe}_{20}$	6.422 (1)	1161	0.16	990	407	71	175	
$\text{NaPb}_9\text{Sn}_9\text{SbTe}_{20}$	6.395 (2)	1137	<0.1	1518	700	47	121	
$\text{NaPb}_5\text{Sn}_{13}\text{SbTe}_{20}$	6.371 (2)	1111	<0.1	1948	890	36	119	
$\text{NaPb}_2\text{Sn}_{16}\text{SbTe}_{20}$	6.378 (2)	1093	<0.1	3080	1717	34	87	
$\text{NaSn}_{18}\text{SbTe}_{20}$	6.325 (1)	1074	0.1-0.15	4379	2443	42	74	

With a= lattice constant, T_m = melting point, E_g = band gap, σ = electrical conductivity and S= thermopower.

Table 4-4. Summary of the physical and electronic properties of the materials $\text{NaPb}_{18-x}\text{Sn}_x\text{BiTe}_{20}$

Composition	a (Å)	T_m (K)	E_g (eV)	σ (S/cm)			S ($\mu\text{V}/\text{K}$)	
				300 K	550 K	300 K	550 K	
$\text{NaPb}_{18}\text{BiTe}_{20}$	6.483 (1)	1198	0.25	1447	306	95	300	
$\text{NaPb}_{15}\text{Sn}_3\text{BiTe}_{20}$	6.446 (2)	1175	<0.1	636	152	100	257	
$\text{NaPb}_{13}\text{Sn}_5\text{BiTe}_{20}$	6.436 (2)	1162	<0.1	885	258	81	195	
$\text{NaPb}_9\text{Sn}_9\text{BiTe}_{20}$	6.412 (2)	1137	<0.1	1351	576	41	134	
$\text{NaPb}_5\text{Sn}_{13}\text{BiTe}_{20}$	6.365 (2)	1112	<0.1	1288	648	40	118	
$\text{NaPb}_2\text{Sn}_{16}\text{BiTe}_{20}$	6.342 (2)	1093	<0.1	2314	1254	39	94	
$\text{NaSn}_{18}\text{BiTe}_{20}$	6.337 (1)	1084	0.19	4926	2487	37	76	

T

N

w

te

g

d

to

te

ti

ce

ha

T

ai

th

th

el

th

to

el

co

Thermal Transport Properties.

NaPb_{18-x}Sn_xSbTe₂₀. Thermal diffusivity measurements were carried on the *NaPb_{18-x}Sn_xSbTe₂₀* series to determine the thermal conductivity and respective trends with composition. The data could not be measured for *NaSn₁₈SbTe₂₀* as the samples tended to break during sample preparation. The resulting total thermal conductivities are given in Table 4-5 and Figure 4-12a. For all compositions, the total thermal conductivity decreases with increasing temperature. Compositions rich in Sn showed clearly higher total thermal conductivity along the temperature range 300-700 K. For example, the room temperature thermal conductivity for *NaPb₂Sn₁₆SbTe₂₀* is ~ 3.9 W/m·K, which is 2.7 times the value for *NaPb₁₅Sn₃SbTe₂₀* (1.37 W/m·K). The room temperature thermal conductivity of *NaPb_{18-x}Sn_xSbTe₂₀* (x=0, 3, 5), (1.85, 1.37 and 1.58 W/m·K respectively) have values close to what was reported for *Na_{0.95}Pb₂₀SbTe₂₂* (1.8 W/m·K) (Table 4-5). The lowest total thermal conductivity was ~ 0.84 W/m·K at 670 K for *NaPb₁₈SbTe₂₀*. For all compositions studied, the total thermal conductivities are systematically lower than those reported for *Pb_{1-x}Sn_xTe* samples.³⁰

In order to understand the influence of the Pb:Sn ratio on the thermal transport, the electronic and lattice components of the thermal conductivity were evaluated. The electronic contribution was estimated using the Wiedemann-Franz law and the lattice thermal conductivity was determined by subtracting the electronic component to the total thermal conductivity. It is clear that Sn-rich compositions have the highest electronic thermal contributions because of their high electrical conductivity. A comparison between the lattice components of the different compositions is shown on

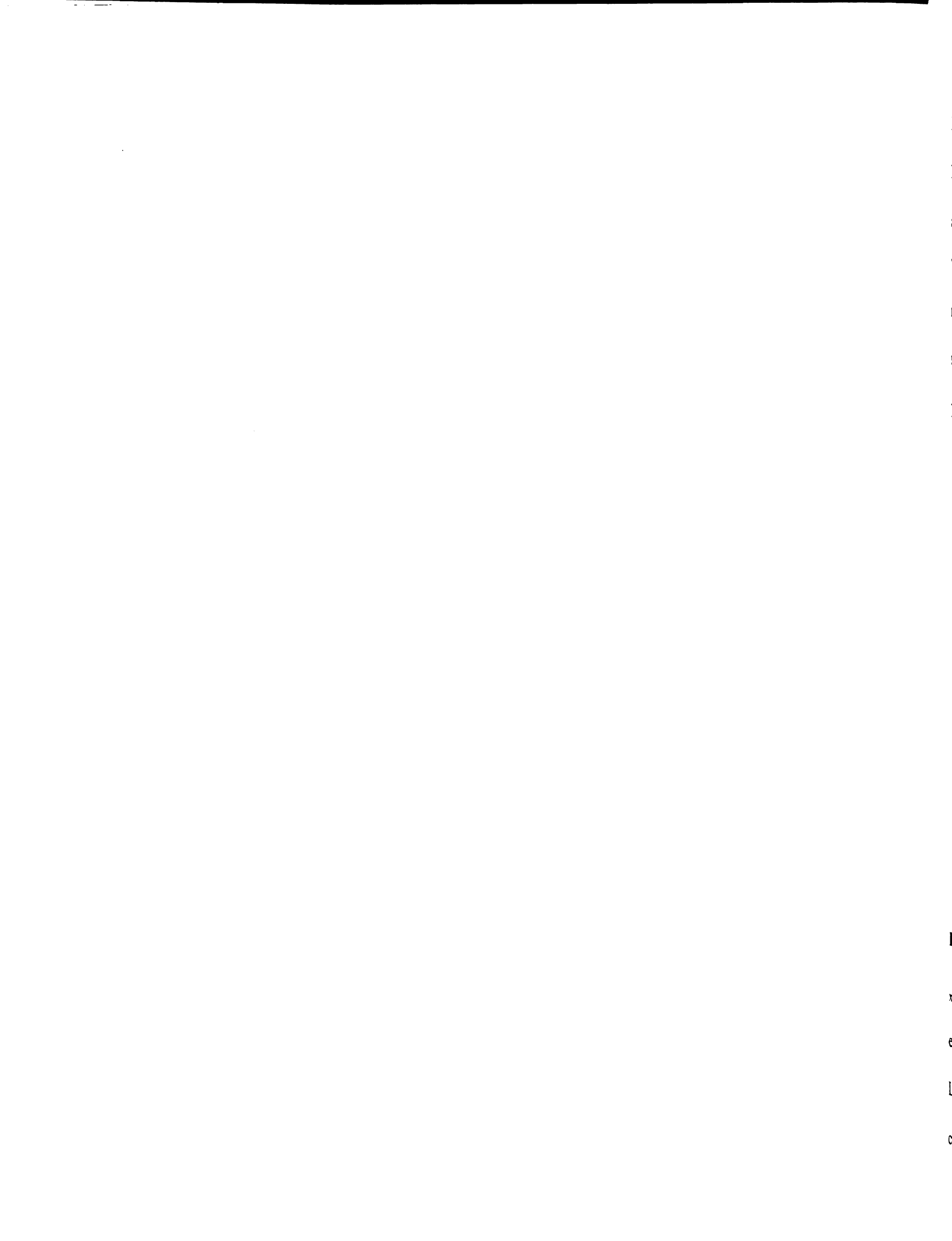


Figure 4-12b. Over the temperature range 300-570 K, the compositions $\text{NaPb}_2\text{Sn}_{16}\text{SbTe}_{20}$ and $\text{NaPb}_5\text{Sn}_{13}\text{SbTe}_{20}$ have a higher lattice thermal conductivity (1.6 and 1.4 W/m·K respectively at room temperature) than the compositions richer in Pb. These values however are still lower than the value reported for PbTe (2.2 W/m·K).³⁰ The reduction is a consequence of the contribution of solid solution alloying to the reduction in thermal conductivity. Above 500 K, the compositions $\text{NaPb}_{13}\text{Sn}_5\text{SbTe}_{20}$ and $\text{NaPb}_9\text{Sn}_9\text{SbTe}_{20}$ exhibit the lowest lattice component.

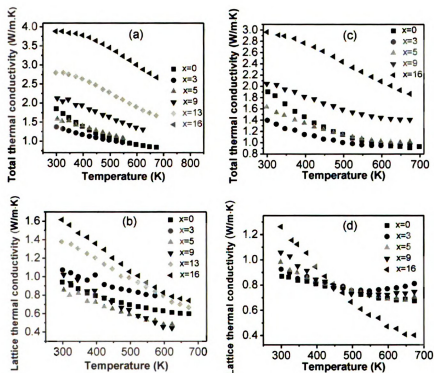


Figure 4-12. Temperature dependence of (a) the total thermal conductivity of the $\text{NaPb}_{18-x}\text{Sn}_x\text{SbTe}_{20}$ compositions and (b) their lattice thermal conductivity component (the electronic thermal conductivity was estimated using the Wiedemann-Franz law with $L_0=2.45 \cdot 10^{-8} \text{ W}\Omega\text{K}^{-1}$); (c) the total thermal conductivity of the $\text{NaPb}_{18-x}\text{Sn}_x\text{BiTe}_{20}$ compositions and (d) their lattice thermal conductivity component.

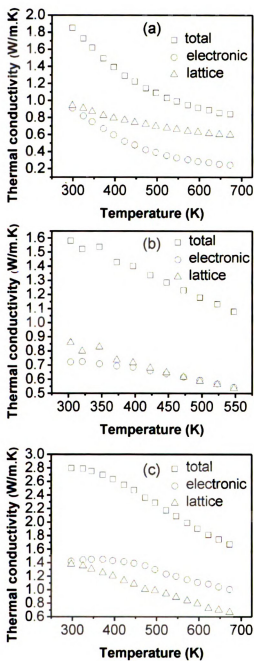


Figure 4-13. Temperature dependence of the thermal conductivity for the compositions (a) $\text{NaPb}_{18}\text{SbTe}_{20}$, (b) $\text{NaPb}_9\text{Sn}_9\text{SbTe}_{20}$ and (c) $\text{NaPb}_5\text{Sn}_{13}\text{SbTe}_{20}$.

The lattice thermal conductivity of $\text{NaPb}_{13}\text{Sn}_5\text{SbTe}_{20}$ at room temperature is estimated $\sim 0.86 \text{ W/m}\cdot\text{K}$, which is 40 % that of PbTe ($2.2 \text{ W/m}\cdot\text{K}$).³⁰ This value drops to $\sim 0.48 \text{ W/m}\cdot\text{K}$ at 625 K. For $\text{NaPb}_{13}\text{Sn}_5\text{SbTe}_{20}$ and more Pb-rich compositions, the values of the lattice thermal conductivity are quite low and comparable to those of $\text{Na}_{1-x}\text{Pb}_m\text{Sb}_y\text{Te}_{m+2}$ ¹⁷ and $\text{Ag}(\text{Pb}_{1-y}\text{Sn}_y)_m\text{SbTe}_{2+m}$.¹⁸ The relative contributions of electronic and lattice thermal components vary for different x values. For example, the lattice and electronic components are almost equivalent for $\text{NaPb}_{13}\text{Sn}_5\text{SbTe}_{20}$ (Figure 4-13b). For more Sn-rich compositions, the electronic contribution dominates (Figure 4-13a) whereas for more Pb-rich compositions, the lattice component dominates (Figure 4-13c).

NaPb_{18-x}Sn_xBiTe₂₀. Figure 4-12c shows the total thermal conductivity of $\text{NaPb}_{18-x}\text{Sn}_x\text{BiTe}_{20}$ ($x=0.3, 5, 9$ and 16). The compositions $x=13$ and 18 could not be measured due to the quality issue of the samples. The thermal conductivity decreases with temperature for all compositions and decreases with decreasing Sn:Pb ratio. The lowest thermal conductivity at 300 K was found for $\text{NaPb}_{15}\text{Sn}_3\text{BiTe}_{20}$ with value $\sim 1.4 \text{ W/m}\cdot\text{K}$. At high temperature, the compounds $x=0, 3$ and 5 have similar thermal conductivity $\sim 1 \text{ W/m}\cdot\text{K}$. This value is as almost low as that observed for $\text{NaPb}_{18-x}\text{Sn}_x\text{SbTe}_{20}$ above. The lattice thermal conductivity for the system $\text{NaPb}_{18-x}\text{Sn}_x\text{BiTe}_{20}$ was estimated using the same method as described above for the Sb analogs (Figure 4-12d). The materials $x=0, 3, 5$ and 9 have close lattice thermal conductivities with value $\sim 0.9\text{-}1.1 \text{ W/m}\cdot\text{K}$ at 300 K. At 675 K, the thermal conductivity falls down $\sim 0.7\text{-}0.8 \text{ W/m}\cdot\text{K}$. The decrease in thermal conductivity is sharper for $\text{NaPb}_2\text{Sn}_{16}\text{BiTe}_{20}$ with values ~ 1.3 and $0.4 \text{ W/m}\cdot\text{K}$ at 300 and 675K respectively.

When comparing the thermal conductivities of Bi and Sb analogs (Table 4-5 and 4-6), similar values were found for the $x=0, 3$ and 5 stoichiometries over the temperature range $300\text{-}600\text{ K}$. $\text{NaPb}_9\text{Sn}_9\text{SbTe}_{20}$ had lower thermal conductivity than its Bi counterpart. Only for the composition $\text{NaPb}_2\text{Sn}_{16}\text{MTe}_{20}$, the Bi analog exhibited lower thermal conductivity.

In Figure 4-13, the figures of merit of the $\text{NaPb}_{18-x}\text{Sn}_x\text{MTe}_{20}$ materials calculated from the above data are plotted. The Sn-free compositions $\text{NaPb}_{18}\text{MTe}_{20}$ exhibit the highest ZT over the temperature range $300\text{-}675\text{ K}$ with a ZT as high as ~ 1.2 at 675 K . ZT does not exceed 0.8 for the other Sb analogs ($\text{NaPb}_{13}\text{Sn}_5\text{SbTe}_{20}$) and 0.7 for the Bi analogs ($\text{NaPb}_{13}\text{Sn}_5\text{BiTe}_{20}$). Even though $\text{NaPb}_{13}\text{Sn}_5\text{MTe}_{20}$ materials have low thermal conductivities, its power factor is not as high as that of $\text{Na}_{1-x}\text{Pb}_m\text{Sb}_y\text{Te}_{m+2}$. This is attributed to the presence of tin in the composition, which results in lower thermopower values. The temperature dependence of ZT varies with Sn fraction. For Sn-rich compositions the slope around room temperature is less steep but it increases rapidly at higher temperature.

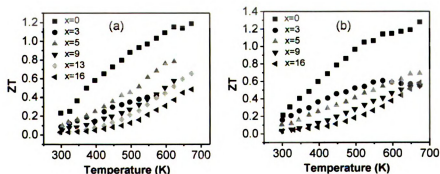


Figure 4-14. Temperature dependence of the figure of merit ZT for (a) $\text{NaPb}_{18-x}\text{Sn}_x\text{SbTe}_{20}$ ($x=0, 3, 5, 9, 13, 16$) and (b) $\text{NaPb}_{18-x}\text{Sn}_x\text{BiTe}_{20}$ ($x=0, 3, 5, 9$ and 16).

Table 4-5. Total and lattice thermal conductivities of $\text{NaPb}_{18-x}\text{Sn}_x\text{SbTe}_{20}$ ($x=0, 3, 5, 9, 13$ and 16) at 300 and 550 K.

Composition	κ_{total} (W/m·K) 300 K	κ_{total} (W/m·K) 550 K	κ_{latt} (W/m·K) 300 K	κ_{latt} (W/m·K) 550 K
$\text{NaPb}_{18}\text{SbTe}_{20}$	1.85	0.99	0.93	0.66
$\text{NaPb}_{15}\text{Sn}_3\text{SbTe}_{20}$	1.37	0.97	1.07	0.80
$\text{NaPb}_{13}\text{Sn}_5\text{SbTe}_{20}$	1.58	1.08	0.86	0.54
$\text{NaPb}_9\text{Sn}_9\text{SbTe}_{20}$	2.13	1.47	1.28	0.64
$\text{NaPb}_5\text{Sn}_{13}\text{SbTe}_{20}$	2.80	2.07	1.38	0.89
$\text{NaPb}_2\text{Sn}_{16}\text{SbTe}_{20}$	3.88	3.22	1.60	0.94

Table 4-6. Total and lattice thermal conductivities of $\text{NaPb}_{18-x}\text{Sn}_x\text{BiTe}_{20}$ ($x=0, 3, 5, 9$ and 16) at 300 and 550 K.

Composition	κ_{total} (W/m·K) 300 K	κ_{total} (W/m·K) 550 K	κ_{latt} (W/m·K) 300 K	κ_{latt} (W/m·K) 550 K
$\text{NaPb}_{18}\text{BiTe}_{20}$	1.91	1.04	0.86	0.72
$\text{NaPb}_{15}\text{Sn}_3\text{BiTe}_{20}$	1.40	0.97	0.92	0.75
$\text{NaPb}_{13}\text{Sn}_5\text{BiTe}_{20}$	1.63	1.06	0.98	0.72
$\text{NaPb}_9\text{Sn}_9\text{BiTe}_{20}$	1.57	1.15	1.05	0.72
$\text{NaPb}_2\text{Sn}_{16}\text{BiTe}_{20}$	2.97	2.25	1.25	0.55

High Resolution Transmission Electron Microscopy. Based on a wide variety of experimental results, a consensus is emerging that nanostructures are capable of causing large reductions in the lattice thermal conductivity of materials. Because of the very low lattice thermal conductivity observed for the compositions $\text{NaPb}_{18-x}\text{Sn}_x\text{SbTe}_{20}$ series, we have investigated the presence of any nanostructures in the bulk samples using HRTEM. Figures 4-15a and 4-15b show HRTEM images of a sample with composition $\text{NaPb}_{13}\text{Sn}_5\text{BiTe}_{20}$. Similar features were also observed for the Sb analog. Figures 4-15c and 4-15d show HRTEM images of a sample with composition $\text{NaPb}_{13}\text{Sn}_5\text{SbTe}_{20}$. Evenly dispersed nanoscale features $\sim 10\text{-}20$ nm in size can be observed in the images.

In order to learn about the composition and the lattice distortion of the inclusions and the strain distribution at the boundaries, the sample $\text{NaPb}_{13}\text{Sn}_5\text{BiTe}_{20}$ was studied using STEM, HRTEM and EDS. Figure 4-16a, a low magnification STEM image, clearly shows varied size dark inclusions, which means the inclusions are rich in light elements. (Figure 4-16b is a high magnification STEM image recorded along the $[110]$ direction still with inhomogeneous contrast due to the contribution of very small inclusions. We also confirmed the ordered composition by line scanning profile of a selected array of atoms (Figure 4-16c). The high intensity columns marked by blue arrows are Te atoms, those pointed by red arrows mainly come from Pb.

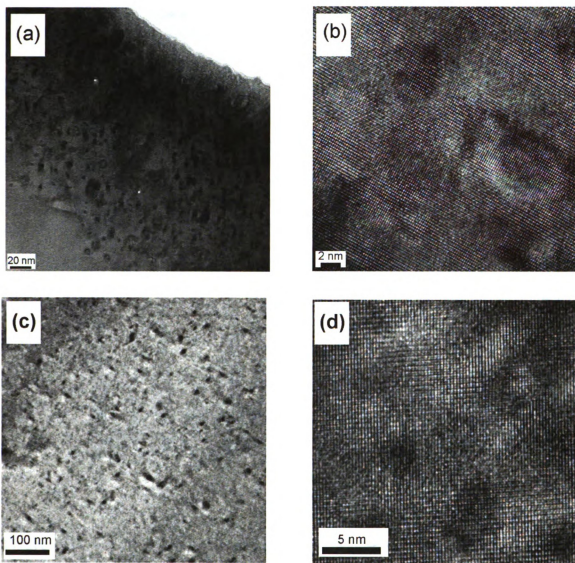


Figure 4-15. Typical HRTEM images of (a) and (b) $\text{NaPb}_{13}\text{Sn}_5\text{BiTe}_{20}$ and (c) and (d) $\text{NaPb}_{13}\text{Sn}_5\text{SbTe}_{20}$.

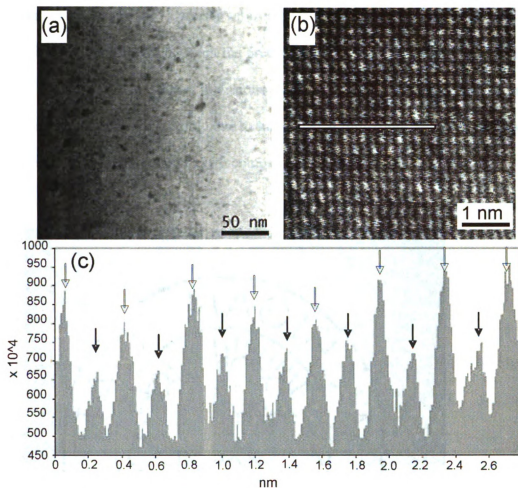


Figure 4-16. (a) A multitude of precipitates were observed in low magnification Z-contrast image for $\text{NaPb}_{13}\text{Sn}_5\text{BiTe}_{20}$; (b) high magnification STEM image showing the weak contrast of some small precipitates; (c) Line scanning profile of the selected atomic array in (b), the positions that the dark arrows point out are Te, and those marked by gray arrows mainly come from Pb.

Figure 4-17a present a particular HRTEM image of $\text{NaPb}_{13}\text{Sn}_5\text{BiTe}_{20}$ showing a large size inclusion within the matrix. The lattice parameter of the precipitate was found to be twice that of the matrix (Figure 4-17a-b). Fast Fourier Transform images of the two

selected regions in Figure 4-17a are shown in Figure 4-17c and 4-17d and confirmed the difference in lattice parameter between the precipitate and the matrix. The nature and the elemental compositions of these inclusions were analyzed by EDS. But accurate quantitative analysis was not possible due to instrumental limitation. The inclusions were found to be richer in Sn and poorer in Pb compared to the matrix.

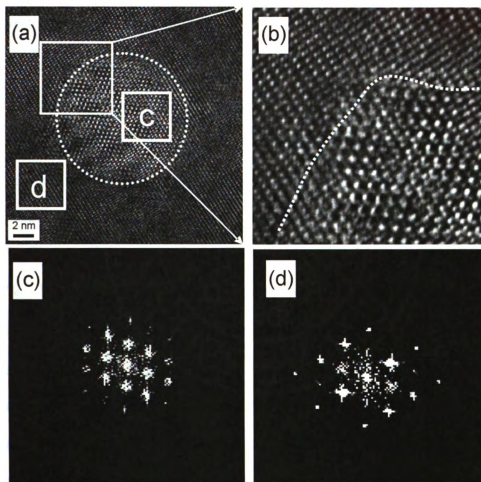


Figure 4-17. (a) High magnification high resolution TEM image for $\text{NaPb}_{13}\text{Sn}_5\text{BiTe}_{20}$ and (b) enlarged part show the lattice parameters of the precipitate and that of the matrix are different; (c) and (d) FFT images of the two regions C and D in (a).

Interestingly, aside from the discrete nanoprecipitates, nanoscale lamellar features also were observed for $\text{NaPb}_{13}\text{Sn}_5\text{BiTe}_{20}$. Figure 4-18a shows such lamellar stripes oriented in the [001] direction with their boundaries along the [110] direction. Strain field analysis^{31, 32} performed with a geometric phase analysis (GPA) program was used to investigate the variation in lattice parameter along these layers. Figure 4-18b shows the power spectrum of the image 15(a) with $\mathbf{g}_1=002$ and $\mathbf{g}_2= 220$ chosen as the Fourier vectors. The strain map profiles along the [001] direction (ϵ_{yy}) and the shear direction (ϵ_{xy}) are reported in Figures 4-18c, 4-18d, 4-18e and 4-18f. The line scan profiles indicate that the lattice parameter along the [001] direction of the lamella B differs from that of the lamella A by $\sim 6\%$. This means that the lamellae A and B have a different lattice constant. EDS analysis could not give any information about compositional fluctuation because of the thin thickness of the layers. This lamella features may unlikely be due to local segregation between PbTe and SnTe phases as they lattice constant differ only $\sim 2\%$. To our surprise, other lamellar features were observed for the sample $\text{NaPb}_{13}\text{Sn}_5\text{BiTe}_{20}$ (Figure 4-19). Saw shape features were observed at the edge of the sample. These stripes are oriented along the [112] direction, which is a different orientation than that described above. This may be the result of local ordering between PbTe and SnTe phases. The Sn-Te bond is stronger than the Pb-Te bond (bond enthalpies ~ 369 and 251 kJ/mol respectively). Hence during the sample milling, the SnTe layer may be more easily destroyed than the PbTe layer. The presence of both disperse precipitates and lamellar features with nanometer size results in an increase in interfaces, which will enhance phonon scattering and result in a reduction of the lattice thermal conductivity.

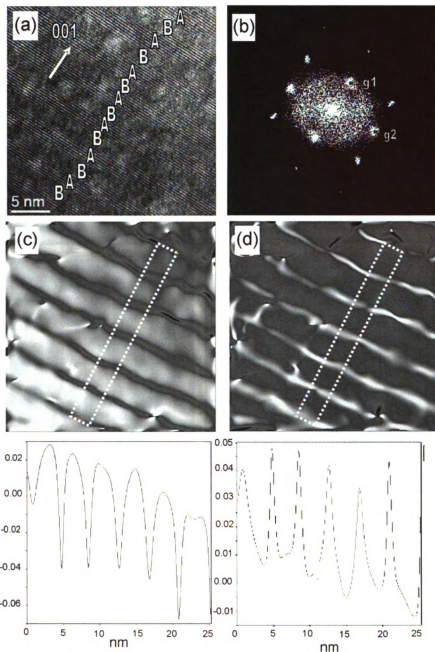


Figure 4-18. (a) Different precipitate from $\text{NaPb}_{13}\text{Sn}_5\text{BiTe}_{20}$ with different contrast lamella structure labeled as ABAB... (b-f) are strain mapping for this precipitate; (b) power spectrum image in (a) with $\mathbf{g}_1=002$ and $\mathbf{g}_2=220$. (c) and (d) 4.2.1. show the strain map profile along the 001 direction (ϵ_{yy}) and the shear direction(ϵ_{xy}), respectively.

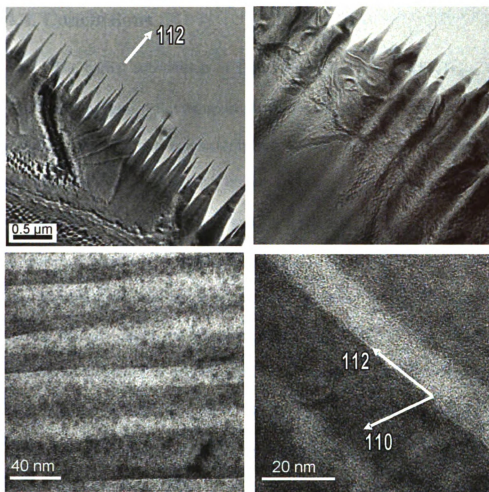


Figure 4-19. (a)-(d) Different magnification images for $\text{NaPb}_{13}\text{Sn}_5\text{BiTe}_{20}$ with another type of lamellar structure. (a) only shows the saw shape at the edge of sample; (b) further ion milling for sample, the lamella profile appear in the region close to edge, (c) strong contrast was observed in the area far from the edge; (d) From the high resolution image, the lamella was indexed as 112 direction, which is different from the first type lamella in Figure 4-16.

4.4. Conclusions

The partial substitution of Pb by Sn in the $\text{Na}_{1-x}\text{Pb}_m\text{Sb}_y\text{Te}_{m+2}$ system causes significant changes in the transport properties of these materials. High fractions of Sn result in higher electrical conductivity and lower thermopower. This increase in electrical conductivity is mainly caused by an increase in the carrier concentration. As a consequence the mobility of these carriers is relatively low ($\leq 54 \text{ cm}^2/\text{V}\cdot\text{s}$). The increase in electrical conductivity does not compensate for the decrease in thermopower, thus resulting in lower power factor compared to the parent system. The addition of Sn in the system has an impact on the thermal properties. Sn-rich compositions have higher electrical conductivities resulting in high electronic thermal conductivities. From all compositions, $\text{NaPb}_{18}\text{MTe}_{20}$, $\text{NaPb}_{13}\text{Sn}_5\text{SbTe}_{20}$ and $\text{NaPb}_9\text{Sn}_9\text{SbTe}_{20}$ exhibit the lowest lattice thermal conductivity values over the temperature range 300-650 K because of the effect of solid solution alloying combined with the presence of nanostructuring. TEM analysis on $\text{NaPb}_{13}\text{Sn}_5\text{BiTe}_{20}$ revealed the existence of different types of nanostructuring in the sample. In addition to disperse inclusions, lamella features with thickness $\sim 10 \text{ nm}$ were observed. Further reduction in the lattice thermal conductivity is achieved through the combination of these nano-size features. The highest $ZT \sim 1.2$ were obtained for the Sn-free $\text{NaPb}_{18}\text{MTe}_{20}$. Doping studies on the $\text{NaPb}_{13}\text{Sn}_5\text{SbTe}_{20}$ showed an increase in thermopower with decreasing Na:Sb ratio. Further experiments on Na-deficient compositions are in progress. The trivalent element i.e. Sb vs. Bi seems to affect the mechanical properties of the materials with Sb analogs being less brittle. No clear trend about the effect of the pnictogen on the electrical properties could be observed. Lattice

thermal conductivities are similar at room temperature but at high temperature lower values are achieved for Sb analogs.

References

1. Di Salvo, F. J., *Science* **1999**, 285, 703.
2. Tritt, T. M.; Subramanian, M. A., *MRS Bulletin* **2006**, 31, 188.
3. Snyder, G. J.; Toberer, E. S., *Nat. Mater.* **2008**, 7, 105.
4. Harman, T. C.; Taylor, P. J.; Walsh, M. P.; LaForge, B. E., *Science* **2002**, 297, 2229.
5. Harman, T. C.; Taylor, P. J.; Walsh, M. P.; LaForge, B. E., *J. Electron. Mater.* **2005**, 34, L19.
6. Venkatasubramanian, R.; Siivola, E.; Colpitts, T.; O'Quinn, B., *Nature* **2001**, 413, 597.
7. Caylor, J. C.; Coonley, K.; Stuart, J.; Colpitts, T.; Venkatasubramanian, R., *Appl. Phys. Lett.* **2005**, 87, (2), 023105.
8. Hicks, L. D.; Dresselhaus, G., *Phys. Rev. B* **1993**, 47, 16631.
9. Hicks, L. D.; Dresselhaus, M. S., *Phys. Rev. B* **1993**, 47, (19), 12727.
10. Kim, W.; Singer, K. L.; Majumdar, A.; Vashaee, D.; Bian, Z.; Shakouri, A.; G., Z.; Bowers, E. J.; Zide, J. M. O.; Gossard, C., *Appl. Phys. Lett.* **2006**, 88, 242107.
11. Hochbaum, A. I.; Chen, R.; Delgado, R. D.; Liang, W.; Garnett, E. C.; Najarian, M.; Majumdar, A.; Yang, P., *Nature* **2008**, 451, 163.
12. Boukai, A. I.; Bunimovich, Y.; Tahir-Kheli, J.; Yu, J.-K.; Goddard, W. A.; Heath, J. R., *Nature* **2008**, 451, 168.
13. Hsu, K. F.; Loo, S.; Guo, F.; Chen, W.; Dyck, J. S.; Uher, C.; Hogan, T.; Polychroniadis, E. K.; Kanatzidis, M. G., *Science* **2004**, 303, 818.

14. Quarez, E.; Hsu, K. F.; Pcioneck, R.; Frangis, N.; Polychroniadis, E. K.; Kanatzidis, M. G., *J. Am. Chem. Soc.* **2005**, 127, 9177.
15. Androulakis, J.; Lin, C. H.; Kong, H. J.; Uher, C.; Wu, C. I.; T., H.; Cook, B. A.; T., C.; Paraskevopoulos, M.; Kanatzidis, M. G., *J. Am. Chem. Soc.* **2007**, 129, 9780.
16. Poudeu, P. F. P.; D'Angelo, J.; Kong, H. J.; Short, J. L.; Pcioneck, R.; Hogan, T.; Uher, C.; Kanatzidis, M. G., *J. Am. Chem. Soc.* **2006**, 128, 14347.
17. Poudeu, P. F. P.; D'Angelo, J.; Downey, A. D.; Short, J. L.; Hogan, T.; Kanatzidis, M. G., *Angew. Chem., Int. Ed.* **2006**, 45, 3835.
18. Androulakis, J.; Hsu, K. F.; Pcioneck, R.; Kong, H. J.; Uher, C.; D'Angelo, J.; Downey, A. D.; Hogan, T.; Kanatzidis, M. G., *Adv. Mater.* **2006**, 18, 1170.
19. Han, M.; Hoang, K.; Kong, H. J.; Pcioneck, R.; Uher, C.; Paraskevopoulos, M.; Mahanti, S. D.; Kanatzidis, M. G., *Chem. Mater.* **2008**, 20, 3512.
20. Wendlandt, W.; Hecht, H. G., *Reflectance Spectroscopy*. New York, 1966.
21. Kotuem, G., *Reflectance Spectroscopy*. New York, 1969.
22. Tandon, S. P.; Gupta, J. P., *Status Solidi* **1970**, 38, 363.
23. Kittel, C., *Introduction to Solid State Physics*. Wiley: 2005.
24. Bouad, N.; Chapon, L.; Marin-Ayral, R. M.; Bouree-Vigneron, F.; Tadenac, J. C., *J. Solid State Chem.* **2003**, 173, 189.
25. Rogacheva, E. I.; Gorne, G. V.; Laptev, S. A.; Arinkin, A. V.; Vesiene, T. B., *J. Solid State Chem.* **1982**, 43, 364.
26. Orihashi, M.; Noda, Y.; Chen, L.; Hirai, T., *Mater. Trans., JIM* **2000**, 41, 1196.
27. Henger, G.; Peretti, E. A., *Journal of the Less-Common Metals* **1965**, 8, 124.

28. Ravich, Y. I.; Efimova, B. A.; Smirnov, I. A., *Semiconducting Lead Chalcogenides*. New York, London, 1970.
29. Kushev, D. B., *Phys. Stat. Sol. (b)* **1980**, 100, 731.
30. Orihashi, M.; Noda, Y.; Chen, L. D.; Goto, T.; Hirai, T., *J. Phys. Chem. Solids* **2000**, 61, 919.
31. Williams, D. B.; Carter, C. B., *Transmission Electron Microscopy*. Springer: 1996.
32. Hytch, M. J.; Snoeck, E.; Kilaas, R., *Ultramicroscopy* **1998**, 74, 131.

Chapter 5

Synthesis and Characterization of the $\text{KPb}_{18-x}\text{Sn}_x\text{SbTe}_{20}$

($x=0, 2, 5, 9, 13, 16$ and 18) series

5.1. Introduction

Development of efficient thermoelectric devices could have a significant impact on our daily lives: Cooling devices may help in faster computing processes whereas devices that generate power could reuse waste heat from a vehicle's exhaust pipe to supply additional energy to the engine. For such devices to be economically viable, materials with enhanced figure of merit need to be developed. The figure of merit ZT is defined as $ZT = \sigma S^2 T / \kappa$ with σ , S and κ being respectively the electrical conductivity, the thermopower and the thermal conductivity of the compound. The thermal conductivity has two components: electronic and thermal contributions. Current devices use materials with maximum $ZT \sim 1$ at their operating temperature.¹ Competitive devices should have $ZT \sim 3-4$.² Over the last decade, significant improvement of the figure of merit has been reported for low dimensional materials³⁻⁵ and mixed-phase nanocomposites.⁶⁻⁹ Theoretical studies first predicted enhancement of the power factor in quantum confined system.^{8, 10} The nano-components also play an important role in scattering mid-to-long wavelength phonons, thus reducing the lattice thermal conductivity.

The proof-of-principle of these concepts was confirmed experimentally. In uniform $\text{Bi}_2\text{Te}_3/\text{Bi}_2\text{Te}_{2.83}\text{Se}_{0.17}$ superlattices of ~ 6 nm period, Venkatasubramanian et al.

were able to reduce the lattice thermal conductivity at room temperature in the cross-plane direction to ~ 0.58 W/m·K compared to ~ 1.7 for bulk Bi_2Te_3 .⁵ Harman et al. prepared superlattices made of PbSe quantum dots sandwiched between layers of PbTe over thousands of arrays.^{3, 4, 11} Using Bi as a n-type dopant, $ZT \sim 1.6$ and 3.5 were reported for these quantum dot superlattices at 300 and 570 K respectively. Our group has reported on the n-type system $\text{AgPb}_m\text{SbTe}_{m+2}$ (so-called LAST system)¹² with $ZT \sim 1.8$ at 725 K for $\text{AgPb}_{18}\text{SbTe}_{20}$. The reason for such good thermoelectric properties of these materials comes from their extremely low thermal conductivity (~ 1 W/m·K at 780 K). Careful TEM analysis revealed the material not to be a true solid solution but to contain nano-size inclusions dispersed in the PbTe matrix.^{12, 13} The presence of such inclusions is believed to scatter phonons more efficiently than electrons, thus a significant reduction in lattice thermal conductivity without much impact on the electronic properties. This system is a good illustration of the concept of bulk nanostructured materials, which is more viable for high scale production than low dimensional systems.

We have extended that research area by preparing alkali metal analogs of the LAST system. It has been reported that the combination of alkali metal with Sb tends to form stable clusters of the type A_nSb_4 ($\text{A}=\text{Na}, \text{K}$).¹⁴ As a consequence, alkali metal based, Sb-doped PbTe systems have higher potential to form nanostructures when compared to the Ag-based analog system. Moreover, the formation of such clusters is favored by the low solubility of Sb in PbTe.¹⁵ The $\text{Na}_{1-x}\text{Pb}_m\text{Sb}_y\text{Te}_{m+2}$ system (so-called SALT)¹⁶ exhibits promising p-type thermoelectric properties with ZT value as high as

1.7 at 650 K for the composition $\text{Na}_{0.95}\text{Pb}_{20}\text{SbTe}_{22}$. Such a high figure of merit derives mainly from its low total thermal conductivity ($\sim 0.85 \text{ W/m}\cdot\text{K}$ at 675 K). Nano-size inclusions embedded in the PbTe matrix were observed by TEM but no compositional analysis could be performed due to instrumental limitation.

Surprisingly, the potassium analogs $\text{K}_{1-x}\text{Pb}_{m+\delta}\text{Sb}_{1+\gamma}\text{Te}_{m+2}$ ($1-x = 0.85, 0.9, 0.95$; $m = 19, 20, 21$; $\delta = 0, 0.2, \gamma = 0, 0.2$)¹⁷ are n-type materials with electrons as major charge carriers. The thermopower has values as high as $\sim -250 \mu\text{V/K}$ at 700 K for all compositions. This result agrees with *ab initio* calculations. Calculations within density functional theory (DFT) of PbTe with and without monovalent impurities showed an increase in the density of states (DOS) near the top of the valence band for Ag and K dopant whereas Na does not change the DOS within 0.5 eV of the band maxima.¹⁸ A maximum ZT of 1.6 was achieved at 750 K for the n-type composition $\text{K}_{0.95}\text{Pb}_{20}\text{Sb}_{1.2}\text{Te}_{22}$. As for the LAST and SALT systems, the specimens exhibited low lattice thermal conductivity. The room temperature value for samples with $m = 19$ range from $1 \text{ W/m}\cdot\text{K}$ for the composition $\text{K}_{0.8}\text{Pb}_{19}\text{Sb}_{1.2}\text{Te}_{21}$ to $0.6 \text{ W/m}\cdot\text{K}$ for the sample $\text{K}_{0.8}\text{Pb}_{19.2}\text{Sb}_{1.2}\text{Te}_{21}$. These values are two to four times lower than the typical lattice thermal conductivity of undoped PbTe ($2.2 \text{ W/m}\cdot\text{K}$).¹⁹ At 550 K the values are between 0.4 and $0.7 \text{ W/m}\cdot\text{K}$. Similar values of the lattice thermal conductivity were obtained for samples with $m = 20$ and 21 . TEM studies again confirmed the presence of nanocrystals randomly oriented in the matrix. The presence of such nano inclusions in PbTe is a key feature to improve the figure of merit of PbTe.

Partial substitution of Pb by Sn into the LAST system appeared to change significantly the transport properties of the system. $ZT \sim 1.45$ at 627 K was reported for the p-type composition $Ag_{0.5}Pb_6Sn_2Sb_{0.2}Te_{10}$.²⁰ In order to evaluate the impact of partial substitution of Pb by Sn on the properties of $K_{1-x}Pb_{m+\delta}Sb_{1+\gamma}Te_{m+2}$, the compositions $KPb_{18-x}Sn_xMTe_{20}$ ($x=0, 2, 5, 9, 13, 16$ and 18 , Bi) were prepared. In order to study the effect of the pnictogen, Bi analogs were synthesized as well. The homogeneity of the cast ingots were investigated with powder X-ray diffraction, DTA and SEM. Thermoelectric measurements on Sb and Bi analogs over the temperature range 300-600 K indicated a switch from n-to-p type for different Pb/Sn ratios. In the case of Sb-doped materials, all compositions with $x \geq 5$ were p-type. For Bi analogs, the change in charge carrier type appeared for the composition $KPb_9Sn_9SbTe_{20}$.

5.2. Experimental

5.2.1. Synthesis

All samples were prepared by mixing appropriate ratios of high purity elemental starting materials in silica tubes. Before loading, the tubes were carbon-coated to avoid any reaction of the potassium metal with the silica. All components (except K) were loaded into the silica tubes under ambient atmosphere and the corresponding amount of K was later added under inert atmosphere in a dry glove box. The tubes were then sealed under residual vacuum of $\sim 10^{-4}$ Torr and heated at 980 °C for 4 hours in a furnace mounted on a rocking table. During that period, the furnace was allowed to rock for two hours in order to get a homogeneous melt. After, the furnace was maintained in vertical

position for crystal growth. The tubes were slow cooled to 550 °C (10 °C per hour) and then cooled rapidly to room temperature. The resulting ingots were silvery-metallic in color with a smooth dark surface. The samples were found quite brittle. During polishing, leaching issues were observed when the samples were in contact with water. After drying with acetone, the samples were stable.

In order to improve the mechanical strength of the ingots, the Sb-analogs were prepared with a slower cooling rate (5 °C per hour) but the samples were even more brittle.

Table 5-1 and 5-2 summarize the amount of elements used for each reaction.

Table 5-1. Amounts of elements used to prepare $\text{KPb}_{18-x}\text{Sn}_x\text{SbTe}_{20}$.

Composition	K, g (mmol)	Pb, g (mmol)	Sn, g (mmol)	Sb, g (mmol)	Te, g (mmol)
$\text{KPb}_{18}\text{SbTe}_{20}$	0.085 g (2.17)	8.1082 g (39.13)	0	0.2647 g (2.17)	4.9818 g (43.48)
$\text{KPb}_{16}\text{Sn}_2\text{SbTe}_{20}$	0.085 g (2.17)	7.2073 g (34.78)	0.5162 g (4.35)	0.2647 g (2.17)	5.5481 g (43.48)
$\text{KPb}_{13}\text{Sn}_5\text{SbTe}_{20}$	0.100 g (2.56)	6.8893 g (33.25)	1.5181 g (12.79)	0.3114 g (2.56)	6.5271 g (51.15)
$\text{KPb}_9\text{Sn}_9\text{SbTe}_{20}$	0.110 g (2.81)	5.2465 g (25.32)	3.0058 g (25.32)	0.1951 g (1.60)	4.4971 g (35.24)
$\text{KPb}_5\text{Sn}_{13}\text{SbTe}_{20}$	0.110 g (2.81)	2.9147 g (14.07)	4.3418 g (36.57)	0.3426 g (2.81)	7.1799 g (56.27)
$\text{KPb}_2\text{Sn}_{16}\text{SbTe}_{20}$	0.115 g (2.94)	1.2189 g (5.88)	5.5866 g (47.06)	0.3581 g (2.94)	7.5062 g (58.83)
$\text{KSn}_{18}\text{SbTe}_{20}$	0.120 g (3.07)	0	6.5582 g (55.25)	0.3737 g (3.07)	7.8326 g (61.38)

Table 5-2. Amounts of elements used to prepare $\text{KPb}_{18-x}\text{Sn}_x\text{BiTe}_{20}$.

Composition	K, g (mmol)	Pb, g (mmol)	Sn, g (mmol)	Sb, g (mmol)	Te, g (mmol)
$\text{KPb}_{18}\text{BiTe}_{20}$	0.085 g (2.17)	8.1082 g (39.13)	0	0.4543 g (2.17)	5.5481 g (43.48)
$\text{KPb}_{16}\text{Sn}_2\text{BiTe}_{20}$	0.068 g (1.73)	5.7316 g (27.81)	0.4105 g (3.46)	0.3613 g (1.73)	4.4121 g (34.58)
$\text{KPb}_{13}\text{Sn}_5\text{BiTe}_{20}$	0.095 g (2.43)	6.5448 g (31.59)	1.4422 g (1.21)	0.5078 g (2.43)	6.2008 g (48.60)
$\text{KPb}_9\text{Sn}_9\text{BiTe}_{20}$	0.100 g (2.56)	4.7695 g (23.02)	2.7326 g (23.02)	0.5345 g (2.56)	6.5271 g (51.15)
$\text{KPb}_5\text{Sn}_{13}\text{BiTe}_{20}$	0.100 g (2.56)	2.6497 g (12.79)	3.9471 g (33.25)	0.5345 g (2.56)	6.5271 g (51.15)
$\text{KPb}_2\text{Sn}_5\text{BiTe}_{20}$	0.084 g (2.15)	0.8903 g (4.30)	4.0804 g (34.37)	0.4490 g (2.15)	5.4825 g (42.95)
$\text{KSn}_{18}\text{BiTe}_{20}$	0.100 g (2.56)	0	5.4652 g (46.04)	0.5345 g (2.56)	6.5271 g (51.15)

5.2.2. Characterization techniques

Powder X-ray Diffraction. Powder X-ray patterns of the grinded materials were recorded using Cu K_α radiation on a CPS-120 Inel X-ray powder diffractometer operating at 40 kV and 20 mA equipped with a position sensitive detector.

DTA Analysis. Differential thermal analysis (DTA) data were collected with a Shimadzu DTA-50 thermal analyzer. Approximately 35 mg of finely ground powder of material was sealed in a carbon-coated quartz ampoule under residual pressure of $\sim 10^{-4}$ torr. Another ampoule containing similar amount of alumina and prepared the same way was used as a reference. The samples were heated to 1273 K at a rate of 10 K/min, held at 1273 K for two minutes and cooled down to 323 K at a rate of -10 K/min.

Scanning Electron Microscopy. The surface of several samples was polished very carefully using silica suspension solution (0.05 μm) in order to get a smooth, mirror-like surface. The samples were then studied with a scanning electron microscopy (Hitachi

S3400N-II) with 25 kV acceleration voltage using both energy-dispersive spectroscopy (EDS) and back-scattered electron imaging (BSE).

Electrical Transport Properties. Thermopower and electrical conductivity properties were measured simultaneously under helium atmosphere using a ZEM-3 Seebeck coefficient/electrical resistivity measurement system (ULVAC-RIKO, Japan). Samples for transport measurement were cut to size $10 \times 3 \times 3 \text{ mm}^3$ using a diamond saw (Buehler isomet 1000), a wire saw (South Bay Technology) and a polishing machine (Buehler ecomet 3000). Rectangular shape samples with approximately $3 \times 3 \text{ mm}^2$ cross-section were sandwiched vertically by two nickel electrodes (current injection) with two Pt/PtRh thermocouples (for temperature difference and voltage measurements) attached on one side. The sample and measurement probes were covered by a nickel can to maintain a constant temperature during the measurement and the base temperature was measured by a thermocouple attached to the outside of the can. The sample, electrodes, and nickel can were placed in a vacuum chamber then evacuated and refilled with He gas (0.1 atm) to provide necessary heat transfer. Properties were measured from room temperature to 670 K under helium atmosphere.

Thermal Conductivity. The thermal conductivity was determined as a function of temperature using the flash diffusivity method on a LFA 457/2/G Microflash Netzsch. The front face of a small disc-shaped sample (diameter $\sim 8 \text{ mm}$; thickness $\sim 2 \text{ mm}$) coated with a thin layer of graphite is irradiated with a short laser burst, and the resulting rear face temperature rise is recorded and analyzed. The experiments were carried out under nitrogen atmosphere. Thermal conductivity values were calculated using the equation $\kappa = \alpha C_p d$, where α is the thermal diffusivity, C_p the specific heat and d the bulk density of

the material calculated from the sample's geometry and mass. A pyroceram reference was used to determine the heat capacity of the sample. The thermal diffusivities were measured typically over the temperature range 300-670 K. The electronic component of the thermal conductivity was quantified through the Wiedemann-Franz law according to which $\kappa_{el} = \sigma.T.L_o$ (L_o being the Lorenz number, $L_o=2.45.10^{-8} \text{ W}\Omega\text{K}^{-1}$).²¹ The lattice contribution was then derived by subtracting the electronic component from the total thermal conductivity.

5.3. Results and discussion

Structural Characterization. Figure 5-1 shows the X-ray powder diffraction for the compositions $\text{KPb}_{18-x}\text{Sn}_x\text{MTe}_{20}$ ($x=0, 2, 5, 9, 13, 16$ and 18 , $\text{M}=\text{Sb, Bi}$). These patterns can be indexed as NaCl-type structure. No additional peaks were observed. The Bragg peaks shift towards higher diffraction angle with increasing Sn/Pb ratio, consistent with a decreasing lattice constant. The variation of the lattice constant as a function of x is plotted in Figure 6-1b and 6-1d. This trend is expected as the radius of Pb^{2+} is larger than that of Sn^{2+} . For example, the lattice constant varies from 6.448 (1) \AA for $\text{KPb}_{16}\text{Sn}_2\text{SbTe}_{20}$, which is closer to PbTe (6.459 \AA)²² to 6.340 (2) \AA for $\text{KPb}_2\text{Sn}_{16}\text{BiTe}_{20}$, which is closer to SnTe (6.328 \AA)²³.

Figure 5-2a shows DTA data for $\text{KPb}_{18}\text{SbTe}_{20}$. The plot shows only one endothermic peak of melting during the heating cycle and one exothermic peak of crystallization on the cooling cycle. Similar curves were obtained for the other compositions $\text{KPb}_{18-x}\text{Sn}_x\text{SbTe}_{20}$ and their Bi analogs. Melting and crystallization points

for the $\text{KPb}_{18-x}\text{Sn}_x\text{MTe}_{20}$ series are summarized in Tables 5-3 and 5-4. The melting point decreases with increasing Sn fraction. It varies from 1175 K for $\text{KPb}_{16}\text{Sn}_3\text{SbTe}_{20}$ to 1071 K for $\text{KPb}_2\text{Sn}_{16}\text{SbTe}_{20}$ (Figure 5-2b). This trend is consistent with the expected solid solution alloying between the high melting PbTe (1196 K) and the lower melting SnTe (1063 K) compounds.

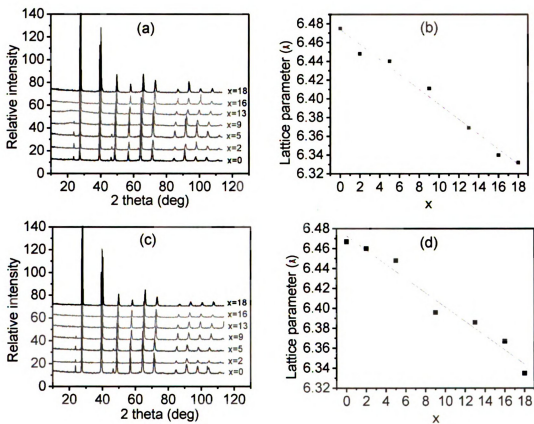


Figure 5-1. X-ray powder diffraction patterns of $\text{KPb}_{18-x}\text{Sn}_x\text{MTe}_{20}$ with $x=0, 2, 5, 9, 13, 16$ and 18 for (a) $\text{M}=\text{Sb}$ and (c) $\text{M}=\text{Bi}$; variation of the unit cell parameter as a function of x for (b) $\text{M}=\text{Sb}$ and (d) $\text{M}=\text{Bi}$.

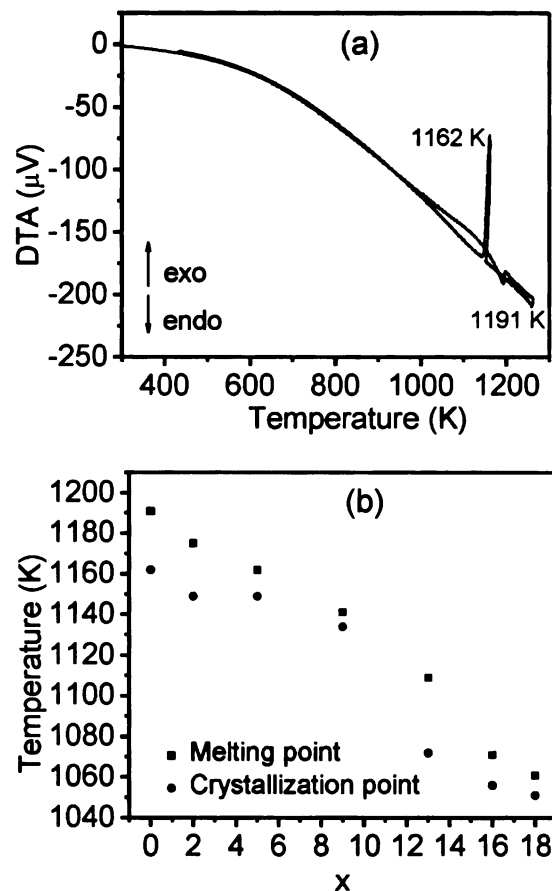


Figure 5-2. Typical DTA results of the composition $\text{KPb}_{18}\text{SbTe}_{20}$, (b) variation of the melting and crystallization points of $\text{KPb}_{18-x}\text{Sn}_x\text{SbTe}_{20}$ as a function of x .

Scanning Electron Microscopy. The surface of several samples was polished very carefully and analyzed using both secondary and back-scattered electron microscopies. In the case of Sb analogs, inclusions of $\sim 60\text{-}70\ \mu\text{m}$ diameter, randomly dispersed inside the matrix, were observed. In average, these inclusions are $\sim 500\ \mu\text{m}$ far away from each other. Figure 5-3a ($\text{KPb}_{13}\text{Sn}_5\text{SbTe}_{20}$) and 5-3b ($\text{KPb}_9\text{Sn}_9\text{SbTe}_{20}$) show typical images of such inclusions. It must be noticed that these inclusions are widely dispersed in the matrix. EDS analysis of a large area of the inclusion in Figure 5-3a gave the resulting atomic

percentages: Pb: 2.73, K: 4.59, Sb: 27.59, Te: 65.09. A peak for oxygen was also observed. Probably a phase containing K formed upon cooling and tends to oxidize as it is water-sensitive. EDS analysis on the matrix indicated the presence of Sn, Pb and Te in ratio consistent with the nominal composition. EDS analysis on the inclusion observed for $\text{KPb}_9\text{Sn}_9\text{SbTe}_{20}$ gave a higher amount of K: Pb: 2.32, K: 14.87, Sb: 23.38, Te: 59.43. Few areas rich in Sb were observed. Figure 5-4a for example shows an inclusion of Sb in $\text{KPb}_5\text{Sn}_{13}\text{SbTe}_{20}$. Figure 5-4b shows a different inclusion observed in the same sample. Different phases are visible: EDS analysis on area 1 indicated the phase to be Sb_2Te_3 (Sb: 37.95 at %, Te: 62.05 at. %). EDS analysis on the area 2 gave the results Pb: 6.32, K: 3.80, Sb: 13.51, Te 76.37 (at. %).

Similar analysis was carried on Bi analogs. Figures 5-5a and 5-5b show different inclusions observed for $\text{KPb}_9\text{Sn}_9\text{BiTe}_{20}$. Two different phases are distinguishable in the inclusion in Figure 6-5a. The bright area 1 contains only Bi whereas the area 2 is a quaternary phase. The EDS analysis gave the following atomic percentages: Pb: 8.14, Sn: 15.02, Bi: 32.17 and Te 44.67. This is not charge-balanced. But as Bi and Pb have close L emission lines, there is a larger uncertainty on the respective Pb and Bi amounts than for the other elements. EDS analysis on a large area on the inclusion in Figure 6-5b indicated the area to be rich in Te: Pb: 1.36 at.%, K: 4.77 at.%, Sn: 22.90 at.% and Te : 70.95 at.%.

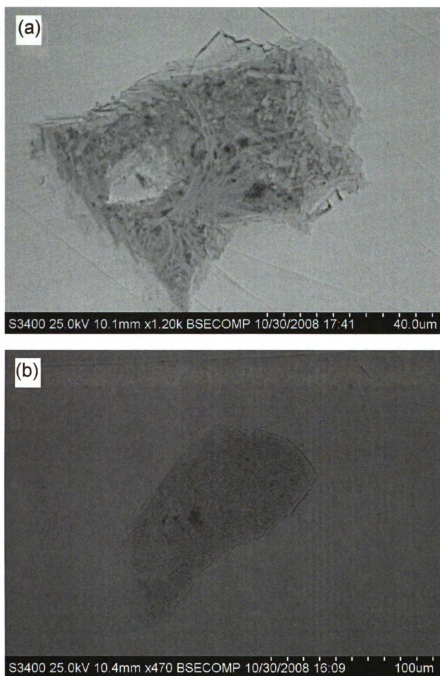


Figure 5-3. BSE images of the surface of (a) $\text{KPb}_{13}\text{Sn}_5\text{SbTe}_{20}$ showing a precipitate with the atomic percentages Pb:2.73, K: 4.59, Sb:27.59 and Te:65.09 and (b) $\text{KPb}_9\text{Sn}_9\text{SbTe}_{20}$ showing an inclusion with atomic percentages Pb:2.32, K: 14.87, Sb:23.38 and Te:59.43. EDS analysis on the matrices indicated Pb, Sn and Te with ratios consistent with the nominal composition.

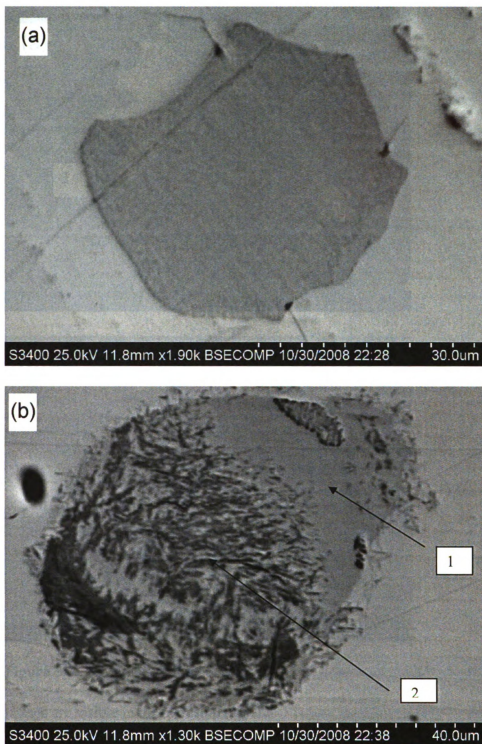


Figure 5-4. BSE image of (a) a Sb-rich inclusion and (b) a mixed-phase inclusion in $\text{KPb}_3\text{Sn}_{13}\text{SbTe}_{20}$. EDS on area 1 showed the presence of Sb_2Te_3 and EDS on area 2 gave the atomic percentages Pb:6.32, K: 3.80, Sb:13.51 and Te:76.37.

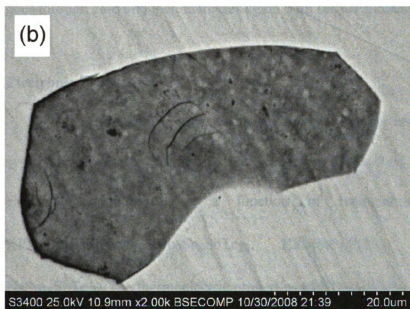
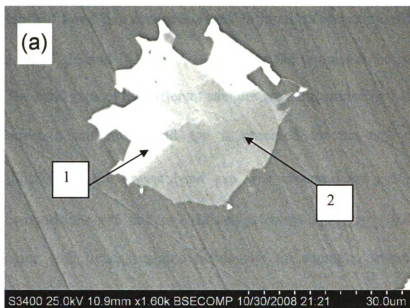


Figure 5-5. BSE images of inclusions (a) and (b) observed for $\text{KPb}_9\text{Sb}_9\text{BiTe}_{20}$. Different phases are visible in the inclusion (a): area 1 is pure Bi whereas area 2 contains Pb, Sn, Bi and Te with the following atomic percentages: 8.14, 15.02, 32.17 and 44.67. EDS analysis on inclusion (b) gave the atomic percentages Pb: 1.36, K: 4.77, Sn: 22.90 and Te: 70.95.

Optical band gap measurements. Infrared spectroscopy of $\text{KPb}_{18-x}\text{Sn}_x\text{MTe}_{20}$ ($x=0, 2, 5, 9, 13, 16$ and $18, \text{M}=\text{Sb, Bi}$) indicate the samples to be narrow gap semiconductors. The band gaps of the different samples are summarized in Table 5-3 and 5-4. For the Sb series, a minimum band gap is observed for the $x=9$ composition. For $\text{NaPb}_{18-x}\text{Sn}_x\text{SbTe}_{20}$, the lowest band gap was observed for $x=9$. For the Bi analogs, the compositions $x=5$ and $x=9$ showed a lowest band gap ≤ 0.05 eV. These observations agree with trends reported previously: for example, several investigations^{24, 25} have shown that the band gap of the $\text{Pb}_{1-x}\text{Sn}_x\text{Te}$ system decreases as the tin content increases, goes through zero and then increases again with further increase in tin content.

Electronic Properties.

KPb_{18-x}Sn_xSbTe₂₀. The electronic transport properties of the $\text{KPb}_{18-x}\text{Sn}_x\text{MTe}_{20}$ systems can be tuned by varying the Sn:Pb ratio. Figure 5-6a shows the evolution of the electrical conductivity as a function of temperature for $\text{KPb}_{16}\text{Sn}_2\text{SbTe}_{20}$, $\text{KPb}_{13}\text{Sn}_5\text{SbTe}_{20}$, $\text{KPb}_9\text{Sn}_9\text{SbTe}_{20}$, $\text{KPb}_5\text{Sn}_{13}\text{SbTe}_{20}$, $\text{KPb}_2\text{Sn}_{16}\text{SbTe}_{20}$ and $\text{NaSn}_{18}\text{SbTe}_{20}$. The thermoelectric properties of $\text{KPb}_{18}\text{SbTe}_{20}$ could not be measured due to the high brittleness of the sample. Regardless of the composition, the electrical conductivity decreases with increasing temperature, indicating degenerate conduction for the whole temperature range. The electrical conductivity increases with increasing Sn concentration with the exception of $\text{KPb}_{13}\text{Sn}_5\text{SbTe}_{20}$. The room temperature value of the electrical conductivity of $\text{KSn}_{18}\text{SbTe}_{20}$ was ~ 3875 S/cm, which is about ten times that of $\text{KPb}_{16}\text{Sn}_2\text{SbTe}_{20}$. This trend is the same as that observed in the case of NaPb_{18} .

$x\text{Sn}_x\text{SbTe}_{20}$. Presumably, in the $\text{KPb}_{18-x}\text{Sn}_x\text{SbTe}_{20}$ system, vacancies become more and more dominant with increasing fraction of SnTe (i.e. x).

The composition $\text{KPb}_{16}\text{Sn}_2\text{SbTe}_{20}$ exhibited n-type behavior whereas positive thermopower values were measured for $\text{KPb}_{13}\text{Sn}_5\text{SbTe}_{20}$, $\text{KPb}_9\text{Sn}_9\text{SbTe}_{20}$, $\text{KPb}_5\text{Sn}_{13}\text{SbTe}_{20}$, $\text{KPb}_2\text{Sn}_{16}\text{SbTe}_{20}$ and $\text{NaSn}_{18}\text{SbTe}_{20}$ (Figure 5-6b). By introducing Sn into the system, more holes are added and for x between 2 and 5, the concentration of holes surpasses that of electrons. For $\text{KPb}_{16}\text{Sn}_2\text{SbTe}_{20}$, the thermopower varies between $-159 \mu\text{V/K}$ at room temperature and $-269 \mu\text{V/K}$ at 559 K. For p-type samples, the thermopower increases with decreasing amount of Sn. $\text{KPb}_{13}\text{Sn}_5\text{SbTe}_{20}$ exhibits the highest thermopower among the p-type compositions over the temperature range 300-550 K. $\text{KPb}_{13}\text{Sn}_5\text{SbTe}_{20}$ has thermopower $\sim 161 \mu\text{V/K}$ at room temperature and reaches a maximum of $\sim 275 \mu\text{V/K}$ at 462 K. At higher temperatures, the thermopower $\text{KPb}_9\text{Sn}_9\text{SbTe}_{20}$ becomes higher than that of $\text{KPb}_{13}\text{Sn}_5\text{SbTe}_{20}$.

The power factors calculated from the above data are plotted in Figure 5-6c. Clearly, different trends are observed. The n-type composition $\text{KPb}_{16}\text{Sn}_2\text{SbTe}_{20}$ exhibits the highest power factor over the temperature range 300-550 K. Its power factor is almost constant, $\sim 12 \mu\text{W/cm}\cdot\text{K}^2$. The power factor for $\text{KPb}_{13}\text{Sn}_5\text{SbTe}_{20}$ decreases with temperature from $10 \mu\text{W/cm}\cdot\text{K}^2$ at room temperature to 1 at 600 K. For the other members, the power factor increases rapidly with temperature. For example, the power factor of $\text{KPb}_2\text{Sn}_{16}\text{SbTe}_{20}$ increases from $0.9 \mu\text{W/cm}\cdot\text{K}^2$ at room temperature to $12.5 \mu\text{W/cm}\cdot\text{K}^2$ at 600 K.

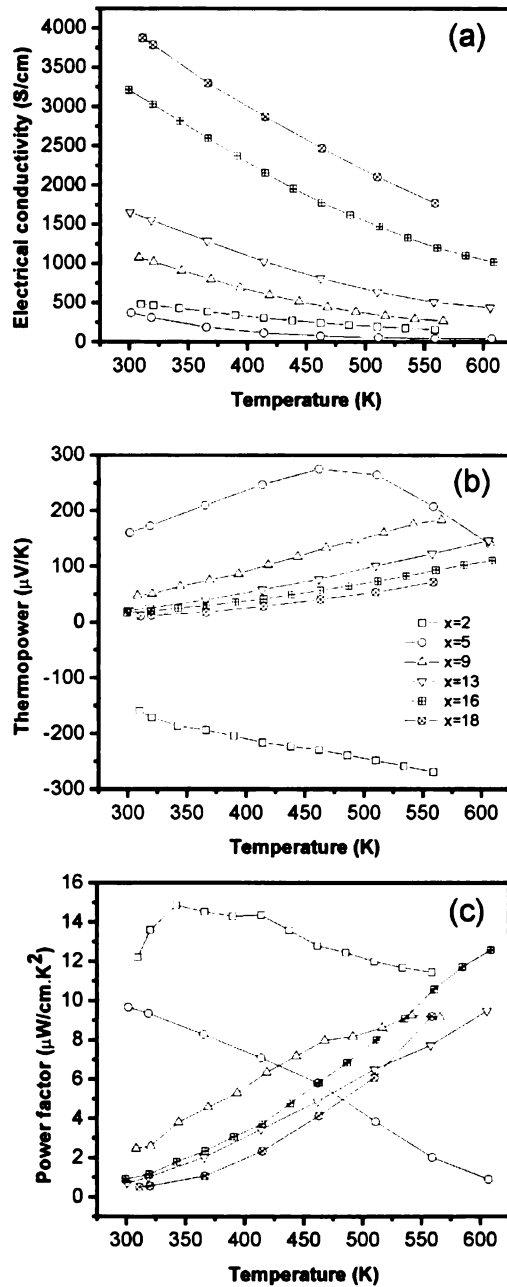


Figure 5-6. Electronic transport properties of the $\text{KPB}_{18-x}\text{Sn}_x\text{SbTe}_{20}$ samples: (a) electrical conductivity, (b) thermopower, (c) power factor. The point marks in the inset of panel (b) identify all samples and apply to panels (a) and (c).

*NaPb*_{18-x}*Sn*_x*BiTe*₂₀. Because of the high brittleness of the ingots, only the thermoelectric properties of *KPb*_{18-x}*Sn*_x*BiTe*₂₀ (x= 5, 9, 13 and 18) were measured. The temperature dependence of the electrical conductivity of the compositions x=5, 9, 13 and 18 are plotted in Figure 5-7a. All compositions are degenerate semiconductors with electrical conductivity decreasing with temperature. For the Sb analogs, the electrical conductivity increases with increasing amount of Sn. At room temperature, the electrical conductivity of *KSn*₁₈*BiTe*₂₀ is ~ 2347 S/cm, which is 8 times larger than that of *KPb*₁₃*Sn*₅*BiTe*₂₀ (296 S/cm).

The composition *KPb*₁₃*Sn*₅*BiTe*₂₀ showed n-type behavior (Figure 5-7b). At room temperature the thermopower is ~ -100 μ V/K and a maximum of ~ -180 μ V/K at 585 K. In the case of *KPb*₁₃*Sn*₅*MTe*₂₀, the difference in the nature of charge carriers between the Sb and Bi analogs emphasizes the importance of the pnictogen atom. The compositions *KPb*_{18-x}*Sn*_x*BiTe*₂₀ (x=9, 13 and 18) have positive thermopower values which increase linearly with temperature. The x=9 sample has the highest thermopower over the range 300-600 K with values between 61 μ V/K at 300 K and 230 μ V/K at 606 K.

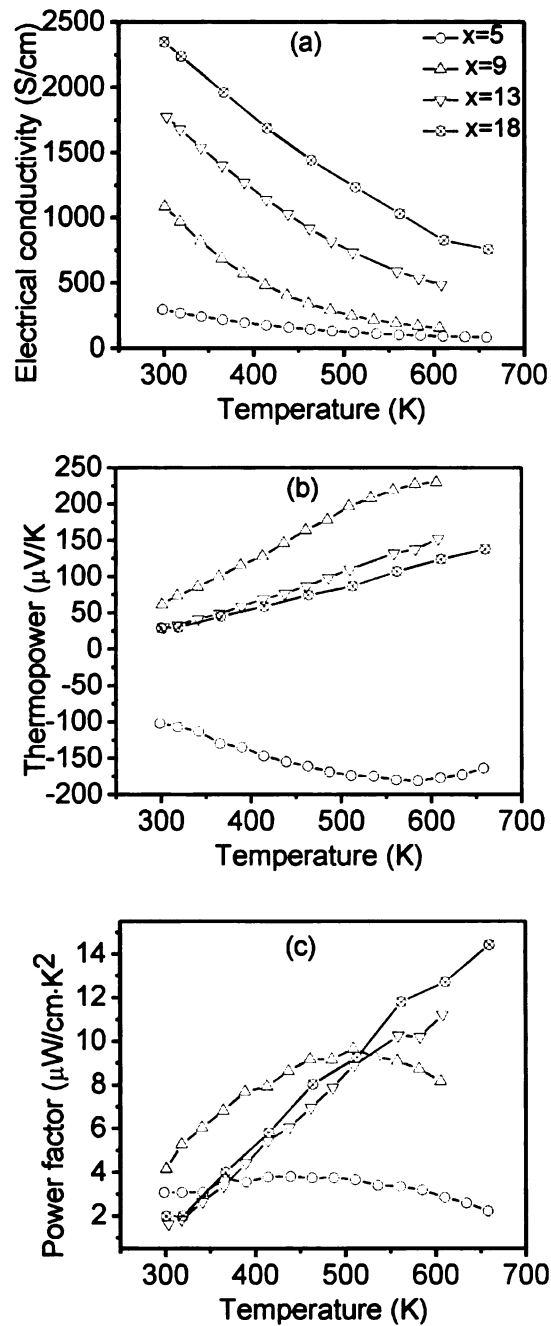


Figure 5-7. Electronic transport properties of the $\text{KPb}_{18-x}\text{Sn}_x\text{BiTe}_{20}$ samples: (a) electrical conductivity, (b) thermopower, (c) power factor. The point marks in the inset of panel (a) identify all samples and apply to all panels (b) and (c).

A recent study on the influence of the pnictogen on the properties of the n-type $\text{Ag}_{1-x}\text{Pb}_{18}\text{MTe}_{20}$ materials indicated larger thermopower values for Sb analogs compared to Bi samples.²⁶ Band structure calculations for $\text{Ag}_{1-x}\text{Pb}_{18}\text{MTe}_{20}$ were performed using the lower energy configuration (i.e. Ag and M pairs are the second nearest neighbors of one another). There are band splittings due to the presence of the (Ag,M) pairs because the symmetry is lowered compared to the undoped PbTe. The top of the valence is perturbed predominantly by Ag with an impurity-derived band formed predominantly out of Te p and Ag d states. The bottom of the conduction is, on the other hand, perturbed predominantly by Sb or Bi. In the case of the (Ag, Sb) pair, a group of three nearly degenerate bands forms the lowest conduction band with a nondegenerate band (at ~ 0.06 eV above that group) at the Γ point (Figure 5-8a). In contrast, in the case of the (Ag, Bi) pair, the nondegenerate band forms the lowest conduction band and the group of three nearly degenerate bands is ~ 0.04 eV above the nondegenerate band at the Γ point (Figure 5-8b). Due to this basic difference in the arrangement of the bands and lower carrier concentration in the Sb analog, one expects to see larger negative Seebeck coefficient in Sb compounds compared to the Bi compounds.

Combining the above data, the resulting power factors are plotted in Figure 5-7c. For the composition $x=5$, the power factor is constant over the temperature range but does not exceed $3 \mu\text{W}/\text{cm}\cdot\text{K}^2$. The composition $x=9$ reaches a maximum $\sim 9.5 \mu\text{W}/\text{cm}\cdot\text{K}^2$ at 509 K. For the other members, the power factors increase linearly with temperature with a maximum power factor $\sim 14 \mu\text{W}/\text{cm}\cdot\text{K}^2$ at 660 K. Such values derive mainly through a high electrical conductivity.

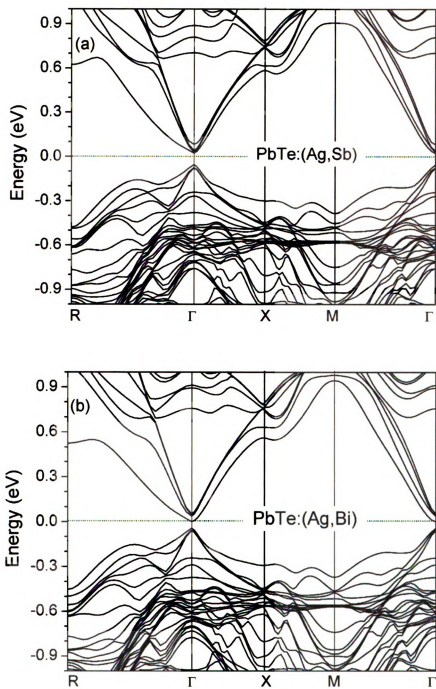


Figure 5-8. Band-structure of PbTe doped with (a) (Ag, Sb), (b) (Ag, Bi). Ag and Sb/Bi atoms in the pair are the second-nearest neighbors of one another in a 64-atom supercell.

Table 5-3. Summary of the physical and electronic properties of the materials $KPb_{18-x}Sb_xSn_{10}Te_{20}$

Composition	a (Å)	T_m (K)	E_g (eV)	σ (S/cm)			S (μ V/K)	
				300 K	550 K	550 K	300 K	550 K
$KPb_{18}SbTe_{20}$	6.475 (2)	1191	0.30					
$KPb_{16}Sn_2SbTe_{20}$	6.448 (1)	1175	0.26	500	151		-159	-268
$KPb_{13}Sn_5SbTe_{20}$	6.440 (1)	1162	0.24	375	39		163	209
$KPb_9Sn_9SbTe_{20}$	6.411 (1)	1141	<0.08	1072	263		48	184
$KPb_5Sn_{13}SbTe_{20}$	6.369 (3)	1109	0.08	1659	512		22	124
$KPb_2Sn_{16}SbTe_{20}$	6.340 (2)	1071	0.08	3216	1173		15	92
$KSn_{18}SbTe_{20}$	6.332 (1)	1061	0.09	3889	1771		8	71

Table 5-4. Summary of the physical and electronic properties of the materials $KPb_{18-x}Sn_xBiTe_{20}$

Composition	a (Å)	T_m (K)	E_g (eV)	σ (S/cm)			S (μ V/K)	
				300 K	550 K	550 K	300 K	550 K
$KPb_{18}BiTe_{20}$	6.467 (1)	1183	0.32					
$KPb_{16}Sn_2BiTe_{20}$	6.460 (2)	1175	0.24					
$KPb_{13}Sn_5BiTe_{20}$	6.448 (3)	1162	0.19	294	101		-102	-179
$KPb_9Sn_9BiTe_{20}$	6.396 (1)	1135	~0.05	1085	633		63	216
$KPb_5Sn_{13}BiTe_{20}$	6.386 (3)	1100	~0.05	1780	618		30	124
$KPb_2Sn_{16}BiTe_{20}$	6.347 (2)	1078	~0.06					
$KSn_{18}BiTe_{20}$	6.335 (2)	1058	~0.07	2349	1033		30	103

Thermal Transport Properties.

$KPb_{18-x}Sn_xSbTe_{20}$. Thermal diffusivity measurements for the samples $KPb_{18-x}Sn_xSbTe_{20}$ ($x=5, 9, 13$ and 16) were used to calculate their total thermal conductivity (Figure 5-9a). For all compositions, the total thermal conductivity decreases with temperature. At similar temperature, the thermal conductivity decreases with Pb content. For example at 300 K the total thermal conductivity of $KPb_2Sn_{16}SbTe_{20}$ is ~ 3.6 W/m·K, which is three times higher than that of $KPb_{13}Sn_5SbTe_{20}$ (1.1 W/m·K). This trend is similar to that observed in the case of Na analogs. Samples with high amount in Sn have high electrical conductivity; as a result, their electronic contribution to the total thermal conductivity is higher than the lattice contribution. The electronic component of the sample was estimated using Wiedemann-Franz law and the lattice contribution was evaluated by subtracting the electronic contribution to the total thermal conductivity. The results are plotted in Figure 5-9b and 5-9c. For Sn-rich composition such as $KPb_2Sn_{16}SbTe_{20}$, the electronic contribution at room temperature (2.4 W/m·K) is slightly higher than the lattice component (1.9 W/m·K). For Pb-rich composition, the electronic component at room temperature is low (0.3 W/m·K), three times smaller than the lattice conductivity (0.9 W/m·K). At room temperature, for all compositions, the lattice component is lower than that of pure PbTe (2.3 W/m·K).²⁷ At room temperature, the $x=5$ and $x=9$ compositions have the lowest lattice thermal conductivity (~ 0.9 W/m·K). At high temperature, lattice thermal conductivity as low as 0.6 W/m·K was found for $KPb_9Sn_9SbTe_{20}$. These values are close to that reported for the Na analogs and for the $K_{1-x}Pb_{m+\delta}Sb_{1+\gamma}Te_{m+2}$. The reason of such low lattice thermal conductivity is probably

the existence of nanostructures embedded in the $\text{Pb}_{1-y}\text{Sn}_y\text{Te}$ matrix as was observed in the case of $\text{NaPb}_{18-x}\text{Sn}_x\text{SbTe}_{20}$ (see Chapter 4).

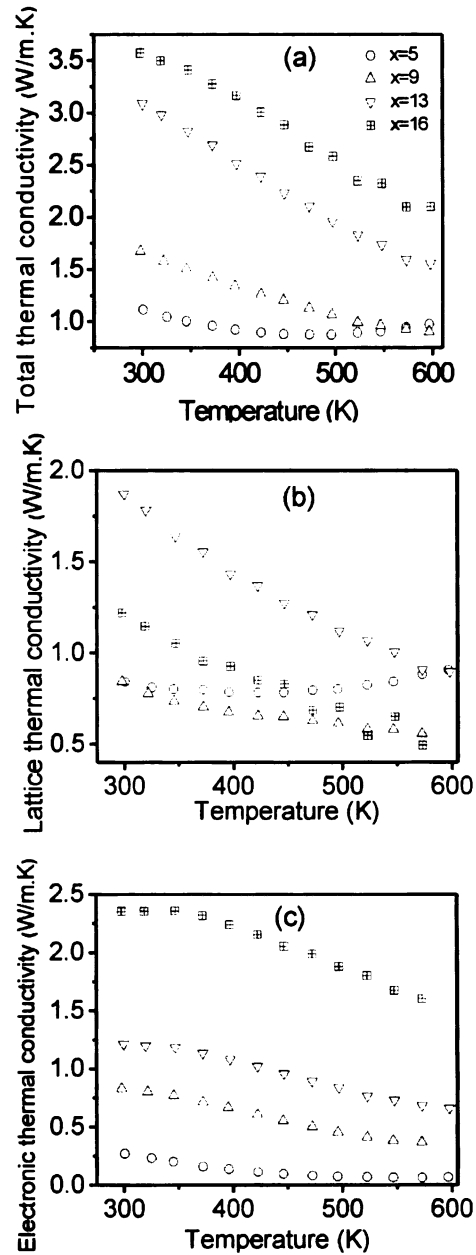


Figure 5-9. Temperature of the (a) total thermal conductivity, (b) lattice thermal conductivity and (c) electronic thermal conductivity for $\text{KPb}_{18-x}\text{Sn}_x\text{SbTe}_{20}$ ($x=5, 9, 13$ and 16).

The temperature dependence of the figures of merit (ZT) of the $\text{KPb}_{18-x}\text{Sn}_x\text{SbTe}_{20}$ ($x=5, 9, 13$ and 16) calculated from the above data are compared in Figure 5-10. For all compositions except $x=5$, the figure of merit increases with temperature. The figure of merit of the $x=5$ compound reaches a maximum ~ 0.33 at 422 K. The figure of merit of $\text{KPb}_9\text{Sn}_9\text{SbTe}_{20}$ increases more rapidly than that of $\text{KPb}_5\text{Sn}_{13}\text{SbTe}_{20}$ and $\text{KPb}_2\text{Sn}_{16}\text{SbTe}_{20}$ with a maximum ZT ~ 0.57 at 572 K. For compositions more rich in Sn, the highest ZT are shifted to higher temperature with ZT ~ 0.59 at 673 K.

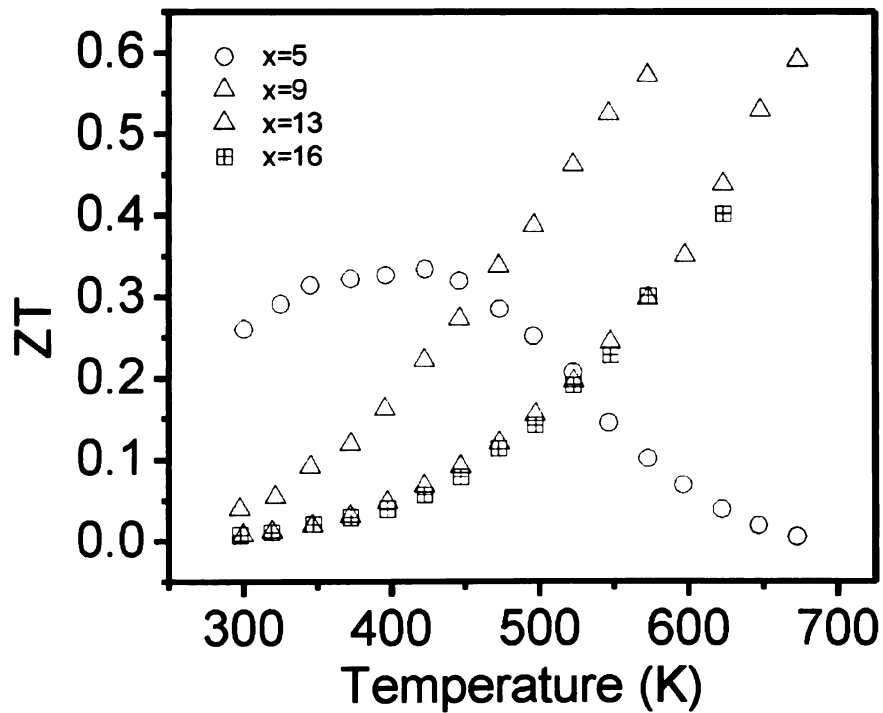


Figure 5-10. Temperature dependence of the figure of merit ZT for $\text{KPb}_{18-x}\text{Sn}_x\text{SbTe}_{20}$ ($x=0, 3, 5, 9, 13, 16$).

5.4. Conclusions

The series $\text{K Pb}_{18-x} \text{ Sn}_x \text{ M Te}_{20}$ ($x=0, 2, 5, 9, 13, 16$ and 18 , $\text{M}=\text{Sb, Bi}$) were prepared via high temperature solid state synthesis. From powder X-ray diffraction studies, the ingots appeared homogeneous with patterns similar to that of PbTe . However, SEM and BSE studies indicated the presence of micro-size inclusions. Some of these inclusions consist of Sb_2Te_3 precipitates were but the majority of these inclusions contain more than one phase. The roughness of their surfaces and the presence of potassium and oxygen peaks are indications that unstable phases containing K precipitate in the $\text{Pb}_{1-x} \text{ Sn}_x \text{ Te}$ matrix upon cooling but decompose upon contact with water. This stability issue is a serious drawback for industrial application. Partial substitution of Pb by Sn increases the hole concentration, resulting in a switch from n-to-p type. However the absolute thermopower values measured for the two series is still lower to that of the $\text{K}_{1-x} \text{ Pb}_{m+\delta} \text{ Sb}_{1+\gamma} \text{ Te}_{m+2}$. As a result, the highest power factor ($\sim 13\text{-}14 \mu\text{W}/\text{cm}\cdot\text{K}^2$) are obtained at high temperature for Sn-rich compositions because of their high electrical conductivity. The low lattice thermal conductivity of $\text{K Pb}_{13} \text{ Sn}_5 \text{ Sb Te}_{20}$ and $\text{K Pb}_9 \text{ Sn}_9 \text{ Sb Te}_{20}$ ($0.9 \text{ W}/\text{m}\cdot\text{K}$ at 300 K), similar to the values reported for the $\text{K}_{1-x} \text{ Pb}_{m+\delta} \text{ Sb}_{1+\gamma} \text{ Te}_{m+2}$ system, is an indication of the existence of nanostructures inside the matrix.

References

1. *MRS Bulletin* **2006**, 31, (3).
2. J., D. F., *Science* **1999**, 285, 703.
3. Harman, T. C.; Taylor, P. J.; Walsh, M. P.; LaForge, B. E., *Science* **2002**, 297, 2229.
4. Harman, T. C.; Taylor, P. J.; Walsh, M. P.; LaForge, B. E., *J. Electron. Mater.* **2005**, 34, L19.
5. Venkatasubramanian, R.; Siivola, E.; Colpitts, T.; O'Quinn, B., *Nature* **2001**, 413, 597.
6. Caylor, J. C.; Coonley, K.; Stuart, J.; Colpitts, T.; Venkatasubramanian, R., *Appl. Phys. Lett.* **2005**, 87, (2), 023105.
7. Hicks, L. D.; Dresselhaus, G., *Phys. Rev. B* **1993**, 47, 16631.
8. Hicks, L. D.; Dresselhaus, M. S., *Phys. Rev. B* **1993**, 47, (19), 12727.
9. Kim, W.; Singer, K. L.; Majumdar, A.; Vashae, D.; Bian, Z.; Shakouri, A.; G., Z.; Bowers, E. J.; Zide, J. M. O.; Gossard, C., *Appl. Phys. Lett.* **2006**, 88, 242107.
10. Hicks, L. D.; Dresselhaus, M. S., *Phys. Rev. B* **1993**, 47, 16631.
11. Harman, T. C.; Taylor, P. J.; Spears, P. J.; Walsh, M. P., *J. Electron. Mater.* **2000**, 29, L1.
12. Hsu, K. F.; Loo, S.; Guo, F.; Chen, W.; Dyck, J. S.; Uher, C.; Hogan, T.; Polychroniadis, E. K.; Kanatzidis, M. G., *Science* **2004**, 303, 818.
13. Quarez, E.; Hsu, K. F.; Pcionek, R.; Frangis, N.; Polychroniadis, E. K.; Kanatzidis, M. G., *J. Am. Chem. Soc.* **2005**, 127, 9177.

14. Hagelberg, F.; Neeser, S.; Sahoo, N.; Das, P. T.; Weil, K. G., *Phys. Rev. A* **1994**, **50**, 557.
15. Henger, G.; Peretti, E. A., *Journal of the Less-Common Metals* **1965**, **8**, 124.
16. Poudeu, P. F. P.; D'Angelo, J.; Downey, A. D.; Short, J. L.; Hogan, T.; Kanatzidis, M. G., *Angew. Chem., Int. Ed.* **2006**, **45**, 3835.
17. Poudeu, P. F. P.; Kong, H.; Gueguen, A.; Wu, C. I.; Pcionek, R.; Shi, X.; Uher, C.; Hogan, T.; Kanatzidis, M. G., *manuscript in preparation*.
18. Ahmad, S.; Mahanti, S. D., *Phys. Rev. B* **2006**, **74**, 155205.
19. Orihashi, M.; Noda, Y.; Chen, L. D.; Goto, T.; Hirai, T., *J. Phys. Chem. Solids* **2000**, **61**, 919.
20. Androulakis, J.; Hsu, K. F.; Pcionek, R.; Kong, H. J.; Uher, C.; D'Angelo, J.; Downey, A. D.; Hogan, T.; Kanatzidis, M. G., *Adv. Mater.* **2006**, **18**, 1170.
21. Kittel, C., *Introduction to Solid State Physics*. Wiley: 2005.
22. Bouad, N.; Chapon, L.; Marin-Ayral, R. M.; Bouree-Vigneron, F.; Tadenac, J. C., *J. Solid State Chem.* **2003**, **173**, 189.
23. Rogacheva, E. I.; Gorne, G. V.; Laptev, S. A.; Arinkin, A. V.; Vesiene, T. B., *J. Solid State Chem.* **1982**, **43**, 364.
24. Dimmock, J. O.; Melngailis, I.; Strauss, A. J., *Physical Review Letters* **1966**, **16**, (26), 1193-6.
25. Abramof, E.; Ferreira, S. O.; Rappl, P. H. O.; Closs, H.; Bandeira, I. N., *Journal of Applied Physics* **1997**, **82**, (5), 2405-2410.
26. Han, M.; Hoang, K.; Kong, H. J.; Pcionek, R.; Uher, C.; Paraskevopoulos, M.; Mahanti, S. D.; Kanatzidis, M. G., *Chem. Mater.* **2008**, **20**, 3512.
27. Ioffe, A. F., *Can. J. Phys.* **1956**, **34**, 1342.

Chapter 6

The systems $\text{CuPb}_m\text{SbTe}_{m+2}$ ($m=8, 12, 18, 20, 22, 30, 40, 50$), $\text{CuPb}_{18-x}\text{Sn}_x\text{SbTe}_{20}$ ($x=0, 5, 9, 13, 18$), $\text{Cu}_2\text{Te}/\text{Sb}_2\text{Te}_3$ and $\text{Cu}_2\text{Te}/\text{PbTe}$

6.1. Introduction

Improved figures of merit have been reported for materials prepared in low dimensional form such as quantum well (QW) two dimensional multilayered structures¹,², one dimensional quantum wire array structures³ and even lower dimensionality such as quantum dot arrays and superlattices structures.^{4, 5} A significant reduction in the lattice thermal conductivity was reported for these systems as a result of the increase in phonon-boundary scattering. Our group reported on the bulk n-type system $\text{AgPb}_m\text{SbTe}_{m+2}$ (so-called LAST).⁶ A figure of merit ~ 1.7 at 700 K was obtained for the composition $\text{AgPb}_{18}\text{SbTe}_{20}$. The electrical conductivity and the thermopower were respectively ~ 200 S/cm and $-335 \mu\text{V/K}$, resulting in a power factor $\sim 28 \mu\text{W/cm}\cdot\text{K}^2$. In addition to a high power factor, the thermal conductivity obtained from thermal diffusivity measurements was ~ 1.1 W/m·K at 700 K. To understand the reason of such low thermal conductivity, detailed structural analysis was performed on the samples. Powder X-ray diffraction indicated the material to be single phase with NaCl structure-type. However the presence

of nanocrystals embedded in the PbTe matrix was observed with high resolution TEM studies.^{6, 7} Because of instrumental limitation, the precise composition of these nanocrystals could not be determined. We can suppose these regions to be rich in Sb and Ag in order to maintain locally the electroneutrality of the system. Using the LAST system as an exploration platform, other systems derived from this family of compounds were investigated: the n-type systems $\text{Pb}_{1-x}\text{Sn}_x\text{Te-PbS}^8$, $\text{Pb}_{9.6}\text{Sb}_{0.2}\text{Te}_{10-x}\text{Se}_x^9$ and the p-type systems $\text{Na}_{1-x}\text{Pb}_m\text{Sb}_y\text{Te}_{m+2}$ (SALT)¹⁰ and $\text{Ag}(\text{Pb}_{1-y}\text{Sn}_y)_m\text{SbTe}_{2+m}$ (LASTT).¹¹ Low thermal conductivity was reported for the bulk p-type system $\text{Na}_{1-x}\text{Pb}_m\text{Sb}_y\text{Te}_{m+2}$ resulting in $ZT \sim 1.7$ at 650 K for $\text{Na}_{0.95}\text{Pb}_{20}\text{SbTe}_{22}$.¹⁰ High resolution TEM studies again indicated the presence of nanostructures embedded in the PbTe matrix.

In the two first parts of this chapter, we study the impact of substituting Ag by Cu in $\text{AgPb}_m\text{SbTe}_{m+2}$ and $\text{AgPb}_{18-x}\text{Sn}_x\text{SbTe}_{20}$ on the structural and electronic properties of these two systems. Powder X-ray diffraction indicated the materials to be not single phase but to contain Cu_2Te and Sb_2Te_3 as well as PbTe. The results were confirmed by back-scattered electron imaging. In order to understand why the two phases Cu_2Te and Sb_2Te_3 segregate together, mixtures of Cu, Sb and Te with ratio 1:1;2 were prepared in part III. These attempts did not result in the hypothetical compound CuSbTe_2 but in a mixture of Cu_2Te and Sb_2Te_3 . Finally, in part IV, some doping studies on PbTe using Cu_2Te only resulted in the segregation of Cu_2Te in the PbTe matrix and provides some insight about the role of Sb_2Te_3 in the properties of $\text{CuPb}_m\text{SbTe}_{m+2}$ and $\text{CuPb}_{18-x}\text{Sn}_x\text{SbTe}_{20}$.

6.2. CuPb_mSbTe_{m+2} (m = 8, 12, 18, 20, 22, 30, 40 and 50)

6.2.1 Experimental section

6.2.1.1. Synthesis.

CuPb_mSbTe_{m+2}. All samples were prepared as polycrystalline ingots in silica by mixing high purity elements in the appropriate stoichiometric ratio in 10 mm outer diameter fused silica tubes. The fused silica tubes were carbon-coated prior to use as glass attack was observed during preliminary reactions. The tubes were then flame-sealed under a residual pressure of $\sim 10^{-4}$ Torr, placed into a tube furnace (mounted on a rocking table) and heated at 1373 K for 4 h to allow complete melting of all components. While molten the furnace was allowed to rock for 2 h to facilitate complete mixing and homogeneity of the liquid phase. The furnace was finally immobilized at the vertical position and was cooled from 1373 to 820 K over 55 h followed by a fast cooling to room temperature. The resulting ingots were silvery-metallic in color with a smooth surface. Table 6-1 summarizes the amount of elements used for each reaction.

Table 6-1. Amounts of elements used to prepare the series $\text{CuPb}_m\text{SbTe}_{m+2}$.

Composition	Cu, g (mmol)	Pb, g (mmol)	Sb, g (mmol)	Te, g (mmol)
$\text{CuPb}_8\text{SbTe}_{10}$	0.2481 g (3.90)	6.4717 g (31.23)	0.4754 g (3.90)	4.9818 g (39.04)
$\text{CuPb}_{12}\text{SbTe}_{14}$	0.1595 g (2.51)	6.2408 g (30.12)	0.3056 g (2.51)	4.4839 g (35.14)
$\text{CuPb}_{18}\text{SbTe}_{20}$	0.1046 g (1.65)	6.1391 g (29.63)	0.2004 g (1.65)	4.2007 g (32.92)
$\text{CuPb}_{20}\text{SbTe}_{22}$	0.1018 g (1.60)	6.6386 g (32.04)	0.1951 g (1.60)	4.4971 g (35.24)
$\text{CuPb}_{22}\text{SbTe}_{24}$	0.0972 g (1.53)	6.9725 g (33.65)	0.1862 g (1.53)	4.6842 g (36.71)
$\text{CuPb}_{30}\text{SbTe}_{32}$	0.0779 g (1.23)	7.6201 g (36.78)	0.1493 g (1.23)	5.0055 g (39.23)
$\text{CuPb}_{40}\text{SbTe}_{42}$	0.0544 g (0.86)	7.0951 g (34.49)	0.1042 g (0.86)	4.5879 g (35.96)
$\text{CuPb}_{50}\text{SbTe}_{52}$	0.0420 g (0.66)	6.8473 g (33.05)	0.0805 g (0.66)	4.3855 g (34.37)

6.2.1.2. Characterization techniques

Powder X-ray Diffraction. Powder X-ray patterns of the grinded materials were recorded using Cu K_α radiation ($\lambda = 1.54056 \text{ \AA}$) in reflection geometry on a CPS-120 Inel X-ray powder diffractometer operating at 40 kV and 20 mA equipped with a position sensitive detector.

DTA Analysis. Differential thermal analysis (DTA) data were collected with a Shimadzu DTA-50 thermal analyzer. Approximately 35 mg of finely ground powder of material was sealed in a carbon-coated quartz ampoule under residual pressure of $\sim 10^{-4}$ torr. Another ampoule containing similar amount of alumina and prepared the same way was used as a reference. The samples were heated to 1273 K at a rate of 10 K/min, held at 1273 K for two minutes and cooled down to 323 K at a rate of -10 K/min.

Scanning Electron Microscopy. The surface of several samples was polished very carefully using silica suspension solution (0.05 μm) in order to get a smooth, mirror-like surface. The samples were then studied with a scanning electron microscopy (Hitachi S3400N-II) with 25 kV acceleration voltage using both energy-dispersive spectroscopy (EDS) and back-scattered electron imaging (BSE).

Electrical Transport Properties. Thermopower and electrical conductivity properties were measured simultaneously under helium atmosphere using a ZEM-3 Seebeck coefficient/electrical resistivity measurement system (ULVAC-RIKO, Japan). Samples for transport measurement were cut to size $10 \times 3 \times 3 \text{ mm}^3$ using a diamond saw (Buehler isomet 1000), a wire saw (South Bay Technology) and a polishing machine (Buehler ecomet 3000). Rectangular shape samples with approximately $3 \times 3 \text{ mm}^2$ cross-section were sandwiched vertically by two nickel electrodes (current injection) with two Pt/PtRh thermocouples (for temperature difference and voltage measurements) attached on one side. The sample and measurement probes were covered by a nickel can to maintain a constant temperature during the measurement and the base temperature was measured by a thermocouple attached to the outside of the can. The sample, electrodes, and nickel can were placed in a vacuum chamber then evacuated and refilled with He gas (0.1 atm) to provide necessary heat transfer. Properties were measured from room temperature to 670 K under helium atmosphere.

Hall Measurements. Above 300 K, Hall measurements were carried out by an in-house high temperature/high magnetic field Hall apparatus. It consists of a nine Tesla air-bore superconducting magnet with a water-cooled oven inside the bore of the magnet, and a Linear Research AC bridge with 16 Hz excitation. Four-wire AC Hall measurements

were performed on parallelepiped samples with the typical size of $1.5 \times 3 \times 10 \text{ mm}^3$ to temperatures of at least 800K with the protection of Argon gas.

Thermal Conductivity. The thermal conductivity was determined as a function of temperature using the flash diffusivity method on a LFA 457/2/G Microflash NETZSCH. The front face of a small disc-shaped sample (diameter $\sim 8 \text{ mm}$; thickness $\sim 2 \text{ mm}$) coated with a thin layer of graphite is irradiated with a short laser burst, and the resulting rear face temperature rise is recorded and analyzed. The experiments were carried out under nitrogen atmosphere. Thermal conductivity values were calculated using the equation $\kappa = \alpha C_p d$, where α is the thermal diffusivity, C_p the specific heat and d the bulk density of the material calculated from the sample's geometry and mass. A pyroceram reference was used to determine the heat capacity of the sample.. The thermal diffusivities were measured typically over the temperature range 300-670 K. The electronic component of the thermal conductivity was quantified through the Wiedemann-Franz law according to which $\kappa_{el} = \sigma T L_o$ (L_o being the Lorenz number, $L_o = 2.45 \cdot 10^{-8} \text{ W}\Omega\text{K}^{-1}$).¹² The lattice contribution was then derived by subtracting the electronic component from the total thermal conductivity.

6.2.2 Results and discussion

Structure and Characterization. Figure 6-1 shows the X-ray diffraction patterns from powders taken from top and bottom of the ingot for the compositions $\text{CuPb}_m\text{SbTe}_{m+2}$ ($m=5, 12, 18, 20, 22, 30, 40$ and 50). Extra peaks which do not belong to the cubic structure PbTe are clearly visible. The two small peaks at 28 and 38 deg could be identified to the phase Sb_2Te_3 and the peaks present $\sim 42-43$ to Cu_2Te . The presence of

such phases can be expected due to the low solubility of Sb¹³ and Cu in PbTe. As the m value increases, the intensity of the peaks belonging to these minor phases decreases.

Scanning Electron Microscopy. To obtain precise information about the repartition of the Cu₂Te and Sb₂Te₃ phases in the PbTe matrix, detailed back-scattered electron (BSE) analysis on the fine-polished surface of samples was carried out. Figure 6-2 shows a typical BSE-image observed in the case of CuPb₁₈SbTe₂₀. Regions rich in Cu₂Te and Sb₂Te₃ are randomly dispersed in the PbTe matrix. These features are observed for all CuPb_mSbTe_{m+2} compounds with more dense networks observed for low m values. For example, BSE imaging on CuPb₄₀SbTe₄₂ (Figure 6-3) shows smaller regions rich in Cu₂Te-Sb₂Te₃ embedded in the PbTe matrix. It can be noticed that these Cu₂Te and Sb₂Te₃ always segregate in the same regions forming a microcomposite network inside the matrix. This is because according to the Cu₂Te-Sb₂Te₃ phase diagram there is a eutectic composition very close to the 50:50 atomic percent ratio.¹⁴

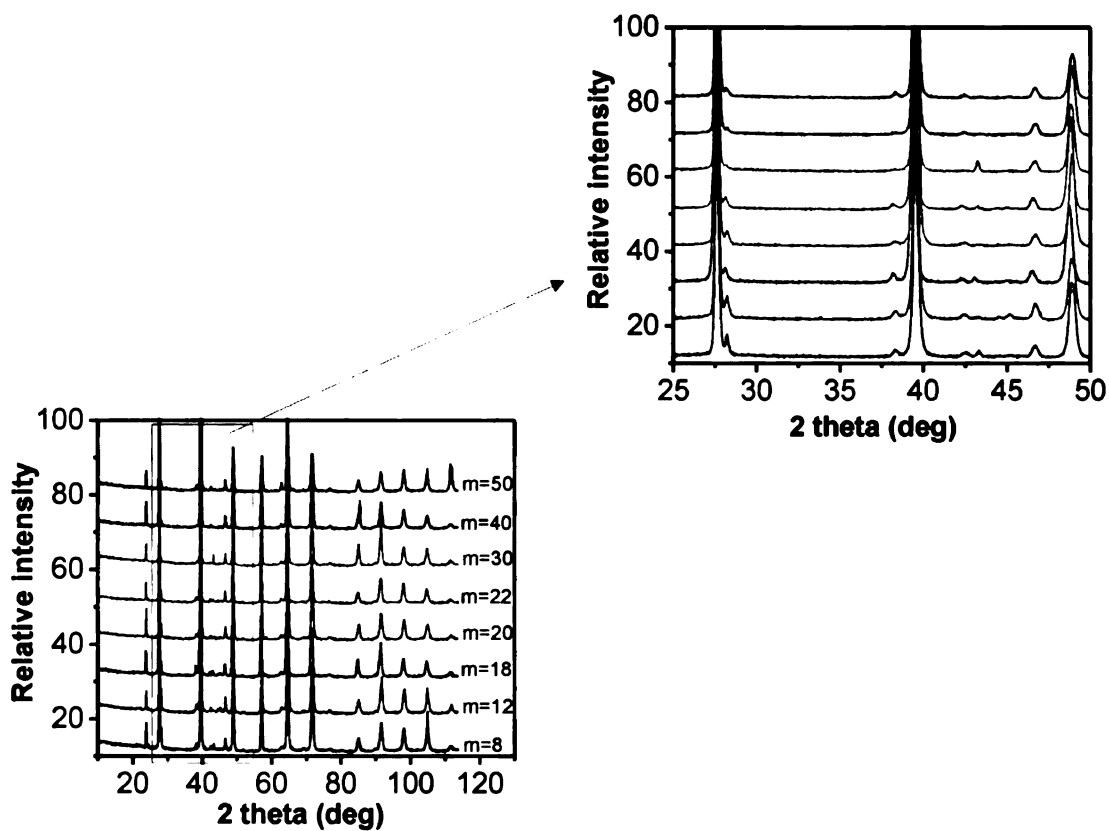


Figure 6-1. Powder X-ray diffraction of the series $\text{CuPb}_m\text{SbTe}_{m+2}$ ($m=5, 12, 18, 20, 22, 30, 40$ and 50), the area between $2\theta = 25$ and 50 deg is enlarged to show the presence of extra peaks that do not belong to the NaCl structure-type. Two small peaks at 28 and 38 deg are characteristic of Sb_2Te_3 . Small peaks $\sim 42\text{-}43$ deg belong to Cu_2Te .

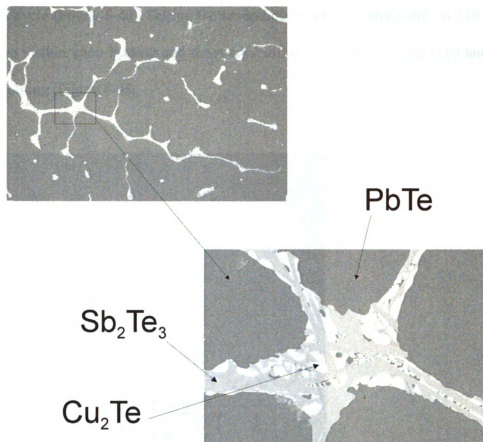


Figure 6-2. BSE images of a sample with composition $\text{CuPb}_{18}\text{SbTe}_{20}$ showing regions rich in Cu_2Te and Sb_2Te_3 embedded in the PbTe matrix. The two phases form dendritic ribbons as long as 3 mm in all directions.

Thermal Analysis. Figure 6-4a and 6-4b shows the DTA results for $\text{CuPb}_8\text{SbTe}_{10}$. A single melting point ~ 1185 K and a single crystallization point ~ 1165 K were observed upon heating and cooling. A single melting point ~ 1193 K and a single crystallization point ~ 1155 K were also visible in the case of $\text{CPb}_{30}\text{SbTe}_{32}$ (Figure 6-4c and 6-4d). For the composition $m=50$, the spectrum showed a single melting point ~ 1198 K upon cooling but two crystallization points were observed during cooling at ~ 1165 and 1139 K

during the first cycle (Figure 6-4e). During the second cycle, two melting points at 1194 and 1204 K are visible upon heating and three crystallization points ~ 1104, 1119 and 1149 K upon cooling (Figure 6-4f).

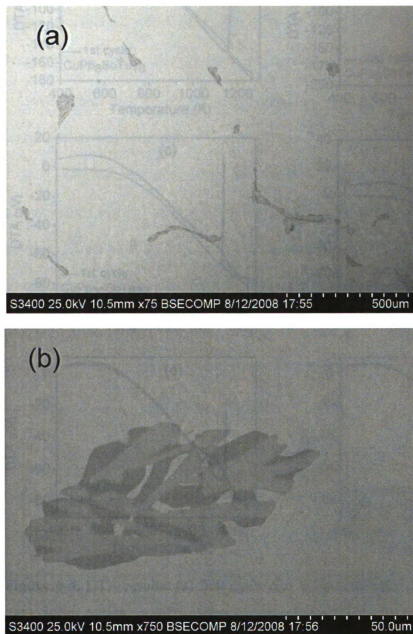


Figure 6-3. BSE images of the compound $\text{CuPb}_{40}\text{SbTe}_{42}$. More dispersed regions composed of Cu_2Te and Sb_2Te_3 are visible in the PbTe matrix.

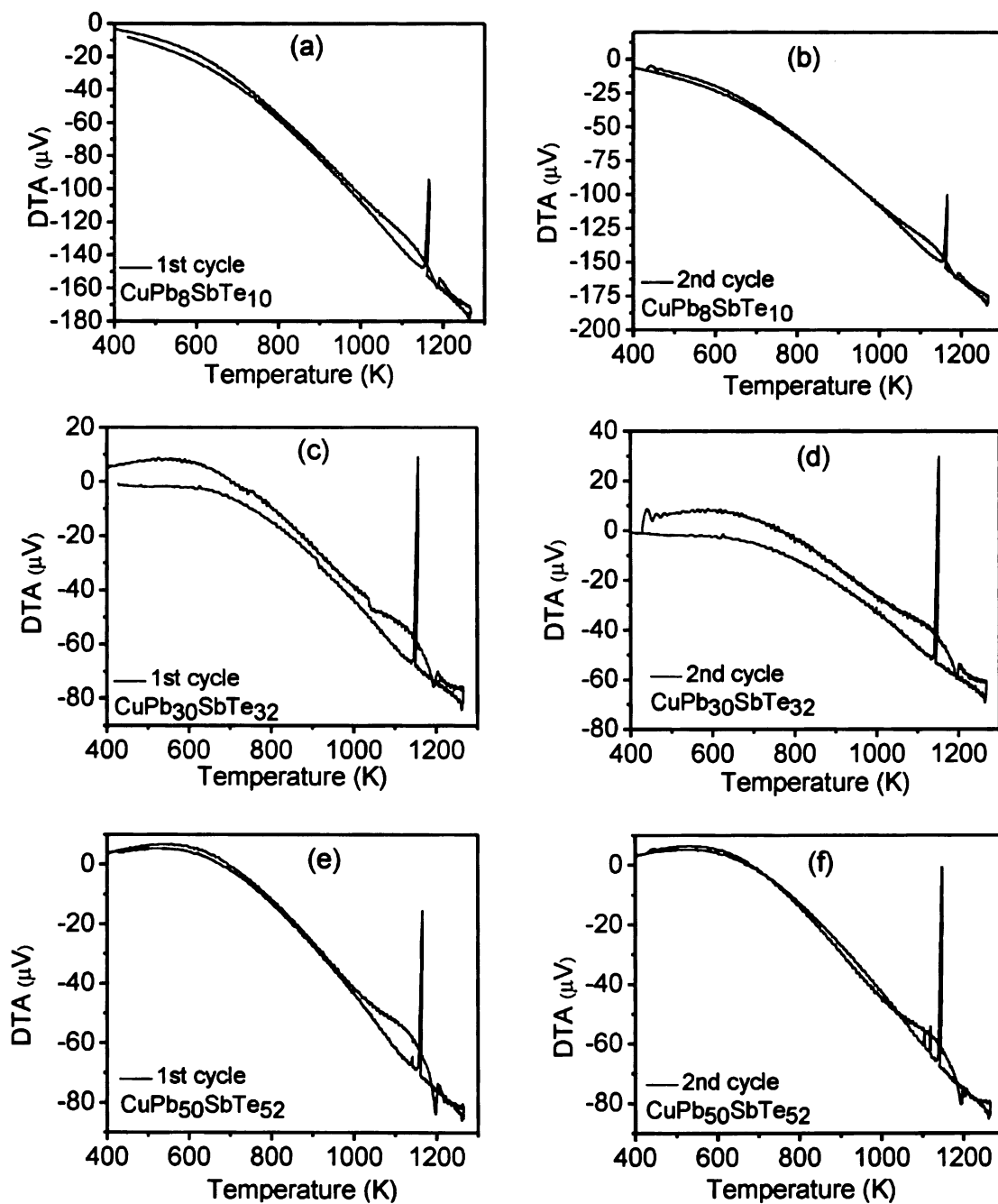


Figure 6-4. DTA results: (a) first cycle and (b) second cycle for $\text{CuPb}_8\text{SbTe}_{10}$; (c) first and (d) second cycle of $\text{CuPb}_{30}\text{SbTe}_{32}$; (e) first cycle and (f) second cycle of $\text{CuPb}_{50}\text{SbTe}_{52}$.

Electronic Transport Properties. Figure 6-5a shows the temperature dependence of the electrical conductivity for the series of compounds $\text{CuPb}_m\text{SbTe}_{m+2}$. For all compositions, the electrical conductivity decreases with increasing temperature. Except for $m=50$, other compositions exhibit similar electrical conductivity values for the range 300-725 K. Room temperature values are typically in the range 1600-1800 S/cm and decrease to ~ 400 -500 S/cm. $\text{CuPb}_{50}\text{SbTe}_{52}$ shows higher electrical conductivity at room temperature (~ 2680 S/cm) but at higher temperature no significant difference with the other compositions was observed.

The trends in thermopower are reported in Figure 6-5b. All compositions showed n-type behavior. No significant trend as a function of m can be determined. Values vary between -70 and -100 $\mu\text{V/K}$ at room temperature and ~ -150 and -205 $\mu\text{V/K}$ at 675 K. The power factor calculated from the electrical conductivity and thermopower are plotted in Figure 6-5c. In the range 300 – 500 K, the material $\text{CuPb}_{18}\text{SbTe}_{20}$ exhibits the highest power factor with a maximum value of ~ 23 $\mu\text{W/m}\cdot\text{K}^2$ at 345 K. At higher temperatures, $\text{CuPb}_{50}\text{SbTe}_{52}$ has a higher power factor.

Hall coefficient measurements were carried on the samples $\text{CuPb}_{18}\text{SbTe}_{20}$ and $\text{CuPb}_{22}\text{SbTe}_{24}$. The resulting carrier concentrations are reported on Figure 5d. For both compositions, the Hall coefficients are negative, indicated electrons as the major charge carriers. This confirms the negative sign observed for the thermopower. Room temperature carrier concentrations are respectively 1.6 and $1.7 \cdot 10^{19}$ / cm^3 . These values are lower than that measured for $\text{Na}_{0.95}\text{Pb}_{20}\text{SbTe}_{22}$ ($\sim 6 \cdot 10^{19}$ / cm^3).

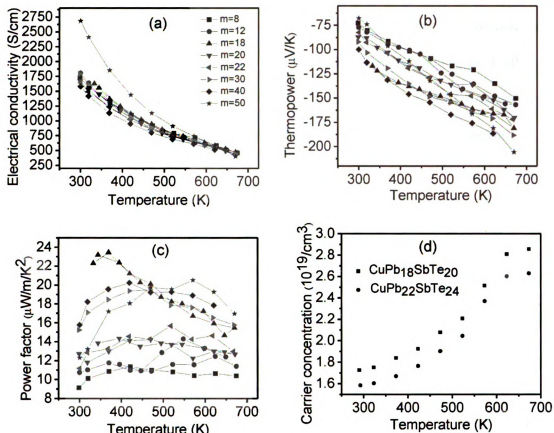


Figure 6-5. Temperature dependence of (a) the electrical conductivity, (b) the thermopower and (c) the power factor for the series $\text{CuPb}_m\text{SbTe}_{m+2}$ ($m=8, 12, 18, 20, 22, 30, 40, 50$); (d) carrier concentration as a function of temperature for $\text{CuPb}_{18}\text{SbTe}_{20}$ and $\text{CuPb}_{22}\text{SbTe}_{24}$.

Thermal Transport Properties. Thermal diffusivity measurements were collected for the compounds $m = 8, 18, 20, 30$ and 40 . The thermal conductivity values calculated from thermal diffusivity data are reported in Figure 6-6a. For all samples, the thermal conductivity decreases with temperature. The composition $\text{CuPb}_8\text{SbTe}_{10}$ exhibits higher

thermal conductivity than the other materials, with a value of ~ 3.2 W/m·K at room temperature and decreasing to ~ 2.2 W/m·K at 675 K. The compositions with $m=18, 20, 40$ have similar thermal conductivity values, starting $\sim 2.5 - 2.2$ W/m·K at room temperature and falling down to $\sim 1.4 - 1.6$ W/m·K at 675K. The sample $\text{CuPb}_{30}\text{SbTe}_{32}$ has slightly higher room temperature thermal conductivity but at high temperature the thermal conductivity is similar to that of the compounds with $m=18, 30$ and 40 .

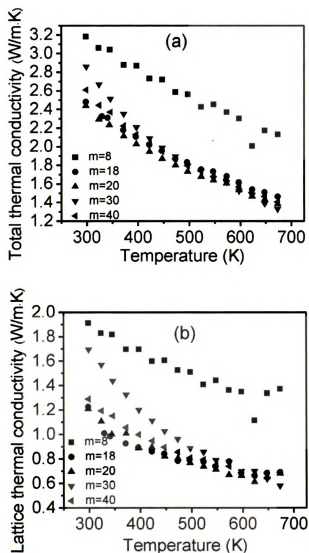


Figure 6-6. Temperature dependence of the (a) total and (b) lattice thermal conductivity for the compounds $\text{CuPb}_m\text{SbTe}_{m+2}$ ($m=8, 18, 20, 30, 40$).

The electronic contribution was estimated using the Wiedemann-Franz law and the lattice thermal conductivity was quantified by subtracting the electronic component to the total thermal conductivity. The resulting lattice components are plotted in Figure 6-6b. The highest lattice contribution was found for $\text{CuPb}_8\text{SbTe}_{10}$ with values varying between 1.9 $\text{W/m}\cdot\text{K}$ at room temperature and 1.4 $\text{W/m}\cdot\text{K}$ at 675 K. The composition $\text{CuPb}_{30}\text{SbTe}_{32}$ showed the sharpest decrease in lattice thermal conductivity with values at 675 K as low as those of $\text{CuPb}_{18}\text{SbTe}_{20}$, $\text{CuPb}_{20}\text{SbTe}_{22}$ and $\text{CuPb}_{40}\text{SbTe}_{42}$. For these three compositions, the lattice thermal conductivity varies between ~ 1.2 $\text{W/m}\cdot\text{K}$ at room temperature and ~ 0.6 - 0.7 $\text{W/m}\cdot\text{K}$ at 675K. The lattice thermal contribution for these compositions at 675 K is slightly higher than the value reported for $\text{Na}_{0.95}\text{Pb}_{20}\text{SbTe}_{22}$ (minimum lattice thermal conductivity ~ 0.55 $\text{W/m}\cdot\text{K}$ at 675 K).

From the above data, the figure of merit ZT was evaluated for the compositions $\text{CuPb}_m\text{SbTe}_{m+2}$ ($m=8, 18, 20, 30$ and 40) (Figure 6-7).

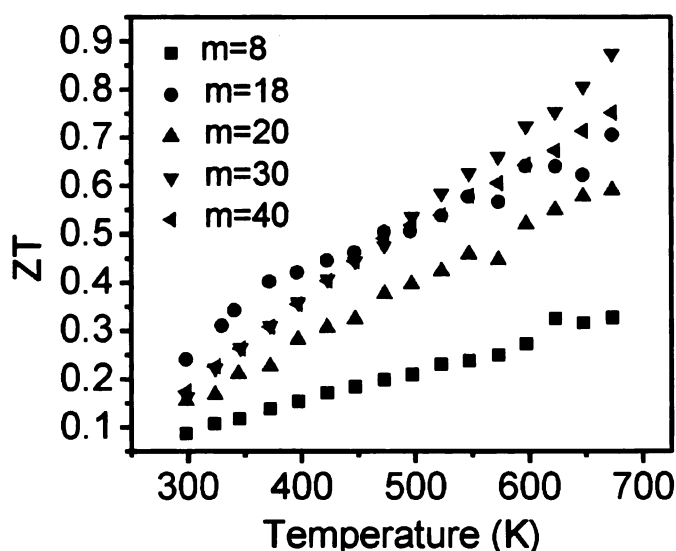


Figure 6-7. Figure of merit ZT for the compounds $\text{CuPb}_m\text{SbTe}_{m+2}$ ($m= 8, 18, 20, 30, 40$).

As expected the lowest figure of merit is found for $\text{CuPb}_8\text{SbTe}_{10}$. For the other compositions, the figure of merit increases more rapidly with temperature. The maximum $ZT \sim 0.85$ is achieved at 675 K for $\text{CuPb}_{30}\text{SbTe}_{32}$.

6.3. $\text{CuPb}_{18-x}\text{Sn}_x\text{SbTe}_{20}$ ($x=0, 5, 9, 13, 18$)

6.3.1. Experimental section

Synthesis. The samples were prepared following the same procedure as that described above for the $\text{CuPb}_m\text{SbTe}_{m+2}$ series. Table 6-2 summarizes the amount of material used for each composition.

Table 6-2. Amount of elements used for to prepare the series $\text{CuPb}_{18-x}\text{Sn}_x\text{SbTe}_{20}$.

Composition	Cu, g (mmol)	Pb, g (mmol)	Sn, g (mmol)	Sb, g (mmol)	Te, g (mmol)
$\text{CuPb}_{18}\text{SbTe}_{20}$	0.1046 g (1.65)	6.1391 g (29.63)	0	0.2004 g (1.65)	4.2007 g (32.92)
$\text{CuPb}_{13}\text{Sn}_5\text{SbTe}_{20}$	0.1246 g (1.96)	5.2816 g (25.49)	1.1638 g (9.80)	0.2387 g (1.96)	5.0039 g (39.22)
$\text{CuPb}_9\text{Sn}_9\text{SbTe}_{20}$	0.1223 g (1.92)	3.5890 g (17.32)	2.0562 g (17.32)	0.2343 g (1.92)	4.9116 g (38.49)
$\text{CuPb}_5\text{Sn}_{13}\text{SbTe}_{20}$	0.1323 g (2.08)	2.1569 g (10.41)	3.2129 g (27.07)	0.2535 g (2.08)	5.3132 g (41.64)
$\text{CuSn}_{18}\text{SbTe}_{20}$	0.1781 g (2.80)	0	5.9887 g (50.45)	0.3413 g (2.80)	7.1525 g (56.05)

The synthesized compounds were characterized by powder X-ray diffraction, scanning electron microscopy. Electronic transport properties and thermal diffusivity data of the samples were also measured.

6.3.2. Results and discussion

Structure and Characterization. Figure 6-8 shows the powder X-ray diffraction patterns of (a) $\text{CuPb}_{18}\text{SbTe}_{20}$, (b) $\text{CuPb}_9\text{Sn}_9\text{SbTe}_{20}$ and (c) $\text{CuSn}_{18}\text{SbTe}_{20}$. It can be observed that the peaks corresponding to Sb_2Te_3 get weaker as the content of Sn increases. The peaks corresponding to Cu_2Te are present for all compositions.

Scanning Electron Microscopy. In order to have complementary information about the presence of other phases in the PbTe matrix, BSE imaging was performed on different samples. Figure 6-9 shows two pictures obtained for the sample $\text{CuPb}_{13}\text{Sn}_5\text{SbTe}_{20}$. Regions with different compositions are visible in the PbTe matrix. EDS analysis on area 1 gave the results: Cu: 2.5 %, Pb: 6.20 %, Sb 28.40% and Te: 62.90%. EDS on area 2 indicated Cu: 63.42% and Te 36.88 %. As we saw for $\text{CuPb}_m\text{SbTe}_{m+2}$, phases rich in Cu_2Te and Sb_2Te_3 precipitate in the PbTe matrix during the cooling process. In the case of $\text{CuPb}_{13}\text{Sn}_5\text{SbTe}_{20}$, the regions containing Cu_2Te and Sb_2Te_3 form more complex composite areas. Similar features were observed for $\text{CuPb}_9\text{Sn}_9\text{SbTe}_{20}$ (Figure 6-10a) and $\text{CuPb}_5\text{Sn}_{13}\text{SbTe}_{20}$ (Figure 6-10b). BSE imaging on the compound $\text{CuSn}_{18}\text{SbTe}_{20}$ is different from what was obtained for the compositions discussed above (Figure 6-11). Only regions with compositions Cu_2Te embedded in the SnTe matrix were visible. No Sb_2Te_3 phase was observed in the SnTe matrix, confirming the powder X-ray data. Sb and Sn have close radii; as a consequence, Sb atoms can easily substitute Sn atoms.

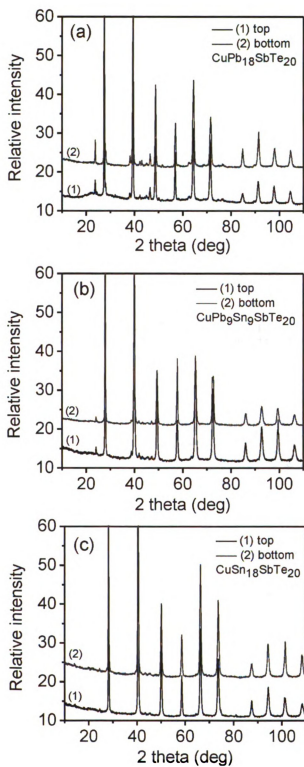


Figure 6-8. Powder X-ray diffraction for (a) $\text{CuPb}_{18}\text{SbTe}_{20}$, (b) $\text{CuPb}_9\text{Sn}_9\text{SbTe}_{20}$ and (c) $\text{CuSn}_{18}\text{SbTe}_{20}$.

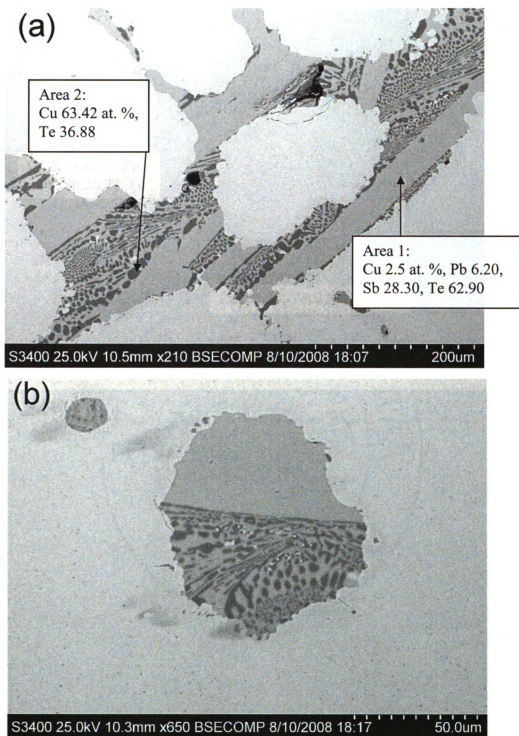


Figure 6-9. BSE images of $\text{CuPb}_{13}\text{Sn}_5\text{SbTe}_{20}$. Complex regions rich in Cu_2Te and Sb_2Te_3 are clearly visible in the $\text{Pb}_{1-x}\text{Sn}_x\text{Te}$ matrix.

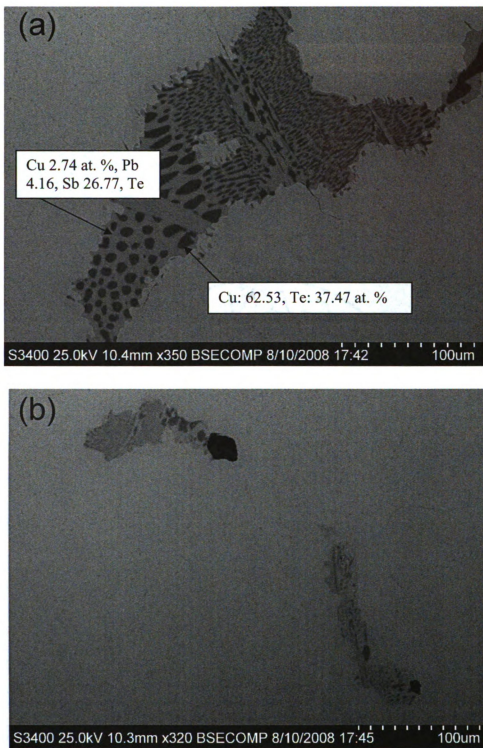


Figure 6-10. BSE images of (a) $\text{CuPb}_9\text{Sn}_9\text{SbTe}_{20}$ and (b) $\text{CuPb}_5\text{Sn}_{13}\text{SnTe}_{20}$.

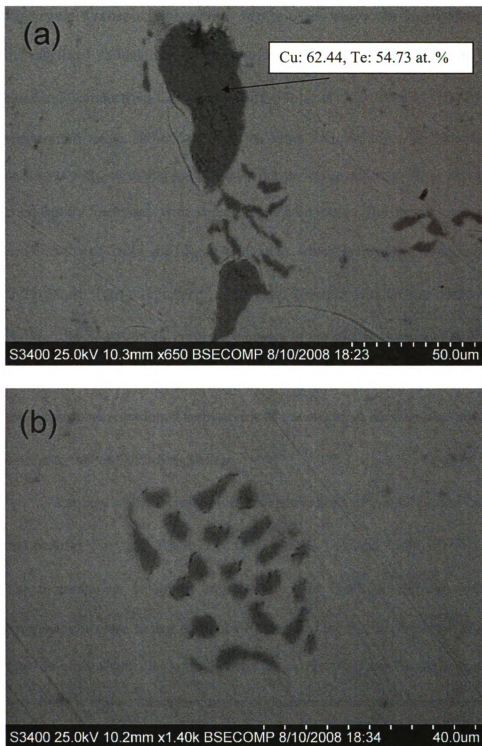


Figure 6-11. BSE images obtained for $\text{CuSn}_{18}\text{SbTe}_{20}$. Only Cu_2Te regions segregated in the SnTe matrix.

Electronic Transport Properties. Figure 6-12a shows the temperature dependence of the electrical conductivity for the series $\text{CuPb}_{18-x}\text{Sn}_x\text{SbTe}_{20}$ ($x=0, 5, 9, 13, 18$). The electrical conductivity of $\text{CuPb}_{13}\text{Sn}_5\text{SbTe}_{20}$ is low (below 100 S/cm) over the temperature range 300-675 K. For the other compositions, the electrical conductivity decreases with increasing temperature. For the composition $x=9, 13$ and 18, the electrical conductivity increases with decreasing Pb:Sn ratio. The room temperature electrical conductivity of $\text{CuSn}_{18}\text{SbTe}_{20}$ is 4100 s/cm, which is three times the value measured for $\text{CuPb}_9\text{Sn}_9\text{SbTe}_{20}$ (~ 1150 S/cm). This trend is similar to what was observed for the series $\text{NaPb}_{18-x}\text{Sn}_x\text{SbTe}_{20}$. This dramatic increase in the electrical conductivity with addition to Sn is consistent with the high electrical conductivity of SnTe, which drastically increases the carrier concentration. The behavior of the electrical conductivity of $\text{CuPb}_{18}\text{SbTe}_{20}$ is similar to that of $\text{CuPb}_5\text{Sn}_{13}\text{SbTe}_{20}$.

The sign of the thermopower is negative for $\text{CuPb}_{18}\text{SbTe}_{20}$ and $\text{CuPb}_{13}\text{Sn}_5\text{SbTe}_{20}$ and positive for $\text{CuPb}_9\text{Sn}_9\text{SbTe}_{20}$, $\text{CuPb}_5\text{Sn}_{13}\text{SbTe}_{20}$ and $\text{CuSn}_{18}\text{SbTe}_{20}$ (Figure 6-12b). The thermopower is almost equal to zero for $\text{CuPb}_{13}\text{Sn}_5\text{SbTe}_{20}$, indicating that for compositions close to that particular Pb:Sn ratio the thermopower switches from n- to p-type. In other words, for compositions $x < 5$, electrons are the main charge carriers. For $x=5$, there is almost the same number of positive and negative charge carriers. As a result, the thermopower for that particular composition is almost zero. For n-type behavior, a maximum thermopower of ~ - 225 $\mu\text{V/K}$ was obtained for $\text{CuPb}_{13}\text{Sn}_5\text{SbTe}_{20}$ at 475 K.

For p-type samples, the highest thermopower was found for $\text{CuPb}_9\text{Sn}_9\text{SbTe}_{20}$ ($\sim 200 \mu\text{V/K}$ at 550 K).

The power factors obtained from the above data are plotted in Figure 6-12c. In the temperature range 300-625 K, the sample $\text{CuPb}_{18}\text{SbTe}_{20}$ exhibits the highest power factors with room temperature values $\sim 23 \mu\text{W/cm}\cdot\text{K}^2$. For the compositions $x=0$ and $x=9$, the power factor reaches a maximum and then slowly goes down whereas for $x=13$ and $x=18$, the power factor starts from very low values at room temperature and constantly increases till 675 K. At 75 K, the compounds $x=0$ and $x=18$ have similar power factor, $\sim 14\text{-}15 \mu\text{W/cm}\cdot\text{K}^2$. Such high values derive from a relatively high thermopower for $\text{CuPb}_{18}\text{SbTe}_{20}$ and a relatively high electrical conductivity for $\text{CuSn}_{18}\text{SbTe}_{20}$.

Thermal Transport Properties. Thermal diffusivity measurements were collected for $\text{CuSn}_{18}\text{SbTe}_{20}$ as that composition exhibited high power factor at high temperature. Figure 6-13 shows the total, electronic and lattice thermal conductivity of the sample. The room temperature total thermal conductivity is high compared to $\text{CuPb}_{18}\text{SbTe}_{20}$, the main reason being the high electrical conductivity of the sample. As a result, the electronic component of the thermal conductivity is high ($\sim 3 \text{ W/m}\cdot\text{K}$). From 300-675 K, the electronic contribution dominates the thermal conductivity. The lattice thermal conductivity ranges from $3 \text{ W/m}\cdot\text{K}$ at 300 K to $\sim 1.2 \text{ W/m}\cdot\text{K}$ at 675 K. As a result, the figure of merit ZT does not exceed 0.3 at 675 K.

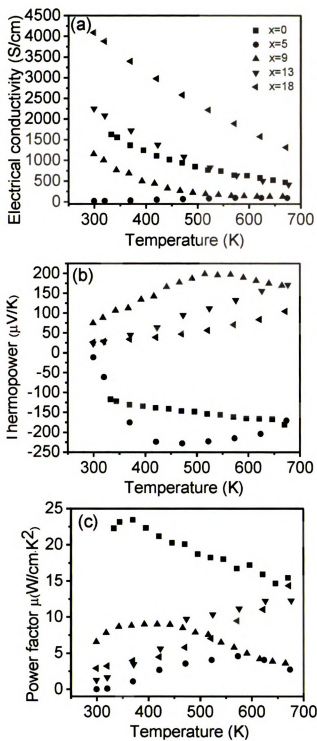


Figure 6-12. Temperature dependence of the (a) electrical conductivity, (b) thermopower and (c) power factor of the series $\text{CuPb}_{18-x}\text{Sn}_x\text{SbTe}_{20}$ ($x=0, 5, 9, 13, 18$).

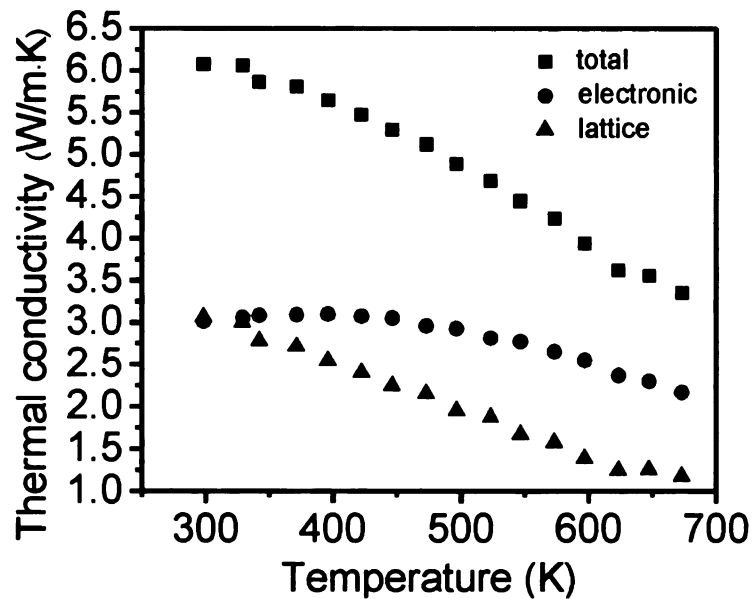


Figure 6-13. Total, electronic and lattice thermal conductivities of $\text{CuSn}_{18}\text{SbTe}_{20}$.

6.4. Investigation of the system Cu/Sb/Te.

6.4.1. Motivation

BSE studies on the compounds $\text{CuPb}_m\text{SbTe}_{m+2}$ and $\text{CuPb}_{18-x}\text{Sn}_x\text{SbTe}_{20}$ showed the presence of Cu_2Te and Sb_2Te_3 as second phases inside the cubic matrix. No ternary phase such as CuSbTe_2 was observed. In the system Ag/Sb/Te, AgSbTe_2 is a compound known since 1957.¹⁵ AgSbTe_2 crystallizes in the NaCl structure with similar lattice constant that PbTe.¹⁶ Rosi and al. recognized the potential of AgSbTe_2 as a thermoelectric material.¹⁷

It has a large thermopower $\sim 200 \mu\text{V/K}$ ^{18, 19} and low lattice thermal conductivity ($\sim 0.6 \text{ W/m}\cdot\text{K}$).^{19, 20} Experiments indicated that the Ag and Sb atoms in the structure may not be randomly occupying the Na-sites of the NaCl lattice.⁷ Recent electronic structure

calculations showed that the lowest energy structure is one where Ag and Sb atoms are ordered.²¹ This could be the explanation of the low lattice thermal conductivity reported for the material. In the Cu system, contradictory reports on the possible existence of the phase CuSbTe₂ can be found in the literature.²²⁻²⁴ To check on the existence of such a phase, several reactions were prepared using different cooling profiles.

6.4.2. Experimental section

Synthesis. Mixtures of elemental Cu, Sb and Te with ratio 1:1:2 were loaded in three 10 mm outer diameter, carbon-coated silica tubes in ambient atmosphere. The tubes were heated up to 1373 K and kept at that temperature 6 hours. Three different cooling profiles were studied. In the first case, the tube was quenched in water; the second case, the tube was quenched in air. The last tube was slow cooled to 550 °C in 55 hours followed by a fast cooling to 323 K. The furnaces were kept in vertical position during the reaction. Another tube was prepared using similar slow cooling profile but during the time spent at 1373 K, the furnace was rocked during 2 hours to ensure good homogeneity of the liquid phase.

Powder X-ray Diffraction. Same procedure as described in part 2.

Scanning Electron Microscopy. Same procedure as described in part 2.

Electrical Transport Properties. Same procedure as described in part 2.

6.4.3. Results and discussion

Structure and Characterization. The samples had good mechanical properties and were cut into halves with a diamond saw. The presence of two phases could be observed by

eye on the cut surfaces. Figure 6-14 shows the X-ray powder diffraction patterns from the samples prepared without rocking the furnace during the synthesis. Analysis of the patterns indicated the materials to be a mixture of Cu_2Te and Sb_2Te_3 . The same result was observed for the sample prepared by rocking the furnace.

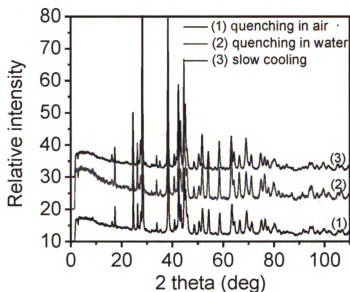


Figure 6-14. Powder X-ray diffraction patterns for samples with nominal composition CuSbTe_2 prepared by water-quenching, air-quenching and slow cooling.

Scanning Electron Microscopy. The BSE study of the samples confirmed the presence of Cu_2Te and Sb_2Te_3 . BSE imaging from the sample quenched in water are shown in Figure 6-15. Sb_2Te_3 strips (clear areas) are embedded in a Cu_2Te matrix (darker area). For the sample cooled in air (Figure 6-16), the features of Sb_2Te_3 regions are less regular and more complex compared to the case of quenching in water. In the case of slow cooling (Figure 6-17), Sb_2Te_3 strips run in all directions. Figure 18 shows BSE images of

the samples for which the furnace was rocked during the reaction. Cu_2Te regions (dark areas, oriented in different directions) are embedded in the Sb_2Te_3 (clear areas).

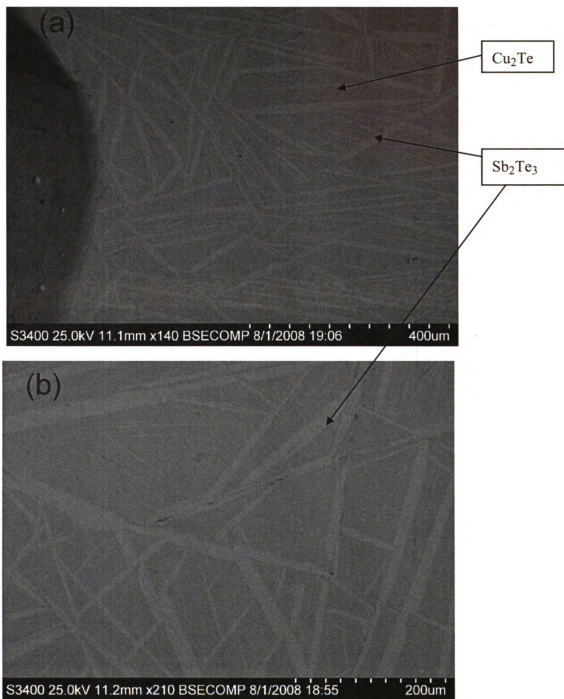


Figure 6-15. BSE images of the sample with nominal composition CuSbTe_2 quenched in water.

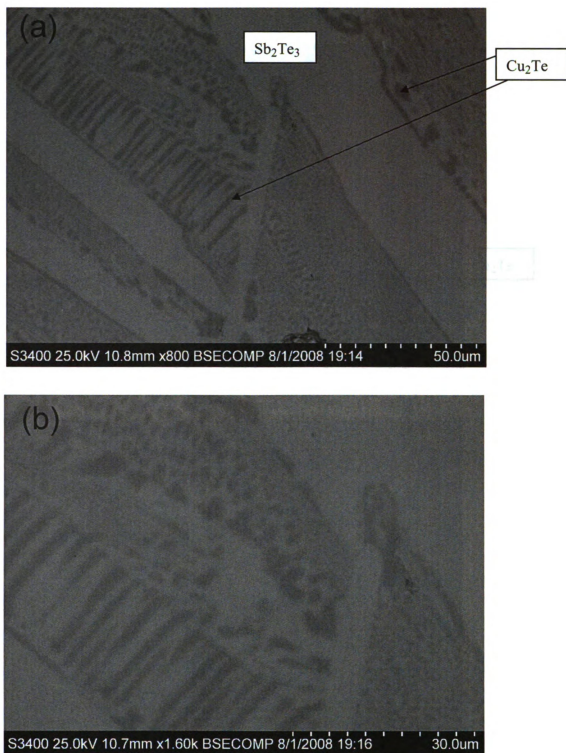


Figure 6-16. BSE images of the sample with nominal composition CuSbTe_2 quenched in air.

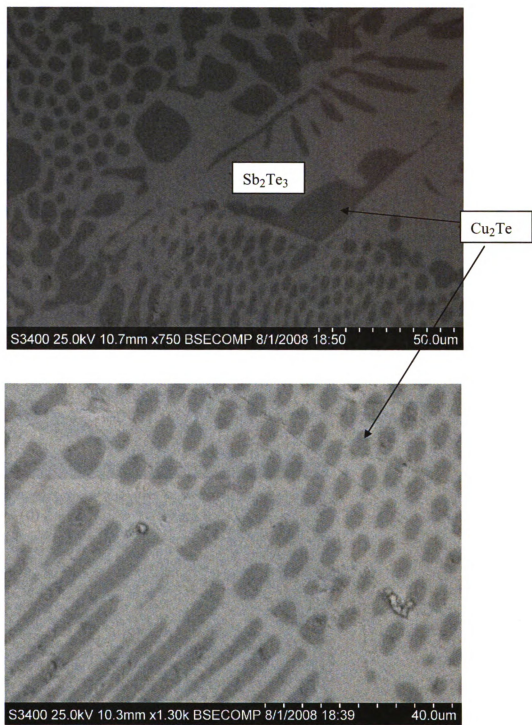


Figure 6-17. BSE images of the sample with nominal composition CuSbTe_2 prepared by slow cooling.

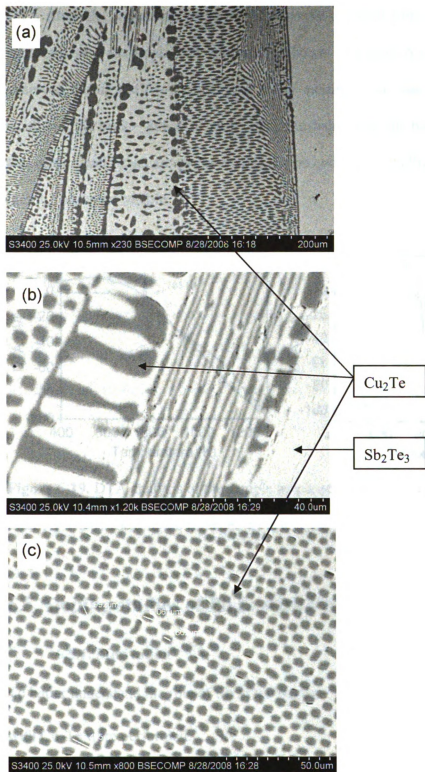


Figure 6-18. BSE imaging of a sample prepared with nominal composition CuSbTe_2 with the furnace being rocked during the reaction.

DTA Analysis. An amount of 35 mg of a sample prepared with a rocking step during the synthesis was analyzed. The results are shown in Figure 6-19. Similar results were observed during the two cycles. One major melting point was observed at ~ 785 K. A small melting peak ~ 806 K is hardly distinguishable from the background. About 623 K, two other small peaks are hardly visible. Upon cooling, crystallization points close to the melting peaks are visible.

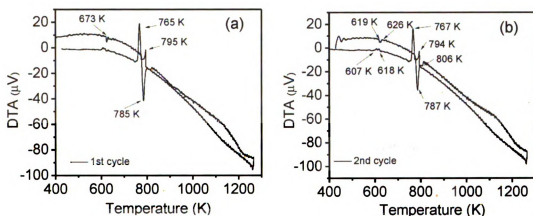


Figure 6-19. DTA analysis of the sample prepared by mixing Cu, Sb and Te with the ratio 1:1:1:2 by rocking the furnace: (a) first cycle, (b) 2nd cycle.

6.5. Doping studies of PbTe with Cu_2Te

6.5.1. Motivation

To better understand the role of Sb in the system $\text{CuPb}_m\text{SbTe}_{m+2}$, doping studies of PbTe with Cu_2Te were performed.

6.5.2. Experimental section

Synthesis. Direct combinations of elemental Cu, Pb and Te were mixed with appropriate ratios in order to dope PbTe with 1, 2 and 5 % Cu₂Te. The tubes (10mm outer diameter, carbon-coated) were sealed under residual pressure. Then they were heated up to 1373 K and kept at that temperature for four hours. While molten, the furnace was rocked for 2 hours to facilitate complete mixing and homogeneity of the liquid phase. The furnace was finally immobilized in the vertical position and cooled down to 820 K in 55 hours followed by a fast cooling to room temperature.

Powder X-ray Diffraction. Same procedure as described in part 1.

Scanning Electron Microscopy. Same procedure as described in part 1.

Electrical transport properties. Same procedure as described in part 1.

6.5.3. Results and discussion

Structure and Characterization. Additional peaks than those characteristic of the PbTe phase are clearly visible in the powder X-ray diffraction patterns for the 5% doping sample (Figure 6-20). For the 1 and 2 % doping compositions, these peaks are hardly distinguishable from the background.

Scanning Electron Microscopy. In order to examine the composition of these materials, BSE imaging on polished samples were performed. Figure 6-21 shows results for the 5% doping sample. Darker areas correspond to the Cu₂Te phase. As the doping level decreases, the Cu₂Te phases get more dispersed and are hardly visible in the case of 1 % doping composition (Figure 6-22b).

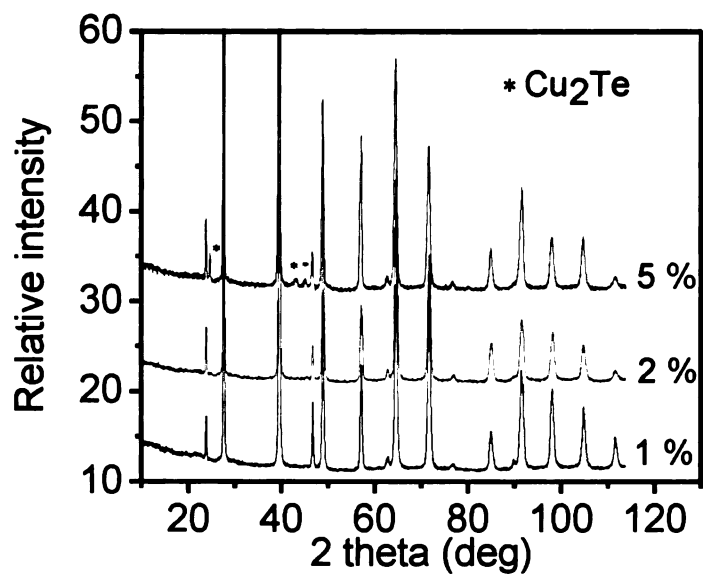


Figure 6-20. Powder X-ray diffraction of PbTe doped with 1, 2 and 5 % Cu₂Te. The small stars indicate diffraction peaks that do not belong to the PbTe structure-type and indicate the presence of Cu₂Te as a minor phase.

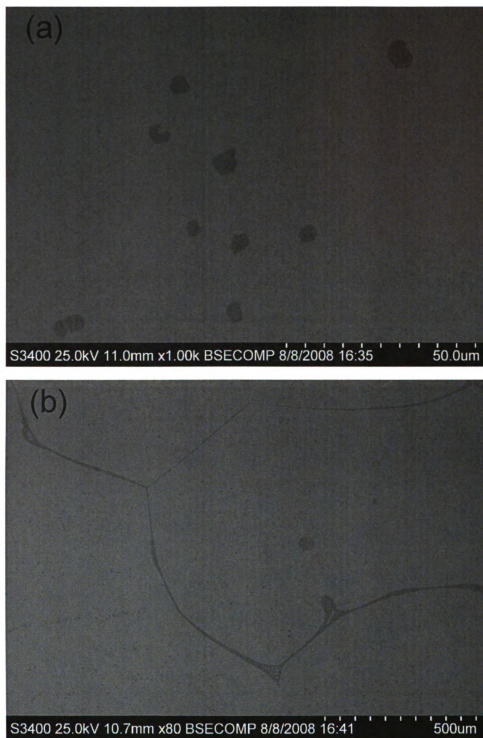


Figure 6-21. BSE images of PbTe doped with 5 % Cu₂Te.

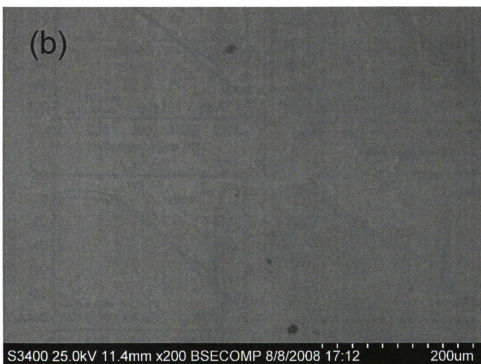
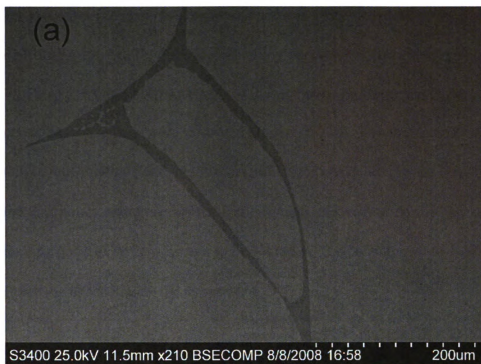


Figure 6-22. BSE images of PbTe samples doped with (a) 2 % and (b) 1 % Cu_2Te .

DTA Analysis. Figure 6-23a shows the result obtained during the first run for PbTe doped with 1% Cu₂Te. One single melting point and one single crystallization point are visible at 1208 and 1170 K. However during the second run, two melting points and two crystallization points were observed (Figure 6-23b). For the sample doped with 2 % Cu₂Te, one melting point and two crystallization peaks are present (Figure 6-23c). Three melting points and three crystallization points are visible during the second run. The melting point of PbTe is known to be ~ 1196 K. Cu₂Te is known to exist under different structures depending on the temperature.

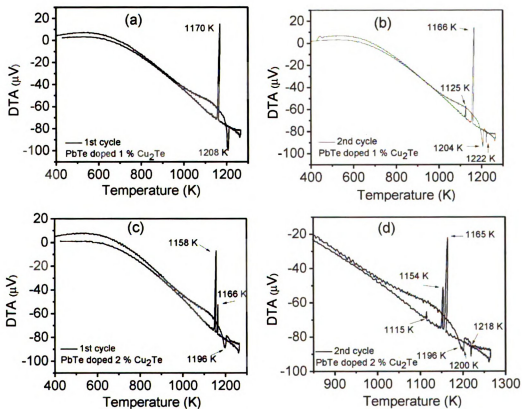


Figure 6-23. Differential thermal analysis results for (a) the first run and (b) second for the PbTe doped with 1% Cu₂Te; (c) the first run and (d) second run of PbTe doped with 2 % Cu₂Te.

Electronic Transport Properties. Data were collected for the 1 and 2 % Cu_2Te doping compositions (Figure 6-24). It must be noticed that after the measurements, the aspect of the surface changed and looked dark blue. EDS analysis on the surface after measurement gave the following atomic percentages: Pb: 46.05, Cu: 32.59, Te: 35.71. As a consequence, measurements upon heating and cooling showed a hysteresis due to thermal instability.

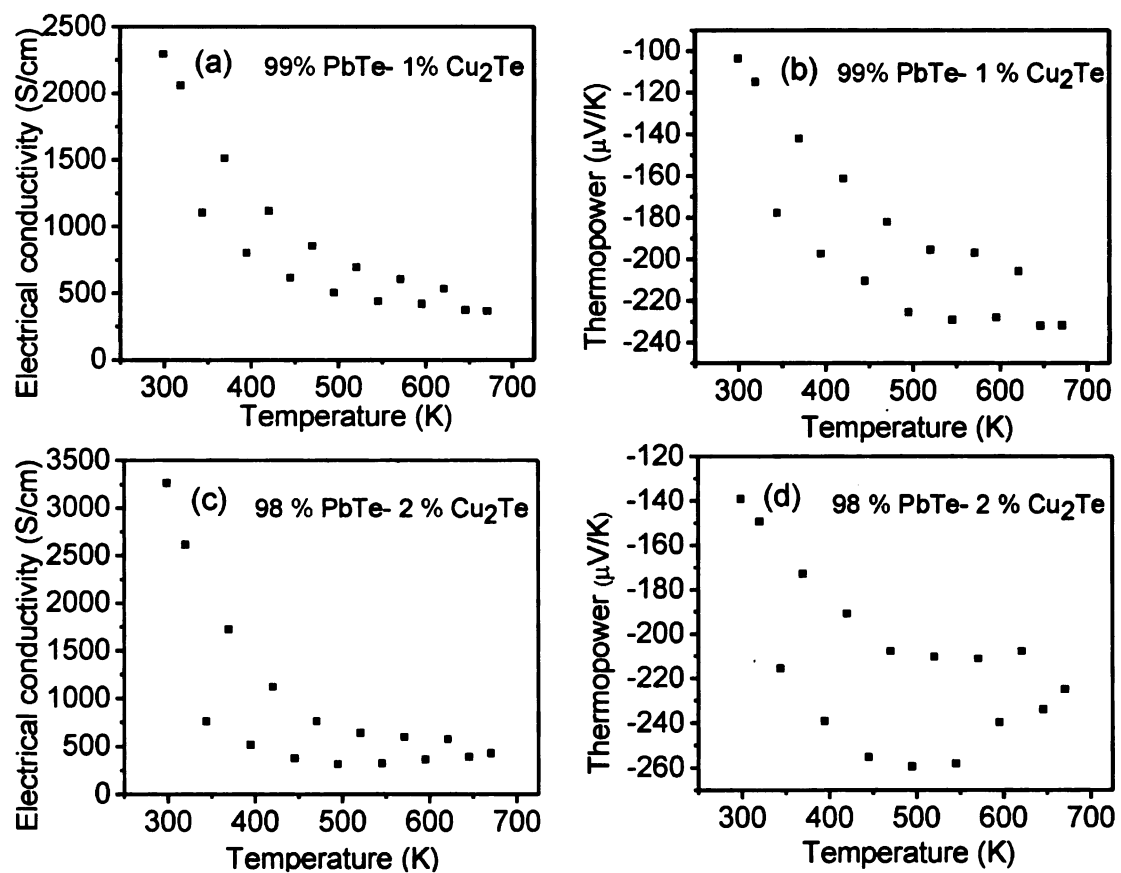


Figure 6-24. Temperature dependence of (a) the electrical conductivity and (b) the thermopower of PbTe doped with 1 % Cu_2Te , temperature dependence of (c) the electrical conductivity and (d) the thermopower of PbTe doped with 2 % Cu_2Te .

6.6. Conclusions

Powder X-ray diffraction and BSE characterizations on samples $\text{CuPb}_m\text{SbTe}_{m+2}$ and $\text{CuPb}_{18-x}\text{Sn}_x\text{SbTe}_{20}$ indicate that Cu_2Te and Sb_2Te_3 phases precipitate together in the PbTe and $\text{Pb}_{1-x}\text{Sn}_x\text{Te}$ matrices. These regions are micro-size and run along all directions. No ternary phase in the system Cu/Sb/Te was observed. Attempts to prepare the compound CuSbTe_2 using either fast or slow cooling resulted in a mixture of Cu_2Te and Sb_2Te_3 . CuSbTe_2 does not seem to be a stable nor a metastable phase. Electrical conductivity measurements on $\text{CuPb}_m\text{SbTe}_{m+2}$ ($m=8, 18, 20, 22, 30, 40$) indicated values between 1800 S/cm at 300 K and ~ 400 S/cm at 675 K. This is similar to the values reported for $\text{AgPb}_{18}\text{SbTe}_{20}$. The presence of the micro-size inclusions in the cubic matrix does not seem to affect the electrical conductivity. The thermopower at high temperatures has values $\sim -150, -180$ $\mu\text{V/K}$, which are not as high as those of $\text{AgPb}_{18}\text{SbTe}_{20}$. Further doping studies may result in materials with higher thermopowers. The highest power factor was obtained $\text{CuPb}_{18}\text{SbTe}_{20}$. The lattice thermal conductivities for $m= 18, 20$ and 40 are ~ 1.2 $\text{W/m}\cdot\text{K}$ at room temperature. At 675 K, the lattice thermal conductivity falls down to ~ 0.6 $\text{W/m}\cdot\text{K}$. Partial substitution of Pb by Sn results in an increase in hole concentration in the system. For compositions close to $\text{CuPb}_{13}\text{Sn}_5\text{SbTe}_{20}$, holes become the major charge carriers and the thermopower changes from n- to p-type. The electrical conductivity also increases with increasing amount of Sn. The presence of Sb_2Te_3 seems to improve the thermal stability of the $\text{CuPb}_m\text{SbTe}_{m+2}$ and $\text{CuPb}_{18-x}\text{Sn}_x\text{SbTe}_{20}$. PbTe

samples doped only with Cu_2Te exhibited thermal instability issues associated with Cu migrating towards the surface of the sample.

References

1. Hicks, L. D.; Dresselhaus, M. S., *Phys. Rev. B* **1993**, 47, (19), 12727.
2. Hicks, L. D.; Harman, T. C.; Dresselhaus, M. S., *Appl. Phys. Lett.* **1993**, 63, 3230.
3. Sofo, J. O.; D., M. G., *Appl. Phys. Lett.* **1994**, 65, 2690.
4. Harman, T. C.; Taylor, P. J.; Spears, P. J.; Walsh, M. P., *J. Electron. Mater.* **2000**, 29, L1.
5. Harman, T. C.; Spears, P. J.; Manfra, M. J., *J. Electron. Mater.* **1996**, 25, 1121.
6. Hsu, K. F.; Loo, S.; Guo, F.; Chen, W.; Dyck, J. S.; Uher, C.; Hogan, T.; Polychroniadis, E. K.; Kanatzidis, M. G., *Science* **2004**, 303, 818.
7. Quarez, E.; Hsu, K. F.; Pcionek, R.; Frangis, N.; Polychroniadis, E. K.; Kanatzidis, M. G., *J. Am. Chem. Soc.* **2005**, 127, 9177.
8. Androulakis, J.; Lin, C. H.; Kong, H. J.; Uher, C.; Wu, C. I.; T., H.; Cook, B. A.; T., C.; Paraskevopoulos, M.; Kanatzidis, M. G., *J. Am. Chem. Soc.* **2007**, 129, 9780.
9. Poudeu, P. F. P.; D'Angelo, J.; Kong, H. J.; Short, J. L.; Pcionek, R.; Hogan, T.; Uher, C.; Kanatzidis, M. G., *J. Am. Chem. Soc.* **2006**, 128, 14347.
10. Poudeu, P. F. P.; D'Angelo, J.; Downey, A. D.; Short, J. L.; Hogan, T.; Kanatzidis, M. G., *Angew. Chem., Int. Ed.* **2006**, 45, 3835.
11. Androulakis, J.; Hsu, K. F.; Pcionek, R.; Kong, H. J.; Uher, C.; D'Angelo, J.; Downey, A. D.; Hogan, T.; Kanatzidis, M. G., *Adv. Mater.* **2006**, 18, 1170.
12. Kittel, C., *Introduction to Solid State Physics*. Wiley: 2005.
13. Henger, G.; Peretti, E. A., *Journal of the Less-Common Metals* **1965**, 8, 124.
14. Kuliev, R. A.; Krestovnikov, A. N.; Glazov, V. M., *Zhurnal Fizicheskoi Khimii* **1969**, 43, (12), 3063-6.

15. Wernick, J. H.; Benson, K. E., *Physics and Chemistry of solids* **1957**, 3, 157.
16. Geller, S.; Wernick, J. H., *Acta Crystallographic* **1959**, 12, 46.
17. Rosi, F. D.; Hockings, E. F.; Lindenblad, N. E., *RCA Rev.* **1961**, 22, 121.
18. Irie, T.; Takahama, T.; Ono, T., *Jpn. J. Appl. Phys.* **1963**, 2, 72.
19. Wolfe, R.; Wernick, J. H.; Haszko, S. E., *J. Appl. Phys.* **1960**, 31, 1959.
20. Hockings, E. F., *J. Phys. Chem. Solids* **1959**, 10, 341.
21. Ye, L.-H.; Hoang, K.; Freeman, A. J.; Mahanti, S. D.; He, J.; Tritt, T. M.; Kanatzidis, M. G., *Phys. Rev. B* **2008**, 7, 245203.
22. Zhuse, V. P.; Sergeeva, V. M.; Shtrum, E. L., *Zhurnal Tekhnicheskoi Fiziki* **1958**, 3, 1925.
23. Kuliev, R. A.; Kretonikov, A. N.; Glazov, V. M., *Russian Journal of Physical Chemistry* **1969**, 43, 12.
24. Sharaf, K. A.; Abdel Mohsen, N.; Naser, S.; Abou El-Ela, A. F. H., *Fizika (Zagreb)* **1991**, 23, (4), 317-23.

Chapter 7

Conclusion and Future Directions

For low temperature thermoelectric applications, the highest figure of merit reported in the past decade is for CsBi_4Te_6 ($ZT \sim 0.8$ at 225 K).^{1, 2} The material exhibits features suitable for thermoelectric properties. The Cs atoms weakly bonded to the $[\text{Bi}_4\text{Te}_6]^-$ framework act as rattlers and contribute to the reduction of the lattice thermal conductivity. Moreover the existence of Bi-Bi bonds within the framework results in a very narrow band gap. Using CsBi_4Te_6 as a platform for exploratory synthesis, the introduction of Pb in the anionic framework resulted in the discovery of the homologous family $\text{CsPb}_m\text{Bi}_3\text{Te}_{5+m}$ ($m=1, 2, 3, 4$).^{3, 4} The crystal structure of these compounds is similar to that of CsBi_4Te_6 , the main difference being the loss of Bi-Bi bonds due to the mixed occupancy of the Bi sites with Pb in the layered framework. The electronic properties of the four members are not as promising as those of CsBi_4Te_6 . Substituting Pb and Cs by other elements may be a tool to tune the electronic properties. In the first chapter of this dissertation, attempts to substitute Pb and Cs by other elements in $\text{CsPbBi}_3\text{Te}_6$, the first member of the homologous family $\text{CsPb}_m\text{Bi}_3\text{Te}_{5+m}$, were reported. The reactions lead to the discovery of nine new compounds $\text{Cs}_{0.76}\text{K}_{0.74}\text{Bi}_{3.5}\text{Te}_6$ (1), $\text{CsNa}_{0.98}\text{Bi}_{4.01}\text{Te}_7$ (2), $\text{Cs}_{0.69}\text{Ca}_{0.65}\text{Bi}_{3.34}\text{Te}_6$ (3), $\text{Rb}_{0.82}\text{Pb}_{0.82}\text{Bi}_{3.18}\text{Te}_6$ (4), $\text{Rb}_{0.19}\text{K}_{1.31}\text{Bi}_{3.50}\text{Te}_6$ (5), $\text{RbSnBi}_3\text{Te}_6$ (6), $\text{Rb}_{0.94}\text{Ca}_{0.94}\text{Bi}_{3.06}\text{Te}_6$ (7), $\text{RbYbBi}_3\text{Te}_6$ (8) and

KSnSb₃Te₆ (9). Refinements of single crystal X-ray diffraction data indicated that Cs_{0.74}K_{0.76}Bi_{3.5}Te₆, Cs_{0.69}Ca_{0.65}Bi_{3.34}Te₆, Rb_{0.82}Pb_{0.82}Bi_{3.18}Te₆, Rb_{0.19}K_{1.31}Bi_{3.50}Te₆, RbSnBi₃Te₆ and Rb_{0.94}Ca_{0.94}Bi_{3.06}Te₆ crystallize in the orthorhombic space group *Cmcm* and are isostructural to CsPbBi₃Te₆. CsNa_{0.98}Bi_{4.01}Te₇ is isostructural to CsPb₂Bi₃Te₇, the second member of the family. KSnSb₃Te₆ exhibits a different crystal structure found for the selenides CsAg_{0.5}Bi_{3.5}Se₆ and CsCdBi₃Se₆.⁵ The thermoelectric properties of these compounds could not be assessed because these compounds can not be prepared as pure phases so far. Alkali tellurides and the ternary phases CsBi₄Te₆ and RbBi_{3.66}Te₆ were identified as side products. The quality of the needles also was quite poor.

For high temperature applications, the bulk nanostructured-systems based on PbTe showed promising thermoelectric properties. These are both n-type (AgPb_mSbTe_{m+2} (LAST),⁶ Pb_{1-x}Sn_xTe-PbS⁷) and p-type (Na_{1-x}Pb_mSb_yTe_{m+2} (SALT),⁸ Ag(Pb_{1-y}Sn_y)_mSbTe_{2+m} (LASTT)⁹) thermoelectric materials. The work done in this dissertation was related to the p-type systems NaPb_mSbTe_{m+2} (Chapter 3), NaPb_{18-x}Sn_xMTe₂₀ (Chapter 4) and KPb_{18-x}Sn_xMTe₂₀ (Chapter 5).

Among these systems, NaPb_mSbTe_{m+2} exhibited the most promising thermoelectric properties. Characterization of members with m=6, 8 and 12 showed thermal conductivity values varying between 1.05 W/m·K at 300 K and 0.65 W/m·K at 670 K for m=6. This is slightly lower than that reported for Na_{0.95}Pb₂₀SbTe₂₂ (0.85 W/m·K at 670 K).⁸ This decrease in thermal conductivity derives mainly through their low lattice thermal conductivity (~ 0.45 W/m·K at 650 K for NaPb₈SbTe₁₀). TEM studies

on low and high m members of $\text{NaPb}_m\text{SbTe}_{m+2}$ revealed the presence of nanostructures embedded in the PbTe matrix. This is believed to be the reason for the low lattice thermal conductivity. High and low m value members exhibit large positive thermopower at high temperature ($\geq 300 \mu\text{V/K}$ at 650 K) with electrical conductivity $\sim 100\text{-}200 \text{ S/cm}$ at 650 K.

Addition of Sn to $\text{NaPb}_{18}\text{SbTe}_{20}$ and $\text{KPb}_{18}\text{SbTe}_{20}$ improved the mechanical strength of the specimens but did not improve the electrical properties of the parent materials. $\text{NaPb}_{18}\text{SbTe}_{20}$ is a p-type material. Partial substitution of Pb by Sn resulted in an increase in the hole carriers and the electrical conductivity. However, this increase in electrical conductivity did not compensate for the decrease in thermopower and increase of the electronic thermal conductivity. As a consequence, the power factor of the $\text{NaPb}_{18-x}\text{Sn}_x\text{SbTe}_{20}$ compounds is not as high as that of $\text{NaPb}_{18}\text{SbTe}_{20}$. SEM and TEM analysis indicated the cast ingots to be not true solid solutions. Micro-size inclusions rich in Sb were observed by SEM and nano-size precipitates were observed by TEM. The accurate chemical composition of these nano-size phases could not be determined due to instrumental limitation. However their dark aspect suggests that these areas are rich in light elements.

The $\text{KPb}_{18-x}\text{Sn}_x\text{MTe}_{20}$ series has weaker mechanical properties than its Na analog. They are also not so water-stable. Different types of inclusions were observed by BSE microscopy. Some of them are rich in Sb whereas others contain Pb, K, Sb, Te and O. Most likely a phase containing K forms upon cooling and tends to oxidize upon contact with water. $\text{KPb}_{18}\text{SbTe}_{20}$ is a n-type semiconductor. Addition of Sn to the system

introduced more holes in the system and a compensation between positive and negative charge carriers occur for a composition close to $x=5$. All compositions with $x \geq 5$ showed p-type behavior. The power factors of these compositions do not exceed that of $\text{KPb}_{18}\text{SbTe}_{20}$ because of the loss in thermopower.

Substituting Sb by Bi in $\text{NaPb}_{18-x}\text{Sn}_x\text{MTe}_{20}$ and $\text{KPb}_{18-x}\text{Sn}_x\text{MTe}_{20}$ resulted in more brittle samples. BSE imaging revealed the presence of micro-size inclusions inside the $\text{Pb}_{1-x}\text{Sn}_x\text{Te}$ matrix. They are mixtures of pure Bi precipitates and quaternary Pb/Sn/Bi/Te phases. TEM studies on $\text{NaPb}_{13}\text{Sn}_5\text{BiTe}_{20}$ showed the presence of nano-size precipitates and lamellar features, which may be an indication of local ordering between the PbTe and SnTe phases. No TEM analysis was done for the K analogs, but the low lattice thermal conductivity of some samples suggests the presence of nanostructures in the matrix. Such features were observed for the parent system $\text{K}_{1-x}\text{Pb}_{m+\delta}\text{Sb}_{1+\gamma}\text{Te}_{m+2}$.

The various systems studied showed low lattice thermal conductivity. Different characterization techniques were used to analyze the samples. SEM analysis on samples indicated the presence of micro-size inclusions rich in Sb/Bi. Because of their size and random distribution, these inclusions could not be observed by X-ray diffraction. HRTEM studies confirmed the presence of nano-size features. Due to experimental limitation, the exact composition of these features is unknown. Because of Coulombic interactions, one could assume that the regions would be rich in alkali metal and pnictogen. However, the existence of micro-size inclusions rich in pnictogen has an impact in the amount of pnictogen in the nano-size precipitates.

Some issues still need to be addressed. The samples are quite weak mechanically, which jeopardizes their potential industrial applications. The more robust samples are

those prepared by slow cooling. Quenched samples are much more brittle. As a result, some gradient of concentration may exist along the ingot for samples prepared by slow cooling. SEM and TEM analysis clearly indicate the existence of micro- and nano-size inclusions. The exact chemical composition of the nanostructures embedded in the PbTe matrix is still unknown as TEM analysis can not give accurate information about the nature of these nano-size inclusions. Hence the understanding of the formation of these phases is not complete. Zhu et al have studied in detail quenched $\text{AgPb}_{18}\text{Sb}_{1-x}\text{Te}_{20}$ samples.¹⁰ Detailed TEM analysis on the samples did not indicate any presence of nanostructures. Their results prove that the formation of nanoprecipitates is favored by slow cooling conditions, which suggest they form through nucleation and growth.

To improve the strength of the samples, more hot press and spark plasma sintering experiments need to be explored. The technique has the advantage of resulting in more homogeneous samples as the powders are mechanically milled for several hours before sintering. Several studies on known thermoelectric systems such as $(\text{Bi/Sb})_2\text{Te}_3$,^{11, 12} Ge/Si ¹³ and TAGS $((\text{GeTe})_x(\text{AgSbTe}_2)_{100-x})$ ¹⁴ alloys have shown significant improvement in the figure of merit compared to their bulk counterpart.

In the case of bismuth antimony alloys, nanopowders from the elemental chunks¹¹ and from grinded cast ingots¹² were pressed by direct-current hot-press. A peak ZT value ~ 1.3 and 1.4 at 473 K was obtained for the pellets prepared from elemental chunks¹¹ and ingots¹² respectively (for comparison, commercial bulk $(\text{Bi/Sb})_2\text{Te}_3$ have maximum ZT ~ 1 at 350 K). Such improvement in ZT derives from a reduction in the thermal conductivity. TEM analysis showed that grains have good crystallinity and large angles

between them, which results in isotropic properties. Nanosized features within the grains were also observed. According to EDS, these features are pure Sb phase in the case of powders from the elements and Te phase in the case of powders from cast ingots.

A maximum $ZT \sim 1.3$ was reported at 1173 K for n-type nanostructured bulk SiGe (bulk commercial materials have maxi $ZT \sim 0.9$ at 1173 K).¹³ The SiGe nanopowders, prepared by mechanical alloying, were hot-pressed by the direct current induced hot pressing at temperatures ~ 1273 -1473 K. A thermal conductivity ~ 2.5 W/m·K was reported for the nanostructured SiGe, much lower than that reported for the bulk alloy (4.6 W/m·K).

In the case of TAGS, ingots with composition $(\text{GeTe})_x(\text{AgSbTe}_2)_{100-x}$ ($x=75, 80, 85$ and 90) were prepared by temperature synthesis. The ingots were then crushed, ball-milled and hot-pressed 773 K under 70 MPa for 30 min. A low lattice thermal conductivity ~ 0.8 W/m·K at room temperature was measured for all compositions.¹⁴ As a result, $ZT \sim 1.5$ at 725 K was reported for $x = 75, 80$ and 85. TEM studies showed nanoscale inhomogeneities embedded in crystallites with sizes varying between tens of nanometers to several microns.

Hot-press experiments have also been carried out on the LAST system.¹⁵ Both stoichiometric, Pb-rich and Te-rich compositions were studied. Maximum $ZT \sim 1.1$ was reported for $\text{Ag}_{0.8}\text{Pb}_{18.3}\text{Sb}_{0.8}\text{Te}_{20}$ but no TEM study was mentioned. Recent studies have reported on the thermoelectric properties of Pb-rich LAST pellets prepared by combining mechanical alloying and spark-plasma sintering (SPS).^{16, 17} The pellets were annealed for different periods. The advantage of using SPS compared to hot-pressing is that the heat is generated internally, which facilitates a very high heating or cooling rate. $ZT \sim 1.5$ was

reported for the pellet with composition $\text{Ag}_{0.8}\text{Pb}_{22.5}\text{SbTe}_{20}$ annealed for 30 days at 700 K. Nanoscopic black regions embedded in the PbTe matrix were observed by HRTEM. The number and size of these precipitates increase with annealing time. The presence of these inclusions further scatters phonons. As a result, the thermal conductivity of annealed samples is lower than that of unannealed samples.

Substitution of Ag by Cu in the $\text{AgPb}_m\text{SbTe}_{m+2}$ (LAST) system resulted in stronger samples. SEM analysis clearly showed precipitates of Cu_2Te and Sb_2Te_3 inside the PbTe matrix. The electrical conductivity of the samples was similar to that of the LAST compounds. All samples showed n-type behavior but the absolute value of the thermopower was not as high as that of LAST. The thermal conductivity of samples with $m \geq 18$ is slightly higher than that of LAST. As a result ZT no higher than 0.9 was obtained for $m=30$. PbTe samples doped only with Cu_2Te exhibited thermal instability issues associated with Cu migrating towards the surface of the sample.

We can see from these studies that partial substitution of Pb by Sn in $\text{NaPb}_{18}\text{SbTe}_{20}$ and $\text{KPB}_{18}\text{SbTe}_{20}$ does not improve the figure of merit ZT of the parent materials. The best p-type materials for thermoelectric materials are the $\text{Ag}(\text{Pb}_{1-y}\text{Sn}_y)_m\text{SbTe}_{2+m}$ (LASTT)⁹ and $\text{Na}_{1-x}\text{Pb}_m\text{Sb}_y\text{Te}_{m+2}$ (SALT)⁸ systems.

More complete experiments should be carried out to better understand the factors influencing the size and dispersion of the nanoparticles embedded in the PbTe matrix for the SALT system. Such experiments would require TEM studies of samples prepared with different cooling profiles and annealed under different conditions (temperature, time). More importantly, hot press and spark plasma sintering experiments should be

pursued. When optimal conditions for processing are determined, more robust specimen can be obtained. Further reduction in lattice thermal conductivity can be expected as a result of grain scattering. These synthesis techniques could be a useful tool to investigate the influence of the m value on the thermoelectric properties. Specimen with m values higher than 20 were too brittle to be characterized. More studies about the influence of the Na/Sb ratio may also help to optimize the power factor of the system.

References

1. Chung, D.-Y.; Hogan, T.; Brazis, P.; Rocci-Lane, M.; Kannewurf, C.; Bastea, M.; Uher, C.; Kanatzidis, M. G., *Science* **2000**, 287, 1024.
2. Chung, D.-Y.; Hogan, T. P.; Rocci-Lane, M.; Brazis, P.; Ireland, J. R.; Kannewurf, C. R.; Bastea, M.; Uher, C.; Kanatzidis, M. G., *J. Am. Chem. Soc.* **2004**, 126, 6414.
3. Hsu, K. F.; Chung, D. Y.; Lal, S.; Mroczek, A.; Kyratsi, T.; Hogan, T.; Kanatzidis, M. G., *J. Am. Chem. Soc.* **2002**, 124, 2410.
4. Hsu, K. F.; Lal, S.; Hogan, T.; Kanatzidis, M. G., *Chem. Commun.* **2002**, 13, 1380.
5. Kim, J. H.; Chung, D. Y.; Kanatzidis, M. G., *Chem. Commun.* **2006**, 15, 1628.
6. Hsu, K. F.; Loo, S.; Guo, F.; Chen, W.; Dyck, J. S.; Uher, C.; Hogan, T.; Polychroniadis, E. K.; Kanatzidis, M. G., *Science* **2004**, 303, 818.
7. Androulakis, J.; Lin, C. H.; Kong, H. J.; Uher, C.; Wu, C. I.; T., H.; Cook, B. A.; T., C.; Paraskevopoulos, M.; Kanatzidis, M. G., *J. Am. Chem. Soc.* **2007**, 129, 9780.
8. Poudeu, P. F. P.; D'Angelo, J.; Downey, A. D.; Short, J. L.; Hogan, T.; Kanatzidis, M. G., *Angew. Chem., Int. Ed.* **2006**, 45, 3835.
9. Androulakis, J.; Hsu, K. F.; Pcionek, R.; Kong, H. J.; Uher, C.; D'Angelo, J.; Downey, A. D.; Hogan, T.; Kanatzidis, M. G., *Adv. Mater.* **2006**, 18, 1170.
10. Zhu, T. J.; Yan, F.; Zhang, S. N.; Zhao, X. B., *J. Phys. D: Appl. Phys.* **2007**, 40, (11), 3537.
11. Ma, Y.; Hao, Q.; Poudel, B.; Lan, Y.; Yu, B.; Wang, D.; Chen, G.; Ren, Z., *Nano Lett.* **2008**, 8, (8), 2580.

12. Poudel, B.; Hao, Q.; Ma, Y.; Lan, Y. C.; Minnich, A.; Yu, B.; Yang, J.; Wang, D. Z.; Muto, A. J.; Vashaee, D.; Chen, X. Y.; Liu, J. M.; Dresselhaus, M. S.; Chen, G.; Ren, Z. F., *Science* **2008**, 320, 634.
13. Wang, X. W.; Lee, H.; Lan, Y. C.; Zhu, G. H.; Joshi, G.; Wang, D. Z.; Yang, J.; Muto, A. J.; Tang, M. Y.; Klatsky, J.; Song, S.; Dresselhaus, M. S.; Chen, G.; Ren, Z. F., *Appl. Phys. Lett.* **2008**, 93, (19), 193121.
14. Yang, S. H.; Zhu, T. J.; Sun, T.; He, J.; Zhang, S. N.; Zhao, X. B., *Nanotechnology* **2008**, 19, (24), 245707.
15. Kosuga, A.; Uno, M.; Kurosaki, K.; Yamanaka, S., *J. Alloys Compd.* **2005**, 391, 288.
16. Wang, H.; Li, J.-F.; Nan, C.-W.; Zhou, M.; Liu, W.; Zhang, B.-P.; Kita, T., *Appl. Phys. Lett.* **2006**, 88, 092104.
17. Zhou, M.; Li, J.-F.; Kita, T., *J. Am. Chem. Soc.* **2008**, 130, (13), 4527.

MICHIGAN STATE UNIVERSITY LIBRARIES



3 1293 03063 4012